Pumping an atom laser

Graham Russell Dennis

A thesis submitted for the degree of
Doctor of Philosophy
at The Australian National University

16 May 2010

In memory of those we have lost these past few months:

Nikki, Elva & Scotchie.

Declaration

Except where acknowledged in the customary manner, the material presented in this thesis is, to the best of my knowledge, original and has not been submitted in whole or part for a degree in any university.

Graham Russell Dennis

May 2010

Acknowledgements

First and foremost, I would like to thank my supervisors: Joe, John and Craig. I have learnt much these past few years, and that could not have happened without your guidance.

My supervisors have been invaluable in the writing of this thesis, as have my other proof-readers: André, Cristina, Daniel, Mattias, Michael, Rob, Robin, and Stuart.

I have had many interesting and enlightening discussions with people too numerous to count, but I must particularly thank Nick for his endless patience explaining the goings on of experimental physics, and Mattias & Simon for teaching me the tricks with performing numerical simulations.

Over the past several years, I have had the great pleasure to work with an incredible group of people in the Physics Olympiad program. In particular, I would like to thank Kate, Matt, Alix & Lucy. Who could ever thought it was possible to have fun while writing an exam? As strange as it sounds, you have helped keep me sane.

Throughout my PhD, I have collaborated closely with the Rubidium and Helium BEC experimental groups at the ANU. In particular, I would like to thank John, Nick & Cristina from the Rubidium group and Andrew & Rob from the Helium group for helping me learn the 'language' of experimental physics.

I would like to thank the many people with whom I have shared my time at the 'department of many names': André, Ben, Cristina, Daniel, Emily, Finn, Gordon, JD, Jean-François, Julien, Justin, Kate, Mahdi, Matthew, Mattias, Michael, Nick, Oliver, Paul A., Paul S., Rachel, Robin, Simon, Stuart, Sven and Tom. You have been excellent company. In time, perhaps, I can repay my debt of baked goods and chocolate.

Finally, I would like to thank my parents Greg & Lynda. You have encouraged me to delve into the nature of things, and to seek the satisfaction of understanding.

Abstract

Measurement is our fundamental tool for learning about the world around us. It is from observing trends in measurements that we develop the theories that enable us to predict future behaviour, and it is against measurements that we determine the validity of these theories. Increases in the precision of our measurements are fundamental to our understanding.

Atom interferometry is a new method for performing precision measurements that uses the matter-wave nature of atoms to perform interferometry experiments analogous to those performed with photons. However, in contrast to optical interferometry, which uses coherent sources of photons, atom interferometry uses thermal atomic sources, in part due to the unavailability of high-flux coherent atomic sources. Although pulsed coherent atomic sources are presently available, continuous sources are not. Creating a truly continuous coherent source for atoms is tricker than for photons. One of the largest challenges is that atom number is conserved. A source of atoms is therefore necessary to produce a truly continuous atom laser. This source must be used to replenish the lasing mode of the atom laser, and the process must operate without significantly disturbing the coherence properties of the lasing mode. It is this replenishment or pumping process that has been investigated theoretically in this thesis.

There are only two choices for the reservoir that makes the replenishment (or pumping) process of an atom laser irreversible: the empty modes of the optical field, and the empty modes of the atomic field. Processes of both forms are considered. Using an optical reservoir has the advantage that atoms are not necessarily lost as part of the pumping process, which is necessary when using an atomic reservoir. The efficiency of processes using an optical reservoir can therefore be higher. Using an atomic reservoir, however, has the advantage that it is easier to implement as one can use the standard experimental technique of evaporation which is commonly used in the production of pulsed coherent atomic sources. We show theoretically in this thesis that although it is possible to produce a continuous atom

laser using an atomic reservoir, the flux achieved in the geometry considered is insufficient to compete with pulsed coherent atomic sources for precision measurement. The results for the pumping process using an optical reservoir are more promising. Although condensed sources were used as the source for this process, a detailed comparison of the theoretical calculations and experimental results indicate that the detrimental reabsorption processes are suppressed. This suggests that it may be possible to use higher-flux thermal atomic sources to replenish the lasing mode of an atom laser with this pumping process.

Contents

Chapter 1

Introduction

Measurement is an essential part of our developed world. We measure the quantities of ingredients when following a recipe, the sizes of pieces of wood when making a cabinet, and we obsessively measure time for fear of running out of it. Many of these measurements are quite imprecise: "The recipe only asks for 100 g of chocolate, but a little more won't hurt," "I can sand it down later if it doesn't quite fit," or the notorious, "I'll be with you in a minute..." Very precise measurements are, however, making an increasing impact on our lives, although usually without our realising it. Perhaps the best example of this is the Global Positioning System (GPS), which uses a system of satellites orbiting the Earth, each of which contains an atomic clock for the very precise measurement of time. By comparing the arrival times of the precisely synchronised signals of these satellites, it is possible to determine one's position on Earth to an accuracy of better than 1 m, even without a precision clock at the receiver.

One way of performing precise measurements is to compare the quantity to be measured against a known scale and count the number of divisions. For example, when measuring the length of a piece of string with a ruler, one counts the number of divisions between the ends of the string. Fortunately, many of the divisions are numbered, making this an easier task. The precision of this kind of measurement is limited by the smallest division on the ruler. If I want to know how long my piece of string is to the nearest micron, I will need a measurement device with a smaller division.

An alternative way of performing precise measurements is using interferometry. At its heart, interferometry is about the measurement of the difference in the readings of two oscillators. This difference can be measured to much less than a single division (a cycle of the oscillator). The precision with which this difference can be measured increases as

more oscillators are compared. While using oscillators with smaller divisions improves interferometric measurements, the precision can also be improved by comparing more oscillators. This is the advantage of using interferometry for precision measurements.

Many different kinds of oscillators can be used in interferometry measurements. Most use the phase oscillations of photons, however some use the matter-wave oscillations of electrons [1], neutrons [2], or atoms [3–6]. Using photons has the advantage that they are easy to produce in large numbers using lasers, while using any of the matter-wave oscillators has the advantage of a significantly higher oscillation frequency, and therefore shorter scale division. The heaviest of these matter-oscillators, the atom, has an oscillation frequency of approximately $Mc^2/\hbar\omega \sim 10^{10}$ times larger than that of a visible photon. The flux difference between photon sources and atom sources is significant however. While the count rate for a watt of photons is approximately $10^{19}\,\mathrm{s}^{-1}$, typical atom interferometers offer only $10^{7}\,\mathrm{s}^{-1}$. Without using entangled sources, the precision of interferometric measurements scales as the square-root of the number of particles measured, so there is still a potential improvement in sensitivity of $10^{10} \times \sqrt{10^7/10^{19}} = 10^4$. It is the aim of atom interferometry to make use of this improvement in sensitivity for precision measurements.

Since the development of the first separated path atom interferometers in 1991 [3–6], atom interferometers have become competitive for the precision measurement of rotations [7] and gravity gradients [8], with sensitivities within about an order magnitude of the best experiments [9–11]. For the absolute measurement of the gravitational field strength, atom interferometry is world-leading [12], with sensitivities more than an order of magnitude below that of competing technologies.

In comparison to optical interferometry experiments, which typically use *coherent* optical sources such as (photon) lasers, the above atom interferometry experiments are performed with cold *thermal* atomic sources (the optical equivalent would be black-body radiation). Coherent sources — which are characterised by a macroscopic occupation of a single quantum state, and typically have a narrow spectral distribution — are useful in optical interferometry experiments in which the interaction time is independent of wavelength, as the measured phase difference depends on the optical frequency and therefore the wavelength. Sagnac interferometers, gravitational wave sensors, and any interferometer that measures path-length differences are all examples of interferometers that fall into this class. For atom interferometers however, it is more common that the phase difference for the equivalent experiment (in which the interaction time is also independent of wavelength)

will be *independent* of the de Broglie wavelength. The reason for this difference is due to the different dispersion relations (the expression for energy — or equivalently, frequency — as a function of wavenumber) of photons and atoms. While it is therefore important that optical interferometers use sources with a narrow range of wavelengths, this is not necessarily the case for atom interferometers.

Coherent atomic sources were developed in 1995 with the achievement of Bose-Einstein Condensation (BEC) in dilute atomic gases [13–15]. Such sources offer several advantages for atom interferometers: a narrower momentum distribution allows better control of systematic uncertainties related to the initial position and velocity; more efficient operation of large-momentum transfer beam splitters, which are highly velocity selective, increasing the interaction time; and quantum degeneracy offers the possibility of increasing sensitivity through the use of squeezed or entangled atomic sources. Unfortunately, the lower fluxes of currently available coherent atomic sources leads to a higher shot noise, which more than offsets the increases in sensitivity discussed above. To access these potential advantages of coherent atomic sources, in particular the interesting possibilities involving the use of squeezed and entangled atomic sources (which are interesting in their own right for fundamental tests of quantum mechanics), it will be necessary to produce a truly continuous high-flux source of coherent atoms: the pumped atom laser.

Pulsed (or quasi-continuous) atom lasers have been produced before. These are sources of highly degenerate coherent atoms outcoupled from a Bose-Einstein condensate. These coherent atomic sources are limited by the atom number of the source condensate; once the atoms run out, the atom laser stops. The condensate must be replenished (or pumped) to produce a truly continuous coherent atomic source. We focus our attention on this pumping process in this thesis.

1.1 Photon lasers and Atom lasers

The basic features necessary of a continuous atom laser are analogous to the features of a continuous photon laser: a resonator, a lasing mode, an outcoupling process, and a Bose-stimulated pumping mechanism (see Figure 1.1). The first three of these features are well understood for an atom laser; experimentally realising the fourth, the pumping mechanism, has presented the greatest challenge.

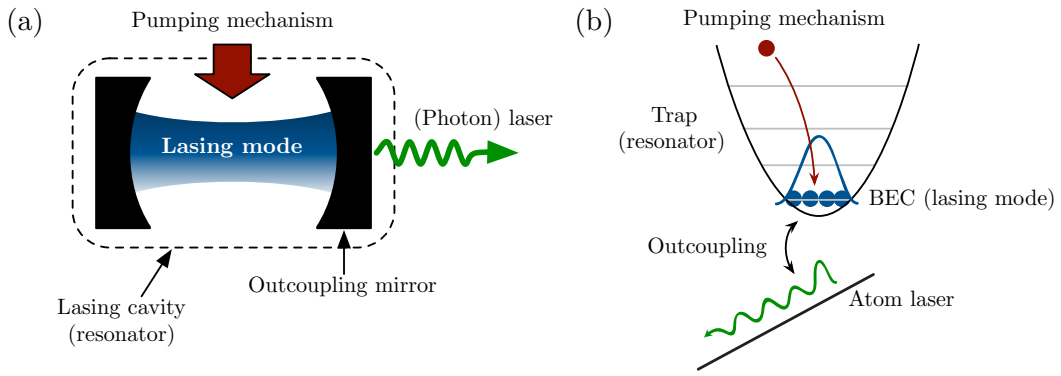

Figure 1.1: Schematic diagrams of (a) a photon laser, and (b) an atom laser.

1.1.1 The resonator

In a photon laser, the resonator is typically a cavity formed between two (or more) mirrors trapping the photons within a region of space. The optical mode trapped within the resonator is the lasing mode. For an atom laser, the resonator is an 'atom trap', either an optical trap using the ac Stark shift to trap the atoms in a region of high optical intensity, or a magnetic trap using the Zeeman shift to selectively trap certain magnetic hyperfine states near a local minimum of the magnetic field strength.

1.1.2 The lasing mode

The necessary property for the lasing mode of a laser — be it optical or atomic — is that it have an occupation much greater than one [17]. For photons, such a highly-degenerate mode was first achieved with the development of the maser [18]; a photon condensate cannot exist in equilibrium as total photon number is not conserved [16, 19]. Total atom number is, however, conserved and Bose-Einstein condensation occurs below a critical temperature [20]. Below this critical temperature, a significant fraction of the atoms in the system occupy a single spatial mode; exactly what is required of the lasing mode of an atom laser.

The process of Bose-Einstein condensation can be understood in a simplified picture in which the atoms are viewed as wave-packets with an extent of the order of the thermal de Broglie wavelength $\lambda_{\mathrm{dB}} = (2\pi\hbar^2/Mk_BT)^{1/2}$, where M is the mass of the atom, k_B is Boltzmann's constant, and T is the temperature of the atoms. At room temperature, the de Broglie wavelength is sufficiently small ($\sim 5 \times 10^{-11}\,\mathrm{m}$ for ^{4}He at $T = 300\,\mathrm{K}$) that the atoms behave as point-like billiard balls (upper panel of Figure 1.2). As the temperature decreases, the de Broglie wavelength increases (second panel of Figure 1.2).

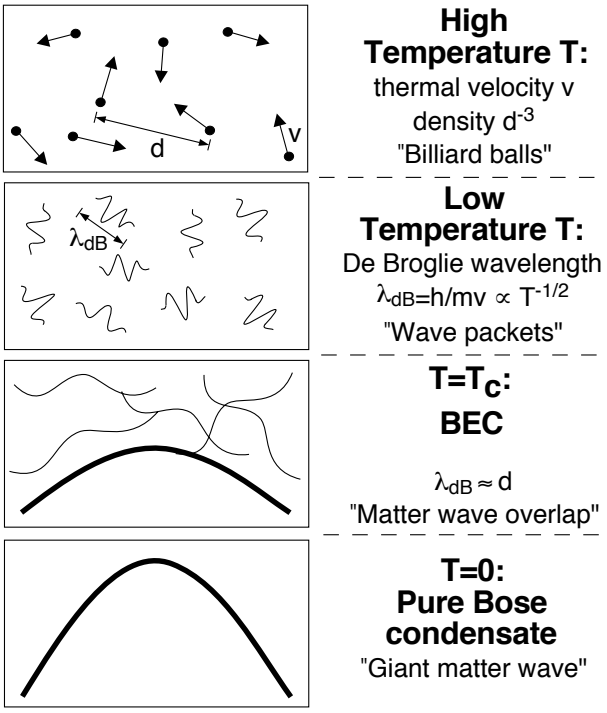

Figure 1.2: Comparison of the behaviour of a Bose gas at different temperatures. See main text. Reproduced from Ketterle *et al.* [16].

As the temperature continues to decrease, the de Broglie wavelength approaches the mean interparticle separation d and the atomic matter waves begin to overlap (third panel of Figure 1.2). Below this temperature, a Bose-Einstein condensate begins to form, until at $T = 0\,\mathrm{K}$, all atoms are in the condensate (lower panel of Figure 1.2). Conservation of total number is necessary for BEC, as it is because of this that the interparticle separation d remains constant as temperature is decreased (in a box of constant volume); for photons, as the temperature is decreased the total number of photons in the system decreases, increasing the mean interparticle separation d faster than the photon wavelength increases. Hence photon condensation cannot occur in equilibrium.

Bose-Einstein condensation is a macroscopic quantum phenomenon with a broad range of applications beyond the production of atom lasers. Perhaps the most interesting of these are the development of *quantum simulators* [21, 22], experiments which directly realise theoretical condensed matter models, which were initially proposed as approximations to other systems. For example, the Bose-Hubbard model [23] of interacting bosons was realised by loading a BEC into an optical lattice. By changing the depth of the optical lattice, the ratio of the tunnelling and interaction terms was changed, permitting direct observation of the superfluid to Mott-insulator transition [24]. Quantum simulators are possible for

a variety of other systems, including Josephson junctions [25], and reduced-dimension systems such as the Tonks-Girardeau model of 1D hard core bosons [26–28]. Dilute gas BECs have also been used in the direct observation of persistent currents in the form of vortices and vortex lattices [29], the coherent control of optical information [30], the observation of quantum optical effects in atoms such as the Hanbury-Brown-Twiss effect [31], and four-wave mixing [32].

One of the advantages of dilute gas BEC that gives these systems such a broad range of applications is the extraordinary degree to which these systems can be controlled and manipulated: their effective dimensionality can be changed by changing shape of the confining potential [28, 33, 34]; the de Broglie wavelength is controllable over many orders of magnitude $1\,\mathrm{nm} \lesssim \lambda_{\mathrm{dB}} \lesssim 10\,\mu\mathrm{m}$; the sign and magnitude of interparticle interactions can be controlled [35], from attractive interactions through to almost infinitely repulsive interactions, including the non-interacting limit; essentially 'pure' potentials (minimal absorption) may be constructed in a range of forms, including highly regular potentials such as harmonic or lattice potentials and random potentials with controllable statistical properties [36–40]. Dilute gas BEC also has a range of available observational tools for probing the system [16] including absorptive imaging, phase-contrast imaging, Bragg scattering [41], and ion detection for metastable species [42].

The goal of atom optics is to use the fundamental differences between atoms and photons in the application of the principles of laser optics to new fields of research.

1.1.3 The outcoupling process

The outcoupling of light from the lasing mode of a photon laser is achieved by making one of the cavity mirrors partially transparent. The emitted light is the output mode of the photon laser. For atom lasers, an analogous technique can be used in optical traps by lowering the depth of the trap until some atoms can tunnel out of the trap with the assistance of gravity. In magnetic traps, electromagnetic radiation is applied to transfer the atoms (either directly with radio-frequency radiation [43, 44], or indirectly via a multi-photon Raman transition [45–47]) into a magnetically-insensitive state in which they fall freely under gravity. These outcoupled atoms form the atom laser beam.

Contemporary atom optics experiments operate in pulsed mode. Without a pumping mechanism, the atom laser beam is limited by the size of the condensate. Once all of the atoms in the BEC have been outcoupled, the atom laser beam stops. This places a

fundamental limit on the linewidth (related to the longitudinal velocity-spread) of the atomic pulse produced: the Fourier limit, proportional to the inverse of the outcoupling time [48]. This limit can be made arbitrarily small (until the energy uncertainty in the BEC due to interatomic scattering becomes significant [49]) at the expense of an arbitrarily low atom flux. Practically however, this trade-off cannot be made because the signal-to-noise ratio for atom laser experiments depends critically on the atomic flux [50]. The only way to achieve a high-flux atom laser with a narrow linewidth is with a continuous pumping process, which has yet to be achieved experimentally.

The outcoupling process for atom lasers displays a range of behaviour. While intuitively one might expect that increasing the outcoupling strength would continuously increase the atom laser flux, this is only true up to a point. In the limit of large outcoupling rates, a bound state forms [51], and the atom laser shuts down [52].

The outcoupling process also strongly affects the transverse profile of the atom laser. Due to the mean-field repulsion the atoms experience as they leave the condensate, significant interference fringes are observed on the atom laser profile [53, 54]. These interference fringes complicate the spatial profile of the atom laser, making any atom interferometry experiment that relies upon separated beam paths more challenging. The interference fringes on the transverse profile increase the sensitivity of the experiment to imperfections in the spatial overlap of the previously-separated beams when they are combined for detection. These interference fringes may be reduced by outcoupling from the bottom of the condensate [55] or by giving the atoms a significant momentum kick as they leave the condensate [56]. The transverse profile of the atom laser is discussed in greater detail in Section 2.4.2.

Even in the absence of a pumping process, atom lasers can be used for a variety of interesting experiments. The correlation and counting statistics of an atom laser have been measured [57], an atom laser has been guided with optical waveguides [58], and a BEC has been probed using an atom laser outcoupled from a separate BEC [59]. There have also been interesting theoretical proposals to produce non-classical atom laser states using the interatomic interaction of the atom laser [60], or by outcoupling with squeezed light [61]. There is even a related proposal to generate controllable atom–light entanglement [62].

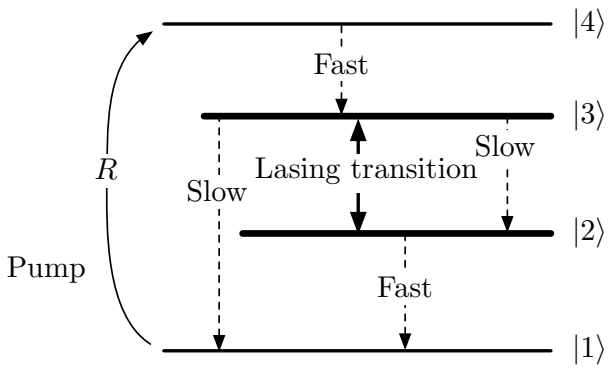

Figure 1.3: Schematic diagram of the atomic levels of a 4-level photon laser. The dashed lines indicate decay processes, and the 'slow' and 'fast' labels indicate the relative speed of the decay processes. Once atoms decay to the $|1\rangle$ ground state, they are pumped to the state $|4\rangle$ with a rate R. This process drives the population inversion on the $|2\rangle \leftrightarrow |3\rangle$ transition. Diagram derived from Figure 13.2-6 of Saleh and Teich [63].

1.1.4 The pumping mechanism

The photon laser

The pumping mechanism of a laser acts as an amplifier for the lasing mode. It is what replenishes the losses of the lasing mode due to outcoupling and any other loss processes. Without a pumping mechanism, an optical laser is simply a leaky cavity emitting an exponentially-decreasing amount of light. The linewidth of this emitted light is limited by the linewidth of the optical cavity. The pumping mechanism for an optical laser not only permits continuous operation of the laser, it also narrows the linewidth of the laser in a process known as *gain-narrowing*. Gain-narrowing results from the saturation of the pumping process for large signals; no physical amplifier can amplify a signal indefinitely.

A pumping mechanism contains excitations that can each increase the occupation of the lasing mode by one. These excitations are replenished at a finite rate, limiting the rate at which the lasing mode may be increased. For example, in the 4-level photon laser model illustrated in Figure 1.3, atoms are pumped from the ground state $|1\rangle$ to the short-lived state $|4\rangle$ at a rate R. The atoms in state $|4\rangle$ may decay into the $|3\rangle$ state, the excited state of the lasing transition. The occupation of the lasing mode cannot therefore be increased at a rate greater than R. Any physical pumping mechanism will also exhibit saturation, and therefore the lasing mode will exhibit gain-narrowing.

Another necessary property of the pumping mechanism is that it be irreversible; once the occupation of the lasing mode has been increased, the probability that the process will reverse should be negligible. This is achieved by coupling to a large number of essentially-

empty modes known as a *reservoir*. In the case of the 4-level photon laser model depicted in Figure 1.3, once an atom in the excited state $|3\rangle$ of the lasing transition has undergone stimulated emission into the $|2\rangle$ state by emitting a photon into the lasing mode, it rapidly decays into the ground state $|1\rangle$. By ensuring that the ground state of the lasing transition $|2\rangle$ decays to the true ground state $|1\rangle$ faster than it can absorb a lasing photon, the pumping process is made irreversible. The reservoir is comprised of the essentially-empty modes of the optical field coupled to the $|1\rangle \leftrightarrow |2\rangle$ transition, as once a photon on this transition is emitted spontaneously, it does not return. This reservoir ensures that the modes of the $|2\rangle$ atomic level are also essentially empty.

Finally, in many circumstances it is desirable that the photon laser have only one lasing mode. If the resonator supports many different modes, and if the gain bandwidth of the pumping mechanism encompasses more than one of these modes, multiple lasing modes may result. As the photon–photon interaction is negligible, these lasing modes do not directly interact, and may operate independently. Multiple-mode operation in a photon laser is naturally suppressed if the pumping process is *homogeneously broadened*. In homogeneously broadened gain media, every excitation of the pumping mechanism contributes to the gain of the lasing modes in the same way, i.e. every excitation is resonant with the same lasing modes. If the gain medium is *inhomogeneously broadened*, some classes of pumping excitations will contribute differently to the total gain profile than others. A classic example of this is Doppler-broadening. Atoms in a gain medium have a finite temperature, and their motion affects what frequencies they are resonant with (in the laboratory frame) due to the Doppler effect. If the size of this frequency broadening is greater than the natural linewidth of the lasing transition, not all of the pumping excitations will be resonant with a given lasing mode. It will therefore only be those pumping excitations resonant with a given lasing mode that are saturated by it; lasing modes resonant with the remaining unsaturated pumping excitations will continue to experience gain and may lase independently. In this case, thse lasing modes will experience gain independently, each without saturating the other. If the pumping process is inhomogeneously broadened, undesirable modes can be removed by increasing their loss in the optical resonator. This is naturally achieved by the addition of a second, smaller cavity inside the resonator that is only resonant with the desired mode. If the pumping process is homogeneously broadened however, while multiple modes may initially experience gain, only the mode with the largest net gain will survive as the gain saturates, resulting in single-mode operation.

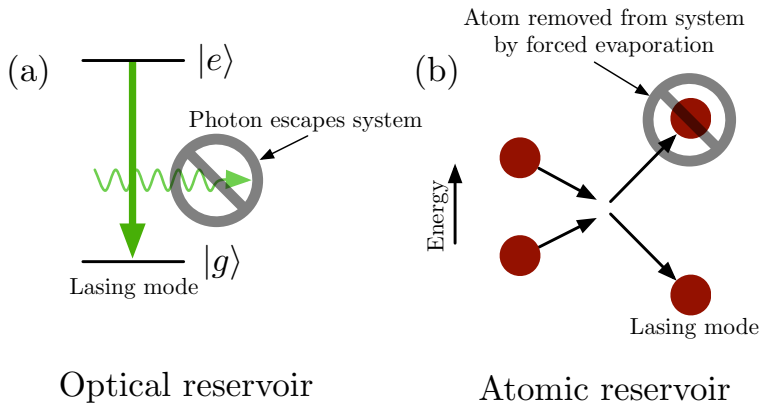

Figure 1.4: Classes of pumping mechanism for an atom laser as defined by the reservoir. The crossed circle indicates which excitation in the process irreversibly leaves the system.

The atom laser

There are two choices of reservoir for the pumping mechanism of an atom laser: the empty modes of the optical field, or the empty modes of the atomic field. Each choice corresponds to a different class of pumping mechanism. These two classes are illustrated in Figure 1.4. In the first, an atom in an excited internal state is brought into resonance with the lasing mode such that it can decay into the lasing mode. It is Bose-stimulated to do so by the occupation of the atomic lasing mode. Once the emitted photon leaves the system, this decay is irreversible. In the second, two atoms scatter into different energy states, one going into the lasing mode, while the other gains sufficient energy to be removed from the system (for example, due to forced evaporation, the same process used in the formation of BEC).

Single-mode operation is not simply desirable for an atom laser, it is necessary. Due to the large interatomic interactions, multiple lasing modes in an atom laser could not operate independently. Significant scattering would occur between the lasing modes, increasing the linewidth of both, possibly destroying any laser-like qualities in the process. While the interatomic interactions can be 'switched off' with the use of a Feschbach resonance [35], the loss processes are such that higher energy modes experience *less* loss than the lower modes in this case, making the atom laser unstable [64]. This instability can be resolved by increasing the interatomic interactions [64], adding a position-dependent loss near the edge of the lasing mode [65], and in the case of non-zero interatomic interactions, by increasing the pumping rate [66].

In all of the phenomenological atom laser pumping models discussed in the previous paragraph, the gain mechanism was effectively 'homogeneously broadened' in the sense

that all pumping excitations contributed equally to the gain of all modes. This is more difficult to achieve for atom lasers than for photon lasers. In the case of photon lasers, the dispersion relation for the by-product of the gain process (the de-excited atom) is relatively flat by comparison to that of the lasing mode. This is a useful property, as it means that pumping excitations with a wider range of momenta are resonant with the lasing mode, as variations in the momentum difference between the pumping excitation and the lasing mode can be compensated for by the by-product with minimal energy cost. In the limit of a perfectly flat dispersion relation for the by-product, pumping excitations of any momentum can result in gain if the decay process conserves energy, and due to the finite linewidth of the transition, energy need only be conserved to within this energy uncertainty. As a concrete example, consider the photon laser pumping mechanism illustrated in Figure 1.3 and the atom laser pumping mechanism illustrated in Figure 1.4(a). The fundamental difference between these two pumping mechanisms is that for the photon laser, the emitted photon goes into the lasing mode with the atom as the by-product, while for the atom laser, it is the decayed atom that enters the lasing mode with the emitted photon as the by-product. The decay process of these pumping mechanisms is illustrated in Figure 1.5. If a violation of energy conservation is permitted in this process of up to $\pm\hbar\Delta\omega$ where $\Delta\omega$ is the linewidth of the $|g\rangle \leftrightarrow |e\rangle$ transition, excited atoms with a wider range of momenta can contribute gain to the lasing mode in the case of the photon laser than in the case of the atom laser. Specifically, for the photon laser, the wavenumber of the excited atom in the direction parallel to the lasing mode may vary by

$$\left(\Delta k_{i,\parallel}\right)_{\mathrm{ph}} \approx \frac{2M\Delta\omega}{\hbar\left|\boldsymbol{k}_{\gamma}\right|},$$

where M is the mass of the atom. The wavenumber of the atom in perpendicular directions is unconstrained. However, for the atom laser, the magnitude of the wavenumber of the excited atom may only vary by (assuming a stationary lasing mode of size d)

$$\left(\Delta\left|\boldsymbol{k}_{i}\right|\right)_{\mathrm{at}} \approx \frac{2\Delta\omega}{c} + \frac{\pi}{d},$$

where the second term is due to the momentum-width of the lasing mode. For the $\lambda = 633\,\mathrm{nm}$ lasing transition of the Helium-Neon gas laser, $\Delta\omega \approx 100\,\mathrm{MHz}$ [67], $M_{\mathrm{Ne}} = 3.3\times10^{-26}\,\mathrm{kg}$, giving $\left(\Delta k_{i,\parallel}\right)_{\mathrm{ph}} \sim 10^{10}\,\mathrm{m^{-1}}$ for the photon laser and $\left(\Delta\left|\boldsymbol{k}_{i}\right|\right)_{\mathrm{at}} \sim 10^{6}\,\mathrm{m^{-1}}$ for an atom laser with a lasing mode of size $d \sim 10\,\mu\mathrm{m}$. This difference significantly constrains

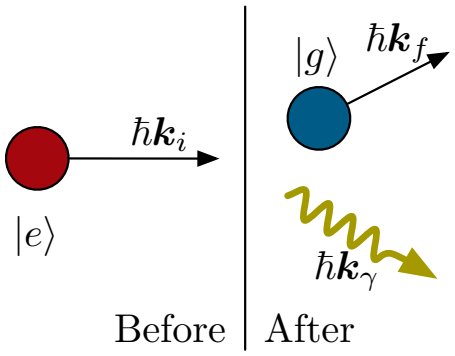

Figure 1.5: Excited state atom in the $|e\rangle$ state with momentum $\hbar\boldsymbol{k}_i$ decays into an atom in the ground state $|g\rangle$ with momentum $\hbar\boldsymbol{k}_f$, and a photon with momentum $\hbar\boldsymbol{k}_\gamma$. In the photon laser pumping mechanism, the photon is in the lasing mode and the atom decays into a mode that is essentially unoccupied (the atom is the by-product of the gain process), while in an atom laser pumping mechanism, the decayed atom is in the lasing mode and the emitted photon is part of the reservoir which is essentially unoccupied (the photon is the by-product of the gain process).

the possible momentum width of the pumping excitations for the pumping mechanism to operate in the 'homogeneously broadened' limit. If the momentum width of the pumping excitations is greater than this, gain for modes other than the main lasing mode will not be saturated by the main lasing mode. The remaining modes experiencing gain will increase the linewidth of the atom laser.

In Chapter 4, a pumping mechanism for an atom laser using an optical reservoir is considered. We attempt to solve the problem of the narrow permissible momentum width of the pumping excitations by making their momentum distribution sufficiently narrow that it can be guaranteed that every atom will be momentum-resonant with the pumping process at some point.

In Chapter 5, a pumping mechanism using atomic modes as the reservoir is considered. Although their dispersion relation cannot be considered flat with respect to that of the lasing mode atoms, it is far more so than that of the photons. The difficulty with this pumping mechanism is that it is inescapable that thermal atoms will be in the vicinity of the lasing mode. Scattering between the lasing and thermal atoms will contribute to the collisional broadening of the lasing mode. Using a Feschbach resonance to cancel these interactions is not an option as the pumping mechanism itself relies upon interatomic collisions.

1.2 Matter wave amplification...

A number of matter-wave amplification processes using the two possible reservoirs have been proposed and demonstrated. These are discussed in this section. While none of these matter-wave amplification processes constitute an atom laser pumping mechanism, it is envisaged that an atom laser pumping mechanism would be based on a similar process.

1.2.1 ... using an optical reservoir

A number of previous experiments observing the process of super-radiant Rayleigh scattering seem to offer a physical mechanism for providing pumping through matter-wave amplification [68, 69]. Super-radiant Rayleigh scattering occurs when a far off-resonant laser illuminates an elongated BEC. A matter-wave grating forms along the long axis of the BEC and atoms are preferentially scattered into non-stationary momentum states. By providing a moving 'seed', researchers were able to demonstrate pulsed coherent amplification via the Rayleigh super-radiance mechanism. However, this type of matter-wave amplification is a transient phenomena, observed over timescales ranging from tens [68] to hundreds of microseconds [69]. On longer timescales, scattering into successively higher momentum modes seems unavoidable [70], resulting in a 'fan'-shaped scattering pattern [71].

Two promising mechanisms for providing a pumping mechanism consistent with a continuous atom laser have recently been demonstrated. The first is far-detuned stimulated Raman scattering [72, 73], in which atoms in one internal atomic state are Bose-stimulated to make transitions into an alternative atomic state. The second, reported by Ginsberg *et al.* [30], is a resonant coupling driven by electromagnetically-induced transparency (EIT), demonstrated as stimulated decay of atom pulses into a condensate in a freely falling frame. In both cases, the coupling from the source mode is irreversible and the laser mode is dark to the photons produced by the stimulated transitions.

In Chapter 4, we consider a pumping mechanism for an atom laser derived from the Raman superradiance and EIT matter-wave amplification processes. A discussion of related theoretical proposals is given in that chapter.

1.2.2 ... using an atomic reservoir

The production of BEC using the standard technique of evaporation [74, 75] is a matter-wave amplification process [76–78]. In this process, atoms with energy greater than a threshold are removed from the system, thus reducing the mean energy of the system. Elastic collisions

between the remaining atoms lead to rethermalisation at a lower temperature. This process has been experimentally demonstrated to give exponential gain of the condensate mode until the thermal cloud becomes significantly depleted [78].

Four-wave mixing of matter-waves [32] is a fundamentally similar process in which two atoms undergo a collision and scatter into different momentum modes. When one of the final momentum modes is already occupied, this process is Bose-enhanced, and is a matter-wave amplification process [79]. If neither of the final momentum modes is occupied, the scattering process gives rise to entanglement between the atoms in the final momentum modes, although only classical correlations have been observed to date [80].

In Chapter 5, we consider a pumping mechanism for an atom laser driven by evaporation. In particular, we consider the temperature and flux requirements of the atomic source that must be used to replenish the thermal cloud.

1.3 Thesis overview

In this thesis, we focus on an investigation of atom laser pumping mechanisms, both using an optical reservoir, which is discussed in Chapter 4, and with an atomic reservoir, which is discussed in Chapter 5. In Chapter 3, we discuss an unusual process in which atomic interaction energy is directly converted into kinetic energy, potentially leading to the formation of entangled atomic beams. An overview of the common theoretical tools and techniques is given in Chapter 2, and concluding remarks to the thesis are given in Chapter 6.

The following is a list of publications written as part of the author's PhD.

1. '*Observation of transverse interference fringes on an atom laser beam*'; R. G. Dall, L. J. Byron, A. G. Truscott, G. R. Dennis, M. T. Johnsson, M. Jeppesen, and J. J. Hope, Opt. Express **15**, 17673 (2007).

2. '*Multibeam atom laser: Coherent atom beam splitting from a single far-detuned laser*'; J. Dugué, G. Dennis, M. Jeppesen, M. T. Johnsson, C. Figl, N. P. Robins, and J. D. Close, Phys. Rev. A **77**, 031603 (2008).

3. '*A pumped atom laser*'; N. P. Robins, C. Figl, M. Jeppesen, G. R. Dennis, and J. D. Close, Nat. Phys. **4**, 731 (2008).

4. '*Approaching the Heisenberg limit in an atom laser*'; M. Jeppesen, J. Dugué, G. R. Dennis, M. T. Johnsson, C. Figl, N. P. Robins, and J. D. Close, Phys. Rev. A **77**, 063618 (2008).

5. '*Paired-atom laser beams created via four-wave mixing*'; R. G. Dall, L. J. Byron, A. G. Truscott, G. R. Dennis, M. T. Johnsson, and J. J. Hope, Phys. Rev. A **79**, 011601 (2009).

6. '*Pulsed pumping of a Bose-Einstein condensate*'; D. Döring, G. R. Dennis, N. P. Robins, M. Jeppesen, C. Figl, J. J. Hope, and J. D. Close, Phys. Rev. A **79**, 063630 (2009).

7. '*Creating EPR entangled matter beams via instabilities in Bose-Einstein condensates*'; G. R. Dennis and M. T. Johnsson, in preparation (2010).

8. '*Quantum kinetic theory model of a continuous atom laser*'; G. R. Dennis, M. Davis, and J. J. Hope, in preparation (2010).

In this thesis, the work of papers 1, 3, and 5–8 are presented. Specifically, the work of paper 1 is presented in Section 2.4.2, that of papers 5 and 7 are presented in Chapter 3, that of papers 3 and 6 is presented in Chapter 4, and that of paper 8 is presented in Chapter 5.

Chapter 2

Background Theory

In this chapter we discuss the theoretical tools and techniques that will be employed in this thesis. In Section 2.4.2, the results of an application of one of these techniques is discussed. These results have been published in Dall *et al.* [81].

2.1 Indistinguishability and Bose-Einstein condensation

All fundamental particles fall into one of two classes determined by their intrinsic spin: *bosons*, which have integral spin (0, 1, 2, 3, ... in units of $\hbar$), and *fermions*, which have half-integral spin ($\frac{1}{2}$, $\frac{3}{2}$, $\frac{5}{2}$, ...). Quantum-mechanically these two classes of particles behave very differently. Due to a deep property of the relationship between quantum mechanics and (special) relativity known as the spin-statistics theorem [82], the many-body wavefunction of a system of identical bosons is invariant under particle interchange,

$$\Psi_{\text{bosons}}(\boldsymbol{x}_1, \boldsymbol{x}_2, \ldots, \boldsymbol{x}_i, \ldots, \boldsymbol{x}_j, \ldots, \boldsymbol{x}_N) = \Psi_{\text{bosons}}(\boldsymbol{x}_1, \boldsymbol{x}_2, \ldots, \boldsymbol{x}_j, \ldots, \boldsymbol{x}_i, \ldots, \boldsymbol{x}_N), \quad (2.1)$$

while for a system of identical fermions it changes sign,

$$\Psi_{\text{fermions}}(\boldsymbol{x}_1, \boldsymbol{x}_2, \ldots, \boldsymbol{x}_i, \ldots, \boldsymbol{x}_j, \ldots, \boldsymbol{x}_N) = -\Psi_{\text{fermions}}(\boldsymbol{x}_1, \boldsymbol{x}_2, \ldots, \boldsymbol{x}_j, \ldots, \boldsymbol{x}_i, \ldots, \boldsymbol{x}_N). \quad (2.2)$$

The consequence of this difference is that while there may be more than one boson in a mode, there cannot be more than one fermion in any mode. Were two fermions to occupy the same mode, (2.2) would require the wavefunction to be identically zero. This difference between fermions and bosons is not always noticed however. For a gas at room

temperature and pressure, the average occupancy of any mode is sufficiently small ($\sim 10^{-6}$ for Helium at $T = 300\,\mathrm{K}$, $p = 10^5\,\mathrm{Pa}$) as to make the probability that one such mode will be multiply-occupied (in the case of a bosonic gas) entirely negligible. Under these conditions bosonic and fermionic systems behave identically.

In the previous paragraph it was neglected that Helium is not a fundamental particle, but a *composite* particle. If the typical energy of particles in a system is sufficiently low that the composite structure of individual particles is not significantly affected during collisions or interactions with other particles, the composite particles may be treated as effectively indivisible. For the room temperature sample of Helium discussed above, the mean kinetic energy of each atom is $3.9 \times 10^{-2}\,\mathrm{eV}$, while the energy required to excite an electron in the atom (and therefore significantly alter the internal state of the atom) is significantly larger at $20\,\mathrm{eV}$.

Bose-Einstein condensation occurs in the opposite limit in which the lowest energy mode of the system gains a significant fraction of the total population of the system. This macroscopically-occupied mode is known as the condensate. Bose-Einstein condensation was originally predicted by Einstein [83, 84] in 1924 who was inspired by Bose's description of photons as identical particles symmetric under interchange [85]. Bose showed that it follows from this property, i.e. (2.1), that the average occupation of a state with energy E in a system of identical non-interacting bosons is

$$\langle n(E) \rangle = \frac{1}{e^{(E-\mu)/k_B T} - 1}, \tag{2.3}$$

where k_B is Boltzmann's constant, and μ is the chemical potential of the system, which is determined by the normalisation condition $N = \sum_i \langle n(E_i) \rangle$, where N is the number of particles in the system. If the zero of energy is chosen to be the lowest energy state in the system, the positivity of $\langle n(0) \rangle$ requires that the chemical potential μ must be negative. Equation (2.3) is known as the Bose-Einstein distribution and reduces to the classical result $e^{-(E-\mu)/k_B T}$ in the limit that $|\mu| \gg k_B T$, i.e. $\langle n(0) \rangle \ll 1$. For a gas of Helium at room temperature and pressure, $\langle n(0) \rangle \approx 10^{-6}$.

Bose-Einstein condensation in weakly-interacting gases occurs below a phase-transition at a critical temperature T_c. In the infinite-particle limit, this transition is sharp, however in any real finite system, it is smooth. While Bose-Einstein condensation occurs in a range of systems, the temperature dependence of the condensate occupation depends on the form of the density of states of the system. The density of states for a free two-dimensional gas

is such that a condensate can only form at $T = 0$, and so true Bose-Einstein condensation does not occur; while for a free three-dimensional gas, the critical temperature is finite and Bose-Einstein condensation occurs for $T < T_c$. While it was the latter case in which Bose-Einstein condensation was originally derived, most BEC experiments are performed in either magnetic or optical traps, which are approximately harmonic near the trap minimum. For a Bose gas trapped in a three-dimensional harmonic trap with trapping frequencies ω_x, ω_y and ω_z the condensate fraction is [20]

$$\frac{N_0}{N} = \left[1 - \left(\frac{T}{T_c}\right)^3\right], \tag{2.4}$$

where $N_0 = \langle n(0) \rangle$ is the occupation of the ground state, and the critical temperature is given by

$$k_B T_c \approx 0.94 \hbar \overline{\omega} N^{1/3}, \tag{2.5}$$

and $\overline{\omega} = (\omega_x \omega_y \omega_z)^{1/3}$ is the geometric mean of the trapping frequencies. For typical parameters of the ^{87}Rb experiment considered in this thesis ($N = 5 \times 10^5$, $\omega_x = \omega_y = 2\pi \times 130\,\text{Hz}$, $\omega_z = 2\pi \times 13\,\text{Hz}$), $T_c \approx 220\,\text{nK}$. At the critical temperature, the condensate is unoccupied ($N_0 \approx 0$), however the condensate occupation increases sharply with decreasing temperature until all particles are in the ground state[1] at $T = 0$. In this limit, all particles in the system are in the same single-particle mode, and the many-body wavefunction of the system is

$$\Psi(\boldsymbol{x}_1, \boldsymbol{x}_2, \ldots, \boldsymbol{x}_N) = \prod_{i=1}^{N} \phi(\boldsymbol{x}_i), \tag{2.6}$$

where $\phi(\boldsymbol{x})$ is the macroscopically-occupied mode. In Section 2.4, a more accurate description of the state of a BEC will be considered, however (2.6) is a useful approximation in many circumstances.

[1] Technically this is only true for a gas of non-interacting bosons. For weakly-interacting bosons, a non-zero fraction of the atoms are not in the condensate at $T = 0$. However this fraction has never been significantly greater than 1% in experiments with ultracold gases [86]. The condensate depletion is neglected in this thesis.

2.2 Hamiltonian

After second-quantisation [87], the Hamiltonian describing an interacting multi-component field of bosonic atoms is

$$\begin{aligned}\hat{H} = &\sum_i \int d\boldsymbol{x}\, \hat{\Psi}_i^\dagger(\boldsymbol{x}) \left(-\frac{\hbar^2\nabla^2}{2M} + V_i(\boldsymbol{x})\right) \hat{\Psi}_i(\boldsymbol{x}) \\ &+ \frac{1}{2}\sum_{ijmn} \int\int d\boldsymbol{x}\, d\boldsymbol{x}'\, \hat{\Psi}_i^\dagger(\boldsymbol{x})\hat{\Psi}_j^\dagger(\boldsymbol{x}')V_{ijmn}(\boldsymbol{x}-\boldsymbol{x}')\hat{\Psi}_m(\boldsymbol{x}')\hat{\Psi}_n(\boldsymbol{x}),\end{aligned} \tag{2.7}$$

where $\hat{\Psi}_i(\boldsymbol{x})$ is the bosonic annihilation operator that removes an atom of mass M in the internal state i at position $\boldsymbol{x}$. These fields obey the commutation relations

$$\left[\hat{\Psi}_i(\boldsymbol{x}),\, \hat{\Psi}_j(\boldsymbol{x}')\right] = 0, \tag{2.8}$$

$$\left[\hat{\Psi}_i(\boldsymbol{x}),\, \hat{\Psi}_j^\dagger(\boldsymbol{x}')\right] = \delta_{ij}\delta(\boldsymbol{x}-\boldsymbol{x}'). \tag{2.9}$$

The potential $V_i(\boldsymbol{x})$ describes the external potential experienced by atoms in the internal state i, and includes contributions from gravity and any optical or magnetic trapping fields present. A common example encountered in this thesis is the cylindrically symmetric harmonic trap of the form

$$V(\boldsymbol{x}) = \frac{1}{2}M\left(\omega_r^2x^2 + \omega_r^2y^2 + \omega_z^2z^2\right), \tag{2.10}$$

where ω_r is the radial trapping frequency, and ω_z is the trapping frequency in the z direction. In this thesis, ω_r is always significantly larger than ω_z. In this case, x and y are referred to as the 'tight' trapping dimensions, and z the 'weak' trapping dimension.

The interatomic interaction potential $V_{ijmn}(\Delta\boldsymbol{x})$ describes scattering processes between two particles in the m and n internal states separated by $\Delta\boldsymbol{x}$ that scatter into the i and j internal states. If the atoms have only a single internal state, this is simply the interatomic potential.

Atoms do, however, have internal structure: the quantum numbers n, l and m_l for the orbit of each electron; the projections m_s for the spin of each electron; and the quantum numbers describing the state of the atom's nucleus. Due to the couplings between these different states, none of these are 'good' quantum numbers in the sense that they label eigenstates of the full single-atom Hamiltonian. The set of good quantum numbers depends on the regime in which the experiment is operated. In the limit of weak magnetic fields,

which is the only case encountered in this thesis, the good quantum numbers are the principal quantum number for the outermost electron n, the total electronic orbital angular momentum L, the total electronic spin S, the total electronic angular momentum J, the nuclear spin I, the total atomic angular momentum F, and its projection m_F [88].

In practice, most of the quantum numbers that determine the internal atomic state are constant for experimentally relevant states, and are omitted when describing the atomic states. For alkali gases, the experimentally relevant states fall into two classes: long-lived 'ground' states, and optically-accessible states which rapidly decay to the 'ground' states. The former are completely determined by the quantum numbers F and m_F (e.g. $|F=1,m_F=-1\rangle$ denotes the magnetically-trapped $\left|n=5,L=0,S=\frac{1}{2},J=\frac{1}{2},I=\frac{3}{2},F=1,m_F=-1\right\rangle$ state of ^{87}Rb), while the optically-accessible excited states are determined by the quantum numbers J, F and m_F. For the alkali gases, the quantum number J for these excited states may take two values, $J=\frac{1}{2}$ and $J=\frac{3}{2}$. Due to the fine-structure splitting between states with different values of J (7 THz for ^{87}Rb), only excited states with a single value of J are typically accessed in a given experiment. The states with $J=\frac{3}{2}$ are the most relevant experimentally as these have a closed transition with the ground states ($|F=2,m_F=2\rangle \leftrightarrow \left|J=\frac{3}{2},F'=3,m_F=3\right\rangle$ for atoms with $I=\frac{3}{2}$, such as ^{87}Rb), which can be used for optical cooling and trapping [89]. As only a single value of J describes the excited states accessed in a given experiment, the excited states are typically denoted only by the quantum numbers F and m_F, with the F quantum number primed to distinguish it from the ground states as in $|F'=3,m_F=3\rangle$. This notation is used in this thesis, with the excited states belonging to the D_2 transition (i.e. the relevant ^{87}Rb excited states have $J=\frac{3}{2}$).

It is the internal structure of atoms that enables them to be manipulated using a rich variety of techniques. In the presence of a magnetic field, the different m_F levels have different energies separated by the Zeeman splitting. This enables atoms in certain m_F levels to be trapped in a local magnetic field minimum. In the presence of radio-frequency radiation resonant with this Zeeman splitting, the m_F levels within a given F manifold are coupled, causing a transfer of population between levels. In the presence of intense optical radiation far-detuned from resonant transitions, depending on the polarisation, all m_F levels can receive the same energy shift and be trapped equally. In the presence of pairs of optical fields, momentum can be coherently transferred to the atoms, and depending on the polarisations, simultaneously change their internal state. The atom–light coupling

term is discussed in detail in Section 4.5.

In the absence of additional coupling terms, the equations of motion for the atomic field operators $\hat{\Psi}_i$ are determined by the Hamiltonian (2.7),

$$\begin{aligned} i\hbar\frac{\partial}{\partial t}\hat{\Psi}_i(\boldsymbol{x}) = &\left(-\frac{\hbar^2\nabla^2}{2M} + V_i(\boldsymbol{x})\right)\hat{\Psi}_i(\boldsymbol{x}) \\ &+ \sum_{jmn}\int d\boldsymbol{x}'\, V_{ijmn}(\boldsymbol{x}-\boldsymbol{x}')\hat{\Psi}_j^\dagger(\boldsymbol{x}')\hat{\Psi}_m(\boldsymbol{x}')\hat{\Psi}_n(\boldsymbol{x}). \end{aligned} \tag{2.11}$$

The most complicated part of this evolution is the non-local term governed by the inter-atomic interaction potential $V_{ijmn}(\Delta\boldsymbol{x})$. The following section discusses an approximation in which this potential may be approximated by a *local* interaction, simplifying the evolution described by (2.11).

2.3 Atomic scattering

The Hamiltonian (2.7) neglects the composite structure of atoms, approximating atoms with different internal states as different 'fundamental' particles. This Hamiltonian is therefore an effective field theory, which is only valid on length scales larger than the atomic size. At the low temperatures and densities typical of ultracold atom experiments, these structures are not probed, and the effective field theory is a good approximation. Indeed, it is usual that the details of the interaction potential $V_{ijmn}(\Delta\boldsymbol{x})$ are not probed either, and the potential can be approximated by a contact interaction [86]

$$V_{ijmn}(\Delta\boldsymbol{x}) \approx U_{ijmn}\delta(\Delta\boldsymbol{x}), \tag{2.12}$$

where $U_{ijmn} = 4\pi\hbar^2 a_{ijmn}/M$, and a_{ijmn} is the scattering length for the corresponding interaction. The scattering length is chosen to reproduce the long-range scattering behaviour of the exact potential $V_{ijmn}(\Delta\boldsymbol{x})$. Equation (2.12) is known as the s-wave scattering approximation, as only collisions in which the atoms have zero relative motional angular momentum occur. This neglects collisions between particles having non-zero relative angular momentum that would otherwise occur due to the finite extent of the full potential. These collisions contribute negligibly at the temperatures typical of ultracold atom experiments (particularly for non-polar particles), as atoms with non-zero relative motional angular momentum cannot approach sufficiently closely for $V_{ijmn}(\Delta\boldsymbol{x})$ to be non-negligible.

In alkali atoms there are two ground-state F manifolds[2], which are separated by the hyperfine splitting. The energy difference between these two manifolds is sufficiently large that collisions between atoms in the lower manifold cannot scatter atoms into the upper manifold. As a result of this restriction, it can be shown [90] that the scattering only depends on the total angular momentum of the colliding atoms. The interaction term of (2.7) can be written as

$$\hat{H}_{\text{int}} = \frac{1}{2}\sum_{S,m_S} g_S \int d\boldsymbol{x}\, \hat{\Xi}^\dagger_{S,m_S}(\boldsymbol{x})\hat{\Xi}_{S,m_S}(\boldsymbol{x}), \tag{2.13}$$

where $g_S = 4\pi\hbar^2 a_S/M$ is the nonlinear interaction strength, and a_S is the s-wave scattering length for the total (of the two colliding atoms) hyperfine spin S channel. For bosons, the total hyperfine spin S is restricted to even values due to symmetry [90]. The quasi-molecular operator $\hat{\Xi}_{S,m_S}$ is defined in terms of the atomic annihilation operators and the appropriate Clebsch-Gordan coefficients

$$\hat{\Xi}_{S,m_S}(\boldsymbol{x}) = \sum_{m_F,m'_F} \left(F, m_F; F, m'_F \middle| S, m_S\right) \hat{\Psi}_{F,m_F}(\boldsymbol{x})\hat{\Psi}_{F,m'_F}(\boldsymbol{x}), \tag{2.14}$$

where $(j_1, m_1; j_2, m_2|J, M)$ is a Clebsch-Gordan coefficient. For the metastable noble gases, the interaction term is also in the form of (2.13) as only one F manifold is accessible. In metastable Helium, the scattering lengths a_S differ by 25%. The consequences of this difference are considered in Chapter 3. For ^{87}Rb, however, the scattering lengths for collisions between $F = 1$ atoms differ by at most 1% [91], permitting the approximation $g_0 \approx g_2$. In this limit, the nonlinear interaction Hamiltonian can be written in the simple form

$$\hat{H}_{\text{int}} = \frac{1}{2}U_{\text{int}}\sum_{ij}\int d\boldsymbol{x}\, \hat{\Psi}^\dagger_i(\boldsymbol{x})\hat{\Psi}^\dagger_j(\boldsymbol{x})\hat{\Psi}_j(\boldsymbol{x})\hat{\Psi}_i(\boldsymbol{x}). \tag{2.15}$$

When interatomic scattering is well-described by the simple interaction (2.15), the operator evolution of (2.11) may be simplified to

$$i\hbar\frac{\partial}{\partial t}\hat{\Psi}_i(\boldsymbol{x}) = \left(-\frac{\hbar^2\nabla^2}{2M} + V_i(\boldsymbol{x}) + U_{\text{int}}\sum_j \hat{\Psi}^\dagger_j(\boldsymbol{x})\hat{\Psi}_j(\boldsymbol{x})\right)\hat{\Psi}_i(\boldsymbol{x}). \tag{2.16}$$

[2] An F manifold is a set levels sharing all quantum numbers except m_F. An example is the $F = 1$ manifold of ^{87}Rb, which contains $|F = 1, m_F = 1\rangle$, $|F = 1, m_F = 0\rangle$, and $|F = 1, m_F = -1\rangle$.

While the approximation made to the nonlinear interaction term of the Hamiltonian has made these equations local, they cannot be solved exactly for the general case. In the absence of the nonlinear term, the atoms do not interact with one another, and the energy eigenstates do not depend on the number of atoms in the system. In this limit, the field operator $\hat{\Psi}_i$ may be decomposed as

$$\hat{\Psi}_i(\boldsymbol{x}, t) = \sum_j \hat{a}_{ij}\phi_{ij}(\boldsymbol{x}, t), \tag{2.17}$$

where the $\phi_{ij}(\boldsymbol{x}, t)$ are a set of orthogonal basis functions (the single-particle modes) obeying

$$i\hbar\frac{\partial}{\partial t}\phi_{ij}(\boldsymbol{x}, t) = \left(-\frac{\hbar^2\nabla^2}{2M} + V_i(\boldsymbol{x})\right)\phi_{ij}(\boldsymbol{x}, t), \tag{2.18}$$

and $\hat{a}_{ij}$ are stationary bosonic annihilation operators for the corresponding single-particle modes.

With the addition of the nonlinear interaction term, the evolution of the field operator may not be decomposed into the sum of *stationary* bosonic annihilation operators and time-dependent basis functions; the evolution of each 'mode' would necessarily depend on the occupation of the other modes. It is this complication that makes (2.16) difficult to solve in the general case, either analytically *or numerically*. The difficulty numerically is the sheer amount of information needed to describe $\hat{\Psi}(\boldsymbol{x})$. For a system with $N = 100$ atoms that can each occupy one of $m = 100$ spatial modes, $\sim 10^{117}$ complex numbers are needed to describe $\hat{\Psi}(\boldsymbol{x})$. Typical BEC's have $N \gtrsim 10^5$. This complexity is a double-edged sword: it is what gives quantum computers their tremendous potential, but it is also what makes it hard to solve interacting many-body quantum problems with classical computers.

The following section discusses a limit in which the field operator can be approximated by a complex-valued function, whose evolution can feasibly be simulated numerically.

2.4 The Gross-Pitaevskii equation

For the moment, we consider the simpler case of a single-component atomic field $\hat{\Psi}(\boldsymbol{x})$.

As the difficulty in solving the evolution equation (2.16) lies in its operator nature, we

may seek to simplify the problem by considering its expectation value instead,

$$i\hbar\frac{\partial}{\partial t}\big\langle\hat{\Psi}(\boldsymbol{x})\big\rangle = -\frac{\hbar^2\nabla^2}{2M}\big\langle\hat{\Psi}(\boldsymbol{x})\big\rangle + V(\boldsymbol{x})\big\langle\hat{\Psi}(\boldsymbol{x})\big\rangle + U_{\mathrm{int}}\big\langle\hat{\Psi}^\dagger(\boldsymbol{x})\hat{\Psi}(\boldsymbol{x})\hat{\Psi}(\boldsymbol{x})\big\rangle. \tag{2.19}$$

This equation certainly does not contain all of the information about the quantum field $\hat{\Psi}(\boldsymbol{x})$; at best it can describe classical properties of the condensate, such as its density and mean local velocity. Neither is it a closed system; (2.19) cannot be solved without knowing the evolution of the higher-order expectation value $\big\langle\hat{\Psi}^\dagger(\boldsymbol{x})\hat{\Psi}(\boldsymbol{x})\hat{\Psi}(\boldsymbol{x})\big\rangle$. This higher-order expectation value should be well-approximated by $\Big|\big\langle\hat{\Psi}(\boldsymbol{x})\big\rangle\Big|^2\big\langle\hat{\Psi}(\boldsymbol{x})\big\rangle$ in the limit that the atomic field $\hat{\Psi}(\boldsymbol{x})$ has a large classical component,

$$\hat{\Psi}(\boldsymbol{x}) = \Psi(\boldsymbol{x}) + \delta\hat{\Psi}(\boldsymbol{x}), \tag{2.20}$$

where $\Psi(\boldsymbol{x}) = \big\langle\hat{\Psi}(\boldsymbol{x})\big\rangle$, and $\delta\hat{\Psi}(\boldsymbol{x})$ is 'small' in some sense (e.g. $\big\langle\delta\hat{\Psi}^\dagger(\boldsymbol{x})\delta\hat{\Psi}(\boldsymbol{x})\big\rangle \ll |\Psi(\boldsymbol{x})|^2$). In this limit, certain quantum-mechanical properties such as entanglement have been neglected. However, as the system is described in terms of an atomic field amplitude (and not a density), Eq. (2.19) will include single-particle interference phenomena; it is a semi-classical description of a BEC.

We might expect that the description of the BEC in terms of the many-body wavefunction (2.6) includes a large classical component in the sense defined above as all N particles are in the same single-particle mode $\phi(\boldsymbol{x})$. In this case, the expectation value of the field operator is

$$\begin{aligned}\big\langle\hat{\Psi}(\boldsymbol{x})\big\rangle &= \Big\langle N,0,0,\ldots\Big|\hat{\Psi}(\boldsymbol{x})\Big|N,0,0,\ldots\Big\rangle \\ &= \Big\langle N,0,0,\ldots\Big|\sqrt{N}\phi(\boldsymbol{x})\Big|N-1,0,0,\ldots\Big\rangle \\ &= 0.\end{aligned} \tag{2.21}$$

This perhaps unexpected result is a consequence of the symmetry of the initial state. The state is unchanged if the single-particle mode $\phi(\boldsymbol{x})$ is modified by an arbitrary global phase $\phi(\boldsymbol{x}) \mapsto e^{i\theta}\phi(\boldsymbol{x})$. This symmetry is preserved by the Hamiltonian (2.7) and results from the conservation of the total number of atoms in the system by Noether's theorem [92].

If we suppose for the moment that it is possible to create states that do not possess this symmetry, the BEC could instead be in the coherent state $|\Psi(\boldsymbol{x})\rangle$, with the expectation

value of the field operator acquiring the non-zero value

$$\left\langle \hat{\Psi}(\boldsymbol{x}) \right\rangle = \Psi(\boldsymbol{x}). \tag{2.22}$$

In this case, (2.19) becomes

$$i\hbar \frac{\partial}{\partial t}\Psi(\boldsymbol{x}) = \left(-\frac{\hbar^2 \nabla^2}{2M} + V(\boldsymbol{x}) + U_{\text{int}} \left|\Psi(\boldsymbol{x})\right|^2 \right) \Psi(\boldsymbol{x}), \tag{2.23}$$

where the condensate expectation value $\Psi(\boldsymbol{x})$ has normalisation $N = \int d\boldsymbol{x} \, |\Psi(\boldsymbol{x})|^2$. Equation (2.23) is known as the Gross-Pitaevskii (GP) equation.

It has been assumed in deriving the GP equation that the condensate will remain in a coherent state. This is an approximation as the nonlinear scattering term gives rise to collapse and revival of the global phase, exactly as occurs in the case of the anharmonic oscillator (see Section 2.6.1). This effect has been observed in BECs held in optical lattices [93], however the time-scale for collapse when BECs are held in magnetic or optical dipole traps is much larger than typical experimental timescales. For a ^{87}Rb condensate of $N = 5 \times 10^5$ atoms held in a trap with trapping frequencies $\omega_r = 2\pi \times 130\,\text{Hz}$ and $\omega_z = 2\pi \times 13\,\text{Hz}$, the time-scale for the collapse of the global phase is 120 ms, significantly longer than typical experimental timescales of the order of tens of milliseconds.

It must be stated at this point that the BEC cannot be created with the kind of broken phase-symmetry necessitated by (2.22). A coherent state is a particular superposition of number states,

$$|\alpha\rangle = e^{-\frac{1}{2}|\alpha|^2} \sum_{n=0}^{\infty} \frac{\alpha^n}{\sqrt{n!}} |n\rangle, \tag{2.24}$$

however any Hamiltonian that conserves number cannot couple states of different total number, and therefore cannot affect the total number distribution. A coherent state therefore cannot be formed by any number-conserving Hamiltonian.

Although derived using the concept of broken symmetry, it will be shown in the following that the GP equation is a good description of condensates where $\Psi(\boldsymbol{x})$ is known as the *order-parameter* of the condensate, and its global phase has no physical significance.

In reality, BECs are not formed in isolation, but a large sample of atoms is evaporatively cooled until a much smaller number of atoms remain in a Bose-condensed state. If the combined system has a total of N atoms, and there is a probability p that each atom may

be in the condensate, the state of the system after evaporation is given by

$$|\Psi\rangle = \sum_{n=0}^{N} \sqrt{\binom{N}{n}} p^{\frac{n}{2}} (1-p)^{\frac{N-n}{2}} e^{i\theta_n} |n\rangle_{\text{condensate}} |N-n\rangle_{\text{rest}}, \tag{2.25}$$

where $|n\rangle_{\text{condensate}}$ is the state of the condensate with n atoms in it, $|N-n\rangle_{\text{rest}}$ describes the rest of the system (the evaporated atoms) with $N-n$ atoms, and θ_n are phases associated with the different elements of the superposition. The prefactors in (2.25) describe a Binomial distribution in which each atom has a probability p of being in the condensate mode. On average, there will be $N_0 = pN$ atoms in the condensate. Note that as this state has a fixed total number of atoms N, it does not possess any of the unphysical broken symmetry assumed previously.

Once the evaporation process is complete, it is only the condensed part of the system that we are interested in. This part of the system is described by a reduced density matrix that is obtained by tracing over the rest of the system,

$$\begin{aligned}
\hat{\rho}_{\text{condensate}} &= \text{Tr}_{\text{rest}} \{|\Psi\rangle\langle\Psi|\} \\
&= \sum_{n=0}^{N} \binom{N}{n} p^n (1-p)^{N-n} \left(|n\rangle\langle n|\right)_{\text{condensate}} \\
&\approx \sum_{n=0}^{\infty} \frac{N_0^n e^{-N_0}}{n!} \left(|n\rangle\langle n|\right)_{\text{condensate}},
\end{aligned} \tag{2.26}$$

where in the last line we have used the result that in the limit $N \to \infty$ with $pN = N_0$ fixed, the Binomial distribution approaches a Poisson distribution with mean N_0. Regardless of how one motivates it, (2.26) is a reasonable approximation to the state of a BEC produced evaporatively; it seems unlikely that a lossy process such as evaporation would leave the system in a pure state, either a pure number state or a pure coherent state.

As a coherent state has a Poisson number distribution, a density matrix which is a Poisson-distributed mixture of number states is equal to a mixture over global phase of coherent states. Thus:

$$\hat{\rho}_{\text{condensate}} = \int_0^{2\pi} \frac{d\theta}{2\pi} \left| e^{i\theta} \Psi(\boldsymbol{x}) \right\rangle \left\langle e^{i\theta} \Psi(\boldsymbol{x}) \right|, \tag{2.27}$$

where $\int d\boldsymbol{x} \, |\Psi(\boldsymbol{x})|^2 = N_0$. We now have a description of the condensate in terms of coherent states once more, but this representation respects the global phase symmetry enforced by the conservation of total atom number.

As quantum mechanics is linear in state vectors and density matrices, the components of superpositions and mixtures can be considered *individually* when determining properties of the system. For example, if the system is in the state $\hat{\rho} = \sum_i p_i |\Psi_i\rangle\langle\Psi_i|$, then the evolution of each $\hat{\rho}_i = |\Psi_i\rangle\langle\Psi_i|$ can be considered individually and expectation values constructed from the expectation values for each $\hat{\rho}_i$. The expectation value of the operator $\hat{O}$ is

$$\langle\hat{O}\rangle = \mathrm{Tr}\{\hat{O}\hat{\rho}\} = \sum_i p_i \langle\Psi_i|\hat{O}|\Psi_i\rangle = \sum_i p_i \,\mathrm{Tr}\{\hat{O}\hat{\rho}_i\}.$$

In the context of (2.27), this means that the evolution of $\left|e^{i\theta}\Psi(\boldsymbol{x})\right\rangle$ for each θ may be considered individually. The evolution of each of these coherent states can be described by the GP equation (2.23). However, as every physical expectation value must conserve total number, they are therefore independent of the global phase θ. It therefore suffices to solve the GP equation for a single θ. In particular, the quantity $\hat{\Psi}(\boldsymbol{x})$ is *not* a physical observable, and therefore the fact that its expectation value depends on θ is not a problem. Physical expectation values such as $\hat{\Psi}^\dagger(\boldsymbol{x})\hat{\Psi}(\boldsymbol{x}')$ are independent of θ,

$$\left\langle\hat{\Psi}^\dagger(\boldsymbol{x})\hat{\Psi}(\boldsymbol{x}')\right\rangle = e^{-i\theta}\Psi^*(\boldsymbol{x})e^{i\theta}\Psi(\boldsymbol{x}') = \Psi^*(\boldsymbol{x})\Psi(\boldsymbol{x}'). \tag{2.28}$$

The concept of symmetry-breaking in this context is therefore a useful calculational aid, not a fundamental physical principle. It can be applied provided one understands that the global phase of the coherent state is meaningless.

The concept of spontaneously-broken symmetry is discussed in greater detail elsewhere [94, 95].

In the rest of this thesis, the symmetry-breaking assumption will be used. It is understood that this is a calculational tool equivalent to assuming the system to be in a state of the form of (2.27), which preserves the global phase symmetry dictated by total number conservation.

The Gross-Pitaevskii equation has been a tremendously successful description of Bose-condensed gases, and has been used to successfully describe a range of phenomenon, including collective excitations of the condensate [96, 97], vortex properties and dynamics [98–101], expansion of the condensate after trap switch-off [102], soliton dynamics [103], and four-wave mixing [32].

The nonlinear term of the Gross-Pitaevskii equation prevents it being solved analytically, however it is tractable numerically. The following section describes a limit in which the approximate form of the ground state of the GP equation may be obtained.

2.4.1 Thomas-Fermi approximation

The ground state of a condensate is described by the time-independent Gross-Pitaevskii equation [86],

$$\mu\Psi(\boldsymbol{x}) = \left(-\frac{\hbar^2\nabla^2}{2M} + V(\boldsymbol{x}) + U_{\text{int}}\left|\Psi(\boldsymbol{x})\right|^2\right)\Psi(\boldsymbol{x}), \tag{2.29}$$

where $\mu = \partial\langle\hat{H}\rangle/\partial N$ is the chemical potential of the condensate. In the limit that the nonlinear term is zero, the condensate ground state in a harmonic trap is Gaussian,

$$\Psi(\boldsymbol{x}) = \sqrt{N}\left(\frac{M\overline{\omega}}{\hbar\pi}\right)^{\frac{3}{4}}\exp\left[-\frac{M}{2\hbar}\left(\omega_x x^2 + \omega_y y^2 + \omega_z z^2\right)\right], \tag{2.30}$$

where $\overline{\omega} = (\omega_x\omega_y\omega_z)^{\frac{1}{3}}$ is the geometric mean of the trapping frequencies. As the nonlinear term is increased, interatomic repulsion will increase the mean separation of atoms and the ground state will become broader. For a sufficiently large scattering length, the kinetic energy term in (2.23) is small in comparison to both the potential and interaction terms as it depends on the second derivative of $\Psi(\boldsymbol{x})$. In the Thomas-Fermi approximation, the kinetic energy term is neglected, and the form of the wavefunction may be explicitly obtained,

$$\Psi(\boldsymbol{x}) = \begin{cases} \sqrt{\frac{\mu - V(\boldsymbol{x})}{U_{\text{int}}}} & \text{if } \mu - V(\boldsymbol{x}) \geq 0, \\ 0 & \text{otherwise.} \end{cases} \tag{2.31}$$

By requiring that $\Psi(\boldsymbol{x})$ be correctly normalised, the chemical potential is found to be

$$\mu = \left(\frac{15NU_{\text{int}}\overline{\omega}^3}{8\pi}\right)^{\frac{2}{5}}\left(\frac{M}{2}\right)^{\frac{3}{5}}. \tag{2.32}$$

The Thomas-Fermi approximation is only valid in the limit that the chemical potential given by (2.32) is much larger than the ground state energy of the harmonic trap, i.e. $\mu \gg \frac{1}{2}\hbar(\omega_x + \omega_y + \omega_z)$.

A comparison of the harmonic oscillator and Thomas-Fermi groundstates is given in

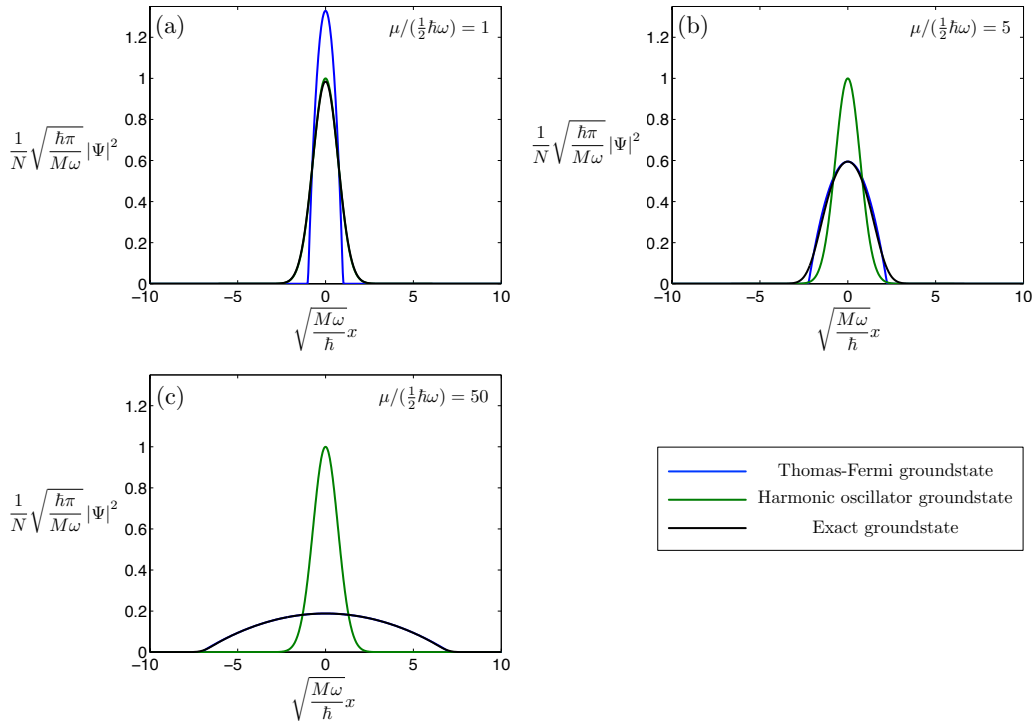

Figure 2.1: Comparison of harmonic oscillator, Thomas-Fermi and exact one-dimensional groundstates in different regimes. (a) $\mu/(\frac{1}{2}\hbar\omega) = 1$, (b) $\mu/(\frac{1}{2}\hbar\omega) = 5$, (c) $\mu/(\frac{1}{2}\hbar\omega) = 50$.

Figure 2.1. The density profile of the Thomas-Fermi wavefunction is that of a truncated inverted parabola. Near the edge of the wavefunction the Thomas-Fermi approximation breaks down. There, the nonlinear term is smaller, and the kinetic energy term is larger. In this region, the density profile of the exact groundstate decays smoothly due to the kinetic energy term. The Thomas-Fermi profile instead has a discontinuous first derivative. This discontinuity gives rise to a well-defined condensate radius in each dimension given by

$$r_{\mathrm{TF}} = \frac{1}{\omega_r}\sqrt{\frac{2\mu}{M}}, \tag{2.33}$$

where ω_r is the trapping frequency of that dimension.

The Thomas-Fermi approximation is useful as a simple description of the condensate when other parts of the system are of primary interest (it is used in this manner in the next section), or as an initial guess when finding the true groundstate of the system numerically.

2.4.2 Application: Transverse profile of the atom laser

As discussed in Section 1.1, an atom laser is formed by outcoupling from a condensate to produce a directional beam of highly coherent atoms. These atom lasers show great

promise for studies of fundamental physics and in high precision measurements [104]. For these applications, it is crucial that the output mode of the atom laser is 'clean' in both amplitude and phase to enable stable mode matching. It is therefore important to understand what influences the transverse profile of an atom laser. In this section, we demonstrate the application of the Gross-Pitaevskii equation to this problem. The results presented here have been published in Dall *et al.* [81].

For a magnetically-trapped condensate in an $F = 1$ manifold, the atoms in one of the m_F Zeeman levels are trapped (the low-field seeking level, either $m_F = 1$ as in metastable Helium or $m_F = -1$ as in ^{87}Rb), the atoms in the $m_F = 0$ level experience no magnetic trapping potential to first order (and are referred to as 'untrapped'), and the atoms in the level with m_F having the opposite sign to the trapped state experience a repulsive potential and are referred to as 'anti-trapped'. For metastable Helium (He*), the potentials experienced by the three levels in a cylindrically-symmetric trap are

$$V_{m_F}(\boldsymbol{x}) = m_F V_{\mathrm{trap}}(\boldsymbol{x}) = m_F \frac{1}{2} M \left(\omega_r^2 x^2 + \omega_r^2 y^2 + \omega_z^2 z^2\right). \tag{2.34}$$

These three levels are coupled by applying radio-frequency (rf) radiation resonant with the Zeeman splitting between the m_F levels. This Zeeman splitting is due to the magnetic trap (and a contribution from a constant bias field), and therefore the outcoupling process will be resonant along a surface of constant $V_{\mathrm{trap}}(\boldsymbol{x})$. Due to gravity, the centre of the condensate is a distance g/ω_y^2 below the centre of the magnetic trap. For weak traps, the outcoupling surfaces will be almost horizontal planes [see Figure 2.2(a)], while for stronger traps, the outcoupling surfaces will be spheroids approximately concentric with the condensate [see Figure 2.2(b)]. As we shall show, the shape of the outcoupling surface significantly impacts the transverse profile of the atom laser.

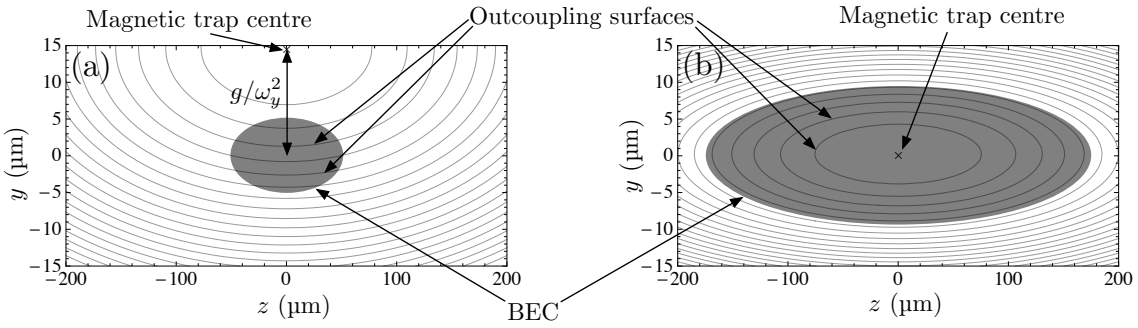

Figure 2.2: Outcoupling surfaces of condensates held in magnetic traps. Pictured is the size of the Thomas-Fermi condensate and contours of the magnetic trap equally spaced in energy. The origin of each coordinate system is the centre of the condensate, and the magnetic trap centres are marked by '×'. Figure (a) illustrates a condensate for typical parameters of the ^{87}Rb experiment at the Australian National University (ANU) [56]; $N = 5 \times 10^5$ atoms, $\omega_r = 2\pi \times 130\,\text{Hz}$, $\omega_z = 2\pi \times 13\,\text{Hz}$. The gravitational sag separating the centre of the condensate from the centre of the magnetic trap is $\Delta y = 15\,\mu\text{m}$. Figure (b) illustrates a condensate for typical parameters of the He* experiment at the ANU [81, 105]; $N = 2 \times 10^6$ atoms, $\omega_r = 2\pi \times 1020\,\text{Hz}$, $\omega_z = 2\pi \times 55\,\text{Hz}$. The gravitational sag separating the centre of the condensate from the centre of the magnetic trap is $\Delta y = 0.2\,\mu\text{m}$. The acceleration due to gravity is in the $-y$ direction. The aspect ratio of this figure is not 1:1 for reasons of clarity; the condensates are significantly more elongated than pictured.

The equations of motion for the system including the rf coupling are

$$i\hbar\frac{\partial}{\partial t}\Psi_1(\boldsymbol{x}) = \left[-\frac{\hbar^2\nabla^2}{2M} + V_{\text{trap}}(\boldsymbol{x}) + Mgy + U_{\text{int}}\left(|\Psi_1|^2 + |\Psi_0|^2 + |\Psi_{-1}|^2\right)\right]\Psi_1(\boldsymbol{x}) + \hbar\Omega\Psi_0(\boldsymbol{x}), \tag{2.35a}$$

$$i\hbar\frac{\partial}{\partial t}\Psi_0(\boldsymbol{x}) = \left[-\frac{\hbar^2\nabla^2}{2M} + Mgy + U_{\text{int}}\left(|\Psi_1|^2 + |\Psi_0|^2 + |\Psi_{-1}|^2\right)\right]\Psi_0(\boldsymbol{x}) + \hbar\Omega\Psi_1(\boldsymbol{x}) + \hbar\Omega\Psi_{-1}(\boldsymbol{x}), \tag{2.35b}$$

$$i\hbar\frac{\partial}{\partial t}\Psi_{-1}(\boldsymbol{x}) = \left[-\frac{\hbar^2\nabla^2}{2M} - V_{\text{trap}}(\boldsymbol{x}) + Mgy + U_{\text{int}}\left(|\Psi_1|^2 + |\Psi_0|^2 + |\Psi_{-1}|^2\right)\right]\Psi_{-1}(\boldsymbol{x}) + \hbar\Omega\Psi_0(\boldsymbol{x}), \tag{2.35c}$$

where Ω is the Rabi frequency, which is chosen to be real.

Initially, the condensate is in the ground state of the trapped $m_F = 1$ state. Once the outcoupling is turned on, the states are coupled and atoms are transferred to the $m_F = 0$ and $m_F = -1$ levels. In the limit of weak outcoupling, the atoms in the $m_F = 0$ level leave the region in which outcoupling is resonant without being significantly coupled into the $m_F = -1$ level. The $m_F = -1$ level is therefore relatively unpopulated and may be

neglected. It is the untrapped $m_F = 0$ level that we are primarily interested in as the freely-falling atom laser forms in this level.

For short times, most of the atoms are in the $m_F = 1$ level and we may use the Thomas-Fermi approximation to determine the effective potential seen by the untrapped $m_F = 0$ atoms. Inside the condensate, the effective potential for the untrapped atoms has contributions from gravity and interatomic interactions,

$$\begin{aligned} V_{\text{eff}}(\boldsymbol{x}) &= Mgy + U_{\text{int}} \left|\Psi_1(\boldsymbol{x})\right|^2 = Mgy + (\mu - V_{\text{trap}}(\boldsymbol{x}) - Mgy) \\ &= \mu - V_{\text{trap}}(\boldsymbol{x}). \end{aligned} \tag{2.36}$$

This effective potential experienced by the untrapped atoms is a repulsive harmonic potential centred at the centre of the magnetic trap. Once the atoms are outcoupled they therefore accelerate away from the centre of the magnetic trap until they reach the edge of the condensate, whereupon they fall under gravity.

There is a great difference in the behaviour of atoms outcoupled from a weak trap and from a tight trap. If the outcoupling surfaces are almost horizontal planes [Figure 2.2(a)], the atoms will be accelerated almost uniformly downwards. If the outcoupling surfaces are prolate spheroids entirely contained within the condensate [Figure 2.2(b)], atoms will be expelled in all directions away from the centre of the magnetic trap. This difference is illustrated in Figure 2.3, which displays the results of 3D GP simulations of the density of the atom laser in the region near the BEC in the cases of a weak trap [$\omega_r = 2\pi \times 50\,\text{Hz}$, $\omega_z = 2\pi \times 50\,\text{Hz}$; Figure 2.3(a)] and a tight trap [$\omega_r = 2\pi \times 460\,\text{Hz}$, $\omega_z = 2\pi \times 50\,\text{Hz}$; Figure 2.3(b)].

It can be seen from the images of the near-field atom laser density in Figure 2.3(a, b) that the transverse profile of the atom laser has significantly greater structure when outcoupling from a tight trap than from a weak trap. This difference is quite dramatic in the far field as shown in Figure 2.3(c), although the atom laser produced from a weak trap also has interference fringes. These interference fringes arise because it is possible for atoms outcoupled from different positions to have the same transverse momentum after leaving the condensate. A large distance below the condensate these two atoms will occupy the same position and will interfere. There are fewer interference fringes in the case of outcoupling from a weak trap as all atoms are accelerated downwards initially and therefore their maximum path length difference (and their maximum phase difference) will be smaller than if the atoms were outcoupled from a tight trap. In the case of outcoupling from a

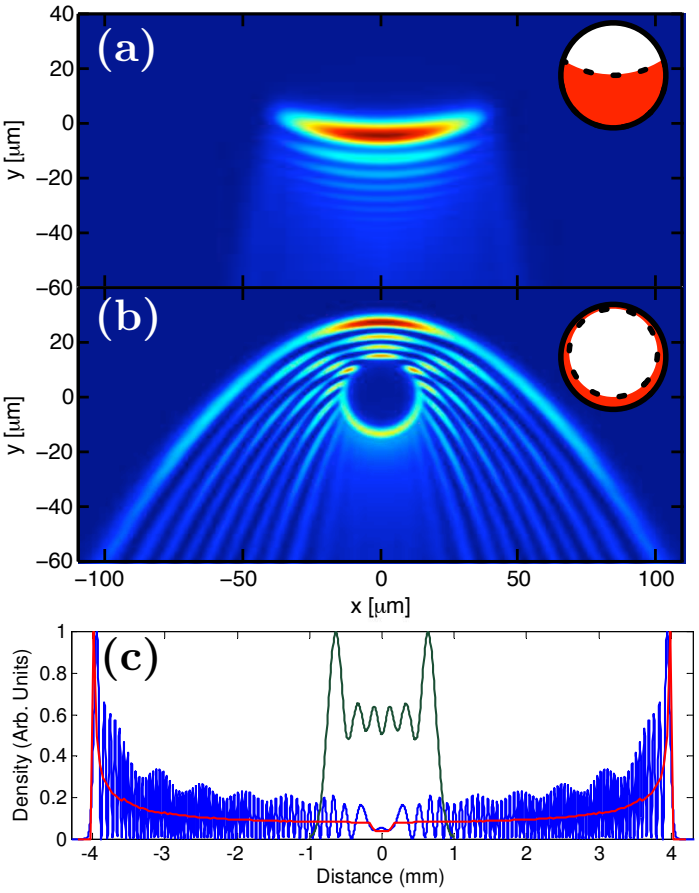

Figure 2.3: Near-field simulations of atom laser profiles, showing vastly different output dynamics depending on whether output-coupling takes place on (a) planes or on (b) prolate spheroids. The output-coupling regions (dashed line), relative to the BEC (circle), used to create these plots are shown diagrammatically in the upper right corner of each plot. In both cases the coordinate origin is the centre of the BEC is located at the origin. The radial trapping frequencies of the two condensates are $\omega_r = 2\pi \times 50\,\text{Hz}$ and $\omega_r = 2\pi \times 460\,\text{Hz}$ for (a) and (b) respectively. The resulting far field atom laser profiles as calculated at a detector $y = 4\,\text{cm}$ below the condensate for (a) and (b) are shown in (c). The green profile results from the near field distribution shown in (a). The blue and red profiles result from the near field distribution shown in (b) and are calculated using the Gross-Pitaevskii equation and classical mechanics respectively. The classical simulation treats atoms as classical particles that begin on the outcoupling surface and are pushed from the BEC due to gravity and the mean field repulsion; the resulting 'two-peak' structure is clearly visible.

tight trap, an atom that was initially accelerated upwards can have the same transverse momentum as an atom that was initially accelerated downwards. The significantly larger maximum path length difference (and maximum phase difference) between these two atoms results in there being a greater number of interference fringes, as each 2π in the maximum phase difference corresponds to an interference fringe. The maximum phase difference between two atoms arriving at the same location will vary from this maximum phase difference to zero.

While the fine structure of the transverse atom laser profile is caused by interference effects, the gross 'double-peaked' structure is well-described classically [compare the red and blue lines of Figure 2.3(c)]. The two peaks arise from the fact that, considered as a function of position on the outcoupling surface, there is a local maximum in the transverse momentum of the outcoupled atoms. In the neighbourhood of this local maximum, the transverse momentum of outcoupled atoms will be approximately constant and therefore a greater number of atoms will contribute to the position on the detector corresponding to the maximum transverse momentum. The 'dip' in the centre of the transverse atom laser profile results from atoms which are outcoupled near the top of the outcoupling surface. These atoms are initially accelerated upwards, but then fall back through the condensate. This creates a shadowed region cast by the condensate, since atoms attempting to pass back through the condensate are pushed off axis due to the mean field repulsion. This shadowed region is clearly visible below the condensate in Figure 2.3(b).

Figure 2.4 demonstrates that the results predicted by the Gross-Pitaevskii model of (2.35) are in good agreement with the experimental results from the Australian National University (ANU) He* experiment [81]. The atom laser profile shown is for the case of outcoupling with Rabi frequency $\Omega = 2\pi \times 50\,\mathrm{Hz}$ from the centre of a condensate of $N = 2 \times 10^6$ atoms held in a magnetic trap with trapping frequencies $\omega_r = 2\pi \times 50\,\mathrm{Hz}$ and $\omega_z = 2\pi \times 460\,\mathrm{Hz}$. While the form of Eqs. (2.35) is not particularly complicated, their solution can be numerically intensive. Producing the theoretical profile of Figure 2.4 required first solving (2.35) for the steady-state of the atom laser in the region near the condensate. This required 2000 hours of CPU time on a supercomputer, significantly longer than the simulations depicted in Figure 2.3. The reason for this difference is that in the case of Figure 2.4, atoms were outcoupled from the centre of the condensate, and therefore the atoms were moving faster and travelled higher after leaving the condensate. This necessitated the use of a much finer grid to resolve the spatial oscillations of the

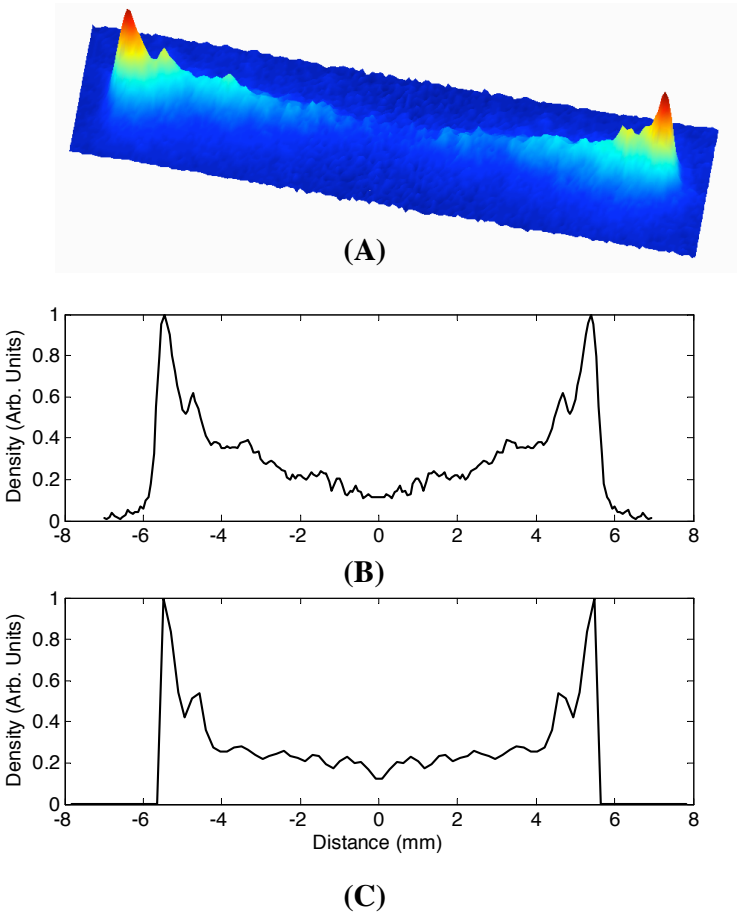

Figure 2.4: Comparison of theory and experiment. Upper trace shows an experimental 2D image of the transverse profile of an atom laser (image size is 13 mm by 3.4 mm) taken $y = 4$ cm below the condensate. Middle trace is an averaged profile taken through the centre of the 2D image. Lower trace is the theoretical profile corresponding to the experimental conditions averaged over the detector resolution.

atom laser on the length scale of the de Broglie wavelength, and a much larger grid to accommodate the atoms that travelled higher. Some of the numerical tools and techniques used in simulations performed as part of this thesis are discussed in Section 2.7.

Although good agreement is seen between the predictions of the Gross-Pitaevskii model and the observed experimental profile, the presence of interference fringes on the atom laser will cause problems in mode matching the atom laser beam to another atom laser, as would be necessary in an atom interferometry experiment. Figure 2.3 demonstrates that outcoupling from a weaker trap improves the transverse profile, making it closer to an ideal Gaussian beam. It is also possible to improve the transverse mode by outcoupling closer to the bottom of the trap [106], however this comes at the cost of reduced flux and a higher sensitivity to technical noise in the frequency of the outcoupling radiation [107]. Other options for improving the transverse profile include using a multiphoton Raman outcoupling process [46, 56, 108] or guiding the atom laser optically [58, 109, 110]. This last possibility, however, may introduce sufficient noise due to fluctuations in the waveguide to preclude its use in atom interferometry experiments [111].

2.5 Loss processes and the master equation

We are not always interested in the entirety of an interacting system; frequently it is only a small part of a system that is of interest. For example, in Section 2.4 we considered a BEC and its environment, which was comprised of the almost empty atomic modes of the vacuum chamber in which the BEC was produced. The environment is vastly larger than the BEC, both in terms of the number of available atomic modes, and in terms of the total occupation of those modes. Condensates containing as many as 10^8 ^{87}Rb atoms have been produced, however many more atoms ($\sim 10^{10}$) were initially in the trap before the evaporation process [112]. The remaining atoms that are not part of the condensate comprise the environment. While the entire system may be described by a many-body wavefunction, much of the information in this wavefunction will be describing the environment. A description is necessary of the state of the condensate independent of the exact state of the environment. The density matrix $\hat{\rho}$ provides that description [113].

As mentioned in Section 2.4, a density matrix for a subsystem may be obtained by averaging (or tracing) over the degrees of freedom of the environment. This simpler description fully describes the state of the subsystem when we are restricted to performing measurements only on that subsystem. With this very natural restriction, it becomes

impossible to distinguish otherwise distinct states of the entire system. This indistinguishability is not fundamental; by performing measurements on the entire system the states may be distinguished. The indistinguishability arises only due to our limited knowledge of the system.

Although not part of the subsystem of interest, the environment typically still influences the evolution of the subsystem. For example, collisions with atoms in the environment will lead to losses from the condensate. While knowledge of the state of the entire system is necessary to treat this exactly, if the interaction between the subsystem and its environment is sufficiently weak, and the subsystem is sufficiently small in comparison to its environment, the interaction may be treated perturbatively using the master equation technique originally derived in the context of quantum optics [114, 115]. Specifically, for subsystem–environment interactions of the form

$$\hat{H}_{\text{int}} = \hbar \sum_m \left(\hat{X}_m^\dagger \hat{\Gamma}_m + \hat{X}_m \hat{\Gamma}_m^\dagger \right), \tag{2.37}$$

where $\{\hat{X}_m\}$ are a set of bosonic annihilation operators acting only on the subsystem, and $\{\hat{\Gamma}_m\}$ are a set of operators acting only on the environment, the equation of motion for the density matrix gains the following term [116, Chapter 5]:

$$\left.\frac{\partial}{\partial t}\hat{\rho}\right|_{\text{int}} = \sum_m K_m \mathcal{D}[\hat{X}_m]\hat{\rho} + \sum_m G_m \mathcal{D}[\hat{X}_m^\dagger]\hat{\rho}, \tag{2.38}$$

where $\mathcal{D}[\hat{a}]\hat{\rho} = \hat{a}\hat{\rho}\hat{a}^\dagger - \frac{1}{2}\left(\hat{a}^\dagger\hat{a}\hat{\rho} + \hat{\rho}\hat{a}^\dagger\hat{a}\right)$ is the decoherence superoperator, and the positive constants K_m and G_m depend on properties of the environment. In the common case that the environment operators $\hat{\Gamma}_m$ are products of annihilation operators, the constants G_m are zero if the modes of the environment are essentially unoccupied.

In the following section, the master equation will be used to model the process of Penning ionisation in metastable helium.

2.5.1 Application: Penning ionisation

The primary attraction of creating Bose-Einstein condensates of metastable helium atoms is that their large internal energy (20 eV) enables single-atom detection with high spatial (µm) and temporal resolution (ns). However, this large internal energy can be released

when two metastable helium atoms collide, resulting in Penning ionisation (PI),

$$\mathrm{He}^* + \mathrm{He}^* \rightarrow \begin{cases} \mathrm{He}^+ + \mathrm{He} + e^- \\ \mathrm{He}_2^+ + e^- \end{cases} . \tag{2.39}$$

While this process dominates for unpolarised cold samples such as magneto-optical traps [117], it does not prohibit the formation of Bose-Einstein condensates as the process is suppressed by five orders of magnitude [118] in polarised samples. This suppression is due to conservation of angular momentum. While the reactants each have a total angular momentum $s = 1$, giving their combined total angular momentum as either $S = 0$ or $S = 2$ (assuming s-wave collisions), the products each have total angular momentum $s = \frac{1}{2}$ (in the case of He^+, e^- and He_2^+) or $s = 0$ (for He), giving the total angular momentum of the products as either $S = 0$ or $S = 1$. Hence spin polarised states having $S = 2$, $m_S = \pm 2$ cannot directly undergo the process (2.39).

In general as S is conserved, any of the $S = 2$ quasimolecule states will be prevented from directly undergoing PI. As collisions with nonzero relative angular momentum can be neglected at BEC temperatures [119, 120] (due to the atoms having insufficient energy to penetrate the centrifugal barrier), it is only the $S = 0$ quasimolecule state that undergoes PI.

The Hamiltonian describing either of the processes (2.39) will be of the form

$$\hat{H}_{\mathrm{int}} = \hbar\epsilon \int d\boldsymbol{x} \left(\hat{\Gamma}^\dagger(\boldsymbol{x}) \hat{\Xi}_{S=0,m_S=0}(\boldsymbol{x}) + \hat{\Xi}^\dagger_{S=0,m_S=0}(\boldsymbol{x}) \hat{\Gamma}(\boldsymbol{x}) \right) , \tag{2.40}$$

where ϵ is a spatially-independent coupling constant, $\hat{\Gamma}$ is a product of annihilation operators for the products of the PI process, and the $S = 0$ quasimolecule state that undergoes PI is given by [see (2.14)]

$$\hat{\Xi}_{S=0,m_S=0} = \frac{1}{\sqrt{3}} \left(2\hat{\Psi}_1 \hat{\Psi}_{-1} - \hat{\Psi}_0 \hat{\Psi}_0 \right) . \tag{2.41}$$

As we are only interested in the metastable helium atoms, and not the products of the PI process, $\hat{\Xi}_{S=0,m_S=0}$ is the subsystem operator of the interaction Hamiltonian (2.40), and $\hat{\Gamma}$ is the environment operator. As the environment operator is of the form of a product of annihilation operators and the products of PI will have sufficient kinetic energy to leave the condensate rapidly (and therefore keep the $\hat{\Gamma}$ modes near the condensate unoccupied),

the master equation term describing Penning ionisation must have the form

$$\left.\frac{d\hat{\rho}}{dt}\right|_{\mathrm{PI}} = \gamma_{\mathrm{PI}} \int d\boldsymbol{x}\, \mathcal{D}\left[\hat{\Xi}_{S=0,m_S=0}\right] \hat{\rho}, \tag{2.42}$$

where γ_{PI} is a positive rate constant. An explicit form for this rate constant is obtained in Section B.1. It is shown there that $\gamma_{\mathrm{PI}} = \frac{9}{2} K_{^4\mathrm{He}}^{(\mathrm{unpol})}$, where $K_{^4\mathrm{He}}^{(\mathrm{unpol})} = 7.7 \times 10^{-17}\,\mathrm{m^3 s^{-1}}$ is the rate constant for the production of ions due to Penning ionisation in an unpolarised thermal sample at 1 µK [120].

2.6 Beyond the Gross-Pitaevskii equation

In deriving the Gross-Pitaevskii equation, the atomic field $\hat{\Psi}(\boldsymbol{x})$ was separated into a classical component $\Psi(\boldsymbol{x})$ and a fluctuations operator $\delta\hat{\Psi}(\boldsymbol{x})$,

$$\hat{\Psi}(\boldsymbol{x}) = \Psi(\boldsymbol{x}) + \delta\hat{\Psi}(\boldsymbol{x}), \tag{2.43}$$

where it was then assumed that the fluctuations operator was 'small'. This is the so-called semiclassical or mean-field approximation, which includes single-particle quantum mechanical effects such as interference and barrier-tunnelling. This approximation neglects some of the more interesting quantum phenomena such as entanglement and squeezing [113]. This section discusses some techniques beyond the Gross-Pitaevskii equation that include these quantum statistical effects to varying levels of approximation.

There are two classes of methods that go beyond semiclassical approximations. In the first class of methods, the state of the system is quite general, and an expansion is performed in the evolution of the system, which is truncated at a certain level. The stochastic phase-space methods are the most common of this class, and are discussed in Section 2.6.1. In the second class of methods, an expansion is performed in the form of the system's state. This expansion is truncated at some level, neglecting correlations above a certain order. Requiring the state of the system to be of a certain form implicitly approximates the evolution of the system as well, however these approximations are of a different kind to those of the first class. The Bogoliubov-type methods are representative of the second class of methods, and are discussed in Section 2.6.2.

2.6.1 Stochastic phase-space methods

Phase-space representations are real-valued functions that are an alternative description of the state of the system, fully equivalent to the density matrix $\hat{\rho}$. In addition to being useful pictorial representations of the state of a system, these phase-space representations can be used to derive stochastic methods for describing the evolution of the system.

There are several phase-space representations, the most common being the P, Q and Wigner distributions. Each of these represent the state of the system in terms of coherent states. This is mostly clearly seen for the P-function,

$$\hat{\rho} = \int d\alpha \, P(\alpha) \, |\alpha\rangle\langle\alpha| \, , \tag{2.44}$$

where $P(\alpha)$ is the P-function for the single-mode system described by the density matrix $\hat{\rho}$. Every density matrix has a unique P-function representation. This P-function representation fully describes the state of the system, and is completely equivalent to the density matrix itself.

While the P-function is real, it is frequently pathological. For example, the coherent state $|\alpha_0\rangle$ has the P-function representation

$$P(\alpha) = \delta^2(\alpha - \alpha_0). \tag{2.45}$$

The Wigner and Q functions are significantly less pathological as they can be obtained by convolving the P-function with $\frac{2}{\pi}e^{-2|\alpha|^2}$ and $\frac{1}{\pi}e^{-|\alpha|^2}$ respectively. Despite this convolution, the Wigner and Q functions are also complete representations of the state of the system [116].

Instead of considering the evolution of the density matrix directly, the stochastic phase-space methods aim to model the evolution of phase-space representations. If the equation of motion for the phase-space representation is of the form of a Fokker-Planck equation [121], the phase-space representation may be interpreted as a classical probability distribution. In this case, the evolution may be equivalently described using stochastic differential equations. Expectation values can then be calculated as averages of appropriate quantities over *independent* realisations of a stochastic differential equation, which requires significantly fewer computational resources than solving the Fokker-Planck equation directly.

In the general case, it is desired to transform the Fokker-Planck equation

$$\frac{\partial}{\partial t}F(\boldsymbol{\alpha},t) = -\sum_j \frac{\partial}{\partial \alpha_j}A_j(\boldsymbol{\alpha},t)F(\boldsymbol{\alpha},t) + \frac{1}{2}\sum_{j,k}\frac{\partial}{\partial \alpha_j}\frac{\partial}{\partial \alpha_k^*}D_{j,k}(\boldsymbol{\alpha},t)F(\boldsymbol{\alpha},t), \tag{2.46}$$

into the Stratonovich stochastic differential equation [121]

$$d\alpha_i = A_i(\boldsymbol{\alpha},t)\,dt - \frac{1}{2}\sum_{j,k}B_{k,j}(\boldsymbol{\alpha},t)\frac{\partial}{\partial \alpha_k}B_{i,j}(\boldsymbol{\alpha},t)\,dt + \sum_j B_{i,j}(\boldsymbol{\alpha},t)\,dW_j(t), \tag{2.47}$$

where the matrix $\boldsymbol{B}(\boldsymbol{\alpha},t)$ is defined by

$$\boldsymbol{D}(\boldsymbol{\alpha},t) = \boldsymbol{B}(\boldsymbol{\alpha},t)\boldsymbol{B}^{\dagger}(\boldsymbol{\alpha},t), \tag{2.48}$$

and the Wiener increments $dW_j(t)$ are independent real Gaussian random variables with zero mean satisfying

$$\overline{dW_i(t)dW_j(t')} = \delta_{ij}\delta(t-t'), \tag{2.49}$$

where $\overline{(\cdot)}$ denotes an average over the random variables. This decomposition is guaranteed when the matrix $\boldsymbol{D}(\boldsymbol{\alpha},t)$ has only positive eigenvalues [121], and may be possible when this requirement is loosened to only nonnegative eigenvalues. Note that the sums in (2.46) and (2.47) are defined to run over both the complex variables α_j and their conjugates α_j^*.

The transformation of a Fokker-Planck equation into a stochastic differential equation can be physically interpreted as the macroscopic and microscopic views of the same process. For example, a Fokker-Planck equation can be used to model the probability distribution of positions and velocities of particles in a gas (macroscopic view), and the corresponding stochastic differential equation would describe the path taken by individual particles (microscopic view). The macroscopic view is useful when it is the distribution of positions and velocities which is of interest, or if it is only a few moments that are of interest, when the equations of motion for those moments form a closed system (such as those describing an ideal gas). Frequently however, the equations of motion are not closed with that for each moment depending on a higher-order moment [for example (2.19)], and an assumption must be made to close the system of equations (in the case of (2.19), that the system remains in a coherent state).

The microscopic view is an alternative approach that is useful when two conditions are

met. The first is that only a finite set of moments of the distribution are of interest, and not the distribution itself. The second is that the motion of the particles are independent of one another (although they may depend on moments of the distribution). That the particles' motions are independent is equivalent to the eigenvalues of $\boldsymbol{D}(\boldsymbol{\alpha}, t)$ being nonnegative. Positive eigenvalues of $\boldsymbol{D}(\boldsymbol{\alpha}, t)$ can be physically interpreted as corresponding to a diffusion process, which microscopically takes the form of Brownian motion. Negative eigenvalues, however, correspond to *negative* diffusion, a highly singular process in which particles tend to drift toward one another[3]. In this case, the evolution of one realisation of (2.47) will depend on the local *distribution*, violating the conditions stated above. One solution to this problem is to increase the dimensionality of the Fokker-Planck equation, and use the additional freedom given by the auxiliary dimensions to ensure that motion in the larger space is purely diffusive (this approach is taken with the Positive-P representation [116]). While this technique is exact in the limit of an infinite number of realisations of the corresponding stochastic differential equation, it is typically limited by the existence of trajectories with arbitrarily large norm [122]. These trajectories significantly increase the sampling error in calculated observables. This problem is particularly acute for BEC systems, as the atomic scattering process described by (2.15) causes the stochastic sampling error to diverge exponentially [122]. Such doubled phase-space techniques can therefore only describe the evolution of the system for short times.

Application: Anharmonic oscillator

We now demonstrate the application of a stochastic phase-space method to the anharmonic oscillator, which is governed by the Hamiltonian

$$\hat{H} = \hbar\omega\hat{a}^\dagger\hat{a} + \frac{1}{2}\hbar\kappa\hat{a}^\dagger\hat{a}^\dagger\hat{a}\hat{a}. \tag{2.50}$$

We wish to consider the evolution of the system with initial state $|\Psi(0)\rangle = |\alpha_0\rangle$. This system can be solved exactly, and has the interesting feature that its two-time correlation function initially decays, but undergoes perfect revivals when $\kappa t = 2\pi n$ for integral n. The

[3]It should be noted that the existence of negative eigenvalues for the matrix $\boldsymbol{D}(\boldsymbol{\alpha}, t)$ does not imply that the *solution* to the Fokker-Planck equation is singular. A good example of this is the equation of motion for the Q-function [113] of the anharmonic oscillator which is periodic in time, yet the corresponding $\boldsymbol{D}(\boldsymbol{\alpha}, t)$ matrix has positive and negative eigenvalues of equal magnitude.

normalised two-time correlation function for this system is

$$\frac{1}{N}\left|\left\langle \hat{a}^\dagger(t)\hat{a}(0)\right\rangle\right|^2 = \exp\left\{2N\left[\cos(\kappa t)-1\right]\right\}, \tag{2.51}$$

where $N = |\alpha_0|^2$.

In this thesis, we will only consider stochastic methods based on the Wigner distribution, which is defined by [113]

$$W(\alpha) = \frac{1}{\pi^2}\int d^2\lambda\, \exp\left(-\lambda\alpha^* + \lambda^*\alpha\right) \mathrm{Tr}\left\{\exp\left(\lambda\hat{a}^\dagger - \lambda^*\hat{a}\right)\hat{\rho}\right\}. \tag{2.52}$$

An equation of motion for the Wigner function can be obtained using the equation of motion for the density matrix

$$\begin{aligned}\frac{\partial}{\partial t}W(\alpha) &= \frac{1}{\pi^2}\int d^2\lambda\, \exp\left(-\lambda\alpha^* + \lambda^*\alpha\right) \mathrm{Tr}\left\{\exp\left(\lambda\hat{a}^\dagger - \lambda^*\hat{a}\right)\frac{\partial}{\partial t}\hat{\rho}\right\} \\ &= \frac{1}{\pi^2}\int d^2\lambda\, \exp\left(-\lambda\alpha^* + \lambda^*\alpha\right) \mathrm{Tr}\left\{\exp\left(\lambda\hat{a}^\dagger - \lambda^*\hat{a}\right)\frac{-i}{\hbar}\left[\hat{H},\,\hat{\rho}\right]\right\},\end{aligned} \tag{2.53}$$

for evolution driven by a Hamiltonian $\hat{H}$. The simplification of this expression is made easier through the application of the following operator correspondences [116, §4.5]

$$\hat{a}\hat{\rho} \leftrightarrow \left(\alpha + \frac{1}{2}\frac{\partial}{\partial\alpha^*}\right)W(\alpha), \tag{2.54a}$$

$$\hat{\rho}\hat{a} \leftrightarrow \left(\alpha - \frac{1}{2}\frac{\partial}{\partial\alpha^*}\right)W(\alpha), \tag{2.54b}$$

$$\hat{a}^\dagger\hat{\rho} \leftrightarrow \left(\alpha^* - \frac{1}{2}\frac{\partial}{\partial\alpha}\right)W(\alpha), \tag{2.54c}$$

$$\hat{\rho}\hat{a}^\dagger \leftrightarrow \left(\alpha^* + \frac{1}{2}\frac{\partial}{\partial\alpha}\right)W(\alpha). \tag{2.54d}$$

These correspondences apply for general density matrix evolution, not only for evolution driven purely by a Hamiltonian (see, for example, Section B.3).

For the anharmonic oscillator Hamiltonian (2.50), the evolution equation for the Wigner distribution is

$$\begin{aligned}\frac{\partial}{\partial t}W(\alpha) = i\left(\frac{\partial}{\partial\alpha}\alpha - \frac{\partial}{\partial\alpha^*}\alpha^*\right)\left[\omega + \kappa\left(|\alpha|^2 - 1\right)\right]W(\alpha) \\ -\frac{1}{4}i\kappa\left(\frac{\partial^2}{\partial\alpha^2}\frac{\partial}{\partial\alpha^*}\alpha - \frac{\partial^2}{\partial\alpha^{*2}}\frac{\partial}{\partial\alpha}\alpha^*\right)W(\alpha).\end{aligned} \tag{2.55}$$

The third-order derivatives in this equation mean that it is not in the form of a Fokker-Planck

equation [cf. (2.46)], and therefore may not be transformed into stochastic differential equations. However, if these higher-order derivatives are neglected the equation of motion will only contain first-order derivatives and may therefore be transformed into a stochastic differential equation. In fact, due to the absence of second-order derivatives, there will be no noise term in the resulting stochastic differential equation. The initial condition is, however, stochastic.

The neglect of third and higher-order derivatives in the equation of motion for the Wigner distribution is known as the Truncated Wigner (TW) approximation. This is an uncontrolled approximation in the sense that there is no explicit small parameter in which this approximation is an expansion in. We can motivate this approximation in the present system by considering the initial state of the Wigner distribution,

$$W(\alpha, t=0) = \frac{2}{\pi} \exp\left(-2\left|\alpha - \alpha_0\right|^2\right). \tag{2.56}$$

As α_0 changes, the initial Wigner distribution simply translates. For small times therefore, each derivative can be considered to be of size $O(1)$ in α_0. The relative importance of each term in (2.55) therefore solely depends on the powers of α and α^*. The size of α and α^* can be considered to be of the order of $O(\alpha_0)$, as it is only in the vicinity of α_0 that the Wigner distribution is significantly different from zero (for small times). The κ-dependent terms of (2.55) involving first-order derivatives therefore scale as $O(\left|\alpha_0\right|^2 \alpha_0)$, while the κ-dependent terms involving third-order derivatives scale as $O(\alpha_0)$. For sufficiently large α_0, the third-order derivative terms in (2.55) can be neglected, at least for small times. The accuracy of the Truncated Wigner approximation has been considered in great detail elsewhere [123–127]. In general it has been shown that it is a good approximation if the total occupation of the system is much greater than the number of available modes [125]. For the anharmonic oscillator, this requires $N = \left|\alpha_0\right|^2 \gg 1$.

We continue now with the application of the Truncated Wigner method to the anharmonic oscillator. With the third-order derivatives neglected, the Stratonovich stochastic differential equation describing the system is

$$d\alpha = -i\left[\omega + \kappa\left(\left|\alpha\right|^2 - 1\right)\right]\alpha\, dt. \tag{2.57}$$

Although the evolution of this 'stochastic' differential equation is deterministic, its initial condition is random, as it must sample the initial condition of the Wigner distribution

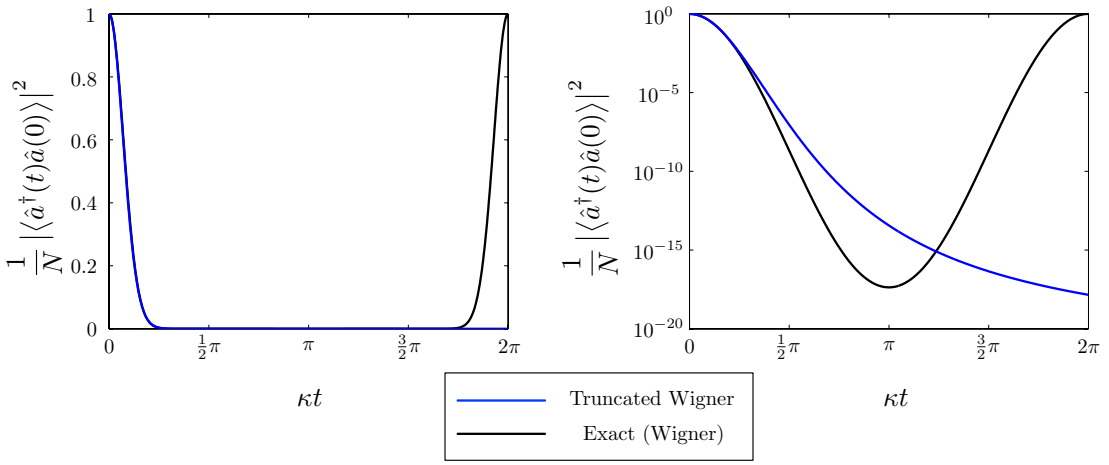

Figure 2.5: Comparison of Truncated Wigner with the exact solution for the two-time correlation function of the anharmonic oscillator. The exact solution (black) for the two-time correlation function exhibits revivals every $\kappa t = 2\pi$, while the Truncated Wigner solution (blue) does not. The Truncated Wigner solution, however, is in good agreement with the exact solution for the collapse of the correlation function. The left and right figures illustrate the normalised two-time correlation function on linear and logarithmic scales respectively. The initial condition was $\alpha_0 = \sqrt{10}$.

(2.56). The initial condition of (2.57) is therefore

$$\alpha(0) = \alpha_0 + \frac{1}{\sqrt{2}}\eta, \tag{2.58}$$

where η is a complex Gaussian random variable satisfying

$$\overline{\eta} = 0, \qquad \overline{\eta\eta} = 0, \qquad \overline{\eta^*\eta} = 1. \tag{2.59}$$

The noise term in the initial state can be considered to be adding, on average, half a 'virtual' particle per mode to the system [128]. These virtual particles represent the contribution of the vacuum fluctuations that is ignored in the Gross-Pitaevskii equation.

In principle, (2.57) can be simulated numerically to determine the dynamics of the system. However, as it is of a particularly simple form, it may be integrated analytically. Within the Truncated Wigner approximation, the normalised two-time correlation function of the anharmonic oscillator is

$$\frac{1}{N}\left|\left\langle\hat{a}^\dagger(t)\hat{a}(0)\right\rangle_{\mathrm{TW}}\right|^2 = \frac{16}{(4+\kappa^2t^2)^2}\exp\left(\frac{-4N\kappa^2t^2}{4+\kappa^2t^2}\right). \tag{2.60}$$

A comparison of the exact and truncated solutions is given in Figure 2.5.

The good agreement between the Truncated Wigner and exact results in Figure 2.5 for

$\kappa t \lesssim \frac{\pi}{4}$ does not imply that the distributions themselves are approximately equal over this time. This is shown not to be the case in Figure 2.6, in which the Wigner and Truncated Wigner distributions for the anharmonic oscillator are compared. Expectation values of higher-order moments will diverge from the exact solutions faster than those for lower-order moments. The validity of Truncated Wigner therefore also depends on the moments that are to be calculated. Typically, it is only second order moments such as $\langle \hat{a}^\dagger \hat{a} \rangle$ that are of interest. This is the case in this thesis.

Stochastic phase-space methods were described as being an expansion in the evolution of the system with no restriction on the state of the system. The expansion in the evolution occurs at the level of the equation of motion for the phase-space distribution. For an unravelling in terms of stochastic differential equations to be possible, all derivatives in this equation above second order must be truncated. Although the requirement that the Truncated Wigner distribution be non-negative does impose a restriction on the state of the system, this restriction is not necessary [129]. Polkovnikov [127] has shown explicitly that the Gross-Pitaevskii equation and the Truncated Wigner method can be considered to be the zeroth and first order terms in an expansion of the system dynamics in terms of its response to quantum fluctuations. In principle, higher-order corrections can be included, however the computational requirements increase rapidly for each additional correction considered.

Although the application of the Truncated Wigner method considered in this section did not involve explicitly stochastic evolution, an application that does is discussed in Appendix B.

2.6.2 Bogoliubov-type methods

The Bogoliubov-type methods consider the evolution of a truncated expansion of the state of the system. These methods begin by decomposing the atomic field operator $\hat{\Psi}$ in terms of a classical component $\Psi = \langle \hat{\Psi} \rangle$ and a fluctuations operator $\delta\hat{\Psi}$,

$$\hat{\Psi} = \Psi + \delta\hat{\Psi}. \tag{2.61}$$

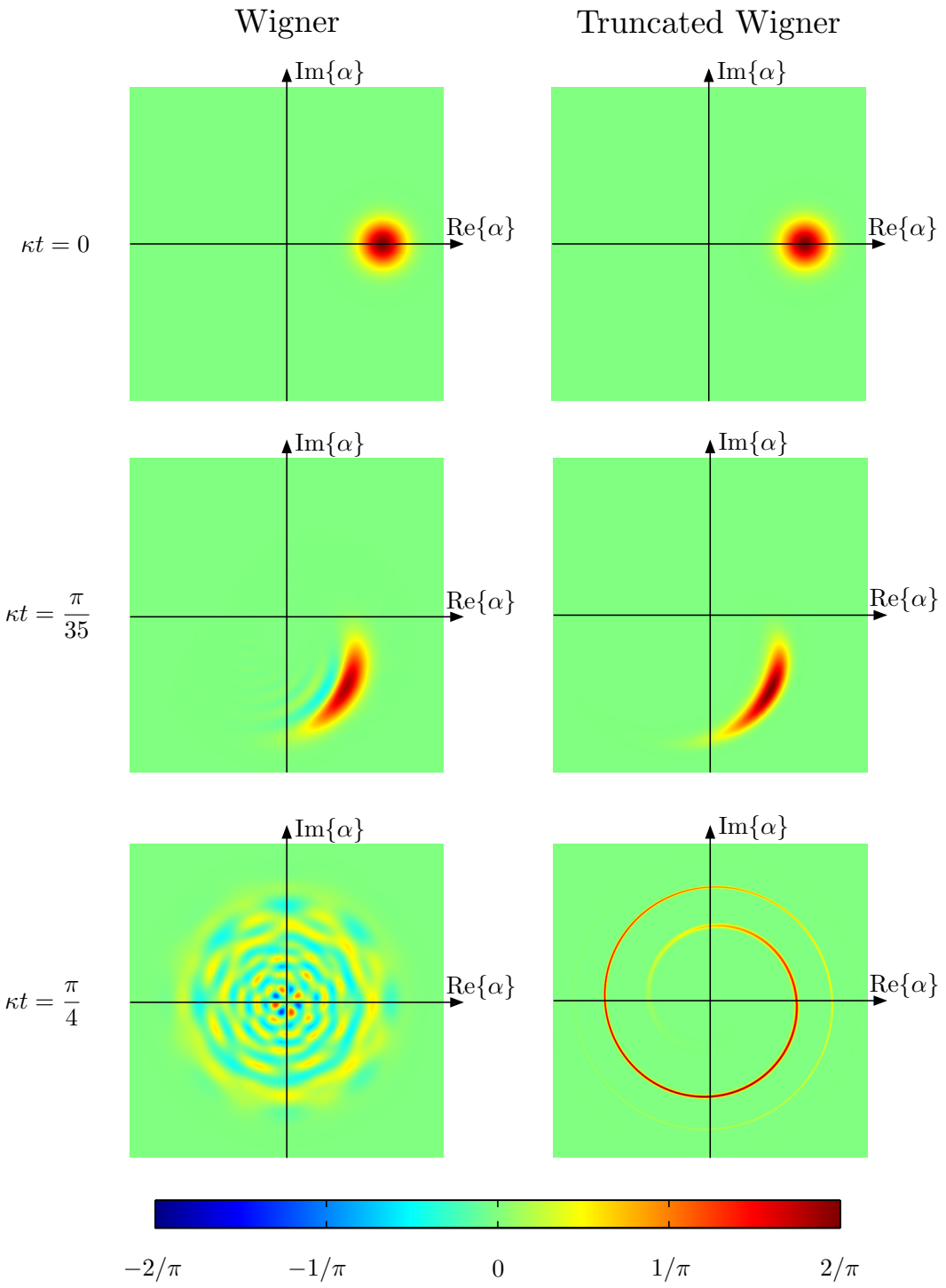

Figure 2.6: Comparison of the Wigner and Truncated Wigner distributions for the anharmonic oscillator. For short times, the two distributions are approximately equal (upper and middle rows), however for longer times (lower row) the Wigner distribution develops a significant negative components (blue). As the Truncated Wigner distribution represents the probability distribution of the stochastic differential equation (2.57), it remains positive. The initial condition was $\alpha_0 = \sqrt{10}$.

The equations of motion for Ψ and $\delta\hat{\Psi}$ may be obtained from (2.19) and (2.16) respectively [130],

$$\begin{aligned} i\hbar\frac{\partial}{\partial t}\Psi &= \left(-\frac{\hbar^2\nabla^2}{2M} + V(\boldsymbol{x}) + U_{\rm int}\left|\Psi\right|^2 + 2U_{\rm int}\left\langle\delta\hat{\Psi}^\dagger\delta\hat{\Psi}\right\rangle\right)\Psi \\ &\quad + U_{\rm int}\left(\left\langle\delta\hat{\Psi}\delta\hat{\Psi}\right\rangle\Psi^* + \left\langle\delta\hat{\Psi}^\dagger\delta\hat{\Psi}\delta\hat{\Psi}\right\rangle\right), \end{aligned} \tag{2.62a}$$

$$\begin{aligned} i\hbar\frac{\partial}{\partial t}\delta\hat{\Psi} &= \left(-\frac{\hbar^2\nabla^2}{2M} + V(\boldsymbol{x}) + 2U_{\rm int}\left|\Psi\right|^2\right)\delta\hat{\Psi} + U_{\rm int}\Psi^2\delta\hat{\Psi}^\dagger \\ &\quad + 2U_{\rm int}\Psi\left(\delta\hat{\Psi}^\dagger\delta\hat{\Psi} - \left\langle\delta\hat{\Psi}^\dagger\delta\hat{\Psi}\right\rangle\right) + U_{\rm int}\Psi^*\left(\delta\hat{\Psi}\delta\hat{\Psi} - \left\langle\delta\hat{\Psi}\delta\hat{\Psi}\right\rangle\right) \\ &\quad + U_{\rm int}\left(\delta\hat{\Psi}^\dagger\delta\hat{\Psi}\delta\hat{\Psi} - \left\langle\delta\hat{\Psi}^\dagger\delta\hat{\Psi}\delta\hat{\Psi}\right\rangle\right). \end{aligned} \tag{2.62b}$$

These equations are completely equivalent to the operator equation of motion (2.16), and are therefore equally infeasible to simulate numerically. An approximation is needed to proceed.

There are a variety of methods that approximate (2.62) to varying degrees. An extensive discussion of these methods is given in [130]. The simplest of these is the Bogoliubov method in which the mean-field evolution (2.62a) is approximated by the Gross-Pitaevskii equation and all terms of second- or higher-order in $\delta\hat{\Psi}$ are neglected. This approximation restricts the applicability of this simplest method to the zero-temperature limit, where the effect of the thermal cloud on the condensate is small. In this limit, however, the equations of motion are of sufficiently simple form as to enable analytic results to be obtained. The Bogoliubov method is discussed in greater detail in Section 3.3, and used in Section 3.4 to determine the stability of a He* condensate to excitations.

While the Bogoliubov method is useful in the zero-temperature limit, it does not consider effects such as scattering between the condensate and thermal fractions that are significant at higher temperatures. In this limit, more accurate methods based on (2.62) such as the Hartree-Fock and Hartree-Fock-Bogoliubov methods are necessary. These methods expand the state in terms of moments of the fluctuation operator. This expansion is typically truncated at second-order, with the state described (in the case of Hartree-Fock-Bogoliubov theory) in terms of the moments

$$\Psi(\boldsymbol{x}) = \left\langle\hat{\Psi}(\boldsymbol{x})\right\rangle, \qquad G_N(\boldsymbol{x},\boldsymbol{x}') = \left\langle\delta\hat{\Psi}^\dagger(\boldsymbol{x}')\delta\hat{\Psi}(\boldsymbol{x})\right\rangle, \qquad G_A(\boldsymbol{x},\boldsymbol{x}') = \left\langle\delta\hat{\Psi}(\boldsymbol{x}')\delta\hat{\Psi}(\boldsymbol{x})\right\rangle.$$

All higher-order moments are approximately expressed in terms of lower-order moments

using Wick's theorem [131, 132]. For example

$$\left\langle \delta\hat{\Psi}^\dagger \delta\hat{\Psi}^\dagger \delta\hat{\Psi} \delta\hat{\Psi} \right\rangle \approx 2\left\langle \delta\hat{\Psi}^\dagger \delta\hat{\Psi} \right\rangle \left\langle \delta\hat{\Psi}^\dagger \delta\hat{\Psi} \right\rangle + \left\langle \delta\hat{\Psi}^\dagger \delta\hat{\Psi}^\dagger \right\rangle \left\langle \delta\hat{\Psi} \delta\hat{\Psi} \right\rangle. \tag{2.63}$$

While these methods are appropriate at intermediate temperatures, other techniques are necessary near the phase transition at $T \sim T_c$. Methods appropriate in this limit are discussed in the following section.

2.6.3 Methods applicable near the critical temperature

Near the critical temperature T_c, the system has a significant thermal fraction [see (2.4)]. In this limit, scattering and particle-exchange between the condensed and thermal fractions are significant. These processes are of particular importance when considering condensate formation and growth. Simple models in which the condensate is described in terms of its occupation N_0, and the thermal cloud in terms of its energy distribution function $g(\varepsilon)$ have been quite successful in describing these processes [133, 134]. Such models use an extension of classical kinetic theory termed Quantum Kinetic theory [133, 135–140]. Quantum Kinetic theory is discussed in greater detail in Chapter 5, in which it is used to describe the evaporation-driven pumping of a condensate.

More detailed models have since been developed that are applicable where the spatial dynamics of either the condensate or thermal cloud is important. These include the c-field methods such as the (Stochastic) Projected Gross-Pitaevskii equation [141], and the ZNG theory [130, 142]. The former includes the statistics of the thermal cloud which is critical in low-dimensional systems [141], while the latter employs a simpler representation of the thermal cloud which is simpler to solve numerically [130].

2.7 Numerical Techniques

Numerical calculations are a common and important part of theoretical (and frequently experimental) physics. While methods for validating the convergence of calculations by comparing results for different grid- and time-step sizes are well-known and understood, other techniques are less commonly discussed. I have chosen to discuss one of these, the use of absorbing boundary layers, in Section 2.7.1. An unusual application of this technique is discussed in Section 3.5.2.

There are a large number of technical details that must be correct for a simulation

to operate correctly. Diagnosing and resolving these issues can be a very difficult and time-consuming process. As a large number of the problems solved within quantum and atom optics fall into the class of initial-value (stochastic) partial differential equations, the vast majority of these simulations are very similar at a mathematical level. To reduce the time required to develop these simulations, the computational package `XMDS` [143] was created several years ago to take a high-level description of a problem and produce a low-level simulation that solves the problem. I have benefitted greatly from this tool throughout my PhD, however some of its limitations required the creation of a successor to this tool. I have developed the package `xpdeint` to fill this role, and a discussion of its capabilities is given in Appendix D.

2.7.1 Absorbing boundary layers

To solve any partial differential equation numerically, it must be restricted to a finite domain with boundary conditions imposed at the edges[4]. For some systems, this poses no additional restriction over the original problem as they are explicitly defined over a finite domain and with the correct boundary conditions this constitutes the problem itself (for example electromagnetic wave propagation in a waveguide). Other systems are naturally restricted to a finite domain (for example a BEC in a trap) and will be unaffected by the imposition of the artificial boundary conditions.

With the exception of systems defined over a finite domain, the choice of boundary conditions at the edges of the computational domain is an artificial one; while in many cases they permit physical interpretation, this interpretation does not usually correspond to the reality of the system under consideration. As an example, consider the case of an atom laser outcoupled from a BEC, which then falls freely under gravity (see Figure 2.3). The natural domain for this problem is infinite, but to solve this system numerically it must be restricted to a finite domain. If periodic boundary conditions are used, when the atom laser falls off the bottom of the computational domain, it will reappear at the top and continue falling. If the wavefunction or its derivative is set to zero on the boundary, then the atom laser will reflect from the bottom of the domain. Each choice of boundary condition gives different results and none correspond to the correct behaviour in which the atom laser would simply leave the computational domain. A strategy is therefore needed to limit the effect of the choice of the boundary conditions on the solution.

[4]This requirement can be avoided when the solution's asymptotic behaviour is known *a priori*, however this case will not be encountered in this thesis.

A first simple strategy would be to choose the computational domain to be large enough such that no part of the atom laser beam will reach the edge of the domain over the time of interest. While effective, this strategy can be computationally expensive, and is particularly demanding in the presence of gravity. Under the influence of gravity, a classical particle starting from rest will travel a distance $d = \frac{1}{2}gt^2$ in time t. Hence the size of the computational domain must increase as t^2. The spatial grid separation cannot remain constant however. As the velocity of the classical particle increases as $v = gt$, the mean wavelength of the particle $\lambda = \dfrac{\hbar}{Mv}$ must then decrease as t^{-1}. To resolve the spatial dynamics of the atom laser, the step size between points must then decrease as t^{-1}. These two effects combine to give the scaling that the total number of spatial grid points required scales as $N_{\text{pts}} \propto t^3$. Choices of uniform or variable spacing for the grid will only differ by an overall constant factor in the number of points required by this strategy; such choices cannot change the overall scaling. A different strategy is needed.

In many circumstances it is the Bose-Einstein condensate and the outcoupling process that produces the atom laser that are of interest. In such situations the remainder of the atom laser that can no longer directly interact with the BEC must be prevented from doing so as a result of its unphysical interactions with the artificial boundary conditions. The solution used in the aforementioned strategy was to continue to model the atom laser, however this is not necessary. An alternative solution is to remove this part of the atom laser from the simulation in a way that has no effect on the BEC and the outcoupling process. One strategy that takes this approach is to add an *absorbing boundary layer* [144, 145] between the domain of interest and the artificial boundary conditions. This absorbing boundary layer takes the form of a negative imaginary potential, which must be chosen to be deep enough to strongly attenuate any wave traversing it and smooth enough to make the probability of reflection negligible. Figure 2.7 illustrates this strategy. Through the use of an appropriate absorbing boundary layer, the computational domain used to solve the system need not change and the scaling problem discussed previously will not occur.

An absorbing boundary layer of finite thickness can only be effective over a finite range of incident wavenumbers. Incident wavefunctions with large wavelengths (low wavenumbers) will be reflected from the absorbing boundary layer due to the rapid variation in the potential over a wavelength. Incident wavenumbers with very short wavelengths (high wavenumbers) will be transmitted through the absorbing boundary layer due to the short amount of time spent in the absorbing boundary layer by any point on the phase-front.

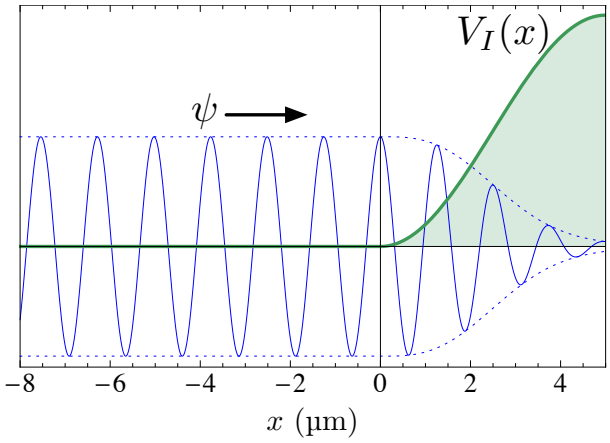

Figure 2.7: Schematic diagram illustrating the use of an absorbing boundary layer. A right-travelling wave is incident on the absorbing boundary layer, which is given by the potential $V(x) = -iV_I(x)$. The wave is attenuated as it crosses the absorbing boundary layer.

Using this argument Neuhasuer and Baer [145] showed that the approximate range of wavenumbers over which an absorbing boundary layer will be effective is

$$\left(\frac{M\overline{V_I}}{\hbar^2\Delta x}\right)^{\frac{1}{3}} \ll k \ll \frac{4M\overline{V_I}\Delta x}{\hbar^2}, \tag{2.64}$$

where $\overline{V_I}$ is a representative value of $V_I(x)$. The maximum and minimum limits for the wavenumber are respectively due to the requirements of negligible transmission and reflection. Although cast in terms of the wavenumber, (2.64) is equivalent to (26) in [145]. While not its purpose, Section C.2 demonstrates how to calculate the reflection and transmission coefficients as a function of wavenumber for arbitrary absorbing boundary layers.

The use of absorbing boundary layers must be slightly modified for use in phase-space methods such as those discussed in Section 2.6.1. In these cases, simply adding an absorbing boundary layer to the potential would lead to unphysical results as the absorbing potential would not discriminate between real particles in a mode and the 'virtual' particles which represent the fundamental vacuum fluctuations inherent in the field. An appropriate way of handling this problem is to add a position-dependent loss term to the master equation of the form

$$\frac{d\hat{\rho}}{dt} = \int d\boldsymbol{x}\, \frac{2}{\hbar} V_I(\boldsymbol{x}) \mathcal{D}[\hat{\Psi}(\boldsymbol{x})]\hat{\rho}, \tag{2.65}$$

where $\mathcal{D}$ is the usual decoherence superoperator. This master equation term leads to the

same imaginary potential term in the equations of motion for the field operator with an additional noise term the for Truncated Wigner and Q function methods that restores the vacuum fluctuations that would otherwise be lost.

In most of this thesis it is only the immediate vicinity of the BEC that is under consideration, and absorbing boundary layers are used to restrict the computational domain to this region. As the use of absorbing boundary layers is a technical issue not related to the underlying physics, they are not included in equations of motion given in this thesis, but should be understood to be included when simulations are performed.

Chapter 3

On the production of entangled beams from a metastable helium BEC

In this chapter, we investigate the production of paired atom laser beams from a metastable helium condensate due to an unusual scattering process. Radio-frequency outcoupling is used to extract atoms from a Bose-Einstein condensate to initiate scattering between trapped and untrapped atoms. The unequal strengths of the interactions for different internal states allows an energy-momentum resonance that leads to the scattering of atoms from the zero-velocity condensate into modes of opposite momenta. This process is shown to be the result of dynamical instabilities within the condensate that originate from a process analogous to optical parametric down-conversion, giving rise to entanglement between the unstable modes. These unstable modes are outcoupled to form scattered beams well-separated from the main atom laser profile, which are observed experimentally.

The results presented in Section 3.4 of this chapter are in preparation for submission, while the results presented in Section 3.5 of this chapter have been published in Dall *et al.* [146]. All of the theoretical work in these papers was my own work with the exception of the classical propagation discussed at the end of Section 3.5.2.

3.1 Introduction

Sources of matter waves gained a dramatic improvement with the achievement of Bose-Einstein condensation (BEC) in dilute gases and the development of the atom laser [13–

15, 43]. Like optical lasers before them, atom lasers can produce Heisenberg-limited beam profiles [53, 55], and promise high spectral density through their dramatically lower linewidth [17]. Another exciting possibility resulting from having such a coherent source of atoms is the generation of nonclassical matter waves such as entangled beams. Entangled beams are useful for tests of quantum mechanics and are required to perform Heisenberg-limited interferometry [50, 147]. In this chapter, we show that the asymmetric scattering lengths between internal states of metastable helium (He*) cause well-defined peaks in the output of an atom laser. These peaks are due to a dynamical instability in the condensate that originates from a process that generates entanglement.

A nonlinear process is required to produce entanglement, and one of the advantages of atomic systems over optical systems is that there are strong inherent nonlinearities due to atomic interactions, although these interactions can also lead to complications. These nonlinearities allow certain analogues of nonlinear optical experiments such as four-wave mixing, parametric down-conversion and Kerr squeezing to be performed directly in the atomic sample [148]. All of these processes produce non-classical states in optical systems. Four-wave mixing in a trapped BEC has been demonstrated experimentally in configurations where three distinct momentum states generated a fourth [32], and where two momentum states generated pairs of correlated atoms [79]. These experiments demonstrated that the output phase was coherent, but the correlation properties were not measured. More recently the pair correlations in a spontaneous scattering of two colliding condensates were measured using the single-atom detectors available for He* atoms [80].

Using these existing sources of entangled pairs of atoms for interferometric experiments will be complicated by the high densities of the sources, where the nonlinearities that generated the correlations ultimately degrade the long-term coherence of the sample. While recent experiments have increased the coherence of atom interferometers by several orders of magnitude by reducing the nonlinearities with a Feschbach resonance [149, 150], it is the nonlinearities that drive the production of entangled pairs. In the scheme presented here, the nonlinear interactions are used to drive dynamical instabilities in the condensate, but the resulting untrapped beams that propagate in free space are dilute, potentially avoiding the decoherence problem. We show that pairs of beams can be produced simply by the process of radio-frequency (rf) outcoupling from a He* BEC, without the need for Feschbach resonances or scattering pulses. Unlike previous methods, which required pairs of atoms travelling at high kinetic energies as a source, this process involves scattering

between atoms initially in the same zero-momentum state to create states with nonzero momentum. Semiclassical and field-theoretic simulations of the experiment show that the beams are generated by the same parametric down-conversion process that generates entangled optical beams. Although the beams in the present experiment will not retain all of the original non-classical correlations produced by the dynamical instabilities, some will remain, and a future experiment is proposed that may enable the full correlations produced by the dynamical instabilities to be extracted from the condensate.

3.2 The metastable helium 'Peaks' experiment

The experimental setup considered in this chapter for creating He* BEC has been reported elsewhere [105]. The experiment discussed in this section was performed by *Robert Dall*, *Lesa Byron* and *Andrew Truscott* at the Research School of Physics and Engineering of the Australian National University (ANU).

Starting from an almost pure BEC containing up to 2×10^6 atoms, an atom laser beam was created by using rf photons to spin flip the BEC atoms from the $m_F = 1$ magnetically trapped state to the $m_F = 0$ untrapped state. After outcoupling, atoms in the atom laser beam fell under gravity for a distance of 4 cm until they hit a double-stacked multichannel plate (MCP). The electrons released by the MCP are incident upon a phosphor screen, which was imaged with a charge-coupled-device (CCD) camera with a resolution of approximately 150 µm at the MCP. To remove any nonuniformities caused by spatial variations in the gain of the MCP, all images were divided by a flat-field image produced by dropping atoms from a MOT onto the detector. Since the MOT temperature is of order ~ 1 mK, the spatial profile of the MOT uniformly illuminates the MCP. Although $m_F = -1$ atoms are produced by the outcoupling, especially for high rf powers, they are in general accelerated away from the detector by the magnetic trap field. Those that are accelerated towards the detector do not show up in the images since they arrive much earlier than the CCD trigger time.

Figure 3.1 shows the dramatic change in the atom laser spatial profile when the dynamical instabilities in the condensate are excited. In the case of low outcoupling Rabi frequencies [Figure 3.1(a)], this process does not occur and we see the usual double-peaked He*-atom laser profile [81] (see also Section 2.4.2). When the Rabi frequencies are high enough to drive the instabilities [Figure 3.1(b)], the atoms in the atom laser beam are scattered to form a halo around the main atom laser beam. Due to conservation of energy,

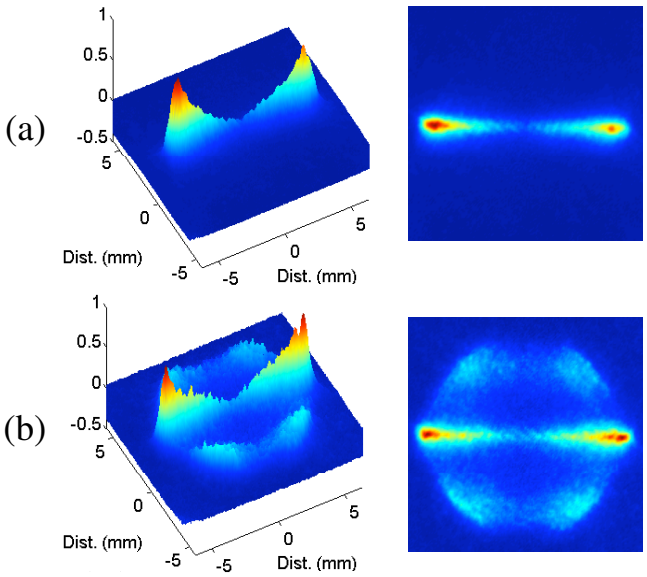

Figure 3.1: Observed transverse atom laser profiles from the ANU He* experiment [146]. The difference between (a) and (b) is that the outcoupling Rabi frequency has been increased by an order of magnitude in (b) to $\Omega = 2\pi \times 500\,\mathrm{Hz}$.

the outer diameter of this halo corresponds to a maximum kinetic energy given by the chemical potential. As well as the ring structure, four peaks are observed on the outskirts of the profile.

These peaks arise from two momentum-correlated cones of particles scattering out of the condensate and falling to the detector, as shown in Figure 3.2. The cones themselves are generated by a dynamical instability that populates momentum modes lying along the weak trapping axis, which expand to rings due to the mean-field repulsion in the tight trapping direction as they leave the BEC. Atoms in these cones then fall under gravity onto the detector, where the time-integrated flux is converted to a spatial density distribution, and each momentum ring appears as a double peak. The background halo is produced during the initial switch-on of the atom laser during which the peaks produced by the instabilities sweep in position from the main atom laser profile towards their final position in Figure 3.1.

A summary of the relevant parameters of the experiment is given in Table 3.1.

3.3 Overview of Bogoliubov theory

The observed features in the atom laser profile presented in the previous section are caused by a dynamical instability in the condensate. The modes that are dynamically unstable are identified in the next section, in which the excitation spectrum of the condensate is

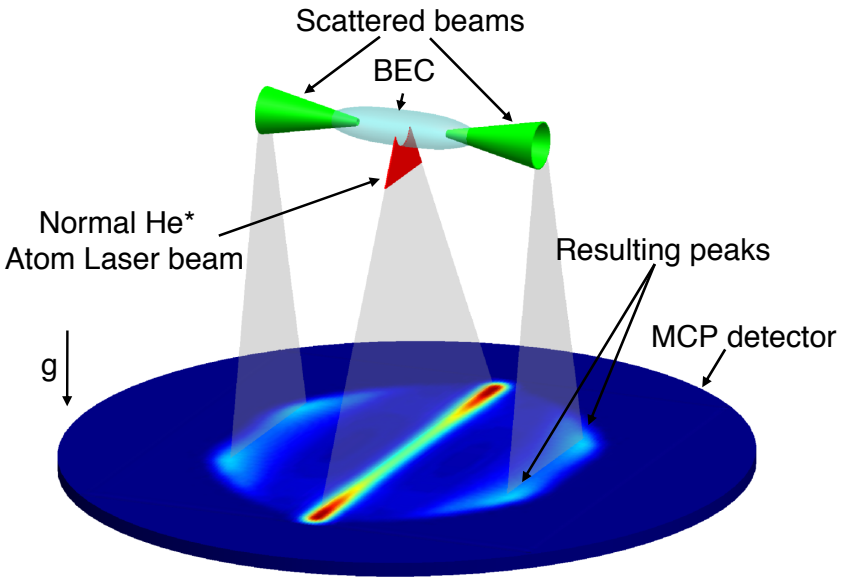

Figure 3.2: Schematic of the experimental setup

Parameter	Value
Condensate number	$N = 2 \times 10^6$
Radial trapping frequency	$\omega_r = 2\pi \times 1020\,\text{Hz}$
Axial trapping frequency	$\omega_z = 2\pi \times 55\,\text{Hz}$
Outcoupling Detuning	$\Delta = 2\pi \times 6.5\,\text{kHz}$
Outcoupling Rabi frequency	$\Omega = 2\pi \times 500\,\text{Hz}$
Quasimolecule $S = 0$ scattering length	$a_{S=0} = 9.46\,\text{nm}$
Quasimolecule $S = 2$ scattering length	$a_{S=2} = 7.51\,\text{nm}$
Penning ionisation rate	$K_{^4\text{He}}^{(\text{unpol})} = 7.7 \times 10^{-17}\,\text{m}^3$ [120]

Table 3.1: Experimental parameters for the metastable helium BEC under consideration. Refer to Section 2.3 for a discussion of the quasimolecule scattering lengths.

obtained. In this section an overview is given of the Bogoliubov theory which is used to obtain the excitation spectrum of the condensate and to determine its stability. More comprehensive treatments of the Bogoliubov theory are given in [20] and in a number of review articles [86, 130, 151].

The problem is to determine the response of the condensate to small fluctuations about the mean-field. Typically the condensate is stable to such fluctuations, and their energy spectrum determines the phase and group velocities of the excitations. In the case that the condensate is dynamically unstable, some modes will undergo exponential growth, which corresponds to the generalised energy spectrum containing nonzero imaginary components. As a concrete example of the techniques demonstrated in this section, we consider a single-component condensate described by the Hamiltonian

$$\hat{H} = \int d\boldsymbol{x}\, \hat{\Psi}^\dagger \left(-\frac{\hbar^2 \nabla^2}{2M} + V(\boldsymbol{x}) + \frac{1}{2} U \hat{\Psi}^\dagger \hat{\Psi} - \mu \right) \hat{\Psi}, \tag{3.1}$$

where an arbitrary energy offset μ has been included. This term is introduced for calculational reasons and has no physical influence on the Hamiltonian[1].

The principal idea in finding the excitation spectrum of (3.1) is to take advantage of the usefulness of the Gross-Pitaevskii equation in describing the mean-field of the condensate to enable the quantum-mechanical fluctuations about the mean-field to be considered. To this end the fluctuation operator $\delta\hat{\Psi} = \hat{\Psi} - \Psi$ is defined, where $\Psi = \langle \hat{\Psi} \rangle$, and $\delta\hat{\Psi}$ is considered to be a small quantity[2]. The Hamiltonian (3.1) can then be expanded in powers of $\delta\hat{\Psi}$,

$$\hat{H} = \hat{H}_0 + \hat{H}_1 + \hat{H}_2 + \hat{H}_3 + \hat{H}_4, \tag{3.2}$$

where $\hat{H}_n$ contains terms of order $(\delta\hat{\Psi})^n$. The excitation spectrum of the Hamiltonian $\hat{H}$ is then approximately given by the eigenvalue spectrum of the lowest order non-trivial term in (3.2).

[1] The energy offset cannot affect any observable expectation values as although it contributes a different energy offset for states with different total number, these states are uncoupled due to the conservation of particle-number.

[2] For $\delta\hat{\Psi}$ to be considered a small quantity, the mean field $\langle \hat{\Psi} \rangle$ must be non-zero. However the state of condensates with a large number of atoms is well approximated by either a state with well-defined total number or as a mixture over global phase of coherent states (see Section 2.4), for both of these the mean field $\langle \hat{\Psi} \rangle$ is zero. Despite this, as any *physical* expectation value is independent of the choice of global phase, the analysis presented here can be performed for a coherent state with a given global phase and the results then averaged over that global phase. As all physical expectation values are independent of the global phase this averaging step cannot change the results and can be omitted.

The zeroth order term in (3.2)

$$\hat{H}_0 = \int d\boldsymbol{x}\, \Psi^* \left(-\frac{\hbar^2 \nabla^2}{2M} + V(\boldsymbol{x}) + \frac{1}{2} U \big|\Psi\big|^2 - \mu \right) \Psi \tag{3.3}$$

is simply a constant and represents the total energy of the unexcited mean-field. The first order term is of the form

$$\hat{H}_1 = \int d\boldsymbol{x}\, \delta\hat{\Psi}^\dagger \left(i\hbar \frac{\partial \Psi}{\partial t} \right) + \int d\boldsymbol{x}\, \left(i\hbar \frac{\partial \Psi}{\partial t} \right)^* \delta\hat{\Psi}, \tag{3.4}$$

where the mean-field Ψ evolves as

$$i\hbar \frac{\partial \Psi}{\partial t} = \left(-\frac{\hbar^2 \nabla^2}{2M} + V(\boldsymbol{x}) + U \big|\Psi\big|^2 - \mu \right) \Psi. \tag{3.5}$$

Although the first order term $\hat{H}_1$ is nonzero, it does not affect the evolution of the fluctuation operator:

$$\begin{aligned}
i\hbar \frac{\partial}{\partial t} \hat{\Psi} &= \big[\hat{\Psi}, \hat{H}\big] \\
i\hbar \frac{\partial}{\partial t} \delta\hat{\Psi} + i\hbar \frac{\partial \Psi}{\partial t} &= \big[\Psi, \hat{H}\big] + \big[\delta\hat{\Psi}, \hat{H}\big] \\
i\hbar \frac{\partial}{\partial t} \delta\hat{\Psi} &= \big[\delta\hat{\Psi}, \hat{H}\big] - i\hbar \frac{\partial \Psi}{\partial t} \\
&= \big[\delta\hat{\Psi}, \hat{H}_1\big] + \big[\delta\hat{\Psi}, \hat{H}_2 + \hat{H}_3 + \hat{H}_4\big] - i\hbar \frac{\partial \Psi}{\partial t} \\
&= i\hbar \frac{\partial \Psi}{\partial t} + \big[\delta\hat{\Psi}, \hat{H}_2 + \hat{H}_3 + \hat{H}_4\big] - i\hbar \frac{\partial \Psi}{\partial t} \\
&= \big[\delta\hat{\Psi}, \hat{H}_2 + \hat{H}_3 + \hat{H}_4\big].
\end{aligned} \tag{3.6}$$

As $\hat{H}_1$ does not occur in (3.6), it does not affect the evolution of the fluctuation operators and so will not contribute to the excitation spectrum[3].

The first term in (3.2) that contributes to the evolution of the fluctuation operators is

$$\begin{aligned}
\hat{H}_2 = \int d\boldsymbol{x}\, \delta\hat{\Psi}^\dagger \left(-\frac{\hbar^2 \nabla^2}{2M} + V(\boldsymbol{x}) + 2U \big|\Psi\big|^2 - \mu \right) \delta\hat{\Psi} \\
+ \frac{1}{2} U \int d\boldsymbol{x}\, \left(\Psi^2 \delta\hat{\Psi}^\dagger \delta\hat{\Psi}^\dagger + (\Psi^*)^2 \delta\hat{\Psi}\, \delta\hat{\Psi} \right).
\end{aligned} \tag{3.7}$$

[3]Typical treatments of the Bogoliubov theory consider the restricted case of a static condensate density and choose μ as the chemical potential such that $\dfrac{\partial \Psi}{\partial t} = 0$, and hence $\hat{H}_1 = 0$. As shown by (3.6), this choice of μ is unnecessary as $\hat{H}_1$ does not influence the evolution of $\delta\hat{\Psi}$, *independent* of the choice of μ, and even in the general case of a non-stationary mean field. This latter case is considered in Section 3.4.

As the fluctuation operator $\delta\hat{\Psi}$ is small compared to the mean field Ψ, the higher-order contributions $\hat{H}_3$ and $\hat{H}_4$ to the total Hamiltonian can be neglected compared to $\hat{H}_2$. The excitation spectrum of the condensate about the mean field Ψ is then given by the energy spectrum of $\hat{H}_2$.

To avoid directly solving the infinite dimensional eigenvalue problem $\hat{H}_2|\Psi\rangle = E|\Psi\rangle$ for the condensate excitation spectrum, it is desirable to apply a linear transformation to $\hat{H}_2$ that will diagonalise it in the form

$$\hat{H}_2 = \sum_i \hbar\omega_i \hat{\Lambda}_i^\dagger \hat{\Lambda}_i, \tag{3.8}$$

for some boson annihilation operators $\hat{\Lambda}_i$ and real frequencies ω_i. In this form, the Hamiltonian can be simply interpreted as representing a set of modes with energies $\hbar\omega_i$, which is the condensate excitation spectrum. The eigenvalues of $\hat{H}_2$ can also be identified as $\{n\hbar\omega_i : n > 0\}$. It is not possible in general to transform $\hat{H}_2$ into the form (3.8) if the Hamiltonian possesses any instabilities [152], however one frequently considers the excitation spectrum of the ground state, which is stable by definition, and in this case such a transformation is always possible.

In the general case, we look for the operators $\hat{\Lambda}_i$ satisfying

$$i\hbar\frac{\partial}{\partial t}\hat{\Lambda}_i = \left[\hat{\Lambda}_i, \hat{H}_2\right] = -\hbar\omega_i\hat{\Lambda}_i \tag{3.9}$$

where ω_i is real if and only if $\hat{\Lambda}_i$ is a boson annihilation operator [152]. In the case that ω_i is complex, boson annihilation operators can be constructed from the $\hat{\Lambda}_i$, as discussed in Appendix A. Hence $\hbar\omega_i$ can be considered to be a generalised energy spectrum of the condensate where nonzero imaginary components correspond to dynamical instabilities. Note that although the eigenvalues of $\hat{H}_2$ must be real as it is Hermitian, the eigenvalues of (3.9) need not be real. For example, the Hamiltonian for degenerate parametric down-conversion $\hat{H} = \hbar\chi\left(\hat{a}\hat{a} + \hat{a}^\dagger\hat{a}^\dagger\right)$ is Hermitian but the corresponding eigenvalues of (3.9) are pure imaginary ($\pm i\hbar\chi$). In this case, the occupation of the mode $\hat{a}$ undergoes exponential growth. The case of complex eigenvalues ω_i is discussed further in Section 3.4.5 and Appendix A.

Equation (3.9) is most easily solved by expanding the $\hat{\Lambda}_i$ in a complete, linearly independent basis $\{\hat{\Upsilon}_j\}$ such that $\hat{\Lambda}_i = \boldsymbol{c}_i^\dagger\hat{\boldsymbol{\Upsilon}}$ where $\boldsymbol{c}_i$ is a complex vector, $\boldsymbol{c}_i^\dagger$ denotes its conjugate-transpose, and $\hat{\boldsymbol{\Upsilon}}$ is the column vector formed by the complete basis $\{\hat{\Upsilon}_j\}$. For

the case of (3.7), an appropriate basis is $\{\hat{\Upsilon}_j\} = \{\delta\hat{\Psi}, \delta\hat{\Psi}^\dagger\}$. As the Hamiltonian $\hat{H}_2$ is quadratic, its commutator with every operator $\hat{\Upsilon}_j$ will be linear in the operators $\{\hat{\Upsilon}_j\}$. Defining the complex matrix $\mathcal{H}$ to represent this relationship

$$\sum_k \mathcal{H}_{jk}\hat{\Upsilon}_k = \left[\hat{\Upsilon}_j, \hat{H}_2\right], \tag{3.10}$$

permits (3.9) to be recast as an eigenvalue problem in $\mathcal{H}$,

$$\left[\boldsymbol{c}_i^\dagger\hat{\boldsymbol{\Upsilon}}, \hat{H}_2\right] = \boldsymbol{c}_i^\dagger\mathcal{H}\hat{\boldsymbol{\Upsilon}} = -\hbar\omega_i\boldsymbol{c}_i^\dagger\hat{\boldsymbol{\Upsilon}}, \tag{3.11}$$

$$\implies \boldsymbol{c}_i^\dagger\mathcal{H} = -\hbar\omega_i\boldsymbol{c}_i^\dagger \tag{3.12}$$

where the last line follows as the components of $\hat{\boldsymbol{\Upsilon}}$ are linearly independent. If the mean-field Ψ is time-independent, then the matrix $\mathcal{H}$ will also be time-independent and (3.12) represents an eigenvalue problem for the left eigenvectors $\boldsymbol{c}_i^\dagger$ and eigenvalues $-\hbar\omega_i$ of the matrix $\mathcal{H}$. If the mean-field Ψ simply evolves due to a global phase rotation, this can be cancelled by appropriate choice of the arbitrary energy offset μ making $\mathcal{H}$ time-independent. In the case of the condensate ground state, that offset will be the chemical potential of the condensate. The eigenvalues $\{\hbar\omega_i\}$ then represent the generalised excitation spectrum of the condensate about the mean field, which was to be determined.

The eigenvalue problem (3.12) may also be obtained by an equivalent method by obtaining a linearised equation for the evolution of the fluctuation operators $\delta\hat{\Psi}$. This technique is used in Section 3.4.2.

It is important to note that for the eigenvalues of $\mathcal{H}$ to determine the solution to (3.9), the matrix $\mathcal{H}$ must be constant. In the next section, these techniques will be generalised to the case of a *periodic* mean-field in which the time-dependence of the matrix $\mathcal{H}$ cannot be removed by any analytic transformation.

In the case of a homogenous condensate ($V(\boldsymbol{x}) = 0$), the matrix $\mathcal{H}$ can be diagonalised analytically to give the condensate excitation spectrum as

$$\hbar\omega(\boldsymbol{k}) = \sqrt{\varepsilon(\boldsymbol{k})\left(\varepsilon(\boldsymbol{k}) + 2nU\right)}, \tag{3.13}$$

where $\boldsymbol{k}$ is the wavevector, $\varepsilon(\boldsymbol{k}) = \dfrac{\hbar^2\boldsymbol{k}^2}{2M}$ is the free-particle energy spectrum, and $n = \left|\Psi\right|^2$ is the condensate density. Equation (3.13) is known as the Bogoliubov excitation spectrum [153].

In the limit of large wavenumbers, the Bogoliubov excitation spectrum becomes

$$\hbar\omega(\boldsymbol{k}) \approx \varepsilon(\boldsymbol{k}) + nU, \tag{3.14}$$

i.e. that of a free particle shifted by the mean field experienced by the rest of the condensate. It is important to note that this spectrum is that of *excitations* to the condensate, not of particles *added* to the system with wavenumber $\boldsymbol{k}$. The energy of a thermal particle added to the system will be given by the excitation spectrum *plus* the chemical potential, i.e. the energy required to add an atom to the system nU. In the limit of large wavenumbers, the energy of a thermal particle is

$$E_{\text{thermal}}(\boldsymbol{k}) \approx \varepsilon(\boldsymbol{k}) + 2nU. \tag{3.15}$$

Thermal particles therefore experience *twice* the mean-field experienced by the condensate. This is because the thermal atoms can be distinguished from the atoms in the condensate, while the atoms in the condensate cannot be distinguished from one another.

The interested reader is referred to the review paper by Ozeri *et al.* [151] for further details about Bogoliubov theory in Bose-Einstein condensates.

3.4 Condensate excitations in the perturbative regime

The observed features in the atom laser profile presented in Section 3.2 are caused by a dynamical instability in the condensate that causes the formation of entangled momentum excitations in a narrow range of momenta along the weak trapping axis. During outcoupling, these excitations are accelerated along the tight trapping directions to form the momentum cones pictured in Figure 3.2. The detection process vertically integrates this momentum profile leading to the observed peaks in Figure 3.1.

The dynamical instability arises because of the significantly different scattering lengths between the Zeeman levels of He*. In Section 3.5, a full multimode quantum-field calculation is discussed, but it is enlightening to first consider a simplified model in which the energy spectrum (and stability) of small excitations to the condensate can be obtained.

The simplified model to be considered is that of a homogenous spinor condensate consisting of two levels with Rabi oscillations coupling them. The approximation that the condensate is homogenous (known as the local density approximation [154, 155]) is justified if the excitations under consideration have wavelengths much smaller than the

Thomas-Fermi radius in that dimension. The local density approximation will hold for this system along the axial direction as the axial momentum of the features observed in Figure 3.1 corresponds to an excitation wavelength of $\sim 5\,\mu\text{m}$, significantly smaller than the Thomas-Fermi radius in the axial direction of $z_{\text{TF}} = 175\,\mu\text{m}$.

The second approximation made in this model is to neglect the antitrapped state $m_F = -1$. Any density in this state leaves the condensate very rapidly due to the combined effects of both the mean-field repulsion and the magnetic field gradient. A classical particle in the centre of the condensate under the influence of the same effective potential experienced by the $m_F = -1$ atoms would reach a momentum equal to the momentum width of the condensate (and hence no longer be able to couple to the stationary atoms in the middle of the condensate) in $\sim 80\,\mu\text{s}$, significantly shorter than the Rabi period of $\sim 2\,\text{ms}$.

With these approximations made, the Hamiltonian for this system is

$$\begin{aligned}\hat{H} = \sum_i \int d\boldsymbol{x}\, \hat{\Psi}_i^\dagger \left(\frac{-\hbar^2\nabla^2}{2M} - \mu\right) \hat{\Psi}_i + \frac{1}{2}\sum_{ij} U_{ij} \int d\boldsymbol{x}\, \hat{\Psi}_i^\dagger \hat{\Psi}_j^\dagger \hat{\Psi}_j \hat{\Psi}_i \\ + \hbar\Omega \int d\boldsymbol{x}\, \left(\hat{\Psi}_1^\dagger \hat{\Psi}_0 + \hat{\Psi}_0^\dagger \hat{\Psi}_1\right),\end{aligned} \tag{3.16}$$

where $U_{ij} = 4\pi\hbar^2 a_{ij}/M$ is the nonlinear interaction strength, a_{ij} is the s-wave scattering length between internal states i and j, Ω is the Rabi frequency which is taken to be real, and μ is an energy offset which has been included to cancel the global phase rotation which would otherwise be present. The equations of motion corresponding to this Hamiltonian are

$$i\hbar\frac{\partial}{\partial t}\hat{\Psi}_1 = -\frac{\hbar^2}{2M}\nabla^2\hat{\Psi}_1 + U\left(\hat{\Psi}_1^\dagger\hat{\Psi}_1 + \hat{\Psi}_0^\dagger\hat{\Psi}_0\right)\hat{\Psi}_1 + \hbar\Omega\hat{\Psi}_0 - \mu\hat{\Psi}_1, \tag{3.17a}$$

$$i\hbar\frac{\partial}{\partial t}\hat{\Psi}_0 = -\frac{\hbar^2}{2M}\nabla^2\hat{\Psi}_0 + U\left(\hat{\Psi}_1^\dagger\hat{\Psi}_1 + \kappa\hat{\Psi}_0^\dagger\hat{\Psi}_0\right)\hat{\Psi}_0 + \hbar\Omega\hat{\Psi}_1 - \mu\hat{\Psi}_0, \tag{3.17b}$$

where $U = U_{11} = U_{10}$ and $\kappa = U_{00}/U_{11}$. For metastable helium in the $F = 1$ manifold, $\kappa \approx 0.74$ [156], while for Rubidium in the $F = 1$ manifold, $\kappa = 1.002$ [91, 157].

3.4.1 The dynamical steady-state

The excitation spectrum of a condensate can be obtained by approximating each field operator as a complex number (the mean-field) plus a small fluctuation term, and then either diagonalising the Hamiltonian [153, 158] or diagonalising the linearised equations of

motion for the fluctuations themselves (see Section 3.3). It is the latter approach that will be taken here, but with the difference that the mean-field about which the linearisation procedure will take place is itself time-dependent.

The relevant mean-field that we wish to consider is the one that describes the state of the BEC in the experiment. At $t = 0$ all of the population in the condensate is in the $m_F = 1$ level, representing the original trapped BEC, while the $m_F = 0$ atom laser level is initially unpopulated. Rabi oscillations transfer population between these two levels, and it will be shown that these oscillations are periodic.

The method for diagonalising the evolution equations of the linearised fluctuations to obtain the excitation spectrum is the same method used to determine the stability of fixed points of systems of nonlinear ordinary differential equations. As mentioned in the previous section, this method relies critically on the fact that it is a stationary solution about which the equations are linearised. Floquet's Theorem [159] allows the stability of *periodic* solutions to be considered, and it is this theorem that will be used to determine the stability of the condensate about these periodic mean-field dynamics. It will now be shown that the evolution of the mean-field of (3.17) is periodic.

Within the local density approximation, we can assume that the mean-field remains homogeneous; only the excitations have spatial dependence. The equations of motion for the mean-field then reduce to the following ordinary differential equations:

$$i\hbar\frac{d}{dt}\Psi_1 = U\left(|\Psi_1|^2 + |\Psi_0|^2\right)\Psi_1 + \hbar\Omega\Psi_0 - \mu\Psi_1, \tag{3.18a}$$

$$i\hbar\frac{d}{dt}\Psi_0 = U\left(|\Psi_1|^2 + \kappa\,|\Psi_0|^2\right)\Psi_0 + \hbar\Omega\Psi_1 - \mu\Psi_0. \tag{3.18b}$$

Although solving (3.18) for $\kappa \neq 1$ is intractable analytically, it can be shown that the solutions are periodic up to a global phase rotation, and exactly periodic with appropriate choice of the arbitrary energy offset μ. This can be shown by recognising these equations as modified optical Bloch equations [113, §5.B] containing a nonlinear term but with no damping. Defining $\Psi_i = c_i\sqrt{n}$, where $n = |\Psi_1|^2 + |\Psi_0|^2$ is the total density, the equations of motion for the density matrix terms $\rho_{10} = c_1 c_0^*$ and $w = \rho_{11} - \rho_{00} = |c_1|^2 - |c_0|^2$ are

$$\frac{d}{dt}\rho_{10} = -i\frac{g}{2}(1-w)\rho_{10} + i\Omega w, \tag{3.19a}$$

$$\frac{d}{dt}w = -4\Omega\,\mathrm{Im}\{\rho_{10}\}, \tag{3.19b}$$

where $g = nU(1-\kappa)/\hbar$. As the evolution is purely Hamiltonian, these equations conserve

the expectation value of the Hamiltonian. In particular, as the number of atoms is also conserved, the mean energy per particle given by

$$E = \frac{\langle \hat{H} \rangle}{\langle \hat{N} \rangle} = -\frac{1}{8}\hbar g(1-w)^2 + 2\hbar\Omega \,\mathrm{Re}\{\rho_{10}\} \tag{3.20}$$

is conserved. The solutions to (3.19) are visualised in Figure 3.3.

As the evolution is purely Hamiltonian, the state can be described by a point on the surface of the Bloch sphere (see Figure 3.3). The state is however not completely free to move on this sphere as the energy per particle E must be conserved by its motion. Equation (3.20) is a holonomic constraint, which together with the identity $w^2 + 4\left|\rho_{10}\right|^2 = 1$ reduce the number of degrees of freedom of the solution from three (w, $2\,\mathrm{Re}\{\rho_{10}\}$, $2\,\mathrm{Im}\{\rho_{10}\}$) to one, restricting the system's motion to a one-dimensional subset of the surface of the Bloch sphere (lines of constant colour in Figure 3.3).

There exists an extension to the Poincaré-Bendixson theorem that states that for certain manifolds, including the sphere S^2, all possible paths traced out by a C^2 action (which includes paths in phase space from a sufficiently smooth Hamiltonian) must approach or be periodic cycles, go to fixed points, or be a curve that covers the entire surface [160]. The last possibility is only possible on manifolds equivalent to a torus [160], which the sphere is not.

In Section C.1 it is shown that the fixed points in the current system are unreachable, meaning that they either cannot be reached in normal evolution, or are a trivial case of periodicity where nothing changes. The final possibility consistent with the theorem proved in [160] is that some trajectories may approach a limit cycle. In Section C.1 it is also shown that limit cycles cannot exist in this system. Consequently, all trajectories in this system must be periodic.

Although it follows from the periodicity of the evolution of the state on the Bloch sphere that all physical expectation values are periodic (as they must be independent of the global phase), the global phase rotation must be cancelled for the mean fields themselves to be periodic. This can be achieved by appropriate choice of the energy offset μ. It is the periodicity of the order parameters Ψ_i that will enable the stability of the condensate to excitations to be determined.

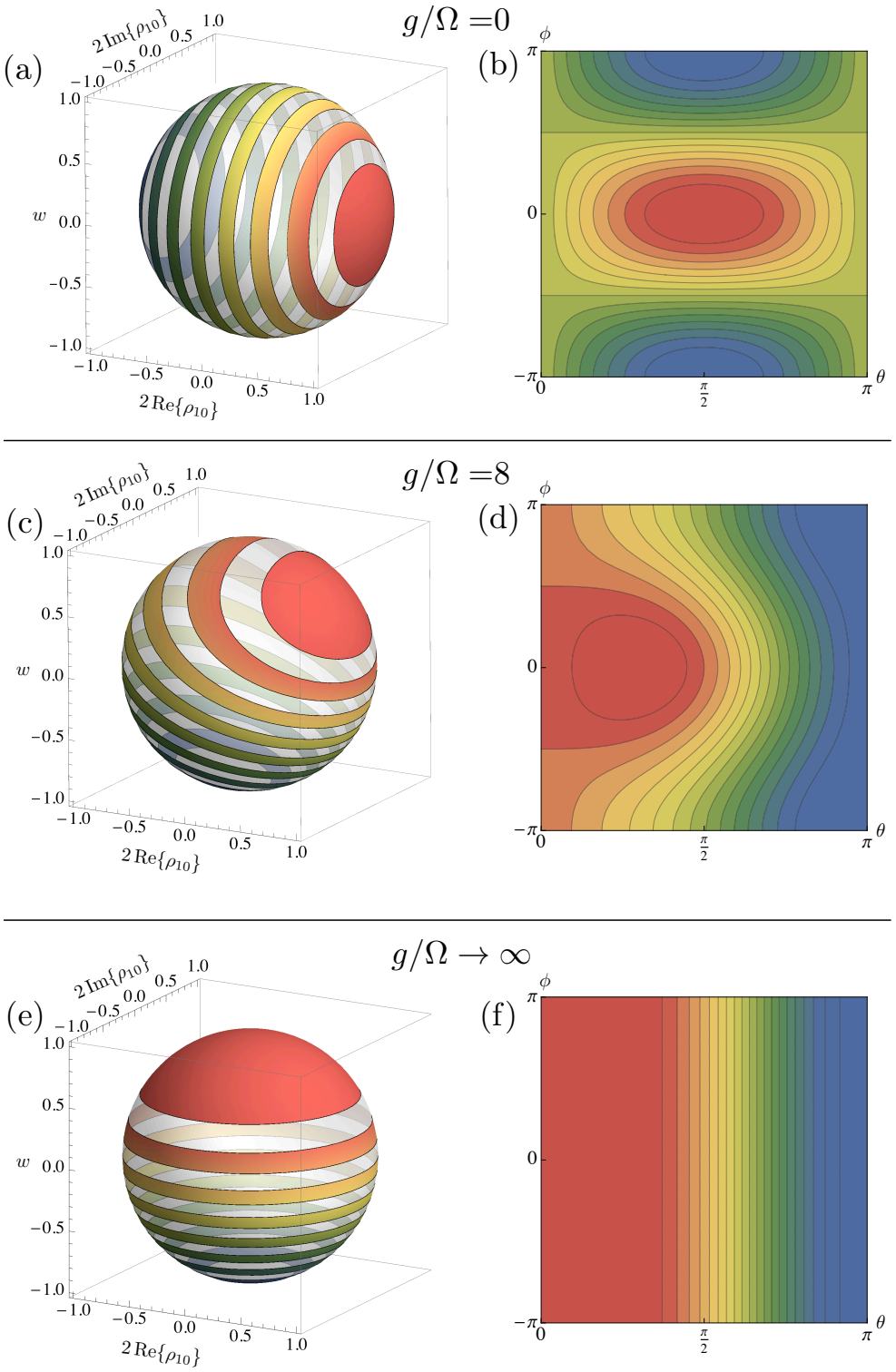

Figure 3.3: Bloch sphere representation of the evolution described by (3.19). The upper figures (a) and (b) represent the case of the usual optical Bloch equations with no damping ($g/\Omega = 0$), middle figures (c) and (d) illustrate the effect of the nonlinear term on the evolution with $g/\Omega = 8$, and the lower figures (e) and (f) illustrate the limit where the nonlinear term dominates ($g/\Omega \to \infty$). The left figures (a), (c), (e) illustrate the Bloch sphere coloured according to the energy per particle E [see (3.20)]. The system is constrained to move on lines of constant colour. Bands have been removed from these spheres for illustration purposes only. The right figures (b), (d), (f) are contour plots of the energy per particle E over the surface of the Bloch sphere.

3.4.2 Excitation dynamics

The evolution of small perturbations about the mean-field dynamics of a condensate define both the excitation spectrum of the condensate and its stability to perturbations. To determine the evolution of these excitations, the mean-field dynamics must be separated from that of the excitations. To this aim, we define the fluctuation operators $\delta\hat{\Psi}_i = \hat{\Psi}_i - \langle\hat{\Psi}_i\rangle$ and treat $\delta\hat{\Psi}_i$ as a small quantity. In this case the $\langle\hat{\Psi}_i\rangle = \Psi_i$ are themselves time dependent, obeying the equations for the mean-field (3.18).

The equations of motion for the fluctuation operators are obtained by replacing the field operators $\hat{\Psi}_i$ in the operator evolution equations (3.17) with $\Psi_i + \delta\hat{\Psi}_i$ and keeping only terms up to first order in the fluctuation operators (see Section 3.3). Applying this procedure gives

$$\begin{aligned} i\hbar\frac{\partial}{\partial t}\delta\hat{\Psi}_1 =& U\left[\left(2\left|\Psi_1\right|^2 + \left|\Psi_0\right|^2\right)\delta\hat{\Psi}_1 + \Psi_1^2\delta\hat{\Psi}_1^\dagger + \Psi_1\Psi_0\delta\hat{\Psi}_0^\dagger + \Psi_0^*\Psi_1\delta\hat{\Psi}_0\right] \\ &- \frac{\hbar^2}{2M}\nabla^2\delta\hat{\Psi}_1 + \hbar\Omega\delta\hat{\Psi}_0 - \mu\delta\hat{\Psi}_1, \end{aligned} \tag{3.21a}$$

$$\begin{aligned} i\hbar\frac{\partial}{\partial t}\delta\hat{\Psi}_0 =& U\left[\left(2\kappa\left|\Psi_0\right|^2 + \left|\Psi_1\right|^2\right)\delta\hat{\Psi}_0 + \kappa\Psi_0^2\delta\hat{\Psi}_0^\dagger + \Psi_1\Psi_0\delta\hat{\Psi}_1^\dagger + \Psi_1^*\Psi_0\delta\hat{\Psi}_1\right] \\ &- \frac{\hbar^2}{2M}\nabla^2\delta\hat{\Psi}_0 + \hbar\Omega\delta\hat{\Psi}_1 - \mu\delta\hat{\Psi}_0. \end{aligned} \tag{3.21b}$$

Having assumed the mean-field (but not the fluctuations) to be homogenous, the evolution equations are spatially translation-invariant and will take their simplest form in a Fourier basis. Performing the Fourier transform of (3.21) yields

$$\begin{aligned} i\hbar\frac{\partial}{\partial t}\delta\hat{\Psi}_1(\boldsymbol{k}) =& U\left[\left(2\left|\Psi_1\right|^2 + \left|\Psi_0\right|^2\right)\delta\hat{\Psi}_1(\boldsymbol{k}) + \Psi_1^2\delta\hat{\Psi}_1^\dagger(-\boldsymbol{k}) + \Psi_1\Psi_0\delta\hat{\Psi}_0^\dagger(-\boldsymbol{k}) + \Psi_0^*\Psi_1\delta\hat{\Psi}_0(\boldsymbol{k})\right] \\ &+ \frac{\hbar^2\boldsymbol{k}^2}{2M}\delta\hat{\Psi}_1(\boldsymbol{k}) + \hbar\Omega\delta\hat{\Psi}_0(\boldsymbol{k}) - \mu\delta\hat{\Psi}_1(\boldsymbol{k}), \end{aligned} \tag{3.22a}$$

$$\begin{aligned} i\hbar\frac{\partial}{\partial t}\delta\hat{\Psi}_0(\boldsymbol{k}) =& U\left[\left(2\kappa\left|\Psi_0\right|^2 + \left|\Psi_1\right|^2\right)\delta\hat{\Psi}_0(\boldsymbol{k}) + \kappa\Psi_0^2\delta\hat{\Psi}_0^\dagger(-\boldsymbol{k}) + \Psi_1\Psi_0\delta\hat{\Psi}_1^\dagger(-\boldsymbol{k}) + \Psi_1^*\Psi_0\delta\hat{\Psi}_1(\boldsymbol{k})\right] \\ &+ \frac{\hbar^2\boldsymbol{k}^2}{2M}\delta\hat{\Psi}_0(\boldsymbol{k}) + \hbar\Omega\delta\hat{\Psi}_1(\boldsymbol{k}) - \mu\delta\hat{\Psi}_0(\boldsymbol{k}). \end{aligned} \tag{3.22b}$$

In this form, it is clear that the Fourier modes are almost completely decoupled from each other. Each fluctuation operator $\delta\hat{\Psi}_i(\boldsymbol{k})$ is only coupled to $\left\{\delta\hat{\Psi}_j(\boldsymbol{k}),\, \delta\hat{\Psi}_j^\dagger(-\boldsymbol{k})\right\}$, with each $\delta\hat{\Psi}_i^\dagger(-\boldsymbol{k})$ also only coupled to this same set. This can be exploited to write the

equations (3.22) in matrix form as

$$i\hbar\frac{\partial}{\partial t}\hat{\boldsymbol{\Upsilon}}(\boldsymbol{k}) = \mathcal{H}(\boldsymbol{k})\hat{\boldsymbol{\Upsilon}}(\boldsymbol{k}), \tag{3.23}$$

where

$$\hat{\boldsymbol{\Upsilon}}(\boldsymbol{k}) = \left(\delta\hat{\Psi}_1(\boldsymbol{k}) \quad \delta\hat{\Psi}_1^\dagger(-\boldsymbol{k}) \quad \delta\hat{\Psi}_0(\boldsymbol{k}) \quad \delta\hat{\Psi}_0^\dagger(-\boldsymbol{k})\right)^{\mathrm{T}}, \tag{3.24}$$

$$\mathcal{H}(\boldsymbol{k}) = \begin{pmatrix} \varepsilon(\boldsymbol{k}) + q_1 - \mu & v_{11} & u_{01} + \hbar\Omega & v_{10} \\ -v_{11}^* & -\varepsilon(\boldsymbol{k}) - q_1 + \mu & -v_{10}^* & -u_{10} - \hbar\Omega \\ u_{10} + \hbar\Omega & v_{10} & \varepsilon(\boldsymbol{k}) + q_0 - \mu & \kappa v_{00} \\ -v_{10}^* & -u_{01} - \hbar\Omega & -\kappa v_{00}^* & -\varepsilon(\boldsymbol{k}) - q_0 + \mu \end{pmatrix}, \tag{3.25}$$

and $q_1 = U\left(2\left|\Psi_1\right|^2 + \left|\Psi_0\right|^2\right)$, $q_0 = U\left(2\kappa\left|\Psi_0\right|^2 + \left|\Psi_1\right|^2\right)$, $u_{ij} = U\Psi_i^*\Psi_j$, $v_{ij} = U\Psi_i\Psi_j$, and $\varepsilon(\boldsymbol{k}) = \dfrac{\hbar^2\boldsymbol{k}^2}{2M}$.

Note that the matrix $\mathcal{H}(\boldsymbol{k})$ is not the Hamiltonian, but is related to it by (3.10). As a consequence, although it will be shown later that in some circumstances $\mathcal{H}(\boldsymbol{k})$ contains complex eigenvalues and is hence not Hermitian, this in no way conflicts with the requirement that the Hamiltonian $\hat{H}$ must be Hermitian and only have real eigenvalues.

If the coefficients of the matrix $\mathcal{H}(\boldsymbol{k})$ were not time-dependent, the excitation spectrum of the condensate could simply be obtained from the eigenvalues of $\mathcal{H}(\boldsymbol{k})$. Non-zero imaginary components for these eigenvalues would indicate the corresponding mode to be unstable[4]. Before continuing with the general case of $\kappa \neq 1$, in the next section the limit in which all scattering lengths are equal ($\kappa = 1$) will be considered and some familiar results recovered.

3.4.3 Excitation spectra in the $\kappa = 1$ limit

In the limit that all the scattering lengths are the same ($\kappa = 1$), the nonlinear term in (3.18) only contributes to a rotation of the global phase of the spinor condensate. In this case, the dynamics can be solved analytically and familiar excitation spectra recovered.

[4]This is true independent of the sign of the imaginary component as the eigenvalues come in pairs with opposite imaginary components. A full discussion of this issue is given in Appendix A.

The general solution to (3.18) for $\kappa = 1$ is

$$\Psi_1(t) = \cos(\Omega t)\Phi_+ + \sin(\Omega t)\Phi_-, \tag{3.26a}$$

$$\Psi_0(t) = -i\sin(\Omega t)\Phi_+ + i\cos(\Omega t)\Phi_-, \tag{3.26b}$$

for some complex constants $\Phi_\pm$, and where the chemical potential $\mu = nU$ has cancelled the global phase rotation. This solution can be viewed as a linear basis transformation from $\hat{\Psi}_i$ to $\hat{\Phi}_\pm$, which are the eigenvectors of the Rabi coupling term in (3.16). Performing this change of basis on the original Hamiltonian (3.16) yields a Hamiltonian of the same form, but without the Rabi coupling term. The equations of motion for the fluctuation operators $\delta\hat{\Phi}_\pm$ therefore give a matrix of precisely the same form as (3.25), but in terms of $\Phi_\pm$ and $\delta\hat{\Phi}_\pm$ instead of the Ψ_i and $\delta\hat{\Psi}_i$, and with Ω replaced by 0. This new matrix $\mathcal{H}'(\boldsymbol{k})$ is time-independent and can be diagonalised to give the eigenvalues

$$\hbar\omega_\uparrow(\boldsymbol{k}) = \sqrt{\varepsilon(\boldsymbol{k})\left(\varepsilon(\boldsymbol{k}) + 2nU\right)}, \tag{3.27a}$$

$$\hbar\omega_\downarrow(\boldsymbol{k}) = \varepsilon(\boldsymbol{k}), \tag{3.27b}$$

where $\varepsilon(\boldsymbol{k}) = \dfrac{\hbar^2\boldsymbol{k}^2}{2M}$, $n = |\Psi_1|^2 + |\Psi_0|^2$ and the remaining two eigenvalues are the negatives of those in (3.27). The first of these, $\hbar\omega_\uparrow(\boldsymbol{k})$, is the usual Bogoliubov spectrum [153], which corresponds to excitations in the total condensate density. The second eigenvalue $\hbar\omega_\downarrow(\boldsymbol{k})$ is the free particle spectrum; this excitation only changes the relative densities of the two states without affecting the total density, hence not affecting the nonlinear term in the Hamiltonian (3.16).

The Hamiltonian for the condensate excitations that corresponds to the eigenvalues (3.27) is (refer to Section 3.3)

$$\hat{H} = \sum_{i=\uparrow,\downarrow} \int d\boldsymbol{k}\, \hbar\omega_i(\boldsymbol{k})\hat{\Lambda}_i^\dagger(\boldsymbol{k})\hat{\Lambda}_i(\boldsymbol{k}), \tag{3.28}$$

where the $\hat{\Lambda}_{\uparrow,\downarrow}(\boldsymbol{k})$ obey boson commutation relations and are the corresponding normalised eigenvectors to the eigenvalues in (3.27). The normalised eigenvectors for the negatives of those eigenvalues are the $\hat{\Lambda}^\dagger_{\uparrow,\downarrow}(-\boldsymbol{k})$.

3.4.4 Floquet's theorem [159, §3.2]

Having considered the limit of equal scattering lengths, it now remains to determine the energy spectrum and condensate stability in the general case of $\kappa \neq 1$. Analytic results cannot be obtained in this limit, but numeric results corresponding to the experimental situation in Section 3.2 can be obtained.

In the general case, the excitation spectrum cannot be obtained from the eigenvalues of the matrix $\mathcal{H}(\boldsymbol{k})$ in (3.25) as the matrix's entries are themselves time-dependent. However, due to the periodicity of the mean-field wavefunctions demonstrated in Section 3.4.1, the entries of $\mathcal{H}(\boldsymbol{k})$ are themselves periodic, which enables Floquet's theorem to be applied.

Floquet's theorem proves that the matrix solution to the initial-value problem

$$\frac{d}{dt}\boldsymbol{\Pi}(t) = \boldsymbol{A}(t)\boldsymbol{\Pi}(t), \tag{3.29a}$$

$$\boldsymbol{\Pi}(0) = \mathbb{I}, \tag{3.29b}$$

where $\mathbb{I}$ is the $n \times n$ identity matrix, and $\boldsymbol{A}(t)$ a periodic $n \times n$ matrix with period T, can be written in the form

$$\boldsymbol{\Pi}(t) = \boldsymbol{P}(t)\exp(-i\boldsymbol{Q}t), \tag{3.30}$$

for some constant matrix[5] $\boldsymbol{Q}$, and $\boldsymbol{P}(t)$ a matrix of periodic functions with period T and $\boldsymbol{P}(0) = \mathbb{I}$. The matrix solution $\boldsymbol{\Pi}(t)$ is the general solution to the related linear system

$$\frac{d}{dt}\boldsymbol{x}(t) = \boldsymbol{A}(t)\boldsymbol{x}(t), \tag{3.31}$$

for any initial condition $\boldsymbol{x}(0)$, where $\boldsymbol{x}(t)$ is a vector. Every solution $\boldsymbol{x}(t)$ to this problem can be written in terms of the matrix $\boldsymbol{\Pi}(t)$ using

$$\boldsymbol{x}(t) = \boldsymbol{\Pi}(t)\boldsymbol{x}(0), \tag{3.32}$$

as may be verified. The matrix solution $\boldsymbol{\Pi}(t)$ thus completely determines the behaviour of all solutions to (3.31).

The eigenvalues of $\boldsymbol{Q}$ are known as *Floquet exponents* (or *characteristic exponents*) and determine the long-term growth or decay of the solutions to (3.31). These eigenvalues can

[5] There are differing definitions of the matrix $\boldsymbol{Q}$. While it is usual in quantum mechanics literature [161–163] to define (3.30) with the $-i$ in the exponent, in mathematics literature [159, 164] the $-i$ is omitted.

be obtained from the *monodromy matrix*,

$$\mathcal{M} = \mathbf{\Pi}(T) = \exp(-i\boldsymbol{Q}T), \tag{3.33}$$

as $\boldsymbol{P}(T) = \boldsymbol{P}(0) = \mathbb{I}$. The existence and uniqueness of the solution to (3.29) guarantees that $\mathbf{\Pi}(t)$, and hence $\mathcal{M}$, will be invertible. The Floquet exponents ξ_i can therefore be obtained from the eigenvalues λ_i of the monodromy matrix using $\lambda_i = \exp(-i\xi_i T)$. It is the Floquet exponents of the matrix $\mathcal{H}(\boldsymbol{k})$ that we wish to calculate in order to determine the stability of the condensate to excitations.

3.4.5 Determination of the dynamical instabilities

The method outlined in the previous section for determining the Floquet exponents of the system (3.23) requires knowledge of its period T, and hence the period of the mean field dynamics given by (3.18). Although this period cannot be determined analytically, it can be found numerically.

It was shown in Section 3.4.1 that up to a global phase rotation $f(T) = e^{i2\pi\Delta\nu T} f(0)$, the mean fields $\Psi_j(t)$ are periodic. The mean fields $\Psi_j(t)$ can be therefore written in the form

$$\Psi_j(t) = \sum_{n=-\infty}^{\infty} \alpha_{j,n} \exp\left[i2\pi\left(n\nu_0 + \Delta\nu\right)t\right], \tag{3.34}$$

for some complex constants $\alpha_{j,n}$, fundamental frequency $\nu_0 = T^{-1}$, and frequency offset $\Delta\nu$. In this form, the $\Psi_j(t)$ are not exactly periodic as $\Psi_j(T) = \exp(i\Delta\nu T)\Psi_j(0)$, but this frequency offset can be cancelled by an appropriate choice of the energy offset $\mu = -2\pi\hbar\Delta\nu$ in (3.16).

The period T and frequency offset $\Delta\nu$ in (3.34) can be determined from the Fourier transform of $\Psi_j(t)$, which will have sharp peaks at the frequencies $n\nu_0 + \Delta\nu$ (see Figure 3.4). Choosing the energy offset $\mu = -2\pi\hbar\Delta\nu$, the frequency offset in (3.34) can be cancelled making the $\Psi_j(t)$ with this energy offset exactly periodic with period T. Figure 3.4 illustrates the Fourier transform of the numerical solutions for $\Psi_j(t)$ for a Rabi frequency of $\Omega = 2\pi \times 3\,\mathrm{kHz}$ from which the period $T = 150\,\mu\mathrm{s}$ and frequency offset $\Delta\nu = -1.78\,\mathrm{kHz}$ have been obtained.

The period and energy offset determined, it remains to calculate the monodromy matrix $\mathcal{M}(\boldsymbol{k})$ from which the Floquet exponents may be derived. This is achieved by numerically

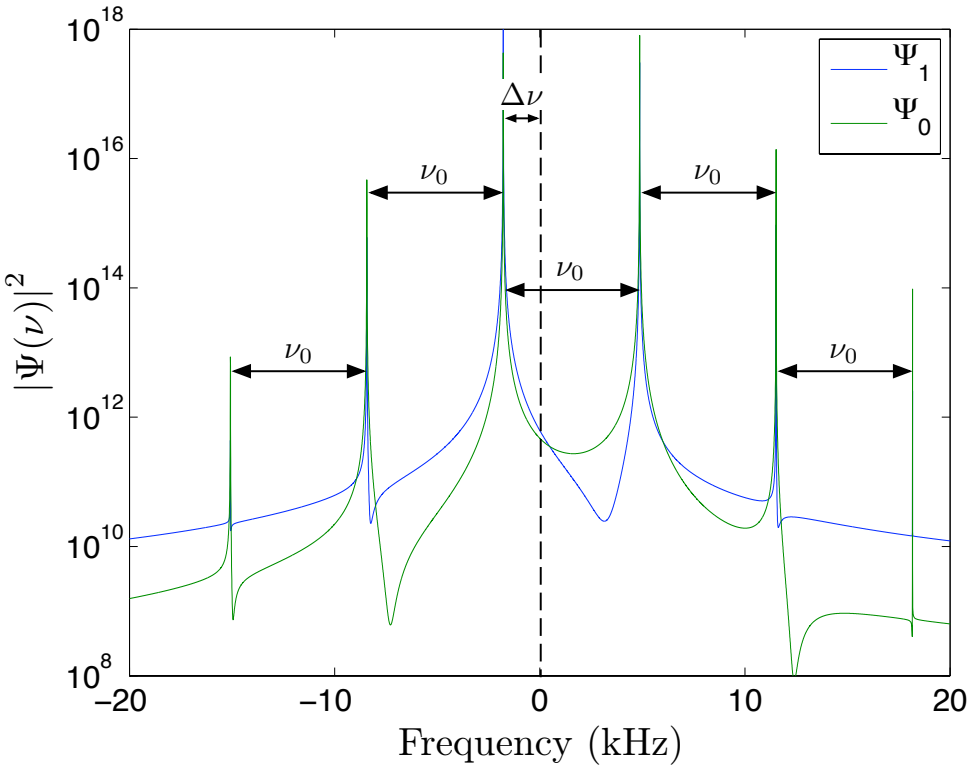

Figure 3.4: Temporal Fourier transform of the calculated mean field evolution defined by (3.18) for the centre of the condensate defined by the experimental parameters given in Table 3.1. The frequency ν_0 is the inverse period of the system, and $\Delta\nu$ represents the global phase rotation. From the data in this figure, the values $\nu_0 = 6.65\,\text{kHz}$ and $\Delta\nu = -1.78\,\text{kHz}$ can be determined, giving the period as $T = 150\,\mu\text{s}$.

solving the related matrix problem to (3.23) from $t = 0$ to $t = T$ [refer to (3.33)]. Noting that the matrix $\mathcal{H}(\boldsymbol{k})$ only depends on $k = |\boldsymbol{k}|$, the solutions for the Floquet exponents $\xi(\boldsymbol{k}) = \omega(\boldsymbol{k}) + i\gamma(\boldsymbol{k})$ are illustrated in Figure 3.5.

In the limit that the mean-field is time-independent (a degenerate case of periodicity), the Floquet exponents $\xi(\boldsymbol{k})$ are related to the eigenvalues $\lambda(\boldsymbol{k})$ of the matrix $\mathcal{H}$ by $\xi(\boldsymbol{k}) = \lambda(\boldsymbol{k})/\hbar$. It was previously stated that eigenvalues of $\mathcal{H}(\boldsymbol{k})$ with nonzero imaginary components would be unstable, this is also true for the Floquet exponents $\xi(\boldsymbol{k})$.

The temporal periodicity of the system implies that the real components $\omega_i(\boldsymbol{k})$ of the Floquet exponents are only uniquely defined modulo $2\pi\nu_0$ [see Figure 3.5(a)]. This is because any eigenvalue λ of the monodromy matrix $\mathcal{M}(\boldsymbol{k})$ corresponds to infinitely many Floquet exponents,

$$\lambda = \exp\left[-i\left(\omega + 2\pi n\nu_0 + i\gamma\right)T\right] = \exp\left[-i\left(\omega + i\gamma\right)T\right]. \tag{3.35}$$

This does not hinder our understanding of the system as our primary interest is in the stability of the condensate to excitations, which is determined by the $\gamma_i(\boldsymbol{k})$.

The normalised eigenvectors of the system are not always annihilation or creation operators; as is discussed in Appendix A, this is only true when the Floquet exponents are purely real. When the Floquet exponents have a nonzero imaginary component, annihilation and creation operators can be constructed from linear combinations of the eigenvectors. Not being eigenvectors, these operators will therefore have nontrivial evolution. As is shown in Appendix A, Floquet exponents with nonzero imaginary parts come in pairs of the form $\omega(\boldsymbol{k}) \pm i\gamma(\boldsymbol{k})$. From the corresponding eigenvectors to these Floquet exponents, the bosonic annihilation operator $\hat{\Lambda}(\boldsymbol{k}, t)$ can be formed, which evolves as

$$\hat{\Lambda}(\boldsymbol{k}, nT) = e^{in\omega(\boldsymbol{k})T}\left(\sinh(n\gamma(\boldsymbol{k})T)\hat{\Lambda}'^{\dagger}(-\boldsymbol{k}, 0) + \cosh(n\gamma(\boldsymbol{k})T)\hat{\Lambda}(\boldsymbol{k}, 0)\right), \tag{3.36a}$$

$$\hat{\Lambda}'(\boldsymbol{k}, nT) = e^{-in\omega(\boldsymbol{k})T}\left(\sinh(n\gamma(\boldsymbol{k})T)\hat{\Lambda}^{\dagger}(-\boldsymbol{k}, 0) + \cosh(n\gamma(\boldsymbol{k})T)\hat{\Lambda}'(\boldsymbol{k}, 0)\right), \tag{3.36b}$$

where n is a positive integer, and where $\hat{\Lambda}'(\boldsymbol{k}, t)$ will be equal to $\hat{\Lambda}(\boldsymbol{k}, t)$ in some circumstances as discussed in Appendix A. Definitions of the $\hat{\Lambda}(\boldsymbol{k}, t)$ and $\hat{\Lambda}'(\boldsymbol{k}, t)$ operators are given in Appendix A. Due to the exponential growth in (3.36), the mode corresponding to $\hat{\Lambda}(\boldsymbol{k})$ represents a dynamical instability of the condensate.

The behaviour of the dynamical instabilities is governed by (3.36) only while the unstable modes have a small occupation compared to the condensate, and scattering

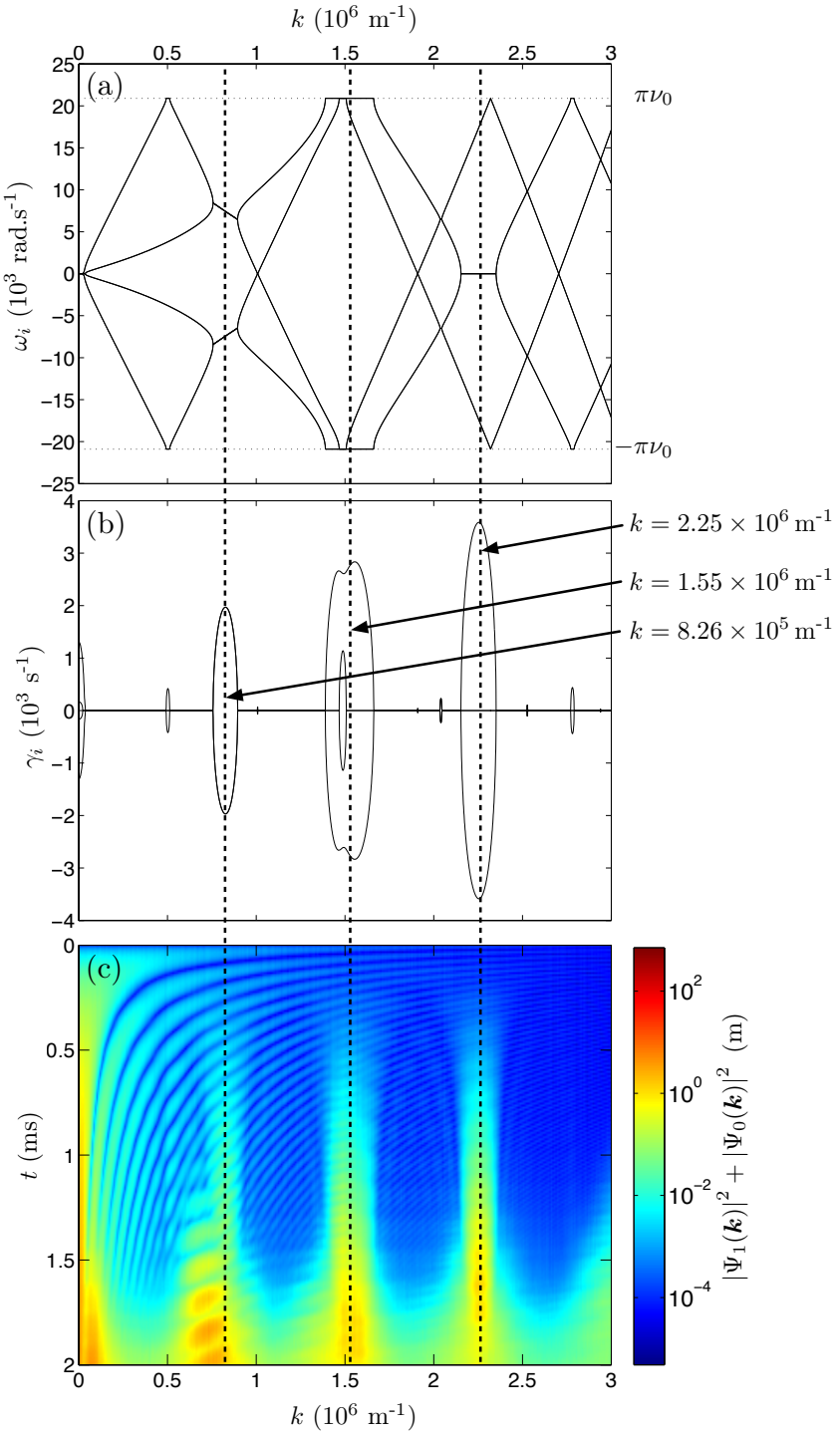

Figure 3.5: Illustration of the Floquet exponents for $\mathcal{H}(\boldsymbol{k})$ and comparison to a corresponding truncated Wigner simulation for $\Omega = 2\pi \times 3\,\mathrm{kHz}$. Upper figure (a) displays the real part ω_i of the Floquet exponents. As the ω_i can only be determined up to a multiple of $2\pi\nu_0$ [see (3.35)], they have been reduced modulo $2\pi\nu_0$ into the range $[-\pi\nu_0, \pi\nu_0]$. The middle figure (b) shows the imaginary part γ_i of the Floquet exponents, which indicate an instability for the corresponding wavenumber when they are nonzero. Note that what appears to be a horizontal line at $\gamma_i = 0$ is not an axis, but a plot of the γ_i which are mostly zero. Lower figure (c) shows the results of a 1D truncated Wigner simulation corresponding to the system under consideration in (a) and (b). The truncated Wigner simulation exhibits growth in the same modes predicted from the results of the perturbative analysis shown in (b). The truncated Wigner results shown are the average of 500 realisations.

between the unstable modes can be neglected. Figure 3.5(c) shows the results of a truncated Wigner simulation of the Hamiltonian (3.16), which is in excellent agreement with the location of the dynamical instabilities as determined by the Floquet exponents [see Figure 3.5(b)]. For later times, there is an additional mode undergoing growth, $k \approx 7.5 \times 10^5\,\mathrm{m}^{-1}$. This mode is the result of scattering between the dynamical instabilities, a process neglected in the perturbative approach taken in this section. Over the 2 ms illustrated in Figure 3.5(c), approximately 10% of the atoms initially in the condensate have scattered into the instabilities.

In summary, the procedure used to find the Floquet exponents of $\mathcal{H}(\boldsymbol{k})$, and hence the stability of the condensate to excitations is:

1. Numerically solve (3.18) with $\mu = 0$ for a long time $t \gg T$ where T is the periodicity of the solution.

2. Perform the temporal Fourier transform of the solutions obtained for $\Psi_i(t)$ to accurately determine the period T and the value of the energy offset μ required to cancel any global phase evolution to make the wavefunctions themselves periodic (see Figure 3.4).

3. Using the calculated period and energy offset, numerically solve the related matrix problem to (3.23) for a range of values of $\boldsymbol{k}$ to obtain the monodromy matrix $\mathcal{M}(\boldsymbol{k})$. In this calculation the matrix $\boldsymbol{A}(t)$ in (3.29) is $-\frac{i}{\hbar}\mathcal{H}(\boldsymbol{k}, t)$.

4. Calculate the eigenvalues λ_i of $\mathcal{M}(\boldsymbol{k})$ and determine the Floquet exponents ξ_i using $\lambda_i = \exp(-i\xi_i T)$. The real parts of these Floquet exponents gives the energy spectrum, with nonzero imaginary parts giving the growth rate for the corresponding instability.

3.4.6 Discussion of the dynamical instabilities

The dynamics of the dynamical instability $\hat{\Lambda}(\boldsymbol{k})$ described by (3.36) are the same as those of the amplified modes in non-degenerate parametric down-conversion [148]. In parametric down-conversion, a non-linear crystal produces pairs of EPR-entangled[6] photons

[6]EPR entanglement was proposed by Einstein, Podolsky and Rosen [165] as a demonstration that quantum mechanics could not simultaneously be local, real and complete. Their preferred option of local and real but *incomplete* has since been demonstrated to be incorrect [166]. For more information about EPR entanglement, see [113, Chapter 18].

at frequencies ω_1 and ω_2 from a classical seed beam at frequency $\omega = \omega_1 + \omega_2$. Analogously, in the case of the He* BEC discussed at the start of this chapter, the evolution represented by (3.36) will result in the spontaneous formation of EPR-entangled pairs of excitations, one in each of the $\hat{\Lambda}(\pm\boldsymbol{k})$ modes. Although these modes will be entangled upon production, it does not necessarily follow that parts of the outcoupled atom laser will be entangled; the entangled $\hat{\Lambda}(\boldsymbol{k})$ modes are each superpositions of $m_F = 1$ and $m_F = 0$ states, but only the $m_F = 0$ atoms can leave the condensate. However, if the $m_F = 1$ components of the entangled modes are outcoupled faster than the time to undergo half an oscillation in the trap and reverse their momenta (9 ms), then number difference squeezing between the atom laser components with opposite axial momenta may be observed. This requires that most of the condensate be outcoupled in less than 9 ms.

The unstable excitations would not necessarily be expected to form along the tight trapping directions. Of the three most unstable modes in Figure 3.5, the shortest wavelength for these excitations is $\lambda \approx 3\,\mu\text{m}$, which is not significantly smaller than the Thomas-Fermi radius in this dimension of $\rho_{\text{TF}} = 9.4\,\mu\text{m}$. Hence the local density approximation will not be satisfied in this dimension as the condensate density decays to zero over a distance a few times larger than the size of the excitation itself. However, as the Thomas-Fermi radius in the axial dimension is $z_{\text{TF}} = 175\,\mu\text{m}$, the local density approximation will be a good approximation for describing the excitations along that dimension. Therefore excitations should form along the axial dimension.

This effect also depends on the scattering length for collisions between $m_F = 0$ atoms being significantly smaller than both the 1–1 and 1–0 scattering lengths as no instabilities were found in the $\kappa = 1$ limit (see Section 3.4.3). Consequently, this effect would not be expected to be observed in atoms like ^{87}Rb for which $\kappa = 1.002$ [91, 157].

Verification that the $\hat{\Lambda}(\boldsymbol{k})$ quasiparticles are the origin of the peak-like structure observed in the experiment required a full 3D field calculation, which is discussed in Section 3.5. The argument made in this section that the observed structure is due to the formation of pairs of quasiparticles driven by a spontaneous four-wave mixing process indicates that a Gross-Pitaevskii model will be unable to reproduce the observations. Such a mean-field model will be insufficient due to the absence of the vacuum fluctuations which are critical to all spontaneous processes.

3.5 Full 3D calculation

In the previous section, it was found that the process of outcoupling from the He* BEC discussed in Section 3.2 results in certain modes within the condensate becoming unstable. It was argued that these instabilities are the original cause of the observed structure in Figure 3.1. However, it is not immediately clear that these instabilities will not be suppressed by Penning ionisation, which causes $m_F = 0$ atoms to ionise but not pure samples of $m_F = 1$ atoms (see Section 2.5.1 and Appendix B). To verify that the instabilities are not suppressed and that they do cause the observed structure, a detailed numerical simulation of the experiment was performed.

The master equation that describes the experiment described in Section 3.2 is given by

$$\frac{d}{dt}\hat{\rho} = \frac{-i}{\hbar}[\hat{H},\, \hat{\rho}] + \frac{9}{2}K_{^4\mathrm{He}}^{(\mathrm{unpol})} \int d\boldsymbol{x}\, \mathcal{D}\left[\hat{\Xi}_{S=0,m_S=0}\right] \hat{\rho}, \tag{3.37}$$

where $\hat{\Xi}_{S,m_S}$ is the annihilation operator for the quasimolecular state with total hyperfine spin S and projection m_S (refer to Section 2.3), $\mathcal{D}[\hat{c}]\hat{\rho} \equiv \hat{c}\hat{\rho}\hat{c}^\dagger - \frac{1}{2}(\hat{c}^\dagger\hat{c}\hat{\rho} + \hat{\rho}\hat{c}^\dagger\hat{c})$ is the usual decoherence superoperator, and the second term[7] on the RHS in (3.37) is due to Penning ionisation (refer to Section 2.5.1 and Appendix B) with $K_{^4\mathrm{He}}^{(\mathrm{unpol})} = 7.7 \times 10^{-17}\,\mathrm{m^3 s^{-1}}$ the Penning ionisation rate for an unpolarised thermal sample of He* [120]. The Hamiltonian in (3.37) is given by

$$\begin{aligned}\hat{H} = &\sum_i \int d\boldsymbol{x}\, \hat{\Psi}_i^\dagger \left(\frac{-\hbar^2\nabla^2}{2M} + V_i(\boldsymbol{x})\right) \hat{\Psi}_i + \frac{1}{2}\sum_{S,m_S} g_S \int d\boldsymbol{x}\, \hat{\Xi}_{S,m_S}^\dagger \hat{\Xi}_{S,m_S} \\ &+ \sqrt{2}\hbar\Omega \sum_{ij} \int d\boldsymbol{x}\, \hat{\Psi}_i^\dagger \left(\delta_{i,j+1} + \delta_{i,j-1}\right) \hat{\Psi}_j,\end{aligned} \tag{3.38}$$

$\hat{\Psi}_i$ is the annihilation operator for the atomic state $|F = 1, m_F = i\rangle$, $V_i(\boldsymbol{x})$ is the potential experienced by that state, and $g_S = 4\pi\hbar^2 a_S/M$ is the nonlinear interaction strength, and a_S is the s-wave scattering length for the total hyperfine spin S channel (refer to Section 2.3). The quasi-molecular annihilation operator $\hat{\Xi}_{S,m_S}$ is defined in terms of the atomic annihilation operators and the appropriate Clebsch-Gordan coefficients [90]. For example $\hat{\Xi}_{S=0,m_S=0} = \frac{1}{\sqrt{3}}\left(2\hat{\Psi}_1\hat{\Psi}_{-1} - \hat{\Psi}_0\hat{\Psi}_0\right)$.

In the first instance, we wish to verify the results of the previous section within a fully three-dimensional model and determine the pattern that would be observed on the detector

[7] The reason for the difference between the 54/5 factor in Dall *et al.* [146] and the 9/2 factor in (3.37) is a difference of a factor of $\sqrt{2}$ in the definition of $\hat{\Psi}_{J=0}^{(\mathrm{mol})}$ in [146] and $\hat{\Xi}_{S=0,m_S=0}$ here, and a calculational error of the order of 20% in [146].

in this case. Although a similar system was solved with the GP equation in Section 2.4.2 when the transverse profile of a He* atom laser was considered, it is not possible to solve the system corresponding to (3.37) with available computational infrastructure. The difference between these two systems is in the axial dimension.

When modelling the transverse profile of the atom laser, the tight aspect ratio of the condensate meant that outcoupled atoms would be accelerated much more along the radial trapping directions than along the axial trapping direction. This permitted the use of a much larger spatial grid step size in the axial dimension than in the radial dimensions. In the present system, it is expected that there will exist instabilities with momenta that correspond to a substantial fraction of that which the atom laser would have after leaving the condensate ($\sim 2 \times 10^6\,\mathrm{m}^{-1}$ as compared to $\sim 4 \times 10^6\,\mathrm{m}^{-1}$). In the present, case the spatial grid step size in the axial dimension must be comparable to that used in the radial dimensions. Exacerbating this problem is that the tighter aspect ratio in the experiment described in this chapter requires this significantly smaller spatial grid step size be used over a larger range. To perform a simulation using a method similar to that used in Section 2.4.2, approximately 500 GB of memory would be needed simply to store the wavefunctions for the system. Additional approximations are necessary to make this system tractable.

One of the most effective ways to reduce the size of a problem is by reducing its dimensionality. Although the master equation (3.37) possesses no continuous symmetries, near the BEC it is approximately cylindrically symmetric. The only term breaking this cylindrical symmetry is the gravitational potential $V_{\mathrm{grav}}(\boldsymbol{x}) = -M\boldsymbol{g}\cdot\boldsymbol{x}$ where $\boldsymbol{g}$ is the gravitational field strength. While this term can be neglected over the region close to the BEC as it varies by only 10% of the chemical potential of the BEC, it certainly cannot be neglected when considering the propagation of the atom laser onto the detector located 4 cm below. However, as discussed in Section 2.4.2, the evolution of the atom laser in the region below the BEC is well described by free fall with the exception of fine-scale interference effects. In this chapter it is only the large-scale structure that is of interest, enabling a classical description for the atom laser to be used after it leaves the immediate vicinity of the condensate where the important dynamics will occur.

Another demonstration of the validity of the assumption of cylindrical symmetry is that the gravitational sag of the centre of the condensate from the centre of the trap is only 0.2 µm, which is small compared to the Thomas-Fermi radius in the tight trapping dimensions of $r_{\mathrm{TF}} = 9.4\,\mu\mathrm{m}$. Consequently, atoms will be repelled from the condensate

almost symmetrically. Such a situation was observed earlier in Section 2.4.2.

To solve the system corresponding to the master equation (3.37), a two-step method is used. First, the system is modelled either with a GP equation or a Truncated Wigner method in a restricted cylindrical region enclosing the condensate using absorbing boundary layers (see Section 2.7.1) to prevent the atom laser interacting with the artificial boundary conditions. Second, the momentum density that left the simulation region (calculated using a method described in Section 3.5.2) is then propagated classically to determine the profile on the detector, which is located 4 cm below the BEC. This two-step procedure will permit the use of cylindrical symmetry to reduce the dimensionality of the computational domain while still considering the full three-dimensional behaviour of the system.

3.5.1 Choice of artificial boundary conditions

The freedom of choice for the artificial boundary conditions (refer to Section 2.7.1) can be used to ensure the accurate calculation of all terms in (3.37) and (3.38). With the exception of the kinetic energy term, all terms in these equations are local in space hence their accurate calculation is guaranteed by any spatial representation. It is appropriate therefore to use the freedom in the choice of the artificial boundary conditions to permit the solution to be equivalently represented as a sum of the eigenfunctions of the kinetic energy operator,

$$f(x) = \sum c_n g_n(x) \tag{3.39}$$

where $f(x)$ is the spatial representation of the solution, $g_n(x)$ are the eigenfunctions of the kinetic energy and hence Laplacian operator, and $\{c_n\}$ are complex constants which form an equivalent representation of the solution (the *spectral* representation [167]). Equation (3.39) can be viewed as a change of basis for the solution from the spectral or momentum representation to the spatial representation. This change of basis is invertible as the $g_n(x)$ are orthogonal and complete. For rectangular domains the eigenfunctions $g_n(x)$ are the complex exponentials, which imply periodic boundary conditions. The Fourier transform and its inverse connect the spatial and spectral representations of the solution on this domain.

In this chapter, it is desired to make use of the cylindrical symmetry of the system, hence it is appropriate to represent the solution as a sum of the cylindrically-symmetric eigenfunctions of the Laplacian operator: Bessel functions. The artificial boundary con-

ditions implied by the use of Bessel functions are analyticity at the origin, and Dirichlet boundary conditions at the edge of the domain where the solution is zero. The spatial and spectral representations of the solution are connected by the Hankel transform [168, Chapter 15] and its inverse. The use of the Bessel basis and the Hankel transform to solve the GP equation is described in [169].

Although the Bessel basis is arguably a more useful basis for cylindrically-symmetric problems, the choice of boundary conditions is artificial and for the results presented in [146], a Fourier basis was used on a domain symmetric about the origin. When using a Fourier basis for cylindrical coordinates, care must be taken due to the form of the Laplacian operator,

$$\nabla^2 u(r,z) = \left(\frac{\partial^2}{\partial r^2} + \frac{1}{r}\frac{\partial}{\partial r} + \frac{\partial^2}{\partial z^2}\right) u(r,z). \tag{3.40}$$

In particular, the radial grid must be chosen to exclude the origin due to the apparent divergence in the r^{-1} term in the Laplacian. Note that this is divergence is not real; for sufficiently well-behaved $u(r,z)$, $\nabla^2 u(r,z)$ will be continuous at the origin.

The reason for the choice of the Fourier basis over the Bessel basis in [146] was purely practical: the computational tool (`XMDS` [143]) we use to solve GP and Truncated Wigner problems was not capable of using the Bessel basis. As discussed in Appendix D, this shortcoming has since been rectified by the creation of a successor to the `XMDS` tool, `xpdeint`. All results presented in this chapter have been calculated using the Bessel basis with `xpdeint`, but differ negligibly from the results presented in [146].

3.5.2 Calculation of the momentum flux density

As discussed previously, it is necessary to calculate the momentum density that leaves the simulation region near the condensate to be able to propagate the atom laser classically onto the MCP detector below the condensate. The simulation will necessarily make use of an absorbing boundary layer (refer to Section 2.7.1) to prevent the outgoing atom laser interacting with the artificial boundary conditions at the edge of the computational domain. In the case of a perfect absorbing boundary layer, the dynamics inside the 'region of interest' (see Figure 3.6) will be exactly the same as if the problem were solved on the infinite domain. We wish to calculate the time-integrated momentum density flux $\int \Phi(\boldsymbol{k},t)\,dt$ leaving the region of interest, where $\Phi(\boldsymbol{k},t)$ is the momentum density flux leaving the region of interest at time t.

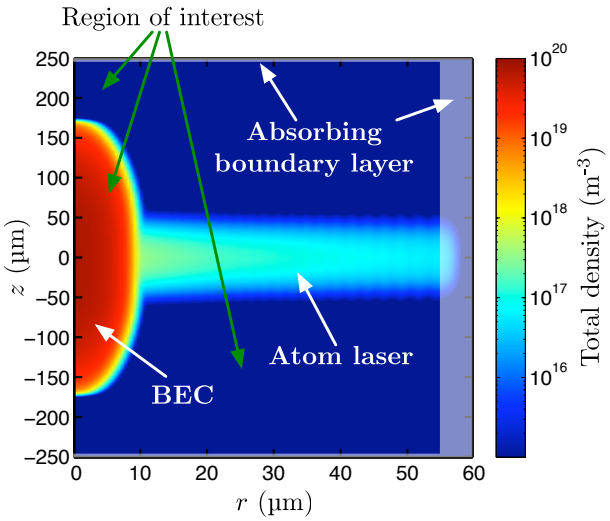

Figure 3.6: A snapshot of the total density from a GP simulation corresponding to the system under discussion in this chapter. It can be observed that the atom laser density is decaying within the absorbing boundary layer. The region of interest and absorbing boundary layer are marked. The region of interest is the entire computational domain except for the absorbing boundary layer. The absorbing boundary layer has a width of 5 µm.

The rate and distribution with which momentum leaves the region of interest can be determined by considering the equation of motion for the wavenumber density in the region of interest,

$$\frac{\partial}{\partial t}\left|\widetilde{\psi}_{\mathrm{roi}}(\boldsymbol{k},t)\right|^2 = 2\,\mathrm{Re}\left\{\widetilde{\psi}^*_{\mathrm{roi}}(\boldsymbol{k},t)\frac{\partial}{\partial t}\widetilde{\psi}_{\mathrm{roi}}(\boldsymbol{k},t)\right\}, \tag{3.41}$$

where $\widetilde{\psi}_{\mathrm{roi}}(\boldsymbol{k},t)$ is the Fourier transform of the restricted wavefunction $\psi_{\mathrm{roi}}(\boldsymbol{x},t)$, which is defined to be nonzero only within the region of interest. The equation of motion for $\widetilde{\psi}_{\mathrm{roi}}(\boldsymbol{k},t)$ is

$$\frac{\partial}{\partial t}\widetilde{\psi}_{\mathrm{roi}}(\boldsymbol{k},t) = -\frac{i}{\hbar}\mathcal{F}\left[\left(-\frac{\hbar^2\nabla^2}{2M} + V(\boldsymbol{x}) + U\left|\psi_{\mathrm{roi}}(\boldsymbol{x},t)\right|^2\right)\psi_{\mathrm{roi}}(\boldsymbol{x},t)\right](\boldsymbol{k}), \tag{3.42}$$

where $\mathcal{F}[f(\boldsymbol{x})](\boldsymbol{k})$ denotes the Fourier transform of the function $f(\boldsymbol{x})$. While the potential and interaction terms in (3.42) redistribute momentum, it is only due to the kinetic term that momentum will leave the region of interest. To see that this is true, consider a Hamiltonian with no kinetic term. In this case the local phase of the wavefunction will rotate, but the density distribution will remain unchanged. Hence it will be the kinetic term in (3.42) that will determine the momentum density flux leaving the region of interest.

The Fourier transform of the kinetic term in (3.42) can be evaluated to give the momentum density flux $\Phi(\boldsymbol{k},t)$ leaving the region of interest in terms of a surface integral

over the boundary of the region of interest,

$$\Phi(\boldsymbol{k},t) = -\frac{\partial}{\partial t}\left|\widetilde{\psi}_{\mathrm{roi}}(\boldsymbol{k},t)\right|^2\Big|_{\mathrm{kinetic}} \tag{3.43}$$

$$= -2\,\mathrm{Re}\left\{\frac{i\hbar}{2M}\widetilde{\psi}^*_{\mathrm{roi}}(\boldsymbol{k},t)\frac{1}{(2\pi)^{\frac{3}{2}}}\oiint e^{-i\boldsymbol{k}\cdot\boldsymbol{x}}\Big[\nabla\psi_{\mathrm{roi}}(\boldsymbol{x},t)+i\boldsymbol{k}\psi_{\mathrm{roi}}(\boldsymbol{x},t)\Big]\cdot d\boldsymbol{A}\right\}. \tag{3.44}$$

The $\psi_{\mathrm{roi}}(\boldsymbol{x},t)$ and $\nabla\psi_{\mathrm{roi}}(\boldsymbol{x},t)$ terms to be evaluated at the boundary in (3.44) should be understood to be defined by the limit from the interior of the region of interest. While (3.44) is the most direct way of evaluating $\Phi(\boldsymbol{k},t)$, it is a computationally inefficient method as it requires the calculation of a surface integral for every point $\boldsymbol{k}$ at which we wish to evaluate $\Phi(\boldsymbol{k},t)$.

A more efficient method can be found by instead considering the evolution of the wavenumber density on the entire computational domain. The momentum flux density that left the region of interest enters the absorbing boundary layer through a term like (3.44), but leaves at a slightly later time due to the negative imaginary potential. As it is not the temporal dynamics of $\Phi(\boldsymbol{k},t)$ in which we are interested, but just the distribution of momentum that left the region of interest at *any* time, this delay is unimportant. On the entire computational domain, the two kinetic transport terms will cancel, leaving the term due to the negative imaginary potential. Assuming that the mean-field interaction energy of the wavefunction reaching the absorbing boundary layer is small compared to its kinetic energy, the momentum flux density leaving the computational domain is given by

$$\Phi(\boldsymbol{k},t) = \frac{2}{\hbar}\,\mathrm{Re}\left\{\widetilde{\psi}^*(\boldsymbol{k},t)\mathcal{F}'\left[V_I(\boldsymbol{x})\psi(\boldsymbol{x},t)\right](\boldsymbol{k})\right\}, \tag{3.45}$$

where $\mathcal{F}'$ is the appropriate Fourier-like transform that connects the spatial and spectral representations of the wavefunction ψ, and guarantees the artificial boundary conditions are satisfied. Equation (3.45) is a more efficient method of evaluating $\Phi(\boldsymbol{k},t)$ than (3.44) as it only requires two Fourier-like transforms to evaluate $\Phi(\boldsymbol{k},t)$ for all $\boldsymbol{k}$, instead of one surface integral *for each* $\boldsymbol{k}$.

The information provided by either (3.44) or (3.45) will only be as good as the absorbing boundary layer. While for a perfect absorbing boundary layer $\int\Phi(\boldsymbol{k},t)\,dt$ would exactly equal the lost momentum density from the region of interest, for an imperfect absorbing boundary layer $\int\Phi(\boldsymbol{k},t)\,dt$ will also include contributions due to any reflection from or

transmission through the boundary layer.

An example calculation of $\Phi(\boldsymbol{k},t)$ for a finite absorbing boundary layer is given in Section C.2. There it is demonstrated that $\Phi(\boldsymbol{k},t)$ is an accurate method for determining the rate of loss of momentum density from a region of space for the same range of momenta for which the absorbing boundary layer is itself accurate.

The simulations described in the remainder of this chapter use the method presented in this section to determine the momentum distribution of atoms that have the left computational domain. This momentum distribution is then propagated classically under gravity to find the corresponding density distribution on the MCP detector below the condensate. This classical propagation was performed by *Mattias Johnsson*. Note that due to the use of cylindrical symmetry, the correct Fourier-like transform for use in (3.45) is the Hankel (or Bessel) transform [168].

3.5.3 Equations of motion

Having described the calculational techniques that will be used, we now turn to the description of the Gross-Pitaevskii and Truncated Wigner equations that were used to model the experiment. The GP equations that correspond to the master equation (3.37) are

$$\begin{aligned}
i\hbar\frac{\partial}{\partial t}\Psi_1 = &\frac{-\hbar^2\nabla^2}{2M}\Psi_1 + \big(V_{\text{trap}}(\boldsymbol{x}) - iV_I(\boldsymbol{x})\big)\Psi_1 + \sqrt{2}\hbar\Omega\Psi_0 \\
&+c_0\sum_j |\Psi_j|^2\Psi_1 + c_2\left(|\Psi_1|^2 + |\Psi_0|^2 - |\Psi_{-1}|^2\right)\Psi_1 + c_2\Psi_{-1}^*\Psi_0^2 \qquad (3.46a)\\
&-i\hbar\frac{3}{2}K_{^4\text{He}}^{(\text{unpol})}\left(2|\Psi_{-1}|^2\Psi_1 - \Psi_{-1}^*\Psi_0^2\right), \\
i\hbar\frac{\partial}{\partial t}\Psi_0 = &\frac{-\hbar^2\nabla^2}{2M}\Psi_0 + \big(\hbar\Delta - iV_I(\boldsymbol{x})\big)\Psi_0 + \sqrt{2}\hbar\Omega\Psi_1 + \sqrt{2}\hbar\Omega\Psi_{-1} \\
&+c_0\sum_j |\Psi_j|^2\Psi_0 + c_2\left(|\Psi_1|^2 + |\Psi_{-1}|^2\right)\Psi_0 + 2c_2\Psi_0^*\Psi_1\Psi_{-1} \qquad (3.46b)\\
&-i\hbar\frac{3}{2}K_{^4\text{He}}^{(\text{unpol})}\left(|\Psi_0|^2\Psi_0 - 2\Psi_0^*\Psi_1\Psi_{-1}\right), \\
i\hbar\frac{\partial}{\partial t}\Psi_{-1} = &\frac{-\hbar^2\nabla^2}{2M}\Psi_{-1} + \big(-V_{\text{trap}}(\boldsymbol{x}) + 2\hbar\Delta - iV_I(\boldsymbol{x})\big)\Psi_{-1} + \sqrt{2}\hbar\Omega\Psi_0 \\
&+c_0\sum_j |\Psi_j|^2\Psi_{-1} + c_2\left(-|\Psi_1|^2 + |\Psi_0|^2 + |\Psi_{-1}|^2\right)\Psi_{-1} + c_2\Psi_1^*\Psi_0^2 \qquad (3.46c)\\
&-i\hbar\frac{3}{2}K_{^4\text{He}}^{(\text{unpol})}\left(2|\Psi_1|^2\Psi_{-1} - \Psi_1^*\Psi_0^2\right),
\end{aligned}$$

where $V_{\text{trap}}(\boldsymbol{x}) = \frac{1}{2}M\left(\omega_r^2 r^2 + \omega_z^2 z^2\right)$ is the trapping potential, $\hbar\Delta$ is the detuning in energy of the resonant outcoupling surface from the centre of the condensate, $c_0 = (g_0 + 2g_2)/3$, $c_2 = (g_2 - g_0)/3$, where $g_S = 4\pi\hbar^2 a_S/M$ is the nonlinear interaction strength, and a_S is the s-wave scattering length for the total hyperfine spin S channel (refer to Section 2.3). A derivation of the Penning ionisation terms in (3.46) is given in Section B.2.

The Truncated Wigner equations corresponding to the master equation (3.37) are very similar to (3.46) but with some additional terms. In Stratonovich form, the equations of motion for the stochastic wavefunctions are approximately

$$\begin{aligned} i\hbar\, d\boldsymbol{\Psi}|_{\text{TW}} \approx\; & i\hbar \frac{\partial}{\partial t}\boldsymbol{\Psi}\bigg|_{\text{GP}} dt - (2c_0 + c_2)\,\frac{1}{\Delta V}\boldsymbol{\Psi}\, dt \\ & + i\sqrt{\hbar V_I(\boldsymbol{x})}\, d\boldsymbol{W}(\boldsymbol{x}) + i\hbar\sqrt{3K_{^4\text{He}}^{(\text{unpol})}} \begin{pmatrix} \Psi_{-1}^* \\ \Psi_0^* \\ \Psi_1^* \end{pmatrix} dW_p(\boldsymbol{x}), \end{aligned} \tag{3.47}$$

where ΔV is the computational grid's volume element (for irregularly spaced grids such as those that are used for cylindrically symmetric problems, ΔV is the local Gaussian quadrature weight [169]), $\boldsymbol{\Psi} = (\Psi_1, \Psi_0, \Psi_{-1})^T$ and $d\boldsymbol{W}(\boldsymbol{x}) = \big(dW_1(\boldsymbol{x}), dW_0(\boldsymbol{x}), dW_{-1}(\boldsymbol{x})\big)^T$ and $dW_p(\boldsymbol{x})$ are the complex Gaussian noises satisfying

$$\overline{dW_i(\boldsymbol{x})\, dW_j(\boldsymbol{x}')} = 0, \tag{3.48}$$

$$\overline{dW_i(\boldsymbol{x})\, dW_j^*(\boldsymbol{x}')} = \frac{1}{\Delta V}\delta_{ij}\delta_{\boldsymbol{x},\boldsymbol{x}'}\, dt, \tag{3.49}$$

where $\overline{(\cdots)}$ denotes the expectation value taken with respect to the noises. The usual spatial Dirac delta function in (3.49) has been replaced by a Kronecker delta function scaled by the inverse volume element due to the discretisation of the problem onto a computational grid.

The origin of the additional terms in (3.47) can be understood qualitatively in terms of the 'virtual' particles added to the initial state required in Truncated Wigner (see Section 2.6.1). The ΔV^{-1} term corrects for the contribution to s-wave scattering due to the virtual particles. The $d\boldsymbol{W}$ term corrects for the loss of virtual particles due to the absorbing boundary layer and the dW_p term does similarly for the virtual particles lost due to Penning ionisation.

The approximation made in obtaining (3.47) was to neglect ΔV^{-1} compared to the field occupations $|\Psi_1|^2$, $|\Psi_0|^2$, $|\Psi_{-1}|^2$ in the Penning ionisation noise term. This is justified

for large occupations where Penning ionisation will be significant. The approximation cannot be made where the density is low, but at these locations the Penning ionisation process itself can be neglected as the associated rate will have decreased proportionally with the density. A derivation of the Penning ionisation noise term in (3.47) is given in Section B.3.

One might like to imagine that the task is essentially complete once a set of equations has been derived that describes a system. Unfortunately, technical considerations often limit which problems are and are not feasible to solve. In this case, although the GP equations given in (3.46) can be solved in a couple of days on a supercomputer, (3.47) represents a much more challenging problem. Not only do these equations need to be solved a large number of times for different initial conditions, but algorithms for solving stochastic differential equations are limited to a lower order[8] than those that can be used for deterministic differential equations, hence significantly smaller time steps are required for solving stochastic differential equations. This problem is mainly due to the Ψ_{-1} state which, due to the antitrapping potential, has a kinetic energy ~ 40 times larger than the Ψ_0 atoms at the edge of the computational domain 60 µm away from the centre of the condensate in the radial direction. The computational domain cannot be restricted to be tighter due to the requirement that the mean-field energy of the Ψ_0 atoms be negligible compared to their kinetic energy for the absorbing boundary layer to be effective. While it is for these practical reasons that we must neglect the Ψ_{-1} state, we are physically justified in doing so by the same arguments given at the start of Section 3.4.

In the next sections the behaviour of the atom laser in the cases of outcoupling from the centre of the condensate (resonant outcoupling) and outcoupling from a detuned surface where the atom laser flux is maximised are considered.

[8]There is no known bound on the order of algorithms for solving stochastic (partial) differential equations, however strongly-convergent algorithms [170] require the evaluation of an exponentially increasing number of higher-order noise integrals with increasing order of the algorithm [171]. For weakly-convergent algorithms [170] (which are all that is required here), the highest-order algorithms known that only require the evaluation of $O(N)$ noise integrals have global order $O(\Delta t^2)$ [172, 173], where N is the number of Gaussian noises required (as the noises are spatially-dependent, N is proportional to the size of the computational grid, and hence the evaluation of $O(N^2)$ or more noise integrals is infeasible).

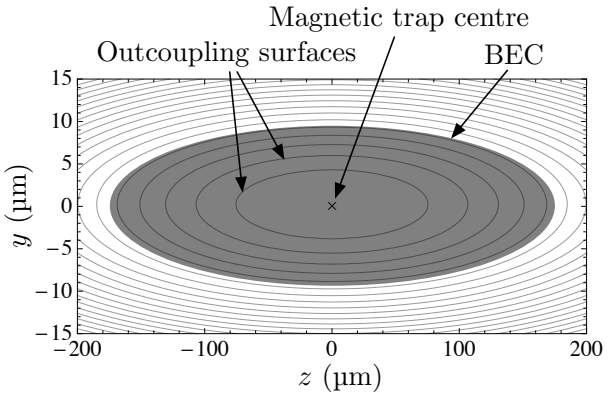

Figure 3.7: Outcoupling surfaces of the He* condensate under consideration in this chapter. The small gravitational sag of $y_{\text{sag}} = 0.2\,\mu\text{m}$ means that the centre of the trap (marked with an '×') and the centre of the condensate almost exactly coincide. Hence the outcoupling surfaces are approximately centred on the centre of the condensate. The contours pictured are equally-spaced in energy. The aspect ratio of this figure is not 1:1 for reasons of clarity; the condensate is significantly more elongated than pictured.

3.5.4 Verification of semianalytical model

As a verification of the results of Section 3.4, we consider outcoupling from the centre of the condensate ($\Delta = 0$). This is the case that corresponds most closely with that of the homogenous condensate considered in Section 3.4 because the shape of the outcoupling surfaces (see Figure 3.7) restricts outcoupling to the centre of the condensate where the density is a local maximum; there the condensate is locally homogeneous.

The results of the GP and TW simulations for the case of resonant outcoupling, but in the absence of Penning ionisation, are presented in Figure 3.8. The atom laser momentum density for the GP and TW simulations are displayed in Figure 3.8(a) and (c) respectively. The primary contribution to the momentum density is around ($k_r \approx 0, k_z \approx 0$) due to Rabi coupling to the Bose-Einstein condensate. Due to the high aspect ratio of the condensate, these atoms are strongly accelerated along the radial direction and hence move to the right in Figure 3.8(a) and (c). At times earlier than $t = 2\,\text{ms}$, which is pictured in Figure 3.8(a) and (c), there is an additional peak at ($k_r \approx 2.8 \times 10^6\,\text{m}^{-1}, k_z \approx 0$) due to the main atom laser after it has accelerated out of the condensate. This peak disappears around $t = 1.8\,\text{ms}$ due to the formation of a bound state (see [107]) causing the atom laser to shutdown.

The primary feature of the MCP detector profiles depicted in Figure 3.8(b) and (d) is the atom laser profile in the middle of both images. The double-peak structure of the atom laser profile was discussed earlier in Section 2.4.2. Briefly, the broad structure is due to the strong acceleration of the atom laser out of the condensate in the radial direction

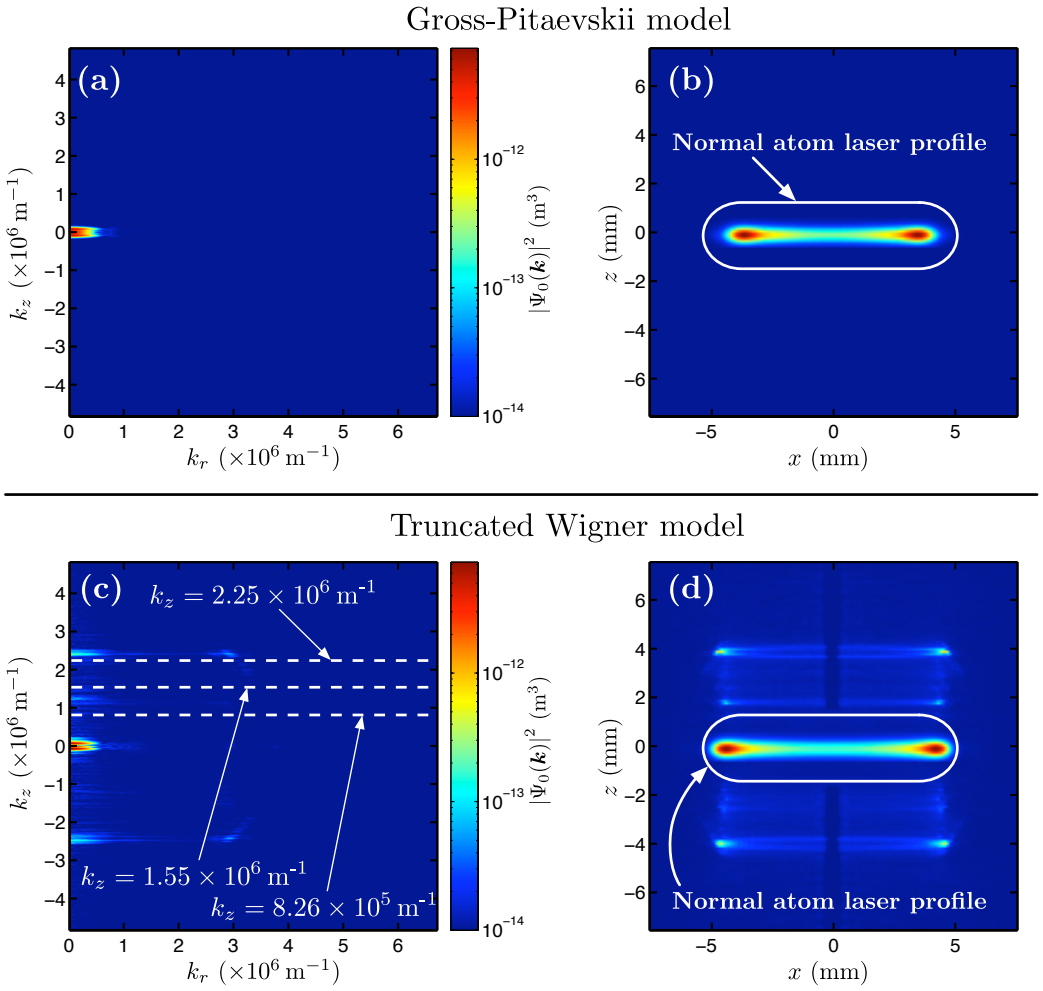

Figure 3.8: Simulation results for outcoupling from the centre of the condensate without Penning ionisation. Left figures (a) and (c) plot the momentum density of the untrapped state at $t = 2\,\mathrm{ms}$ as a function of the radial (k_r) and axial (k_z) wavenumbers. Right figures (b) and (d) plot the normalised density profiles that would be observed on the MCP detector 4 cm below the condensate due to outcoupling from the condensate for $t = 6\,\mathrm{ms}$. The upper figures (a) and (b) plot the results of a GP model where the $m_F = -1$ state is assumed negligible, lower figures (e) and (f) correspond to a Truncated Wigner simulation for the same system averaged over 4 realisations. The wavenumbers of the three fastest-growing instabilities predicted by the perturbation analysis performed in Section 3.4 are marked in (c). The weak axis is in the vertical direction in all figures.

leading to a ring in momentum space [the peak at ($k_r \approx 2.8 \times 10^6\,\mathrm{m}^{-1}, k_z \approx 0$) discussed above]. Due to the expansion of the atom laser as it falls, the measured density on the MCP detector corresponds to the vertically integrated momentum distribution as depicted in Figure 3.2. The vertical integration of the ring-shaped momentum distribution directly leads to the double-peak structure in the main atom laser profile in Figure 3.8(b) and (d). Neither the fine structure nor the 'shadow' of the BEC in the atom laser profile discussed in Section 2.4.2 are observed in Figure 3.8 due to the use of a purely classical method to propagate the momentum density from the edge of the computational region to the detector. However these details are not of interest in this chapter.

The spontaneously-seeded dynamical instabilities predicted in Section 3.4 are observed in the results of the Truncated Wigner model shown in Figure 3.8, but absent from the results of the Gross-Pitaevskii model due to its neglect of spontaneously-seeded processes. Moreover, the dynamical instability with the largest growth rate illustrated in Figure 3.5 at $k = 2.25 \times 10^6\,\mathrm{m}^{-1}$ is in good agreement with the highest growth rate instability in Figure 3.8(c) observed at ($k_r \approx 0$, $k_z \approx \pm 2.4 \times 10^6\,\mathrm{m}^{-1}$). As discussed above, this instability is outcoupled from the condensate and then accelerates radially outwards [to the right in Figure 3.8(c)] to produce rings in momentum space. These rings appear as the double-peaked structures on the MCP detector away from the main atom laser profile in Figure 3.8(d). The formation process of the instabilities is illustrated in Figure 3.9, and a comparison is made to the results of the GP model in which these instabilities do not occur[9].

As discussed in Section 3.4.6 the dynamical instabilities observed in Figure 3.8 will be entangled when they are produced, however the entangled modes are superpositions of the Ψ_1 and Ψ_0 states with opposite momenta. It will not be feasible to directly detect this entanglement as the outcoupling process will significantly complicate the spatial structure of the entangled modes. Although only the Ψ_0 state can leave the magnetic trap, the Ψ_1 component of the entangled mode is likely to be outcoupled faster than the time it would take to perform half an oscillation and reverse the sign of its axial momentum ($\sim 9\,\mathrm{ms}$) if a significant fraction of the condensate is outcoupled in that time. Consequently, number difference squeezing between the opposite momentum components of the entangled modes should be robust enough to survive outcoupling. It cannot be proven due to the small

[9] Although not pictured, the instabilities *are* observed in the GP model, appearing just after $t = 6\,\mathrm{ms}$. The appearance of these instabilities however is not for physical reasons, instead it is caused by the amplification of numerical noise in the simulation. A higher-precision GP simulation would show the instabilities appearing at a time later again.

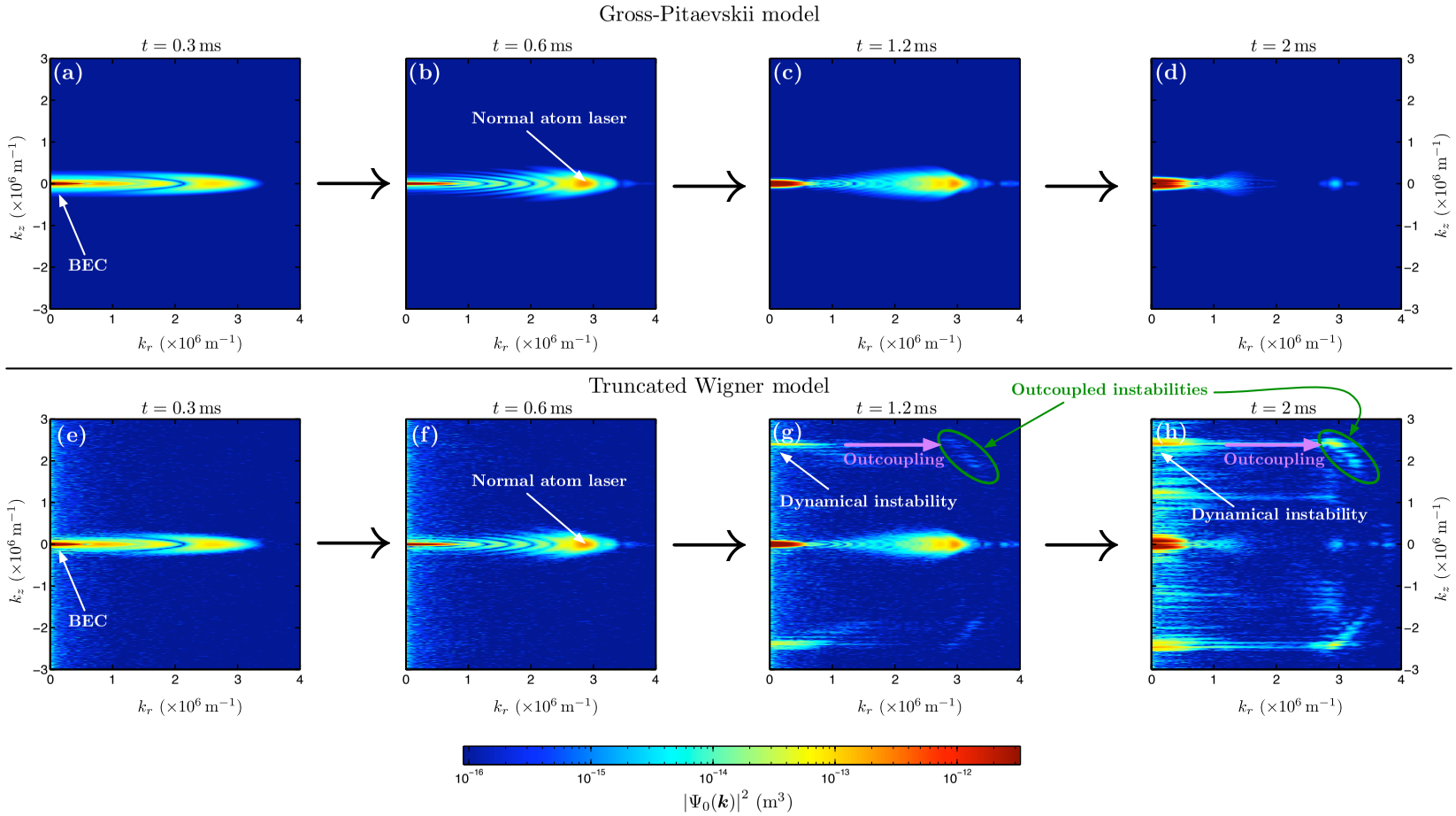

Figure 3.9: Simulation results for outcoupling from the centre of the condensate without Penning ionisation illustrating the formation of the normal atom laser profile and the dynamical instabilities. Upper figures (a)–(d) are the results of a two level Gross-Pitaevskii model, and lower figures (e)–(h) are the results of a two level Truncated Wigner model. The upper and lower rows respectively correspond to the upper and lower rows of Figure 3.8. The columns from left to right show the evolution of the momentum density $|\Psi_0(\boldsymbol{k})|^2$ of the untrapped state at times: 0.3 ms, 0.6 ms, 1.2 ms, and 2 ms. This figure illustrates that the instabilities are spontaneously seeded and that modes between the main atom laser profile and the instabilities are not significantly populated until after the instability has formed. The marked 'Normal atom laser' part of the momentum density distribution is the component that corresponds to the MCP atom laser profile shown in Figure 3.8(b). Note that the vacuum noise in (e)–(h) is not uniform because the initial vacuum noise is proportional to the inverse volume element, which due to the assumed cylindrical symmetry $\Delta V_{\boldsymbol{k}}^{-1} \propto k_r^{-1}$.

number of realisations calculated, however it is expected that there should exist number difference squeezing between the number of atoms above and below the main atom laser beam in Figure 3.8. The main atom laser beam must be excluded as it is produced due to entirely classical means and would not exhibit number-difference squeezing.

Although not pictured, the results of a GP model including all three atomic levels Ψ_1, Ψ_0 and Ψ_{-1} are of the same form as the results presented in Figure 3.8(a) and (b).

3.5.5 Comparison of Theory and Experiment

In the previous section the behaviour of the atom laser when outcoupling from the centre of the condensate was considered. In this limit, it was found that the results of full 3D simulations were in good agreement with the semianalytical model presented in Section 3.4. The features in Figure 3.8(d) and Figure 3.1(b) should therefore be interpreted as the result of the dynamical instabilities discussed in Section 3.4.

While the theoretical results presented in Figure 3.8(d) show some similarity to the experimental results [Figure 3.1(b)], there are qualitative differences. As will be shown in this section, these qualitative differences are due to the difference in detunings used in these two results. While the theoretical results were for the case of outcoupling from the centre of the condensate, the experimental results were for the case of detuned outcoupling. Resonant outcoupling can be understood in terms of the semianalytical model presented in Section 3.4 as the multimode behaviour of the full condensate only affects the dynamics weakly because the net force on atoms outcoupled from the centre of the trap is zero. The direct application of the semianalytical model for detuned outcoupling is complicated by the multimode dynamics which evolve on a comparable timescale to the instabilities due to the nonzero net force on outcoupled atoms. Although the model cannot be directly applied in this case it is reasonable to expect similar behaviour. This expectation must be checked numerically.

The experimental results presented in Figure 3.1 were not obtained by outcoupling from the centre of the condensate but instead a nonzero detuning of $\Delta = 2\pi \times 6.5\,\mathrm{kHz}$ was used, which is a significant fraction of the chemical potential $\mu/\hbar = 2\pi \times 18\,\mathrm{kHz}$. This detuning was for the practical reason that when outcoupling near the centre of the condensate, the atom laser flux *decreases* as the outcoupling surface moves towards the centre of the condensate (for the same rf outcoupling power). This behaviour can be explained using a simple model in which the outcoupled atom laser flux is proportional to the surface area

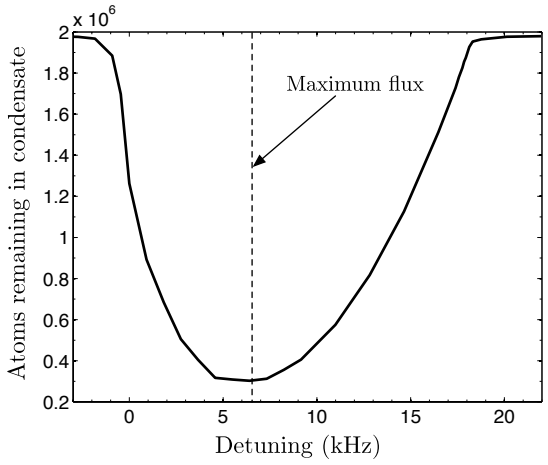

Figure 3.10: Theoretical calculation of the number of atoms remaining in the condensate after 10 ms of outcoupling at a Rabi frequency of $\Omega = 210\,\mathrm{Hz}$ as a function of the detuning of the rf outcoupling from the centre of the condensate. The results shown are obtained from simulations of the 3D GP equations for the condensate under consideration.

of the outcoupling surface times the average density over that surface. Outcoupling from the centre of the condensate will therefore lead to a small atom laser flux due to the small surface area (see Figure 3.7). Detuning will cause the atom laser flux to increase as the surface area increases, before decreasing again as the condensate density drops off towards the edge of the condensate. This behaviour is shown in Figure 3.10. The experimental results presented in Figure 3.1 were for the detuning which maximises the atom laser flux, which can be seen from Figure 3.10 to be $\Delta = 2\pi \times 6.5\,\mathrm{kHz}$.

The results of 2-level TW and 2- and 3-level GP simulations of the experiment for a detuning of $\Delta = 2\pi \times 6.5\,\mathrm{kHz}$ are shown in Figure 3.11. As discussed at the end of Section 3.5.3, a 3-level TW model is too computationally demanding to simulate, although the similarity of the results of the three models presented in Figure 3.11 suggests that the results of such a simulation would differ negligibly from those presented.

The results pictured in Figure 3.11 are of the momentum density $|\Psi_0(\boldsymbol{k})|^2$ of the $m_F = 0$ untrapped state at $t = 5.1\,\mathrm{ms}$. A comparison of the results of simulations with and without Penning ionisation are also shown (right and left columns respectively), which demonstrate that the features depicted are not suppressed by Penning ionisation. As expected, the features of the momentum density profiles in Figure 3.11 have a similar form to those in Figure 3.8(c). An important difference with the results in the limit of zero outcoupling detuning is that for the present detuning, the features at large $|k_z|$ appear in both the TW and GP models indicating that these structures are *not* spontaneously seeded. Figure 3.12 illustrates the formation process of these structures demonstrating that they are produced

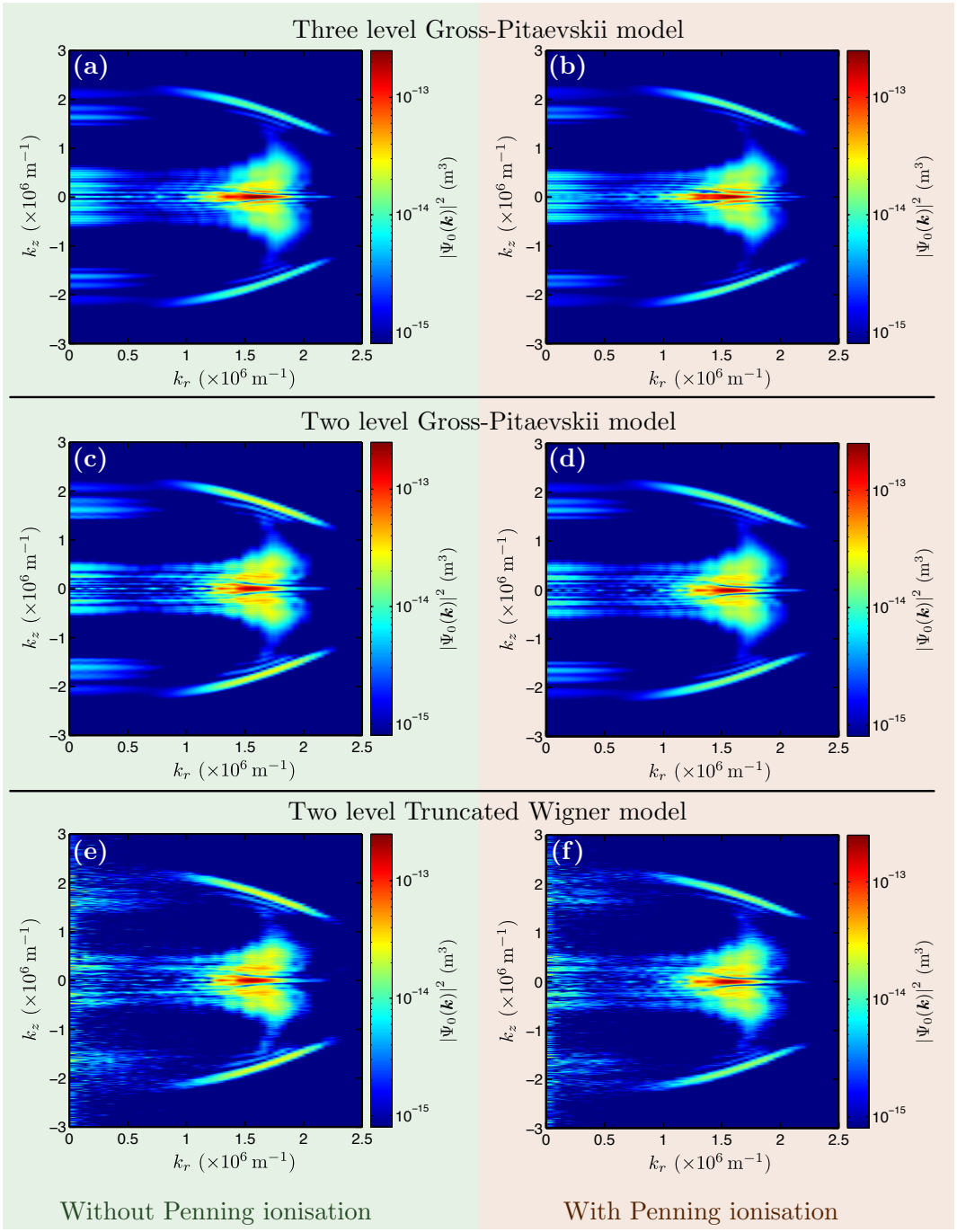

Figure 3.11: Simulation results for outcoupling with a detuning of $\Delta = 2\pi \times 6.5\,\mathrm{kHz}$ from the centre of the condensate, with and without including the effects of Penning ionisation (right and left columns respectively). The upper figures (a) and (b) plot the results of a GP model including all m_F atomic levels. Middle figures (c) and (d) plot the results of a reduced GP model where the $m_F = -1$ is assumed negligible, lower figures (e) and (f) correspond to a Truncated Wigner simulation for the same system averaged over 4 realisations. The negligible difference between the figures in the left and right columns indicate that Penning ionisation has a negligible impact in the simulations depicted.

by a stimulated scattering process from the condensate that sweeps in momentum from $k_z = 0$ towards the final state pictured in Figure 3.11.

A comparison between the experimental atom laser profile and the results of the 3-level GP simulations are presented in Figure 3.13. The theoretical simulations are in excellent agreement with the experiment, demonstrating that the instabilities discussed in Section 3.4 are the origin of the observed experimental atom laser profile. The observed halo between the main atom laser profile and the peak-like structures at the upper and lower ends of the MCP profile are caused by the sweeping of the stimulated scattering process pictured in Figure 3.12. Initially, the atom laser has negligible momentum in the weak trapping dimension [Figure 3.12(a)]. This forms the central component to the atom laser profile in Figure 3.13(f). As outcoupling continues, the stimulated scattering process excites higher momentum modes in the axial dimension, which are then outcoupled [Figure 3.12(b) and (c)] to form the background halo in Figure 3.13(f). Once the stimulated scattering process stabilises at a maximum axial momentum, the peaks furthest from the central atom laser profile in Figure 3.13(f) become emphasised.

3.5.6 Entangled beams?

The dynamical instabilities do not need to be spontaneously seeded to be EPR-entangled. As discussed in Section A.2, the optical parametric down-conversion process that drives the formation of the instabilities gives rise to EPR-entanglement even in the case that one or both of the amplified modes are initially in non-vacuum initial states. In this case the entanglement only exists after a finite delay time.

Although it does not follow that the outcoupled instabilities pictured in Figure 3.13 are not entangled simply because they are predicted by the GP equation, neither can it be concluded that they are. Certainly it cannot be checked by using a GP model, however many more simulation realisations than were used for the TW simulations presented in Figure 3.11 would be necessary to verify whether or not the instabilities are entangled. This calculation is currently infeasible as each realisation takes approximately 20 CPU-hours, and well over 1000 realisations would be necessary.

In the case of resonant outcoupling, the excellent agreement between the results pictured in Figure 3.9 with the semianalytical model of Section 3.4 suggests that we can be confident that the instabilities are entangled upon formation. The outcoupling process itself would complicate the shape of the entangled modes, essentially precluding the use of

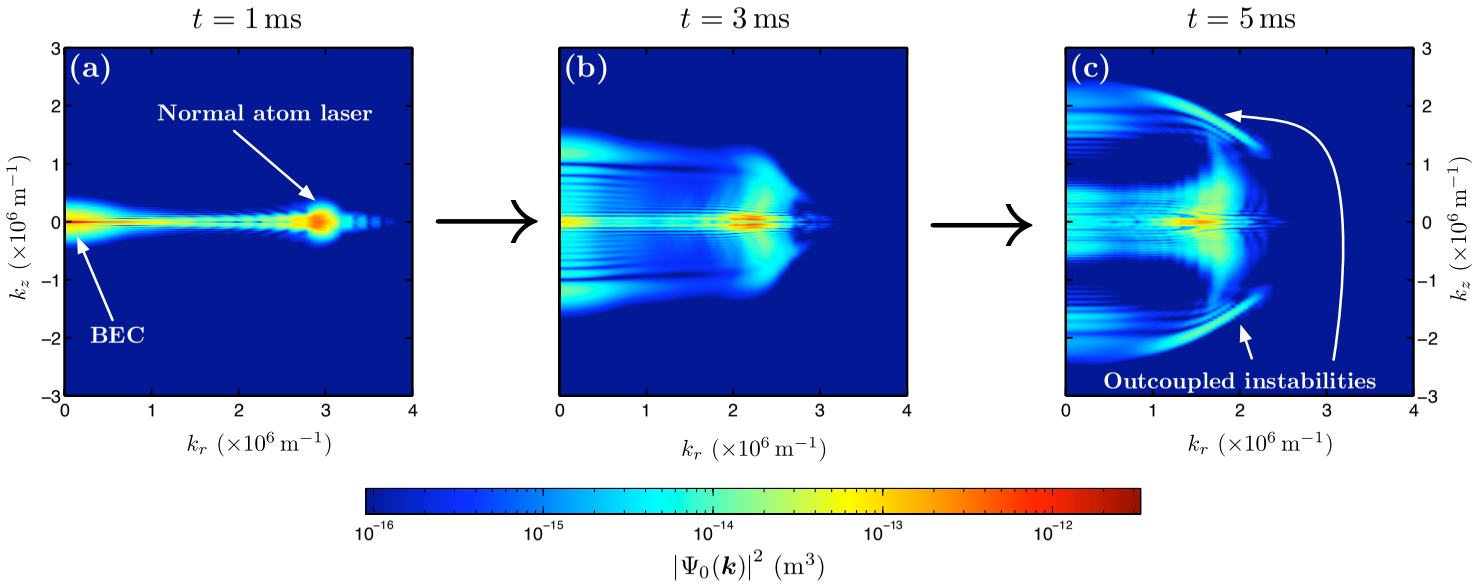

Figure 3.12: Simulation results illustrating the formation of the peak-like structures due to stimulated scattering from the condensate. The results presented are from a three level GP model with a detuning of $\Delta = 2\pi \times 6.5\,\mathrm{kHz}$ and include Penning ionisation [the results correspond to Figure 3.11(b)]. Figures (a), (b), and (c) show the momentum density distribution $|\Psi_0(\boldsymbol{k})|^2$ of the $m_F = 0$ untrapped state at times 1 ms, 3 ms, and 5 ms respectively. The marked outcoupled instabilities are the origin of the structure away from the main atom laser profile in Figure 3.13(e) and (f).

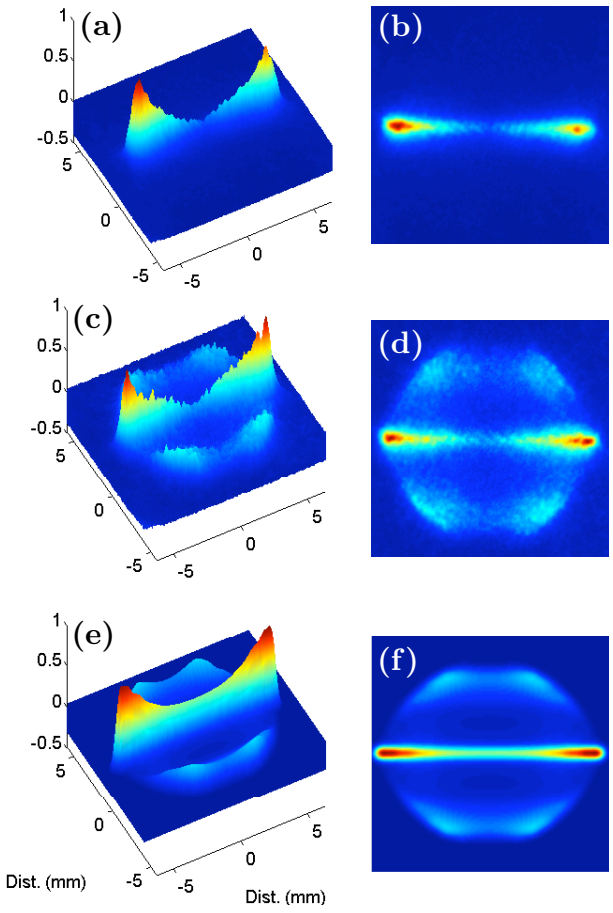

Figure 3.13: First two rows show experimental atom laser spatial profiles on the MCP 4 cm below the trap, in a three-dimensional rendering (left) and a two-dimensional image (right). Both sets of data were taken for an outcoupling detuning of 6.5 kHz; however, the Rabi frequency is increased by an order of magnitude between the two sets. The upper row shows the usual He* atom laser (see Section 2.4.2), while the middle row demonstrates the appearance of the resonant scattering peaks. The bottom row is the result of a simulation of the second experiment. The weak axis of the trap is aligned along the vertical axis of the images on the right.

this mechanism for the direct detection of entangled atomic matter waves (even if atom local oscillators in the correct states could be constructed). That said, for both resonant and detuned outcoupling. number-difference squeezing between opposite sides of the MCP detector should be robust enough to survive outcoupling provided that a significant fraction of the condensate is outcoupled in the time it would take for a trapped atom to execute half an oscillation in the trap (9 ms). These correlations will only exist in the time-integrated profiles as it will not be possible to determine when the other atom in the pair should arrive on the other side of the detector. As the process discussed in this chapter is continuous, a space-time reconstruction of the momentum distribution such as that performed in [80] is not possible.

Although it was not possible to investigate the existence of number-difference squeezing in the experiment described in this chapter, a recent upgrade to the experimental apparatus to include a high-resolution detector similar to that used by Perrin *et al.* [80] has made this a possibility. The author is hopeful that an experiment to look for the predicted number-difference squeezing will be performed in the near future.

3.6 Conclusion

In this chapter, an unusual process in an atom laser was investigated. The process involved the direct conversion of mean-field energy to the kinetic energy of unstable modes in the condensate. This process was shown to generate entanglement in certain regimes, although in the experiment discussed it is unlikely that this entanglement remains in the outcoupled atom laser, and certainly not in any useful form. These problems are however not fundamental. A differently-designed experiment could overcome some of these problems to potentially produce entangled atom lasers.

One possibility worthwhile investigating would be to use a highly elongated two-state condensate in which both states experience the same trapping potential. This could be achieved for example through the use of an optical dipole trap. As the two states of the condensate would experience the same trapping potential, the two components of the dynamical instabilities would propagate together, avoiding the problem of one of the components of the entangled modes leaving the condensate without the other. Further, due to the high aspect ratio, the instabilities would propagate solely along the axial dimension. To extract the entangled beams, one would need to turn off the optical dipole trap after a given interaction time. The atoms would then expand ballistically, with the entangled

beams spatially separating from the main condensate due to their large momentum in the axial direction. This experiment may then enable the production of highly-directional entangled atom lasers. Further theoretical investigation would be necessary to determine if such an experiment were feasible.

The most exciting phrase to hear in science, the one that heralds new discoveries, is not "Eureka!" but "That's funny..." — Isaac Asimov

The interaction between theory and experiment is a two-way street. As a theorist, one might like to think that you can simply do some calculations, make some interesting predictions and then try to convince an experimentalist to test them. While this is certainly a large part of the interaction, it sometimes goes the other way. Sometimes the experimentalist tries something and the results show something that she didn't expect. "That's funny," says the experimentalist. She shows the results to the theorist and asks what might be going on. "That's funny," says the theorist...

This chapter is the story of one such interaction.

Chapter 4

Optical pumping of an atom laser

The development of the continuous-wave photon laser [174] was a significant advance over the first pulsed ruby laser [175], and opened up many applications. The atom laser is a very promising source for both precision measurement and fundamental physics, however to produce a truly continuous atom laser it is necessary to replenish (or pump) the BEC that is the source of the atom laser.

As discussed in Section 1.1.4, the pumping process of an atom laser — just like that of a photon laser — must be irreversible. This irreversibility enters through the coupling of the lasing mode to a much larger system, the reservoir. For the photon laser this is comprised of the (almost) empty modes of the optical field that the atoms decay into after emitting a photon into the lasing mode (see Section 1.1.4). There are two possible choices for the reservoir for an atom laser, and these are considered in this chapter and the next. In this chapter, pumping an atom laser using interactions mediated by light is considered. In this case, the reservoir providing the irreversibility is the vacuum electromagnetic field into which light is scattered by the pumping process. Chapter 5 considers the alternative possibility of using empty modes of an atomic field made accessible by evaporation as the reservoir. In this case, atomic s-wave scattering interactions mediate the pumping process.

The results of Section 4.5.6 have been published in Döring *et al.* [176], which is closely related to our work published in Robins *et al.* [177].

4.1 Introduction

The replenishment process of an atom laser can be divided into two critical components: a delivery system for filling an atomic reservoir with ultracold atoms, and a pumping

mechanism for irreversibly and continuously transferring atoms from the reservoir to the lasing mode. The technical requirements on both parts of the replenishment system are stringent. Nonetheless, recent experiments have demonstrated that a delivery system for atoms is feasible and possible. Chikkatur *et al.* [178] showed that Bose-condensed atoms could be periodically transported over large distances using a moving optical dipole trap. Further experiments with transport, based on interference of two counter-propagating lasers, have shown that dipole trapping techniques could be extended to provide continuous delivery of atoms [179]. Magnetic guiding systems for ultracold atoms may also provide a path to future delivery systems [180–182].

The realisation of the pumping mechanism for a continuous atom laser has proved more problematic. There are four critical requirements that are difficult to satisfy experimentally. First, the atoms should enter the lasing mode continuously and coherently, that is, with the phase and amplitude of the lasing condensate. Thus, atoms must make a transition that is Bose-stimulated by the atomic lasing mode. The second requirement is that the pumping process is irreversible. This requires coupling to a reservoir. There are two reservoirs available, the empty modes of the electromagnetic field accessible via a transition from an excited atomic state, and the empty modes of the atomic field accessible via evaporation. In this chapter, the former is considered, with the latter considered in Chapter 5. The third requirement is that the pumping system must be compatible with a continuous replenishment mechanism. This suggests strongly that there be a physical separation between the source and the lasing condensates. A physical separation with a stimulated transition between the source and the lasing mode isolates the lasing mode from phase kicks and heating that would result either as a necessary consequence of the replenishment system (for example in the replenishment system demonstrated by Chikkatur *et al.* [178] where condensates are merged) or as a consequence of an imperfect delivery system. Finally, the fourth condition on a pumping system is that it should be possible to continuously outcouple atoms from the lasing mode into a beam, while the pumping mechanism is operating.

A number of previous experiments observing the process of super-radiant Rayleigh scattering have demonstrated a physical mechanism for providing pumping through matter-wave amplification [68, 69]. Super-radiant Rayleigh scattering occurs when a far-off-resonant laser illuminates an elongated BEC. A matter-wave grating forms along the long axis of the BEC and atoms are preferentially scattered into non-stationary momentum states. By

providing a moving 'seed' in the $|2\hbar k\rangle$ momentum state, pulsed coherent amplification of this mode was achieved via the Rayleigh super-radiance mechanism. However, this type of matter-wave amplification is a transient phenomena, observed over timescales ranging from tens [68] to hundreds [69] of microseconds. On longer timescales, scattering into successively higher momentum modes seems unavoidable [70], resulting in a 'fan'-shaped scattering pattern [71].

Two promising mechanisms for providing a pumping mechanism consistent with a continuous atom laser have recently been demonstrated. The first is superradiant Raman scattering [72, 73], in which atoms in one internal atomic state are Bose-stimulated to make transitions into an alternative atomic state. The second, reported by Ginsberg *et al.* [30], is a resonant coupling driven by electromagnetically induced transparency (EIT), demonstrated as stimulated decay of atom pulses into a condensate in a freely falling frame. In both cases, the coupling from the source mode is irreversible and the lasing mode is dark to the photons produced by the stimulated transitions. The pumping mechanism considered in this chapter is similar to the mechanisms driving these two experiments, however the implementation is such that the mode experiencing gain (the lasing mode) is stationary, in principle permitting continuous operation. Further, as the lasing mode is stationary, an atom laser can be outcoupled from the lasing mode, enabling the production of a *pumped* atom laser.

4.2 Pumping mechanism

The optical pumping process under investigation in this chapter is illustrated in Figure 4.1(a). In this process atoms in the source mode are driven by a laser into an excited state from which they can decay into the lasing mode (the condensate). Although there is no laser driving this second transition ($|2\rangle \leftrightarrow |3\rangle$), the decay of atoms into the lasing mode is not spontaneous emission in the usual sense. This emission process is *atomically* stimulated by the large occupation of the lasing mode in the same way that emission may be *optically* stimulated in the absence of any population in the atomic ground state.

The final decay of an atom into the lasing mode in Figure 4.1(a) resembles standard photon laser schemes [see Figure 4.1(b)] in which the roles of atoms and light are reversed. In a photon laser an atom in the excited state $|e\rangle$ is stimulated to emit into the lower state $|g\rangle$ by the resonant photons in the laser cavity. Once the atom has emitted it decays rapidly into other internal states with rate $\gamma_{\rm at}$. This significantly limits reabsorption from

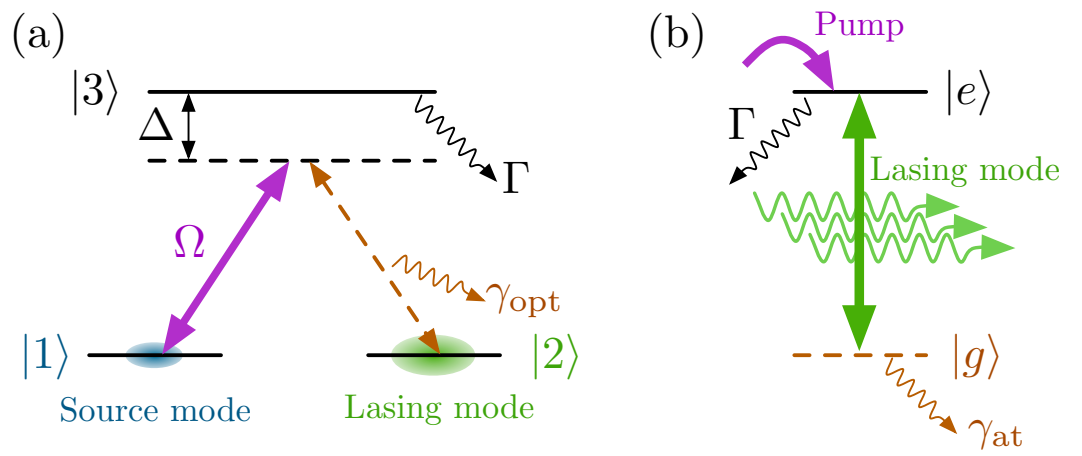

Figure 4.1: Comparison of the atom laser pumping scheme considered in this chapter (a) to the typical photon laser pumping scheme (b). In a photon laser, absorption of lasing mode photons by atoms in the state $|g\rangle$ is suppressed by the fast decay of these atoms to lower atomic levels (represented by a decay process with rate constant $\gamma_{\rm at}$). This fast decay is what makes the pumping process irreversible. This irreversibility in the atom laser pumping mechanism derives from the departure of the photons emitted on the $|2\rangle \leftrightarrow |3\rangle$ transition (represented by a decay process for the $|2\rangle \leftrightarrow |3\rangle$ optical mode with rate constant $\gamma_{\rm opt}$). Once a photon in this mode leaves the system the lasing mode atom cannot be transferred back to the source mode via the excited state $|3\rangle$.

the $|g\rangle$ state. A similar process occurs in the proposed atom laser pumping scheme in which the emitted photon leaves the system rapidly preventing reabsorption. The loss of photons from the system is represented by the decay of the optical mode with rate $\gamma_{\rm opt}$ in Figure 4.1(a).

This similarity between the proposed atom laser pumping mechanism and the usual photon laser pumping mechanism is clearly illustrated by considering the basic form of the atom–light coupling Hamiltonian,

$$\hat{H} = \hbar\epsilon \left(\hat{a}_e^\dagger \hat{a}_g \hat{a}_{\rm ph} + \hat{a}_g^\dagger \hat{a}_{\rm ph}^\dagger \hat{a}_e \right), \tag{4.1}$$

where ϵ is a real coupling constant, the $\hat{a}_e$, $\hat{a}_g$, and $\hat{a}_{\rm ph}$ are annihilation operators for the atomic excited state, atomic ground state and photon mode respectively. The rotating wave approximation has been made in obtaining this Hamiltonian, assuming that the optical mode is not detuned from the atomic transition by a large fraction of the frequency difference between the two states.

The Hamiltonian (4.1) describes both the atom- and photon-laser pumping mechanisms illustrated in Figure 4.1, the difference in the mechanisms being in the occupations of the various states. If the system is initially in a state with N_e atoms in the atomic excited state, N_g atoms in the atomic ground state and $N_{\rm ph}$ photons in the optical mode, the amplitude

(the rate of the process is proportional to the squared magnitude of the amplitude) for an atom in the excited state to emit a photon is

$$\langle N_e - 1, N_g + 1, N_{\rm ph} + 1| \hat{H} |N_e, N_g, N_{\rm ph}\rangle = \hbar\epsilon\sqrt{N_g + 1}\sqrt{N_{\rm ph} + 1}\sqrt{N_e}. \tag{4.2}$$

This emission process can therefore be stimulated either by photons ($N_{\rm ph} > 0$) or by atoms ($N_{\rm g} > 0$). It would also be possible for the emission to be stimulated by both photons *and* atoms, although in this case the amplitude for the absorption process would be non-zero

$$\langle N_e + 1, N_g - 1, N_{\rm ph} - 1| \hat{H} |N_e, N_g, N_{\rm ph}\rangle = \hbar\epsilon\sqrt{N_e + 1}\sqrt{N_{\rm ph}}\sqrt{N_g}. \tag{4.3}$$

It is for this reason that it is desirable in a photon laser to have $N_g \approx 0$, and in the proposed atom laser pumping scheme to have $N_{\rm ph} \approx 0$.

Atom laser pumping schemes of the form illustrated in Figure 4.1(a) have been proposed before [183–194] for the production of BEC without the use of collisional evaporation and its consequent losses. The main problem that they all seek to address is that of reabsorption of photons spontaneously emitted when the atom in the internal state $|3\rangle$ decays to the $|2\rangle$ internal state, but not to the lasing mode. This emitted photon will be resonant with the lasing mode and may be scattered several times before finally leaving the condensate. A single such spontaneously emitted photon can cause significant heating of a condensate as the single photon recoil energy can be as large as or greater than the chemical potential of the condensate.

One proposed method [189, 191] for reducing the heating uses a purely geometric solution: if a condensate is made sufficiently narrow in one or more dimensions such that a photon emitted in one of those directions is negligibly likely to be reabsorbed, the overall probability for reabsorption will also be reduced. While this method may be appropriate for the initial formation of BEC, it is impractical for a large BEC as the trap anisotropy necessary to reach the required regime is extreme. For a ^{87}Rb condensate of $N = 5 \times 10^5$ atoms with trapping frequencies of $\omega_x = \omega_y = 2\pi \times 130\,\text{Hz}$, $\omega_z = 13\,\text{Hz}$, the mean-free path in the centre of the condensate for a resonant photon on the cycling transition ($\lambda = 780\,\text{nm}$) is $1/(n\sigma_0) = 16\,\text{nm}$ where n is the peak condensate density and $\sigma_0 = 3\lambda^2/2\pi$ is the atomic scattering cross-section. This is significantly smaller than the Thomas-Fermi radius in the tight-trapping dimension of $r_{\rm TF} = 5\,\mu\text{m}$. For the Thomas-Fermi radius to be equal to the mean-free path, the ratio of the radial and trapping frequencies would need to be

$\omega_r/\omega_z \sim 10^8$.

Another possibility for reducing reabsorption that works well in optical lattices is to operate in the *festina lente* regime [187, 189, 193, 194] in which the energy levels of the trap are sufficiently separated such that a photon emitted when an atom decays into a particular trap level is only resonant with atoms in that level (and those levels degenerate with it). This prevents the occurrence of 'dangerous' processes in which an excited atom decays into a non-condensate level with the emitted photon being absorbed by the condensate. In the case of resonant optical pumping light [$\Delta = 0$ in Figure 4.1(a)], the *festina lente* regime requires that $\omega_{\rm min} \gg \Gamma$ where $\omega_{\rm min}$ is the minimum of the trapping frequencies. Strictly, the *festina lente* regime has only been investigated in the absence of s-wave scattering interactions, however one would expect that in the presence of s-wave scattering the trap frequency energy scale would simply be replaced by the energy of the relevant Bogoliubov excitation (refer to Section 3.3). Regardless, the *festina lente* regime is impractical to achieve in alkali gases like ^{87}Rb as the relevant decay rate is $\Gamma = 2\pi \times 5.9\,{\rm MHz}$, which is much larger than typical trap frequencies ($\omega \sim 2\pi \times 100\,{\rm Hz}$) and condensate excitations ($\mu/\hbar \sim 2\pi \times 10\,{\rm kHz}$).

A third possibility for reducing reabsorption is to operate in the *boson accumulation regime* (BAR) [186, 195] in which an atom in the excited state is significantly more likely to decay into the condensate mode than into all other modes. In this limit it can be shown that the reabsorption of photons emitted when an atom decays into a mode other than the condensate mode can be neglected. The reabsorption of photons emitted when an atom decays into the condensate mode is not a problem; this simply returns the system to the state before the photon was emitted. In the BAR, it can be expected that a pumping mechanism can operate with high efficiency, and it is in this regime in which we wish to operate our proposed pumping mechanism of Figure 4.1(a).

Up to this point, the statistics of the source mode have not been specified; without consideration of reabsorption the proposed pumping process would work equally well for coherent or thermal states in any source mode that had a non-zero overlap with the lasing mode. As the optical transition between the excited atomic state and the lasing mode is not driven by a laser, the phase of the photons emitted is determined by the relative phase between the source and lasing modes; the direction of population transfer does not depend on the phase difference between these two modes. However the requirement that excited atoms be significantly more likely to decay into the condensate mode than to any

Parameter	Value
$\|F = 2, m_F = 2\rangle$ (source) condensate number	$N_{\text{source}} = (6.7 \pm 0.5) \times 10^5$
$\|F = 1, m_F = -1\rangle$ (laser) condensate number	$N_{\text{laser}} = (5.0 \pm 0.4) \times 10^5$
Radial trapping frequency (for $\|1, -1\rangle$)	$\omega_r = 2\pi \times 130\,\text{Hz}$
Axial trapping frequency (for $\|1, -1\rangle$)	$\omega_z = 2\pi \times 13\,\text{Hz}$

Table 4.1: Experimental parameters for the Rubidium-87 BEC system under consideration.

other mode places a stringent requirement on the source mode of the pumping mechanism. For this requirement to be satisfied, the momentum width of the source atom distribution cannot be significantly larger than the momentum width of the condensate. If this were not the case, a significant fraction of the atoms would not be momentum-resonant with the condensate under the pumping process and will therefore not be in the boson accumulation regime. These atoms would be able to reabsorb spontaneously emitted photons causing the reabsorption problem previously discussed. For an atomic distribution to have a momentum width comparable to that of the target condensate, the atoms must either be condensed or if they are thermal, be trapped in a significantly weaker trap than the target condensate mode and have a temperature below the condensation temperature in the tighter trap.

Although it would be desirable to be able to use a thermal source of atoms as the source mode, the remainder of this chapter will investigate the possibility of using a coherent source of atoms as the source mode of the pumping mechanism. Specifically, this coherent source will be an atom laser extracted from a second, source condensate. Continuous operation of this scheme could in principle be achieved by replacing the source condensate with an independently-produced condensate once it is depleted. As the pumping mechanism is independent of the phase-difference between the source and lasing modes, this will not affect the direction of population transfer.

4.3 The continuous pumping experiment

A summary is provided here of the continuous pumping experiment performed by *Nick Robins*, *Cristina Figl* and *Matthew Jeppesen* at the Department of Quantum Science, ANU. Further details of the experimental setup and results are published in Robins *et al.* [177].

To produce a pumped atom laser two independent condensates are prepared in the $|F = 2, m_F = 2\rangle$ and $|F = 1, m_F = -1\rangle$ magnetically trapped states of ^{87}Rb. Owing to their larger magnetic moment, the $|2, 2\rangle$ atoms are more tightly confined in the magnetic field than the $|1, -1\rangle$ atoms, and hence the evaporation does not directly cool them. They

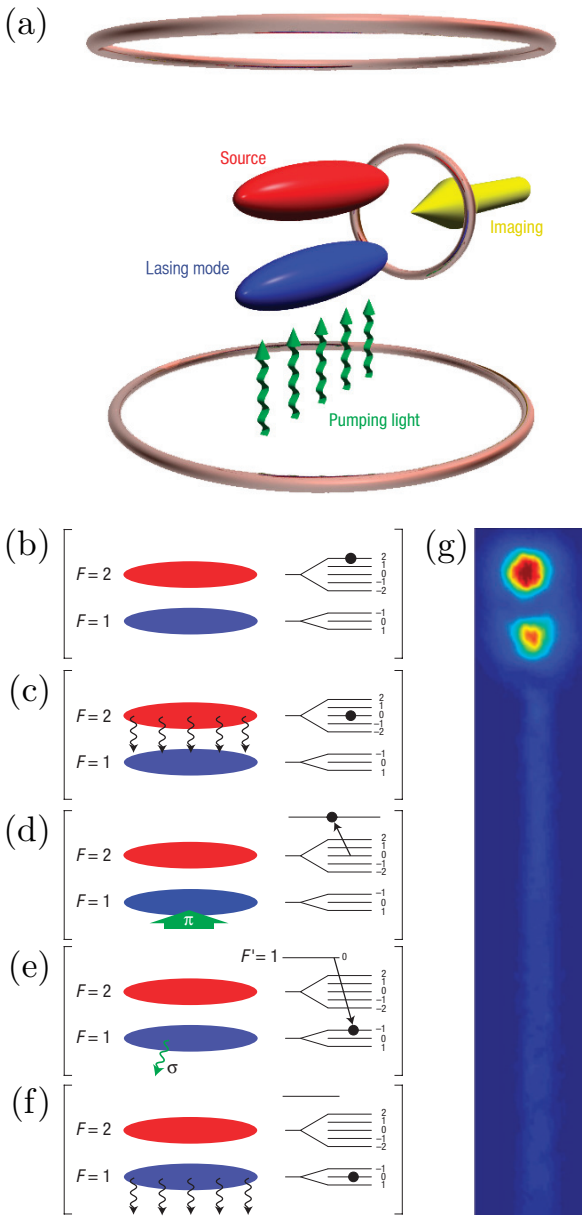

Figure 4.2: Schematic diagram of the experiment (a) and pumping steps (b–f). A radiofrequency field spin-flips the atoms to the $|2,0\rangle$ state (b), and they fall under gravity (c). The light field couples the atoms to the $F' = 1$ excited state from which they are stimulated to emit into the $|1,-1\rangle$ BEC. The atomic momentum is cancelled by the absorption and emission of the photons (d, e). A second radiofrequency field finally outcouples the atoms into the $|1,0\rangle$ atom laser (f). (g), Absorption image of the experimental system, showing source, lasing mode and output beam.

are, however, sympathetically cooled through elastic collisions with the $|1,-1\rangle$ atoms [196]. For the condensate numbers and trapping frequencies given in Table 4.1 the Thomas-Fermi radius of each cloud is approximately 5 µm in the vertical direction. The different magnetic moments of the two clouds leads to a gravitational sag between their centres of 8 µm. Hence, the two clouds of atoms overlap only slightly, with the $|2,2\rangle$ source condensate located above the $|1,-1\rangle$ lasing condensate [see Figure 4.2(a)].

To measure the effect of pumping, it is essential that the number of atoms in each state is stable from one experimental run to the next. For this purpose, many details of the apparatus were refined, including very efficient baffling against stray resonant light, very low uncertainty and drift in laser frequency, intensity and polarisation, and good vibrational and thermal stability of the trap. The stability of the number of atoms in each state was determined for a data set comprising 20 measurements, and found to be as low as 1%.

The operation of the experiment is illustrated in Figure 4.2. Starting with an initial number of atoms in each state [Figure 4.2(b)], a weak continuous radiofrequency field is applied to the upper source cloud which couples atoms from the $|2,2\rangle$ state, through $|2,1\rangle$ to the $|2,0\rangle$ state. This coupling is highly spatially selective and does not affect the $|1,-1\rangle$ cloud. The untrapped $|2,0\rangle$ atoms begin to fall away from the $|2,2\rangle$ source cloud [Figure 4.2(c)]. Simultaneously, approximately 10 pW of upward propagating π-polarised light resonant with the $|F=2\rangle \rightarrow |F'=1\rangle$ transition is applied. Although this light is resonant in energy with the $|2,2\rangle$ source atoms, they are prevented from absorbing photons by atomic selection rules. Hence, the source cloud is unaffected by the pumping light. Atoms in the $|2,0\rangle$ atom laser however will absorb the pumping light [Figure 4.2(d)]. As these atoms fall, they may make a transition into the excited $|F'=1,m_F=0\rangle$ state from which they are stimulated to emit into the lasing mode $|1,-1\rangle$ by the atoms already present in that mode [Figure 4.2(e)]. The σ^+-photon emitted in this process carries the phase difference between the pump atoms and the condensate. Finally, the $|1,-1\rangle$ lasing mode atoms are outcoupled to produce the atom laser beam in the $|1,0\rangle$ state [Figure 4.2(f)]. An absorption image of the experimental system is shown in Figure 4.2(g).

For successful pumping, the pump atoms must be momentum-resonant with the lasing condensate. This means that their atomic velocity after the emission of the photon has to lie within the velocity spread of the BEC. The magnetic trapping frequencies were chosen not only to position the two clouds as closely as possible without significant overlap,

but also such that the velocity acquired by a $|2,0\rangle$ atom in falling from the centre of the $|2,2\rangle$ cloud to the centre of the $|1,-1\rangle$ lasing mode ($12\,\mathrm{mm\,s^{-1}}$) can be cancelled by the absorption of an appropriately directed and phased σ^+-photon; a single-photon recoil corresponds to $6\,\mathrm{mm\,s^{-1}}$. The velocity at the centre of the lasing mode can be tuned by around $\pm 2\,\mathrm{mm\,s^{-1}}$ by moving the coupling surface within the source cloud up or down. While the pump atoms are falling through the $|1,-1\rangle$ lasing mode, the velocity varies by $\pm 3\,\mathrm{mm\,s^{-1}}$ owing to gravity and the time for which the pumping atoms satisfy momentum resonance with the lasing mode is much shorter ($\sim 100\,\mu\mathrm{s}$) than the traversal time across the lasing mode ($\sim 1\,\mathrm{ms}$). The velocity spread of the lasing mode is of the order of $0.3\,\mathrm{mm\,s^{-1}}$; thus, cancelling the atomic momentum of the $|2,0\rangle$ state requires an extreme level of control over pumping parameters. In the experiment, no collective motion, such as sloshing or breathing of either the source- or lasing-mode condensates was observed. This implies that if excitations driven by the pumping exist, they occur with an amplitude of less than 5% of the full-width at half-maximum of the lasing-mode condensate, which was inferred from the resolution limit of the imaging system.

To isolate and study the pumping mechanism, the experiment was first operated without outcoupling from the lasing-mode condensate. Figure 4.3 demonstrates the effect 200 ms of pumping has on the $|1,-1\rangle$ condensate; the left-hand image is taken without outcoupling from either condensate and without the pumping light. The absorption image shows the unpumped $F=1$ lasing-mode BEC (the lower cloud) with the $F=2$ source atoms above. The curves below are horizontal cross-sections through the absorption images showing the optical depth of each atom cloud. The central image shows the effect of 200 ms of pumping on the lasing-mode BEC. The source is almost completely depleted and the lasing-mode atom number has increased to $(7.2 \pm 0.4) \times 10^5$. The third column shows the difference between the pumped and unpumped images. It is important to note that the profile of the lasing-mode condensate after pumping has a significant Thomas-Fermi component with a small increase in the Gaussian thermal component. The pumping efficiency, which is defined as the growth of the lasing mode compared with the loss from the source, is $(35 \pm 10)\%$ for the results presented in Figure 4.3.

A second experiment was also performed simultaneously pumping the lasing-mode BEC and outcoupling from this condensate to demonstrate that the production of the atom laser could be operated independently of the pumping mechanism into the condensate. In this chapter we focus on the results of the first experiment in which the pumping mechanism

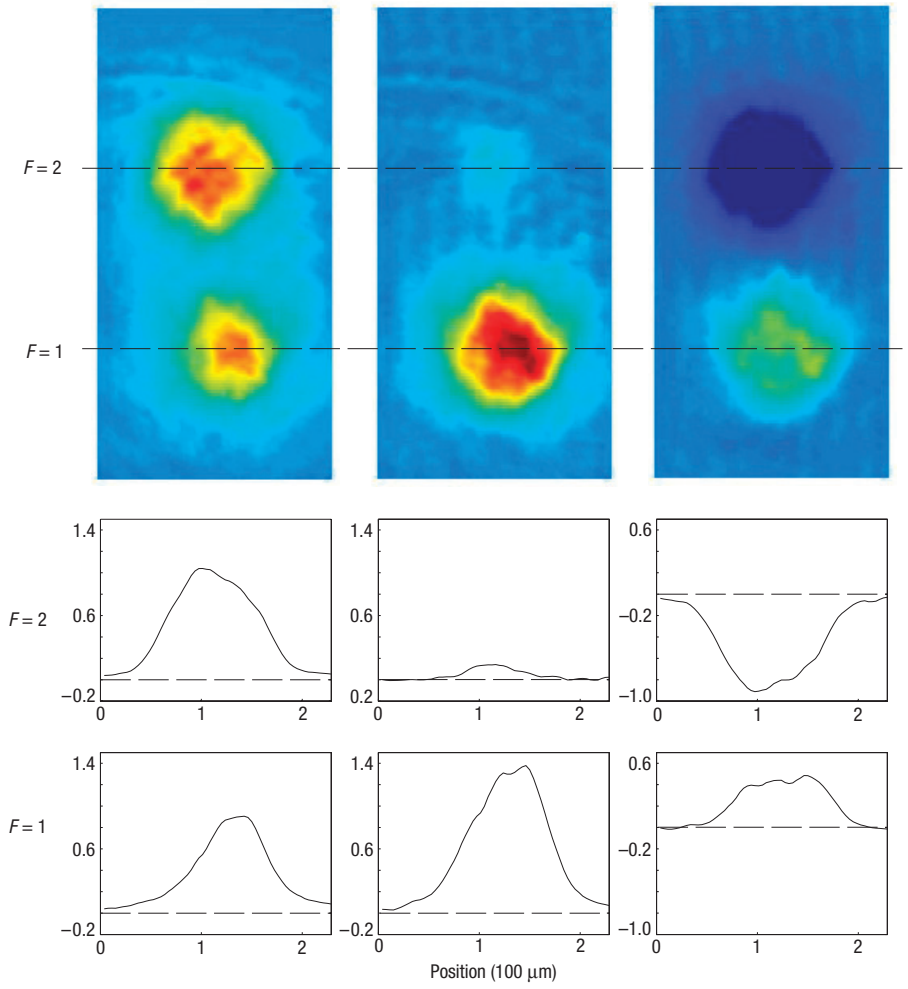

Figure 4.3: Blue-detuned absorption images averaged over three identical runs of the experiment (top row); detuning of the imaging laser from resonance is 7 MHz. The graphs below are horizontal cross-sections through the absorption images, showing optical depth, averaged over 50 µm in the vertical direction. The three columns correspond to: pumping off (left); pumping on (centre); difference between pumped and unpumped (right).

was studied.

The continuous pumping experiment just described was designed to transfer $2\hbar k$ of momentum to the falling $|2,0\rangle$ atoms (by absorbing a photon of momentum $\hbar k$ going up and then emitting a photon of similar momentum directed downwards) as they are transferred to the lasing-mode condensate. However, there is a second way for these atoms to be momentum-resonant with the lasing-mode condensate. If the outcoupling surface for the upper condensate is towards the lower edge of the condensate, the outcoupled atoms will be in close proximity to the lasing-mode condensate immediately below due to the slight spatial overlap. These recently outcoupled atoms will have almost no momentum and will be able to absorb a π-polarised photon with momentum $\hbar k$ upwards and emit a σ^+-polarised photon of similar momentum also directed upwards, decaying into the lower lasing-mode condensate with no net momentum transfer. These two processes are illustrated in Figure 4.4.

Which process is occurring has a significant impact on the potential to extend this experimental scheme to the operation of a continuously pumped atom laser. It was envisaged that this experiment could be extended to the production of a continuously pumped atom laser by replacing the source condensate, once it becomes depleted, with an independently produced condensate. If it is the $0\hbar k$ momentum-transfer process that is occurring, the source and lasing condensates must have a slight spatial overlap for the pumping mechanism to operate. The source condensate will therefore not be able to be replaced once depleted without disturbing the lasing condensate. If it is the $2\hbar k$ momentum-transfer process that is occurring, the source and lasing condensates can be spatially separated, and in principle the source condensate could be replaced without any disruption to the lasing condensate. Determining which of the two processes operated in the pumping experiment is therefore crucial to determining the viability of a continuously pumped atom laser based on this scheme.

These two different processes are examined in greater detail theoretically in Section 4.5, however we begin our theoretical analysis of the experiment and the pumping mechanism more generally with a simple single-mode model of the process illustrated in Figure 4.1(a).

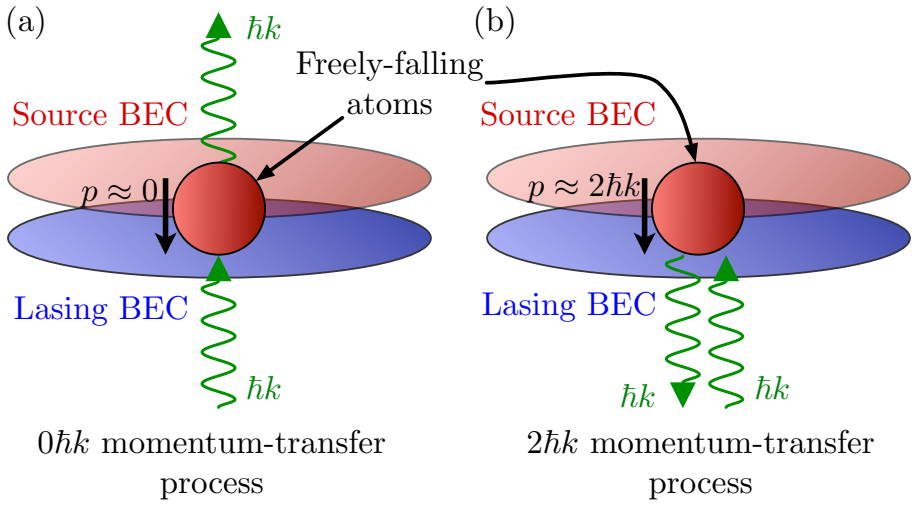

Figure 4.4: Illustration of the two potential pumping processes that could occur in the continuous pumping experiment. The freely-falling atoms form the atom laser in the $|2,0\rangle$ state and can undergo stimulated transitions into the lasing condensate in one of two processes. If the atoms are outcoupled from the lower part of the source condensate, they may immediately absorb a pumping photon from below and emit one in the same direction to decay into the lasing condensate with no net change in momentum (a). If the atoms are outcoupled from the centre of the source condensate, they may fall under gravity for approximately 1 ms gaining approximately $2\hbar k$ of momentum before absorbing a pumping photon from below and emitting one downwards to decay into the source condensate with a net momentum transfer of $2\hbar k$ (b).

4.4 Simple single-mode model

We begin our theoretical investigation of the pumping mechanism behind the previously-described experiment by considering the simplest-possible model, a single spatial-mode mean-field approximation to the process illustrated in Figure 4.1(a). The equations of motion for this model are

$$\frac{d}{dt}c_{\text{source}} = -i\Omega^* c_{\text{excited}}, \tag{4.4a}$$

$$\frac{d}{dt}c_{\text{excited}} = -i\Omega c_{\text{source}} - ig\alpha c_{\text{lasing}} - i\Delta c_{\text{excited}} - \frac{\Gamma}{2}c_{\text{excited}}, \tag{4.4b}$$

$$\frac{d}{dt}c_{\text{lasing}} = -ig^*\alpha^* c_{\text{excited}}, \tag{4.4c}$$

$$\frac{d}{dt}\alpha = -ig^* c^*_{\text{lasing}} c_{\text{excited}} - \frac{\gamma}{2}\alpha, \tag{4.4d}$$

where c_{source}, c_{lasing} and c_{excited} are the amplitudes of the source $|1\rangle$, lasing $|2\rangle$ and excited $|3\rangle$ modes respectively, Ω is the complex Rabi frequency due to the pumping laser coupling the source and excited modes with detuning Δ, α is the amplitude of the optical mode into which the excited atoms emit when decaying into the lasing mode, and g is the complex coupling constant for this transition. The optical mode α will decay as photons propagate

away from the system. This process is modelled phenomenologically with a loss rate γ from the optical mode α. The spontaneous decay of the excited state into modes other than the lasing mode occurs at a rate Γ. It has been assumed that the source mode is sufficiently dilute that the pumping laser is negligibly absorbed. This assumption is relaxed in Section 4.5. The evolution equations (4.4) are given in a rotating frame in which the energy difference between the source, excited and lasing modes have been appropriately removed.

In deriving (4.4) it has been assumed that atoms that undergo spontaneous decay from the excited mode will have no further impact upon the system. In particular, this means that the absorption of photons in the α mode by atoms in modes other than the lasing mode has been neglected. The absorption of these photons by the lasing mode is, however, retained. As discussed in Section 4.2 this is a valid approximation in the boson accumulation regime in which an excited atom is significantly more likely to decay into the lasing mode than into any other mode.

The long-term dynamics of (4.4) will determine the usefulness of the process as a pumping mechanism. The fast-timescale behaviour of this system can therefore be eliminated. By far the fastest process in the system is the decay of the photons in the α mode as they leave the system. The time taken for a photon to cross the width of a typical condensate ($\sim 10\,\mu\text{m}$) is $\sim 10^{-13}\,\text{s}$, giving $\gamma \sim 10^{13}\,\text{s}^{-1}$. By comparison, the spontaneous decay rate of the excited mode is $\Gamma \sim 10^{8}\,\text{s}^{-1}$ for the $F' = 1$ manifold of ^{87}Rb. As the α mode reaches a quasistationary value on the fastest timescale in the system (γ), it can be adiabatically eliminated and replaced with its quasistationary limit,

$$\alpha \approx -\frac{2ig^*}{\gamma} c^*_{\text{lasing}} c_{\text{excited}}. \tag{4.5}$$

We next assume that the pump laser is driving the atoms in the weak-field regime, $\Omega \ll \max(\Delta, \Gamma)$. In this limit, the excited mode c_{excited} evolves on a more rapid timescale than either the source or lasing modes. The excited mode may therefore also be adiabatically eliminated and replaced with its long-term average

$$c_{\text{excited}} \approx \frac{-i\Omega c_{\text{source}}}{\frac{1}{2}\Gamma + 2\frac{|g|^2}{\gamma} N_{\text{lasing}} + i\Delta}, \tag{4.6}$$

where $N_{\text{lasing}} = |c_{\text{lasing}}|^2$ is the number of atoms in the lasing mode.

With these two adiabatic eliminations made, the rate equations for the populations of

the remaining two modes are obtained by substituting (4.5) and (4.6) into (4.4),

$$\frac{d}{dt}N_{\text{source}} = -(\Gamma+\Gamma')N_{\text{excited}} = -\frac{|\Omega|^2(\Gamma+\Gamma')}{\frac{1}{4}(\Gamma+\Gamma')^2+\Delta^2}N_{\text{source}}, \tag{4.7a}$$

$$\frac{d}{dt}N_{\text{lasing}} = \frac{\Gamma'}{\Gamma+\Gamma'}\left(-\frac{d}{dt}N_{\text{source}}\right), \tag{4.7b}$$

where $\Gamma' = 4\dfrac{|g|^2}{\gamma}N_{\text{lasing}}$ is the rate constant with which atoms in the excited mode decay into the lasing mode.

The efficiency of the transfer of atoms in the pumping process is $\Gamma'/(\Gamma+\Gamma')$, which behaves as expected: as the occupation of the lasing mode N_{lasing} is increased, the efficiency increases due to bosonic stimulation. What is perhaps not expected is the behaviour of the transfer rate constant. In the limit of large detuning, $\Delta \gg \Gamma+\Gamma'$, the rate constant for atom transfer is

$$-\frac{d}{dt}N_{\text{source}}\Big/N_{\text{source}} \approx \frac{|\Omega|^2}{\Delta^2}\left(\Gamma+\Gamma'\right), \tag{4.8}$$

which increases as the lasing mode population increases (due to increasing Γ'). In the limit of small detuning ($\Delta \ll \Gamma+\Gamma'$) however, very different behaviour is obtained

$$-\frac{d}{dt}N_{\text{source}}\Big/N_{\text{source}} \approx 4\frac{|\Omega|^2}{\Gamma+\Gamma'}, \tag{4.9}$$

which *decreases* as the lasing mode population increases. This behaviour is due to the depletion of the excited state as Γ' increases (and therefore the occupation of the lasing mode increases). In the limit of small detuning, spontaneous and stimulated decay are the fastest processes reducing the occupation of the excited state, hence increasing either of those rates will reduce the overall population of the excited state. In this limit, as the excited state population decreases proportionally to the squared sum of these rates

$$N_{\text{excited}} \approx 4\frac{|\Omega|^2}{(\Gamma+\Gamma')^2}N_{\text{source}}, \tag{4.10}$$

the overall rate of atom transfer is suppressed [refer to (4.7a)]. In the opposite limit of large detuning, the spontaneous and stimulated decay processes are a perturbation on the Rabi-flopping process which populates the excited state. In this limit, the excited state

population is independent of the spontaneous and stimulated emission rates

$$N_{\text{excited}} \approx \frac{|\Omega|^2}{\Delta^2} N_{\text{source}}, \tag{4.11}$$

and the overall atom transfer rate into the lasing mode can be Bose-enhanced.

The simple model developed in this section can be applied to the continuous pumping experiment described in Section 4.3 to give a limit for the efficiency of the '$2\hbar k$' momentum-transfer process. In this process, falling atoms outcoupled from the upper condensate reach a momentum of $2\hbar k$ vertically downwards before absorbing a pump photon of momentum $\hbar k$ from below and emitting a photon of similar momentum directed downwards to decay into the lasing mode. If it is assumed that the intensity of the pump mode is approximately constant throughout the system, then the rate of transfer of atoms into the lasing mode cannot be faster than the rate of spontaneous emission while the source atoms are not momentum-resonant with the lasing mode[1]. An upper bound for the efficiency of the '$2\hbar k$' momentum-transfer process should therefore be given by the ratio of the time for which the source atoms are momentum-resonant with the condensate ($\sim 100\,\mu$s, see Section 4.3) to the fall time for the atoms to that point (~ 1 ms). As the upper bound for this process ($\sim 10\%$) is lower than the observed efficiency ($\sim 35\%$), either the transfer of atoms into the lasing mode must significantly reduce the intensity of the pump mode (and therefore reduce the spontaneous losses experienced as the atoms fall), or it must be the '$0\hbar k$' process that operates in the continuous pumping experiment. The argument used to obtain an upper bound for the efficiency of the '$2\hbar k$' momentum-transfer process does not apply to the '$0\hbar k$' momentum-transfer process in which atoms outcoupled from the upper condensate can be immediately pumped into the lower condensate.

The simple model considered in this section does not take into account the behaviour of the emitted photons in the α mode as they traverse the source and/or lasing modes as they leave the system. The investigation of this and other multimode effects is the subject of the next section and will be shown to lead to modifications of the behaviour described by the simple single-mode model.

[1] When the source atoms are not momentum-resonant with the lasing mode, it is equivalent to there being no atoms in the lasing mode. In this case, $\Gamma' = 0$ and from (4.9) it can be seen that the spontaneous emission rate must be greater than the transfer rate into the condensate.

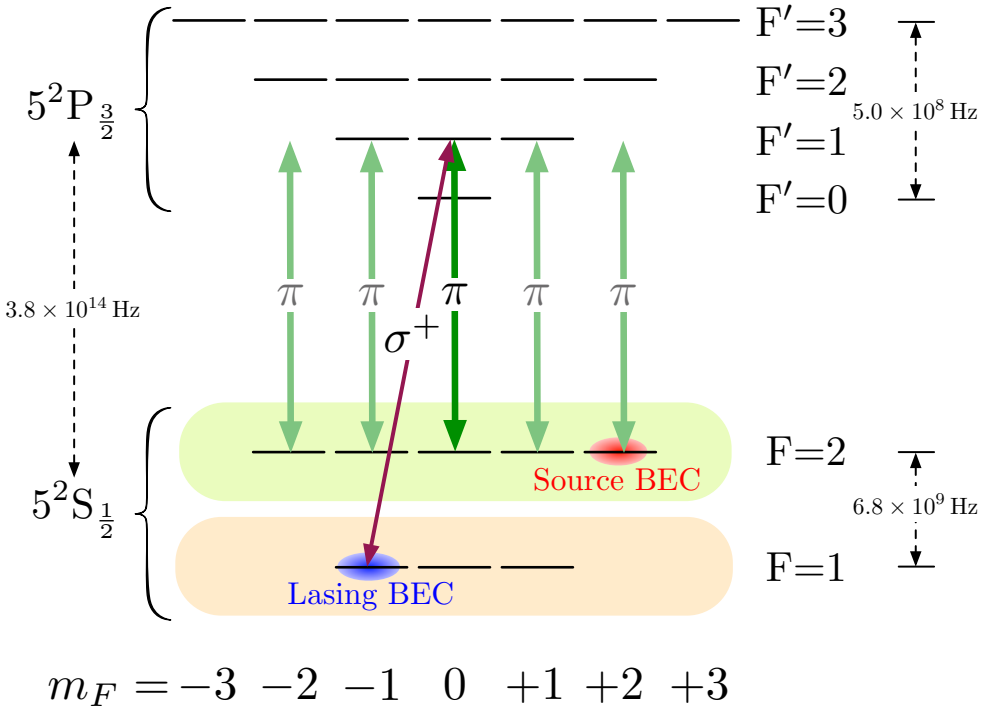

Figure 4.5: Level diagram for the continuous pumping experiment. The $F = 2 \leftrightarrow F' = 1$ transitions are resonantly driven by π-polarised optical pumping light. Although this light couples to several levels, its purpose is to drive $|F = 2, m_F = 0\rangle$ atoms into the $|F' = 1, m_F = 0\rangle$ state from which they may be stimulated to decay into the lasing BEC in the $|F = 1, m_F = -1\rangle$ state and emit σ^+-polarised light.

4.5 Multimode model

The multimode model we use in this chapter to describe the interaction of the BEC with the pumping light is similar to the Maxwell-Schrödinger equations [70, 197] used to describe superradiant Rayleigh scattering in BEC. The difference here is that the pumping light may be much closer to resonance with the source atoms, and atoms can be stimulated to decay into a different internal atomic state from which they were excited (see the level diagram of Figure 4.5).

Although our aim is to model the continuous pumping experiment described in Section 4.3, we also wish to be able to consider the limit in which the pumping light is significantly detuned (by several GHz). In either case, the only relevant optical transitions are those in the D_2 line (those pictured in Figure 4.5) as all other levels are sufficiently detuned to be negligibly populated. The transitions closest in frequency to the D_2 line are those of the D_1 line which are detuned by 7 THz, significantly greater than the maximum expected detuning from the D_2 line.

4.5.1 Model derivation

We begin with the Hamiltonian for the combined atom–light system,

$$\hat{H} = \hat{H}_{\text{atoms}} + \hat{H}_{\text{light}} + \hat{H}_{\text{atoms–light}}, \tag{4.12a}$$

$$\begin{aligned}\hat{H}_{\text{atoms}} = &\sum_i \int d\boldsymbol{x}\, \hat{\Psi}_i^\dagger(\boldsymbol{x}) \left[-\frac{\hbar^2\nabla^2}{2M} + V_i(\boldsymbol{x})\right] \hat{\Psi}_i(\boldsymbol{x}) \\ &+\frac{U}{2}\sum_{ij}\int d\boldsymbol{x}\, \hat{\Psi}_i^\dagger(\boldsymbol{x})\hat{\Psi}_j^\dagger(\boldsymbol{x})\hat{\Psi}_j(\boldsymbol{x})\hat{\Psi}_i(\boldsymbol{x}),\end{aligned} \tag{4.12b}$$

$$\hat{H}_{\text{light}} = \sum_\lambda \int d\boldsymbol{k}\, \hbar c\, |\boldsymbol{k}|\, \hat{\Phi}_\lambda^\dagger(\boldsymbol{k})\hat{\Phi}_\lambda(\boldsymbol{k}), \tag{4.12c}$$

$$\hat{H}_{\text{atoms–light}} = -\int d\boldsymbol{x}\, \hat{\boldsymbol{d}}(\boldsymbol{x}) \cdot \hat{\boldsymbol{E}}(\boldsymbol{x}), \tag{4.12d}$$

where $\hat{\Psi}_i(\boldsymbol{x})$ is the atomic field operator for the internal atomic state i, $\hat{\Phi}_\lambda(\boldsymbol{k})$ is the field operator for photons of polarisation λ, the atomic dipole operator is

$$\hat{\boldsymbol{d}}(\boldsymbol{x}) = \sum_{ij} \boldsymbol{d}_{ij}\hat{\Psi}_i^\dagger(\boldsymbol{x})\hat{\Psi}_j(\boldsymbol{x}), \tag{4.13}$$

where $\boldsymbol{d}_{ij} = -e\,\langle i|\boldsymbol{r}|j\rangle$ is the dipole matrix element for the atomic transition $i \leftrightarrow j$, and the electric field operator is given by

$$\hat{\boldsymbol{E}}(\boldsymbol{x}) = \sum_\lambda \frac{1}{(2\pi)^{3/2}} \int d\boldsymbol{k} \left(\frac{\hbar\omega_{\boldsymbol{k}}}{2\varepsilon_0}\right)^{\frac{1}{2}} \left[\breve{\boldsymbol{u}}_\lambda(\boldsymbol{k})\hat{\Phi}_\lambda(\boldsymbol{k})e^{i\boldsymbol{k}\cdot\boldsymbol{x}} + \text{h.c.}\right], \tag{4.14}$$

where $\breve{\boldsymbol{u}}_\lambda(\boldsymbol{k})$ is the electric polarisation unit vector for polarisation λ (an inverted hat is used to denote unit vectors to avoid confusion with the use of hats for operators).

The Hamiltonian (4.12) describes the full dynamics of the system including the spontaneous decay of excited atomic levels. From this complete description of the system, we wish to obtain a simplified model with which we can investigate the behaviour of the experiment described in Section 4.3, and the underlying pumping mechanism more generally.

The first simplification we will make is to assume that all atomic and optical modes are coherent states, i.e. the mean-field approximation. While this approximation is justified for the condensed atomic fields and the strongly-occupied parts of the optical field (due to the pumping laser and stimulated emission into the lasing BEC), the vacuum fluctuations responsible for spontaneous emission are necessarily neglected by any mean-field model. The effect of spontaneous emission may be partially included by adding a decay term

for the excited atomic levels, however this necessarily neglects the effect of atoms that have undergone spontaneous emission. While some of these atoms will decay into internal atomic states that are dark to both the optical pumping laser and photons emitted by stimulated emission, others will decay into the same internal atomic level as the target condensate, however with non-zero momentum. These decays can cause heating if the photon they emit is absorbed by the lasing condensate as some fraction of the atoms that reabsorb these photons will not decay back into the lasing condensate. This process is neglected by this treatment of spontaneous emission. The effect of this approximation is discussed further in Section 4.6.

The semiclassical mean-field model for this system is readily obtained from the operator evolution equations written in normal order,

$$i\hbar\frac{\partial}{\partial t}\hat{\Psi}_i(\boldsymbol{x}) = \left(-\frac{\hbar^2\nabla^2}{2M} + V_i(\boldsymbol{x}) + U\sum_j \hat{\Psi}_j^\dagger(\boldsymbol{x})\hat{\Psi}_j(\boldsymbol{x})\right)\hat{\Psi}_i(\boldsymbol{x}) - \sum_j \boldsymbol{d}_{ij}\cdot\hat{\boldsymbol{E}}(\boldsymbol{x})\hat{\Psi}_j(\boldsymbol{x}), \tag{4.15a}$$

$$i\hbar\frac{\partial}{\partial t}\hat{\Phi}_\lambda(\boldsymbol{k}) = \hbar c\,|\boldsymbol{k}|\,\hat{\Phi}_\lambda(\boldsymbol{k}) - \left(\frac{\hbar\omega_{\boldsymbol{k}}}{2\varepsilon_0}\right)^{\frac{1}{2}}\check{\boldsymbol{u}}_\lambda^*(\boldsymbol{k})\cdot\left(\frac{1}{(2\pi)^{3/2}}\int d\boldsymbol{x}\,\hat{\boldsymbol{d}}(\boldsymbol{x})e^{-i\boldsymbol{k}\cdot\boldsymbol{x}}\right), \tag{4.15b}$$

by replacing all operators with their expectation values. This yields equations identical in form to (4.15) without the operator hats.

Our next approximation is to neglect the fast-rotating parts of the atom–light coupling terms in (4.15), i.e. the rotating wave approximation (RWA). We achieve this by first separating the purely real electric field into positive and negative frequency terms

$$\boldsymbol{E}(\boldsymbol{x}) = \boldsymbol{E}_+(\boldsymbol{x}) + \boldsymbol{E}_-(\boldsymbol{x}), \tag{4.16}$$

$$\boldsymbol{E}_+(\boldsymbol{x}) = \sum_\lambda \frac{1}{(2\pi)^{3/2}}\int d\boldsymbol{k}\,\check{\boldsymbol{u}}_\lambda(\boldsymbol{k})\left(\frac{\hbar\omega_{\boldsymbol{k}}}{2\varepsilon_0}\right)^{\frac{1}{2}}\Phi_\lambda(\boldsymbol{k})e^{i\boldsymbol{k}\cdot\boldsymbol{x}}, \tag{4.17}$$

$$\boldsymbol{E}_-(\boldsymbol{x}) = \boldsymbol{E}_+^*(\boldsymbol{x}) = \sum_\lambda \frac{1}{(2\pi)^{3/2}}\int d\boldsymbol{k}\,\check{\boldsymbol{u}}_\lambda^*(\boldsymbol{k})\left(\frac{\hbar\omega_{\boldsymbol{k}}}{2\varepsilon_0}\right)^{\frac{1}{2}}\Phi_\lambda^*(\boldsymbol{k})e^{-i\boldsymbol{k}\cdot\boldsymbol{x}}, \tag{4.18}$$

where $\boldsymbol{E}_+(\boldsymbol{x})$ contains the positive frequency terms rotating as $e^{-i\omega_{\boldsymbol{k}}t}$, and $\boldsymbol{E}_-(\boldsymbol{x})$ contains the negative frequency terms $e^{i\omega_{\boldsymbol{k}}t}$. In order to clarify the application of the RWA, we must separate the atomic fields Ψ_i into ground [denoted with an unprimed index, $\Psi_i(\boldsymbol{x})$] and excited [denoted with a primed index, $\Psi_{i'}(\boldsymbol{x})$] states. The RWA is equivalent to retaining only the terms of the atom–light coupling Hamiltonian (4.12d) that rotate at frequencies

significantly lower than the optical frequency (of the order of the optical detuning Δ or less). The terms that satisfy this condition are those of the form $\hat{\boldsymbol{E}}_+^\dagger(\boldsymbol{x})\hat{\Psi}_i^\dagger(\boldsymbol{x})\hat{\Psi}_{j'}(\boldsymbol{x})$ and their Hermitian-conjugates.

Making the rotating wave approximation, the equations of motion for the mean-field become

$$\begin{aligned} i\hbar\frac{\partial}{\partial t}\Psi_i(\boldsymbol{x}) = &\left(-\frac{\hbar^2\nabla^2}{2M} + V_i(\boldsymbol{x}) + U\sum_j |\Psi_j(\boldsymbol{x})|^2\right)\Psi_i(\boldsymbol{x}) \\ &- \sum_{j'} \boldsymbol{d}_{ij'}\cdot\boldsymbol{E}_+^*(\boldsymbol{x})\Psi_{j'}(\boldsymbol{x}), \end{aligned} \tag{4.19a}$$

$$\begin{aligned} i\hbar\frac{\partial}{\partial t}\Psi_{i'}(\boldsymbol{x}) = &\left(-\frac{\hbar^2\nabla^2}{2M} + V_{i'}(\boldsymbol{x}) + U\sum_j |\Psi_j(\boldsymbol{x})|^2 - \frac{i\hbar\Gamma}{2}\right)\Psi_{i'}(\boldsymbol{x}) \\ &- \sum_{j} \boldsymbol{d}_{i'j}\cdot\boldsymbol{E}_+(\boldsymbol{x})\Psi_{j}(\boldsymbol{x}), \end{aligned} \tag{4.19b}$$

$$\begin{aligned} i\hbar\frac{\partial}{\partial t}\Phi_\lambda(\boldsymbol{k}) = &\hbar c\,|\boldsymbol{k}|\,\Phi_\lambda(\boldsymbol{k}) \\ &- \left(\frac{\hbar\omega_{\boldsymbol{k}}}{2\varepsilon_0}\right)^{\frac{1}{2}} \check{\boldsymbol{u}}_\lambda^*(\boldsymbol{k})\cdot\left(\frac{1}{(2\pi)^{3/2}}\int d\boldsymbol{x}\,\sum_{ij'}\boldsymbol{d}_{ij'}\Psi_i^*(\boldsymbol{x})\Psi_{j'}(\boldsymbol{x})e^{-i\boldsymbol{k}\cdot\boldsymbol{x}}\right), \end{aligned} \tag{4.19c}$$

where the damping of the excited atoms due to spontaneous emission at a rate Γ has been included, and the density of the excited atoms has been neglected in the s-wave interaction terms.

Our next approximation is to recognise that most of the photon modes will be empty; the photon field will only be nonzero near a finite set of wavenumbers $\boldsymbol{q}_n$ (for corresponding polarisations λ_n). In the case of the experiment described in Section 4.3, only those modes excited by the optical pumping laser or emitted as atoms undergo stimulated transitions into the target condensate will be occupied (see Figure 4.5). There will also be some small range of wavenumbers occupied around each of these due to spatial variations in the strength of these fields. If we assume that the spatial envelope of each of these occupied modes varies on a length scale much larger than the wavelength (the slowly-varying envelope approximation), then only modes within $\delta k \ll |\boldsymbol{q}_n|$ will be significantly occupied.

If all the occupied photon modes $\boldsymbol{q}_n$ are separated by more than δk, the photon and

electric field may be decomposed as

$$\Phi_\lambda(\boldsymbol{k}) = \sum_n \delta_{\lambda,\lambda_n} \Phi_{\lambda_n,\boldsymbol{q}_n}(\boldsymbol{k}), \tag{4.20}$$

$$\boldsymbol{E}_+(\boldsymbol{x}) = \sum_n \boldsymbol{E}_{+,\boldsymbol{q}_n}(\boldsymbol{x}), \tag{4.21}$$

where δ_{ij} is the Kronecker delta.

As each of the photon fields $\Phi_{\lambda_n,\boldsymbol{q}_n}(\boldsymbol{k})$ will only be occupied within a small range of wavenumbers δk, the photon energy and polarisation vectors can be assumed to differ negligibly from their values at $\boldsymbol{k} = \boldsymbol{q}_n$. This permits the corresponding electric field components to be written as

$$\begin{aligned}
\boldsymbol{E}_{+,\boldsymbol{q}_n}(\boldsymbol{x}) &= \frac{1}{(2\pi)^{3/2}} \int d\boldsymbol{k}\, \check{\boldsymbol{u}}_{\lambda_n}(\boldsymbol{k}) \left(\frac{\hbar\omega_{\boldsymbol{k}}}{2\varepsilon_0}\right)^{\frac{1}{2}} \Phi_{\lambda_n,\boldsymbol{q}_n}(\boldsymbol{k}) e^{i\boldsymbol{k}\cdot\boldsymbol{x}} \\
&\approx \check{\boldsymbol{u}}_{\lambda_n}(\boldsymbol{q}_n) \left(\frac{\hbar\omega_{\boldsymbol{q}_n}}{2\varepsilon_0}\right)^{\frac{1}{2}} \frac{1}{(2\pi)^{3/2}} \int d\boldsymbol{k}\, \Phi_{\lambda_n,\boldsymbol{q}_n}(\boldsymbol{k}) e^{i\boldsymbol{k}\cdot\boldsymbol{x}} \\
&= \check{\boldsymbol{u}}_{\lambda_n}(\boldsymbol{q}_n) \left(\frac{\hbar\omega_{\boldsymbol{q}_n}}{2\varepsilon_0}\right)^{\frac{1}{2}} \Phi_{\lambda_n,\boldsymbol{q}_n}(\boldsymbol{x}) \\
&= \check{\boldsymbol{u}}_{\lambda_n}(\boldsymbol{q}_n) E_{+,\boldsymbol{q}_n}(\boldsymbol{x}),
\end{aligned} \tag{4.22}$$

where $\Phi_{\lambda_n,\boldsymbol{q}_n}(\boldsymbol{x})$ is the inverse Fourier-transform of $\Phi_{\lambda_n,\boldsymbol{q}_n}(\boldsymbol{k})$, and $E_{+,\boldsymbol{q}_n}(\boldsymbol{x})$ is defined by

$$E_{+,\boldsymbol{q}_n}(\boldsymbol{x}) = \left(\frac{\hbar\omega_{\boldsymbol{q}_n}}{2\varepsilon_0}\right)^{\frac{1}{2}} \Phi_{\lambda_n,\boldsymbol{q}_n}(\boldsymbol{x}). \tag{4.23}$$

To obtain separate evolution equations for each of the $\Phi_{\lambda_n,\boldsymbol{q}_n}(\boldsymbol{k})$, the contribution of the atomic coupling terms of (4.19c) to the evolution of $\Phi_\lambda(\boldsymbol{k})$ must be split amongst the evolution equations for the $\Phi_{\lambda_n,\boldsymbol{q}_n}(\boldsymbol{k})$. If each atomic transition is only energy-resonant with a single optical mode $\boldsymbol{q}_n$ (e.g. the π-polarised transition between $|F = 2, m_F = 0\rangle \leftrightarrow |F' = 1, m_F = 0\rangle$ illustrated in Figure 4.5), the splitting is obvious. It is however possible that two or more optical modes may be energy resonant with a single atomic transition (the wavenumbers of all resonant modes will have the same magnitude); this case is more complicated. In this derivation, we wish to consider the possibility that an atomic transition might be resonant with two optical modes propagating in opposite directions[2]. In this

[2]As discussed at the end of Section 4.3, it is unclear in the continuous pumping experiment whether the σ^+ photons emitted as the atoms are stimulated to emit into the lasing condensate are emitted vertically upwards or downwards. If both possibilities are allowed, then both the upward- and downward-propagating modes would be energy-resonant with a single atomic transition. Another case in which two counter-propagating optical modes may be resonant with a single atomic transition is in the Bragg reflection of

case, the contribution of the atomic coupling terms may be separated into two halves: the contribution at wavenumbers $\boldsymbol{k}$ such that $\boldsymbol{q}_n \cdot \boldsymbol{k} > 0$ only affecting $\Phi_{\lambda_n,+\boldsymbol{q}_n}(\boldsymbol{k})$, and the contribution for which $\boldsymbol{q}_n \cdot \boldsymbol{k} < 0$ only affecting $\Phi_{\lambda_n,-\boldsymbol{q}_n}(\boldsymbol{k})$. This separation can be achieved by including the full contribution of the relevant atomic coupling terms in the evolution equations for each of the photon fields $\Phi_{\lambda_n,\boldsymbol{q}_n}(\boldsymbol{k})$, but defining these fields to be zero when $\boldsymbol{q}_n \cdot \boldsymbol{k} < 0$. This is not an additional approximation as it has already been assumed that the photon fields $\Phi_{\lambda_n,\boldsymbol{q}_n}(\boldsymbol{k})$ are only nonzero within a small range $|\boldsymbol{k} - \boldsymbol{q}_n| \ll \delta k$.

We denote the atomic transitions $i \leftrightarrow j'$ coupled to the optical mode $\boldsymbol{q}_n$ by the set T_n. The equations of motion in terms of the separate electric field components are

$$\begin{aligned} i\hbar\frac{\partial}{\partial t}\Psi_i(\boldsymbol{x}) = &\left(-\frac{\hbar^2\nabla^2}{2M} + V_i(\boldsymbol{x}) + U\sum_j |\Psi_j(\boldsymbol{x})|^2\right)\Psi_i(\boldsymbol{x}) \\ &- \sum_{j',n} \boldsymbol{d}_{ij'} \cdot \check{\boldsymbol{u}}^*_{\lambda_n}(\boldsymbol{q}_n) E^*_{+,\boldsymbol{q}_n}(\boldsymbol{x})\Psi_{j'}(\boldsymbol{x}), \end{aligned} \tag{4.24a}$$

$$\begin{aligned} i\hbar\frac{\partial}{\partial t}\Psi_{i'}(\boldsymbol{x}) = &\left(-\frac{\hbar^2\nabla^2}{2M} + V_{i'}(\boldsymbol{x}) + U\sum_j |\Psi_j(\boldsymbol{x})|^2 - \frac{i\hbar\Gamma}{2}\right)\Psi_{i'}(\boldsymbol{x}) \\ &- \sum_{j,n} \boldsymbol{d}_{i'j} \cdot \check{\boldsymbol{u}}_{\lambda_n}(\boldsymbol{q}_n) E_{+,\boldsymbol{q}_n}(\boldsymbol{x})\Psi_j(\boldsymbol{x}), \end{aligned} \tag{4.24b}$$

$$\begin{aligned} i\hbar\frac{\partial}{\partial t}\Phi_{\lambda_n,\boldsymbol{q}_n}(\boldsymbol{k}) = &\hbar c\,|\boldsymbol{k}|\,\Phi_{\lambda_n,\boldsymbol{q}_n}(\boldsymbol{k}) \\ &- \left(\frac{\hbar\omega_{\boldsymbol{q}_n}}{2\varepsilon_0}\right)^{\frac{1}{2}} \check{\boldsymbol{u}}^*_{\lambda_n}(\boldsymbol{q}_n) \cdot \left(\frac{1}{(2\pi)^{3/2}}\int d\boldsymbol{x} \sum_{\{i,j'\}\in T_n} \boldsymbol{d}_{ij'}\Psi^*_i(\boldsymbol{x})\Psi_{j'}(\boldsymbol{x})e^{-i\boldsymbol{k}\cdot\boldsymbol{x}}\right), \end{aligned} \tag{4.24c}$$

where we have made the same approximations made previously that the electric polarisation vectors and the photon energies vary negligibly for each photon field.

It may seem that we have made an unnecessary complication by separating the single equation of motion for the total photon field (4.19c) into the set of equations (4.24c) for each significantly occupied mode $\Phi_{\lambda_n,\boldsymbol{q}_n}(\boldsymbol{k})$. This temporary complication will however enable the equations of motion to be simplified into a form that will be computationally tractable to solve. In their present form, the evolution equations (4.24) have the problem that the fastest timescale in the problem is that of the propagation of the optical field over the length of the condensate. For a condensate with a Thomas-Fermi radius of $\sim 20\,\mu\text{m}$, this timescale is $\sim 10^{-13}\,\text{s}$, which is much shorter than the timescale over which the pumping

light by a matter-wave grating.

was observed to occur in the experiment ($\sim 10^{-1}$ s)! Any numerical method used to solve the system (4.24) must resolve dynamics on the shorter timescale to be accurate, but evolve for long enough to see the transfer of atoms occurring on a much slower timescale. Our aim in the next part of the derivation is to eliminate all fast timescales in the problem to obtain a set of numerically-tractable equations to model the system.

As the equations of motion for the the atomic fields are written in the position basis, it would be convenient to write the equation of motion for the photon fields in the same basis. To simplify this process it is first necessary to approximate the wavenumber magnitude $|\boldsymbol{k}|$ appearing in (4.24c),

$$\begin{aligned}|\boldsymbol{k}| &= |\boldsymbol{q}_n + \delta\boldsymbol{k}| \\ &\approx \sqrt{|\boldsymbol{q}_n|^2 + 2\boldsymbol{q}_n \cdot \delta\boldsymbol{k}} = |\boldsymbol{q}_n| \sqrt{1 + \frac{2\boldsymbol{q}_n \cdot \delta\boldsymbol{k}}{|\boldsymbol{q}_n|^2}} \\ &\approx |\boldsymbol{q}_n| + \check{\boldsymbol{q}}_n \cdot \delta\boldsymbol{k} = |\boldsymbol{q}_n| + \check{\boldsymbol{q}}_n \cdot (\boldsymbol{k} - \boldsymbol{q}_n) \\ &= \check{\boldsymbol{q}}_n \cdot \boldsymbol{k}. \end{aligned} \tag{4.25}$$

With this approximation, the inverse Fourier transform of (4.24c) gives

$$i\hbar \frac{\partial}{\partial t} \Phi_{\lambda_n, \boldsymbol{q}_n}(\boldsymbol{x}) = -i\hbar c \check{\boldsymbol{q}}_n \cdot \nabla \Phi_{\lambda_n, \boldsymbol{q}_n}(\boldsymbol{x}) - \left(\frac{\hbar \omega_{\boldsymbol{q}_n}}{2\varepsilon_0} \right)^{\frac{1}{2}} \check{\boldsymbol{u}}^*_{\lambda_n}(\boldsymbol{q}_n) \cdot \sum_{\{i,j'\} \in T_n} \boldsymbol{d}_{ij'} \Psi^*_i(\boldsymbol{x}) \Psi_{j'}(\boldsymbol{x}). \tag{4.26}$$

In directly taking the inverse Fourier transform of (4.24c), we have neglected to take account of the fact that only the wavenumbers $\boldsymbol{k}$ for which $\boldsymbol{k} \cdot \boldsymbol{q}_n > 0$ may contribute in (4.26). Instead, the contribution at all wavenumbers has been included. These additional contributions will be $2\boldsymbol{q}_n$ out of momentum-resonance, and will average to zero over half a wavelength.

Using (4.23), the photon field may be eliminated in favour of the electric field giving the equation of motion for the electric field:

$$\frac{1}{c} \frac{\partial}{\partial t} E_{+, \boldsymbol{q}_n}(\boldsymbol{x}) = -\check{\boldsymbol{q}}_n \cdot \nabla E_{+, \boldsymbol{q}_n}(\boldsymbol{x}) + i \frac{|\boldsymbol{q}_n|}{2\varepsilon_0} \check{\boldsymbol{u}}^*_{\lambda_n}(\boldsymbol{q}_n) \cdot \sum_{\{i,j'\} \in T_n} \boldsymbol{d}_{ij'} \Psi^*_i(\boldsymbol{x}) \Psi_{j'}(\boldsymbol{x}). \tag{4.27}$$

This equation has the form of a transport process in the $\check{\boldsymbol{q}}_n$ direction (at speed c) with a source term. The propagation of the electric field across the system occurs on a sufficiently short timescale that by comparison to the typical timescales for atomic dynamics, the

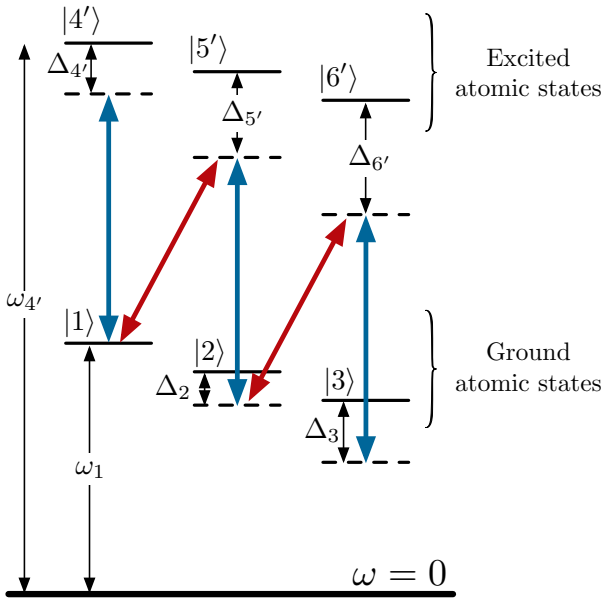

Figure 4.6: Schematic level diagram illustrating the definitions of the detunings in (4.28). The sign of all detunings illustrated are positive.

propagation is effectively instantaneous. By separating the fast phase rotation of the electric and atomic fields from the slowly-varying envelopes, it becomes possible to neglect the finite propagation time of the electric field in (4.27) to obtain a set of algebraic equations for the electric field at a given time. The next step in this process is to remove the fast phase rotation of these fields.

To remove the fast phase rotation of the electric and atomic envelopes, we define (temporally) slowly-varying fields marked with tildes as

$$\Psi_i = \widetilde{\Psi}_i e^{-i(\omega_i - \Delta_i)t}, \tag{4.28a}$$

$$\Psi_{i'} = \widetilde{\Psi}_{i'} e^{-i(\omega_{i'} - \Delta_{i'})t}, \tag{4.28b}$$

$$E_{+,\boldsymbol{q}_n} = \widetilde{E}_{+,\boldsymbol{q}_n} e^{-i\omega_{\boldsymbol{q}_n} t}, \tag{4.28c}$$

where ω_i (and $\omega_{i'}$) are the frequencies of the atomic levels (including mean-field shifts), Δ_i (and $\Delta_{i'}$) are the detunings of those levels. The definitions of these detunings are illustrated in Figure 4.6.

The equations of motion for the slowly-varying fields are

$$i\hbar\frac{\partial}{\partial t}\widetilde{\Psi}_i(\boldsymbol{x}) = \left(-\frac{\hbar^2\nabla^2}{2M} + V_i(\boldsymbol{x}) + U\sum_j\left|\widetilde{\Psi}_j(\boldsymbol{x})\right|^2 - \hbar\omega_i + \hbar\Delta_i\right)\widetilde{\Psi}_i(\boldsymbol{x}) - \sum_{j',n}\boldsymbol{d}_{ij'}\cdot\check{\boldsymbol{u}}^*_{\lambda_n}(\boldsymbol{q}_n)\widetilde{E}^*_{+,\boldsymbol{q}_n}(\boldsymbol{x})\widetilde{\Psi}_{j'}(\boldsymbol{x})e^{-i\left[\omega_{j'}-\Delta_{j'}-(\omega_i-\Delta_i)-\omega_{\boldsymbol{q}_n}\right]t}, \tag{4.29a}$$

$$i\hbar\frac{\partial}{\partial t}\widetilde{\Psi}_{i'}(\boldsymbol{x}) = \left(-\frac{\hbar^2\nabla^2}{2M} + V_{i'}(\boldsymbol{x}) + U\sum_j\left|\widetilde{\Psi}_j(\boldsymbol{x})\right|^2 - \frac{i\hbar\Gamma}{2} - \hbar\omega_{i'} + \hbar\Delta_{i'}\right)\widetilde{\Psi}_{i'}(\boldsymbol{x}) - \sum_{j,n}\boldsymbol{d}_{i'j}\cdot\check{\boldsymbol{u}}_{\lambda_n}(\boldsymbol{q}_n)\widetilde{E}_{+,\boldsymbol{q}_n}(\boldsymbol{x})\widetilde{\Psi}_j(\boldsymbol{x})e^{-i[\omega_j-\Delta_j-(\omega_{i'}-\Delta_{i'})+\omega_{\boldsymbol{q}_n}]t}, \tag{4.29b}$$

$$\frac{1}{c}\frac{\partial}{\partial t}\widetilde{E}_{+,\boldsymbol{q}_n}(\boldsymbol{x}) = -\check{\boldsymbol{q}}_n\cdot\nabla\widetilde{E}_{+,\boldsymbol{q}_n}(\boldsymbol{x}) + i\left|\boldsymbol{q}_n\right|\widetilde{E}_{+,\boldsymbol{q}_n}(\boldsymbol{x}) + i\frac{|\boldsymbol{q}_n|}{2\varepsilon_0}\check{\boldsymbol{u}}^*_{\lambda_n}(\boldsymbol{q}_n)\cdot\sum_{\{i,j'\}\in T_n}\boldsymbol{d}_{ij'}\widetilde{\Psi}^*_i(\boldsymbol{x})\widetilde{\Psi}_{j'}(\boldsymbol{x})e^{-i\left[\omega_{j'}-\Delta_{j'}-(\omega_i-\Delta_i)-\omega_{\boldsymbol{q}_n}\right]t}. \tag{4.29c}$$

If the level detunings are chosen such that all optical fields couple resonantly between the 'detuned levels' (dotted lines in Figure 4.6), the arguments of the exponential terms in (4.29) will all be zero and the terms themselves will be equal to 1. Stated mathematically this requirement is

$$\left(\omega_{j'}-\Delta_{j'}\right)-\left(\omega_i-\Delta_i\right) = \omega_{\boldsymbol{q}_n}\ \forall\ i,j',n : \left\{i,j'\right\}\in T_n. \tag{4.30}$$

An example of the alternative possibility that one or more of the optical fields are not consistent with this criteria would be if an additional optical field were applied in the system pictured in Figure 4.6 which was resonant with the $|2\rangle \leftrightarrow |4'\rangle$ transition. Unless $\Delta_{4'} = \Delta_2$, this additional optical field would not be resonant with a transition between the 'detuned levels' of $|2\rangle$ and $|4'\rangle$. The requirement (4.30) is satisfied by the optical pumping scheme (see Figure 4.5) as the pumping laser defines the detunings of the F' states relative to the $F = 2$ states, and the σ^+ light generated on the $|F = 1, m_F = -1\rangle \leftrightarrow |F' = 1, m_F = 0\rangle$ transition is formed spontaneously, and will therefore be resonant with the transition from the (possibly detuned) $|F' = 1, m_F = 0\rangle$ state such that the overall two-photon process $|F = 2, m_F = 0\rangle \leftrightarrow |F = 1, m_F = -1\rangle$ is resonant.

With the evolution equations for the slowly-varying envelopes obtained, we may now work to eliminate effects on the timescale of the propagation of the electric fields. To

achieve this, we choose an arbitrary electric field $\widetilde{E}_{+,\boldsymbol{q}_n}$ and transform our coordinate system according to

$$\boldsymbol{x}' = \boldsymbol{x}, \tag{4.31}$$

$$t' = t - \frac{1}{c}\check{\boldsymbol{q}}_n \cdot \boldsymbol{x}. \tag{4.32}$$

In the primed coordinates, the propagation equation for $\widetilde{E}_{+,\boldsymbol{q}_n}$ is

$$\begin{aligned}\check{\boldsymbol{q}}_n \cdot \nabla_{\boldsymbol{x}'} \widetilde{E}_{+,\boldsymbol{q}_n}(\boldsymbol{x}', t') = i\,|\boldsymbol{q}_n|\,\widetilde{E}_{+,\boldsymbol{q}_n}(\boldsymbol{x}', t') \\ + i\frac{|\boldsymbol{q}_n|}{2\varepsilon_0}\check{\boldsymbol{u}}^*_{\lambda_n}(\boldsymbol{q}_n) \cdot \sum_{\{i,j'\}\in T_n} \boldsymbol{d}_{ij'} \widetilde{\Psi}^*_i\left(\boldsymbol{x}', t(\boldsymbol{x}', t')\right) \widetilde{\Psi}_{j'}\left(\boldsymbol{x}', t(\boldsymbol{x}', t')\right),\end{aligned} \tag{4.33}$$

where $\widetilde{E}_{+,\boldsymbol{q}_n}$ is written as a function of $(\boldsymbol{x}', t')$, while the atomic fields are written as functions of $(\boldsymbol{x}, t)$. Although the primed and unprimed time coordinates are not exactly equal, if the spatial origin is chosen to be in the centre of the condensate then $t(\boldsymbol{x}', t') \approx t'$ is a very good approximation. We can estimate the size of the terms neglected by this approximation by considering the variation in the atomic fields over the time $t' - t$,

$$\begin{aligned}\widetilde{\Psi}^*_i\left(\boldsymbol{x}', t(\boldsymbol{x}', t')\right) &= \widetilde{\Psi}^*_i\left(\boldsymbol{x}', t' + \frac{1}{c}\check{\boldsymbol{q}}_n \cdot \boldsymbol{x}\right), \\ &\approx \widetilde{\Psi}^*_i(\boldsymbol{x}', t')\left(1 + i\frac{\delta\omega}{c}\check{\boldsymbol{q}}_n \cdot \boldsymbol{x}\right),\end{aligned} \tag{4.34}$$

where the atomic field $\widetilde{\Psi}_i$ is assumed to evolve in time as $e^{-i\,\delta\omega\,t}$ for sufficiently small times, and $\delta\omega$ is of the order of the characteristic frequency of the atomic dynamics. The frequency of atomic excitations is approximately described by the Bogoliubov dispersion relation (3.13). Collective excitations of the system will have energies of at most the chemical potential (refer to the discussion at the end of Section 3.3). For a condensate of maximum spatial extent $\sim 100\,\mu\text{m}$, and chemical potential of order $\mu/\hbar \sim 10^5\,\text{rad}\,\text{s}^{-1}$, the correction term in (4.34) is of the order

$$\left|\delta\widetilde{\Psi}/\widetilde{\Psi}\right| \leq \frac{100\,\mu\text{m} \times 10^5\,\text{rad}\,\text{s}^{-1}}{3 \times 10^8\,\text{m}\,\text{s}^{-1}} \approx 10^{-7}. \tag{4.35}$$

Although neglecting this correction term is a zeroth-order approximation, the term being neglected is sufficiently small to make this approximation as good as (or better than) many of the first-order approximations that are made elsewhere in this derivation. A similar

approximation needs to be made in the evolution equations for the atomic fields (written in the unprimed coordinate system), $\widetilde{E}_{+,\boldsymbol{q}_n}(\boldsymbol{x},t) \approx \widetilde{E}_{+,\boldsymbol{q}_n}(\boldsymbol{x},t')$ with a similarly-sized correction.

The overall effect of this change of coordinate system has been to neglect the temporal derivative in the evolution equation for the electric field mode $\widetilde{E}_{+,\boldsymbol{q}_n}$. To the same degree of approximation, the temporal derivatives of all other electric field modes may also therefore be neglected. These approximations made, the equations of motion become

$$\begin{aligned} i\hbar\frac{\partial}{\partial t}\widetilde{\Psi}_i(\boldsymbol{x}) = &\left(-\frac{\hbar^2\nabla^2}{2M} + V_i(\boldsymbol{x}) + U\sum_j \left|\widetilde{\Psi}_j(\boldsymbol{x})\right|^2 - \hbar\omega_i + \hbar\Delta_i\right)\widetilde{\Psi}_i(\boldsymbol{x}) \\ &- \sum_{j',n} \boldsymbol{d}_{ij'}\cdot\check{\boldsymbol{u}}^*_{\lambda_n}(\boldsymbol{q}_n)\widetilde{E}^*_{+,\boldsymbol{q}_n}(\boldsymbol{x})\widetilde{\Psi}_{j'}(\boldsymbol{x}), \end{aligned} \tag{4.36a}$$

$$\begin{aligned} i\hbar\frac{\partial}{\partial t}\widetilde{\Psi}_{i'}(\boldsymbol{x}) = &\left(-\frac{\hbar^2\nabla^2}{2M} + V_{i'}(\boldsymbol{x}) + U\sum_j \left|\widetilde{\Psi}_j(\boldsymbol{x})\right|^2 - \frac{i\hbar\Gamma}{2} - \hbar\omega_{i'} + \hbar\Delta_{i'}\right)\widetilde{\Psi}_{i'}(\boldsymbol{x}) \\ &- \sum_{j,n} \boldsymbol{d}_{i'j}\cdot\check{\boldsymbol{u}}_{\lambda_n}(\boldsymbol{q}_n)\widetilde{E}_{+,\boldsymbol{q}_n}(\boldsymbol{x})\widetilde{\Psi}_j(\boldsymbol{x}), \end{aligned} \tag{4.36b}$$

$$\check{\boldsymbol{q}}_n\cdot\nabla\widetilde{E}_{+,\boldsymbol{q}_n}(\boldsymbol{x}) = i\left|\boldsymbol{q}_n\right|\widetilde{E}_{+,\boldsymbol{q}_n}(\boldsymbol{x}) + i\frac{|\boldsymbol{q}_n|}{2\varepsilon_0}\check{\boldsymbol{u}}^*_{\lambda_n}(\boldsymbol{q}_n)\cdot\sum_{\{i,j'\}\in T_n}\boldsymbol{d}_{ij'}\widetilde{\Psi}^*_i(\boldsymbol{x})\,\widetilde{\Psi}_{j'}(\boldsymbol{x}), \tag{4.36c}$$

where boundary values for the $\widetilde{E}_{+,\boldsymbol{q}_n}$ over a plane perpendicular to $\check{\boldsymbol{q}}_n$ must be specified to complete the system of equations. With the temporal derivatives of the evolution equations for the electric fields neglected, these equations need to be solved self-consistently at every time point. When all electric fields are propagating in the same direction, the evolution of the electric fields is an initial-value problem propagating in the $\check{\boldsymbol{q}}_n$ direction. This is not the case in the optical pumping scheme in which optical modes may propagate both upwards and downwards. However as the electric fields evolve slowly in time, the self-consistent solutions may be found iteratively starting from the solution found for the previous time point.

After eliminating the light propagation timescale from the problem, the next fastest timescale is that of the excited atomic states $\widetilde{\Psi}_{i'}$. The evolution of these states is dominated either by spontaneous decay at a rate $\Gamma = 2\pi\times 5.9\,\mathrm{MHz}$ or by the detuning term (if the pumping laser is detuned by several linewidths). As these frequencies are much higher than the slower atomic evolution we are interested in ($\sim 10\,\mathrm{kHz}$), the excited states may be adiabatically eliminated.

To adiabatically eliminate the excited atomic states, we first recognise that the $\hbar\omega_{i'}$ term in (4.36b) will approximately balance the kinetic, potential and mean-field terms. With this cancellation made, the adiabatic elimination of the excited atomic states can be made by setting the temporal derivative to zero, yielding

$$\widetilde{\Psi}_{i'}(\boldsymbol{x}) \approx \sum_{j,n} \frac{\boldsymbol{d}_{i'j} \cdot \check{\boldsymbol{u}}_{\lambda_n}(\boldsymbol{q}_n) \widetilde{E}_{+,\boldsymbol{q}_n}(\boldsymbol{x}) \widetilde{\Psi}_j(\boldsymbol{x})}{\hbar\Delta_{i'} - \frac{i\hbar}{2}\Gamma}. \tag{4.37}$$

Substituting this expression back into the remaining evolution equations gives

$$\begin{aligned} i\hbar\frac{\partial}{\partial t}\widetilde{\Psi}_i(\boldsymbol{x}) = &\left(-\frac{\hbar^2\nabla^2}{2M} + V_i(\boldsymbol{x}) + U\sum_j \left|\widetilde{\Psi}_j(\boldsymbol{x})\right|^2 - \hbar\omega_i + \hbar\Delta_i\right)\widetilde{\Psi}_i(\boldsymbol{x}) \\ &- \sum_{\substack{j',n \\ l,m}} \frac{\left[\boldsymbol{d}_{ij'} \cdot \check{\boldsymbol{u}}^*_{\lambda_n}(\boldsymbol{q}_n)\right]\left[\boldsymbol{d}_{j'l} \cdot \check{\boldsymbol{u}}_{\lambda_m}(\boldsymbol{q}_m)\right]}{\hbar\Delta_{j'} - \frac{i\hbar}{2}\Gamma} \widetilde{E}^*_{+,\boldsymbol{q}_n}(\boldsymbol{x}) \widetilde{E}_{+,\boldsymbol{q}_m}(\boldsymbol{x}) \widetilde{\Psi}_l(\boldsymbol{x}), \end{aligned} \tag{4.38a}$$

$$\begin{aligned} \check{\boldsymbol{q}}_n \cdot \nabla\widetilde{E}_{+,\boldsymbol{q}_n}(\boldsymbol{x}) = &\, i\left|\boldsymbol{q}_n\right| \widetilde{E}_{+,\boldsymbol{q}_n}(\boldsymbol{x}) \\ &+ i\frac{|\boldsymbol{q}_n|}{2\varepsilon_0} \sum_{\substack{\{i,j'\}\in T_n \\ l,m}} \frac{\left[\boldsymbol{d}_{ij'} \cdot \check{\boldsymbol{u}}^*_{\lambda_n}(\boldsymbol{q}_n)\right]\left[\boldsymbol{d}_{j'l} \cdot \check{\boldsymbol{u}}_{\lambda_m}(\boldsymbol{q}_m)\right]}{\hbar\Delta_{j'} - \frac{i\hbar}{2}\Gamma} \widetilde{\Psi}^*_i(\boldsymbol{x}) \widetilde{\Psi}_l(\boldsymbol{x}) \widetilde{E}_{+,\boldsymbol{q}_m}(\boldsymbol{x}). \end{aligned} \tag{4.38b}$$

This set of equations for the ground state atomic modes and the optical modes they interact with represents the basic multimode model that will be used in the remainder of this chapter.

Several approximations were made in deriving the model in this section. A summary of the most significant approximations is given below.

- Scattering of spontaneously emitted photons has been neglected. While this process can be neglected if the pumping laser is sufficiently detuned from resonance, this is potentially a significant issue closer to resonance. As discussed in Section 4.2, reabsorption can be negligible when operating in the boson accumulation regime in which excited atoms are significantly more likely to decay into the condensate mode than into all other modes. It is this regime in which the continuous pumping experiment is operated.

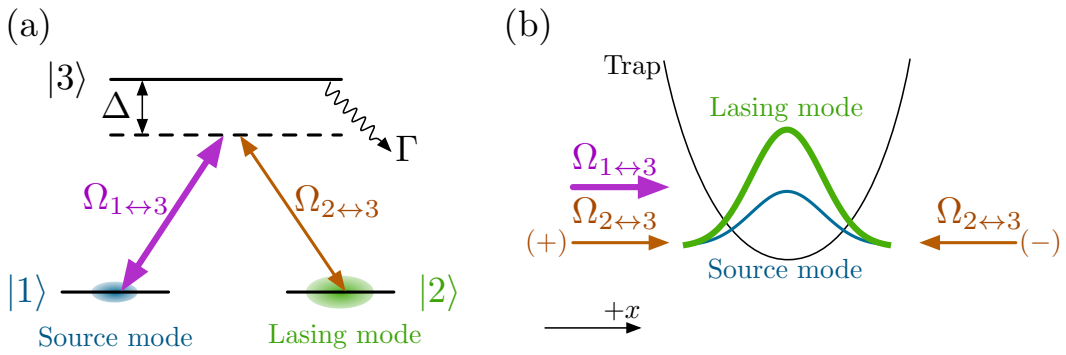

Figure 4.7: Schematic of the two overlapping condensates model. The system consists of two condensates in the two ground states of a Λ level scheme (a). The system is illuminated on the $|1\rangle \leftrightarrow |3\rangle$ transition by light at a detuning Δ and Rabi frequency $\Omega_{1\leftrightarrow 3}$. Light on the $|2\rangle \leftrightarrow |3\rangle$ transition is generated as atoms in the $|3\rangle$ state are stimulated to emit into the lasing mode $|2\rangle$. Depending on the relative momenta of the atoms in the source and lasing modes, the light on the $|2\rangle \leftrightarrow |3\rangle$ transition will travel to the left or right. The '+' sign in (4.39d) corresponds to the optical field $\Omega_{2\leftrightarrow 3}$ propagating to the right [marked with (+)], while the '−' sign corresponds to propagation to the left [marked with (−)].

- Atoms that have undergone spontaneous emission are neglected. These thermal atoms will contribute to collisional heating of the condensate. Provided that they are small in number compared to the condensate, this heating can be neglected. For a continuously pumped atom laser, this requires that more atoms are transferred to the condensate than are lost due to spontaneous emission.

- Various time- and length-scales have been neglected. The results of the model are only valid for timescales greater than the spontaneous lifetime of the system $\sim 27\,\mathrm{ns}$, and for lengthscales larger than the optical wavelength $\lambda = 780\,\mathrm{nm}$.

In the following sections the multimode pumping model derived here will be applied to some idealised systems to further investigate the pumping mechanism before considering the pumping experiment itself.

4.5.2 Two overlapping condensates model

The first idealised (multimode) pumping model to be considered is a simplified model of the transfer process occurring at the centre of the lasing condensate in the continuous pumping experiment. In this model, illustrated in Figure 4.7, the source and lasing modes are the two ground states ($|1\rangle$ and $|2\rangle$ respectively) of atoms with a Λ-level scheme. Light on the $|1\rangle \leftrightarrow |3\rangle$ transition is applied with detuning Δ from the left with an initial Rabi frequency of $\Omega_{1\leftrightarrow 3}(-\infty)$. Light on the $|2\rangle \leftrightarrow |3\rangle$ transition is not supplied externally but

may be produced as a result of atoms in the excited state $|3\rangle$ being stimulated to emit into the lasing mode $|2\rangle$. To investigate possible differences in behaviour if the two optical modes are co-propagating or counter-propagating, we will consider both the case in which the source mode is initially stationary (with the $\Omega_{2\leftrightarrow 3}$ mode propagating to the right) and moving to the left with momentum $2\hbar k$ (with the $\Omega_{2\leftrightarrow 3}$ mode propagating to the left). In both cases, the initial condition is chosen such that the lasing and source modes are in the overall ground state of the system given their respective initial occupations $N_{\text{lasing}}(t=0)$ and $N_{\text{source}}(t=0)$ (i.e. in the absence of any optical coupling the system would remain static). The source mode is assumed to be given its momentum kick to the left (if appropriate) immediately before the optical field $\Omega_{1\leftrightarrow 3}$ is turned on at $t=0$. As the $\Omega_{2\leftrightarrow 3}$ light is generated by (atomic) stimulated emission, its phase will be determined by the phase difference between the source and lasing modes. We may assume there to be a specific phase relationship between the two modes without loss of generality; our results will also apply if the two condensates were independently produced and had a random relative phase.

For the 1D scheme presented in Figure 4.7, we may simplify the multimode equations (4.38) to

$$\begin{aligned} i\hbar\frac{\partial}{\partial t}\Psi_1(x) = &\left[-\frac{\hbar^2}{2M}\frac{d^2}{dx^2} + V_{\text{trap}}(x) + U_{1\text{D}}\left(|\Psi_1|^2 + |\Psi_2|^2\right)\right]\Psi_1 \\ &-\hbar\frac{|\Omega_{1\leftrightarrow 3}|^2\,\Psi_1 + \Omega^*_{1\leftrightarrow 3}\Omega_{2\leftrightarrow 3}\Psi_2}{\Delta - \frac{i}{2}\Gamma}, \end{aligned} \tag{4.39a}$$

$$\begin{aligned} i\hbar\frac{\partial}{\partial t}\Psi_2(x) = &\left[-\frac{\hbar^2}{2M}\frac{d^2}{dx^2} + V_{\text{trap}}(x) + U_{1\text{D}}\left(|\Psi_1|^2 + |\Psi_2|^2\right)\right]\Psi_2 \\ &-\hbar\frac{|\Omega_{2\leftrightarrow 3}|^2\,\Psi_2 + \Omega^*_{2\leftrightarrow 3}\Omega_{1\leftrightarrow 3}\Psi_1}{\Delta - \frac{i}{2}\Gamma}, \end{aligned} \tag{4.39b}$$

$$\frac{d}{dx}\Omega_{1\leftrightarrow 3} = ik\Omega_{1\leftrightarrow 3} + \frac{i}{4}f_{13}\Gamma\frac{\sigma_0}{A_\perp}\frac{|\Psi_1|^2\,\Omega_{1\leftrightarrow 3} + \Psi_1^*\Psi_2\Omega_{2\leftrightarrow 3}}{\Delta - \frac{i}{2}\Gamma}, \tag{4.39c}$$

$$\pm\frac{d}{dx}\Omega_{2\leftrightarrow 3} = ik\Omega_{2\leftrightarrow 3} + \frac{i}{4}f_{23}\Gamma\frac{\sigma_0}{A_\perp}\frac{|\Psi_2|^2\,\Omega_{2\leftrightarrow 3} + \Psi_2^*\Psi_1\Omega_{1\leftrightarrow 3}}{\Delta - \frac{i}{2}\Gamma}, \tag{4.39d}$$

where the electric fields of (4.38) have been replaced with Rabi frequencies[3] using $\hbar\Omega_i = \boldsymbol{d}_{i3}\cdot\breve{\boldsymbol{u}}_{\lambda_i}\widetilde{E}_{+,\boldsymbol{q}_i}$; the remaining dipole matrix elements have been eliminated in favour of the spontaneous emission rate using $\Gamma = \dfrac{\omega^3 d_{\text{total}}^2}{3\pi\epsilon_0\hbar c^3}$, where the total dipole matrix element is $|d_{\text{total}}|^2 = \sum_i |\boldsymbol{d}_{i3}|^2$ with $|\boldsymbol{d}_{i3}|^2 = f_{i3}\,|d_{\text{total}}|^2$, where f_{i3} is the fraction of atoms in the $|3\rangle$

[3]Electric fields must be used in the general case in which a single optical field may couple multiple transitions with different dipole matrix elements. In the present model each optical field drives only a single transition, enabling the electric fields to be replaced with Rabi frequencies.

state that decay to the $|i\rangle$ state; $\sigma_0 = \dfrac{3\lambda^2}{2\pi}$ is the atomic scattering cross-section; and a very simple dimension reduction scheme has been used: $\Psi_i^{(3\mathrm{D})} = \Psi_i^{(1\mathrm{D})}/\sqrt{A_\perp}$, $U_{1\mathrm{D}} = U_{3\mathrm{D}}/A_\perp$, where $A_\perp$ is a representative area of the condensate perpendicular to the x direction. The positive sign in (4.39d) applies if the source mode is initially stationary, causing the $\Omega_{2\leftrightarrow 3}$ mode to propagate to the right, and the negative sign applies if the source mode is initially moving to the left with momentum $2\hbar k$, causing the $\Omega_{2\leftrightarrow 3}$ mode to propagate to the left. The 1D dimension reduction performed in (4.39) is valid provided that transverse modes are not significantly excited.

Before simulating the system numerically, some analytical insight can be obtained by considering the behaviour of the optical fields as they propagate through the condensates. Although propagating in space instead of in time, the equations of motion for the optical fields resemble those for a coupled Λ level scheme with the *atomic* fields governing the strength of the coupling of each transition, a role normally filled by optical fields. Rewriting the evolution equations for the two optical fields elucidates this analogy,

$$i\hbar c\frac{d}{dx}\phi_{1\leftrightarrow 3} = -\hbar\omega\phi_{1\leftrightarrow 3} - \hbar\frac{|\Omega_1|^2\,\phi_{1\leftrightarrow 3} + \Omega_1^*\Omega_2\phi_{2\leftrightarrow 3}}{\Delta - \frac{i}{2}\Gamma}, \tag{4.40a}$$

$$\pm i\hbar c\frac{d}{dx}\phi_{2\leftrightarrow 3} = -\hbar\omega\phi_{2\leftrightarrow 3} - \hbar\frac{|\Omega_2|^2\,\phi_2 + \Omega_2^*\Omega_1\phi_{1\leftrightarrow 3}}{\Delta - \frac{i}{2}\Gamma}, \tag{4.40b}$$

where $\Omega_i = \sqrt{\dfrac{c\Gamma\sigma_0}{8A_\perp}}\Psi_i$, $\phi_{i\leftrightarrow j}$ has been used to replace the optical Rabi frequencies $\Omega_{i\leftrightarrow j}$ to limit the possibility for confusion, and it has been assumed that the two optical transitions are of equal strength, hence $f_{13} = f_{23} = \frac{1}{2}$. The coupling terms between the two fields $\phi_{1\leftrightarrow 3}$ and $\phi_{2\leftrightarrow 3}$ are now clearly in the same form as the atomic coupling terms between Ψ_1 and Ψ_2 in (4.39a)–(4.39b). This similarity is not surprising as the ground state atomic fields and the optical fields may be interchanged in the atom–light coupling Hamiltonian (after making the rotating-wave approximation) without changing its form:

$$\hat{H}_{\text{atom–light}} \propto \hat{\Psi}_e^\dagger\hat{\Psi}_g\hat{\phi} + \hat{\phi}^\dagger\hat{\Psi}_g^\dagger\hat{\Psi}_e, \tag{4.41}$$

where $\hat{\Psi}_e$, $\hat{\Psi}_g$ are the excited and ground atomic fields respectively and $\hat{\phi}$ is the photon field.

This analogy for the photon propagation is illustrated in Figure 4.8. In this model, the two fields $\phi_{1\leftrightarrow 3}$ and $\phi_{2\leftrightarrow 3}$ are coupled by two Rabi frequencies Ω_1 and Ω_2 that vary (in space) as the two fields $\phi_{i\leftrightarrow j}$ evolve (in space). For the counter-propagating case, the

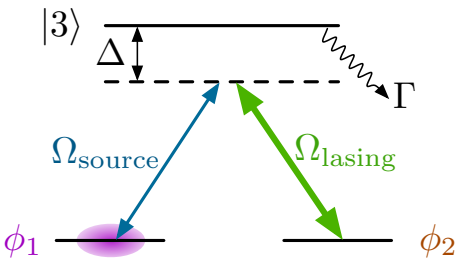

Figure 4.8: The propagation of the photons through the system is analogous to Rabi flopping between two states in a Λ-level scheme. The flopping between the two modes is driven by 'Rabi frequencies' due to the atomic populations of the source and lasing modes.

analogy is imperfect, as one mode propagates forward while the other backward, preventing a direct analogy with propagation in time. For the co-propagating case however, the analogy is perfect and the optical propagation equations can be solved exactly for small times while the source and lasing modes have the same shape. The solution for $\Omega_{2\leftrightarrow 3}$ is

$$\Omega_{2\leftrightarrow 3}(x) = \Omega_{1\leftrightarrow 3}(-\infty)\frac{\Psi_1\Psi_2^*}{|\Psi_1|^2+|\Psi_2|^2}\left[\exp\left(i\frac{\Gamma\sigma_0}{8A_\perp\left(\Delta-\frac{i}{2}\Gamma\right)}\int_{-\infty}^{x} dx\ |\Psi_1|^2+|\Psi_2|^2\right)-1\right]. \tag{4.42}$$

As every photon that leaves the system in the $\Omega_{2\leftrightarrow 3}$ optical mode corresponds to an atom being transferred into the lasing mode, the net rate of atom transfer will be governed by

$$|\Omega_{2\leftrightarrow 3}(+\infty)|^2 = |\Omega_{1\leftrightarrow 3}(-\infty)|^2\,\frac{N_1}{N}\frac{N_2}{N}\,|\alpha-1|^2\,, \tag{4.43}$$

where

$$\alpha = \exp\left(i\frac{N\Gamma\sigma_0}{8A_\perp\left(\Delta-\frac{i}{2}\Gamma\right)}\right), \tag{4.44}$$

N_i is the number of atoms in the $|i\rangle$ state, and $N = N_1 + N_2$ is the number of atoms in the system.

The rate of atom transfer into the lasing mode is then

$$\frac{dN_2}{dt} = |\Omega_{2\leftrightarrow 3}(+\infty)|^2\,\frac{8A_\perp}{\Gamma\sigma_0} \tag{4.45}$$

$$= |\Omega_{1\leftrightarrow 3}(-\infty)|^2\,\frac{8A_\perp}{\Gamma\sigma_0}\frac{N_1}{N}\frac{N_2}{N}\,|\alpha-1|^2\,. \tag{4.46}$$

The rate of atom transfer out of the source mode can be found in a similar way. From

these two rates the efficiency of the pumping process may be obtained,

$$\eta = \frac{dN_2}{dt} \Big/ \left(-\frac{dN_1}{dt}\right) = \frac{N_2 \left|\alpha - 1\right|^2}{2N\left(1 - \mathrm{Re}\{\alpha\}\right) - N_1 \left|\alpha - 1\right|^2}. \tag{4.47}$$

Zero detuning limit ($\Delta = 0$)

The continuous pumping experiment described in Section 4.3 was operated with the pumping light resonant with the $|F = 2, m_F = 0\rangle \leftrightarrow |F' = 1, m_F = 0\rangle$ transition, the transition that is represented by the $|1\rangle \leftrightarrow |3\rangle$ transition in the present model. It is therefore interesting to consider the zero detuning limit ($\Delta = 0$) as it would apply to the experiment. Furthermore, the lasing mode (the $|F = 1, m_F = -1\rangle$ condensate in the experiment) contains significantly more atoms than the source mode (the atom laser state $|F = 2, m_F = 0\rangle$), permitting the approximation $N_1 \ll N_2$.

In these limits, the parameter α becomes

$$\alpha = \exp\left(-\frac{N\sigma_0}{4A_\perp}\right) \approx \exp(-121) \approx 0, \tag{4.48}$$

where a numerical value for α has been obtained using the experimentally-relevant values $\lambda = 780\,\mathrm{nm}$, $N = 5 \times 10^5$, $A_\perp = 3 \times 10^{-10}\,\mathrm{m}^2$. Using $\alpha \approx 0$ the transfer rate and efficiency take the simple forms:

$$\frac{dN_2}{dt} \approx \left|\Omega_{1\leftrightarrow 3}(-\infty)\right|^2 \frac{8A_\perp}{\Gamma\sigma_0}\frac{N_1}{N_2}, \tag{4.49}$$

$$\eta \approx \frac{N_2}{N + N_2} \approx \frac{1}{2}. \tag{4.50}$$

As observed in the single-mode model of Section 4.4 [see (4.9)], the transfer rate *decreases* as the occupation of the lasing mode increases.

An interesting difference with the single-mode model however is that the transfer efficiency in this model (for short times) cannot exceed 50%, while the efficiency of the single-mode model approaches 100% for sufficiently large N_2. This difference can be understood by recognising that the Λ level scheme of Figure 4.8 has a dark eigenstate that does not undergo spontaneous emission due to the quantum-mechanical cancellation of

absorption amplitudes. The dark eigenstate is

$$|D\rangle = \frac{1}{\sqrt{|\Psi_1|^2 + |\Psi_2|^2}} \left(\Psi_2 |1 \leftrightarrow 3\rangle - \Psi_1 |2 \leftrightarrow 3\rangle\right), \tag{4.51}$$

$$= \sqrt{\frac{N_2}{N}} |1 \leftrightarrow 3\rangle - \sqrt{\frac{N_1}{N}} |2 \leftrightarrow 3\rangle \tag{4.52}$$

where $|i \leftrightarrow j\rangle$ is the state for the optical mode resonant with the $|i\rangle \leftrightarrow |j\rangle$ transition. When the optical modes are in this dark eigenstate, the numerators of the atom–light coupling terms of (4.39) are zero. The second form of the dark state (4.52) only applies for short times while the two atomic modes have the same spatial profile (and assuming they have the same phase). It is only the component that is in the dark state that will propagate through the system; all other components will be absorbed rapidly. Although the projection of the initial (optical) state $|\Psi_{\text{initial}}\rangle = |1 \leftrightarrow 3\rangle$ onto the dark state

$$|\langle D|\Psi_{\text{initial}}\rangle|^2 = \frac{N_2}{N} \tag{4.53}$$

may approach 1 arbitrarily, the efficiency only approaches $\frac{1}{2}$,

$$\eta = \frac{|\langle 2 \leftrightarrow 3|D\rangle\langle D|\Psi_{\text{initial}}\rangle|^2}{1 - |\langle 1 \leftrightarrow 3|D\rangle\langle D|\Psi_{\text{initial}}\rangle|^2} = \frac{\frac{N_1}{N}\frac{N_2}{N}}{1 - \left(\frac{N_2}{N}\right)^2}$$

$$= \frac{N_2}{N + N_2} \approx \frac{1}{2}, \tag{4.54}$$

in agreement with (4.50).

The definition of the dark state (4.51) suggests a method of improving this efficiency. If the profiles of the source and lasing modes are not the same but instead the $\Omega_{1\leftrightarrow 3}$ pumping beam first encounters atoms in the lasing mode before atoms in the source mode, the initial projection onto the dark state will be perfect. If the variation of the source and lasing mode densities occurs over length scales significantly larger than the absorption length scale for the non-dark states ($d = \dfrac{4A_\perp}{\sigma_0 |\Psi_2|^2} \sim 60\,\text{nm}$), then the dark state will be followed adiabatically with minimal losses. This situation will arise naturally at later times as the source atoms closest to the pumping beam are transferred to the lasing mode. As this occurs, the pumping beam will encounter a greater proportion of atoms in the lasing mode than at earlier times, thus increasing the efficiency. This behaviour is observed numerically in simulations of the system (4.39) as illustrated in Figure 4.9.

While the efficiency of the population transfer is related to the leading edge of the

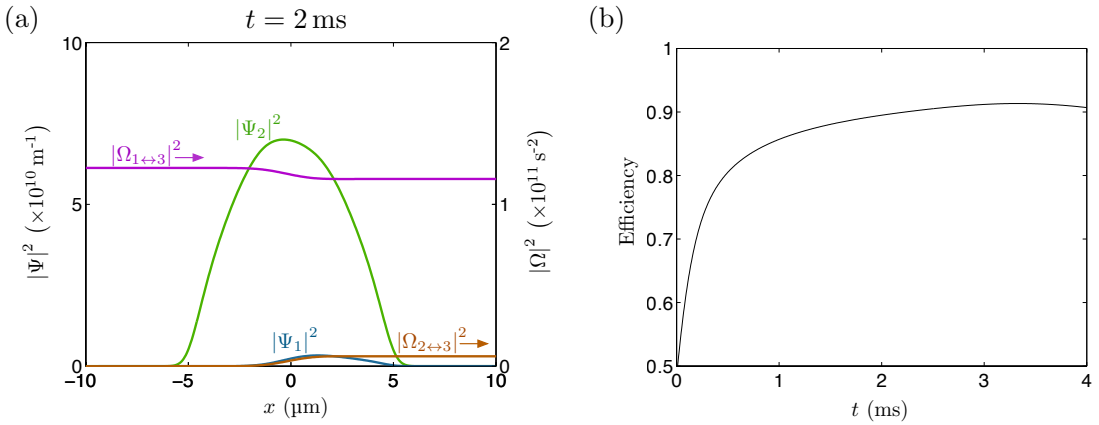

Figure 4.9: Simulation results of the two overlapping condensates model (4.39) driven resonantly. Figure (a) is a snapshot of the densities and magnitudes of the Rabi frequencies at $t = 2\,\mathrm{ms}$. The instantaneous efficiency is shown in (b). There are a total of $N = 5 \times 10^5$ atoms in the system, of which initially 5% are in the source mode ($|1\rangle$), and the system is driven resonantly with $\Omega_{1\leftrightarrow 3}(-\infty) = 3.5 \times 10^5\,\mathrm{s}^{-1}$.

density profiles, the rate of transfer can be related to the trailing edge. The fraction of the photons leaving the system in the $\Omega_{2\leftrightarrow 3}$ mode is determined by the dark state at the trailing edge

$$|\Omega_{2\leftrightarrow 3}(+\infty)|^2 = |\Omega_{1\leftrightarrow 3}(-\infty)|^2 \, |\langle 2 \leftrightarrow 3 | D_{\mathrm{trailing}} \rangle \langle D_{\mathrm{leading}} | \Psi_{\mathrm{initial}} \rangle|^2 \,, \tag{4.55}$$

$$= |\Omega_{1\leftrightarrow 3}(-\infty)|^2 \, \frac{N_1}{N} \frac{N_2}{N}, \tag{4.56}$$

where the second equality only applies for short times while the two atomic modes have the same spatial profile, and is in agreement with (4.43) as $\alpha \approx 0$. The rate of population transfer can therefore be increased by having the dark state at the trailing edge to be almost purely the $|2 \leftrightarrow 3\rangle$ state. This would be achieved by having the density in the lasing mode decay before the density in the source mode. In this limit, every photon in the pumping beam would transfer one atom into the lasing mode. This possibility is related to the idea of adiabatic population transfer [198], and is investigated further in Section 4.5.3.

This system still suffers from the same problem discussed at the end of Section 4.4, i.e. that the transfer rate for atoms momentum-resonant with the lasing condensate is lower than the spontaneous emission rate for atoms that are not momentum-resonant with the lasing condensate. If there is a non-zero time for which the source atoms are not resonant with the lasing condensate (for example, if they must fall from an upper condensate to a lower condensate), this population loss will significantly reduce the overall efficiency of the transfer process. One possible solution to this problem would be if the pumping process

were operated such that every photon in the $\Omega_{1\leftrightarrow 3}$ mode left the system in the $\Omega_{2\leftrightarrow 3}$ mode, which the source atoms do not absorb. This possibility is discussed further in Section 4.5.3.

Far detuned limit ($\Delta \gg \Gamma$)

Although the continuous pumping experiment described in Section 4.3 was operated with resonant pumping light, the opposite limit is interesting due to the suppression of spontaneous emission. In this limit, the α parameter becomes

$$\alpha = \exp\left(-\frac{N\sigma_0}{16A_\perp}\frac{\Gamma^2}{\Delta^2+\frac{1}{4}\Gamma^2}\right)\exp\left(i\frac{N\sigma_0}{8A_\perp}\frac{\Gamma\Delta}{\Delta^2+\frac{1}{4}\Gamma^2}\right) \tag{4.57}$$

$$\approx \exp\left(-\frac{N\sigma_0}{16A_\perp}\frac{\Gamma^2}{\Delta^2}\right)\exp\left(i\frac{N\sigma_0}{8A_\perp}\frac{\Gamma}{\Delta}\right) \tag{4.58}$$

$$\approx \exp\left(-30\frac{\Gamma^2}{\Delta^2}\right)\exp\left(61i\frac{\Gamma}{\Delta}\right), \tag{4.59}$$

where the same values have been used as in the resonant case. Efficiencies close to unity require the magnitude of α to be close to 1. While this can be achieved relatively easily (a detuning of a few 10's of linewidths is enough for the experimental parameters), the rate of population transfer depends strongly on the phase of α [see (4.46)]. If the detuning is not sufficiently large to make the phase of α small, the photons will Rabi flop between the $|1\leftrightarrow 3\rangle$ and $|2\leftrightarrow 3\rangle$ modes, reducing the rate of transfer into the lasing mode. In this limit, the transfer rate into the lasing mode averaged over all phases for α is

$$\overline{\frac{dN_2}{dt}} = |\Omega_{1\leftrightarrow 3}(-\infty)|^2\,\frac{16A_\perp}{\Gamma\sigma_0}\frac{N_1}{N}\frac{N_2}{N} \approx |\Omega_{1\leftrightarrow 3}(-\infty)|^2\,\frac{16A_\perp}{\Gamma\sigma_0}\frac{N_1}{N_2}, \tag{4.60}$$

which is twice that in the zero detuning limit (4.49), and hence decreases as the occupation of the lasing mode increases. The factor of two difference comes from the difference in efficiency: in this case the efficiency is approximately 100%, while it is 50% in the zero detuning limit.

The situation is much improved if the pumping light is sufficiently detuned that the phase of α is small. In the limit

$$\frac{N\sigma_0}{8A_\perp}\frac{\Gamma}{\Delta} \ll 1, \tag{4.61}$$

the transfer rate is

$$\frac{dN_2}{dt} \approx \frac{|\Omega_{1\leftrightarrow 3}(-\infty)|^2}{\Delta}\frac{\sigma_0}{8A_\perp}\frac{\Gamma}{\Delta}N_1N_2, \tag{4.62}$$

with an efficiency

$$\eta \approx \left(1+\frac{8A_\perp}{N\sigma_0}\right)^{-1}. \tag{4.63}$$

The transfer rate for very high detunings displays Bose-enhancement as it increases for increasing occupation of the lasing mode. This is a desirable property for a pumping mechanism (for either a photon-laser or an atom-laser), as it means that the highest-occupied mode will undergo more gain than lesser-occupied modes.

As the transfer rate at high detunings is Bose-enhanced, it can be larger than the spontaneous emission rate for atoms that are not momentum-resonant with the condensate. As a result, the system does not suffer from the problem discussed at the end of Section 4.4. In this case, the time taken to transfer the atoms to the lasing mode does not need to limit the overall efficiency of the pumping process. The spontaneous emission rate of source atoms in the absence of the condensate,

$$\left.\frac{dN_1}{dt}\right|_{\text{no condensate}} \approx -\frac{|\Omega_{1\leftrightarrow 3}(-\infty)|^2}{\Delta^2}\Gamma N_1, \tag{4.64}$$

is significantly lower than the pumping rate in the presence of the lasing mode (4.62),

$$\left.\frac{dN_2}{dt}\right|_{\text{pumping}} \Big/ -\left.\frac{dN_1}{dt}\right|_{\text{no condensate}} \approx \frac{N\sigma_0}{8A_\perp}, \tag{4.65}$$

where this ratio is ~ 60 for the parameters of the continuous pumping experiment.

Counter-propagating optical modes

The behaviour of this system in the case that $\Omega_{1\leftrightarrow 3}$ and $\Omega_{2\leftrightarrow 3}$ are counter-propagating is not qualitatively different from that described previously for the co-propagating case. This is because the pumping beam $\Omega_{1\leftrightarrow 3}$ cannot be significantly reduced by propagating through the system when the source mode is significantly less occupied than the lasing mode ($N_1 \ll N_2$). After propagating through the system (in the co-propagating case),

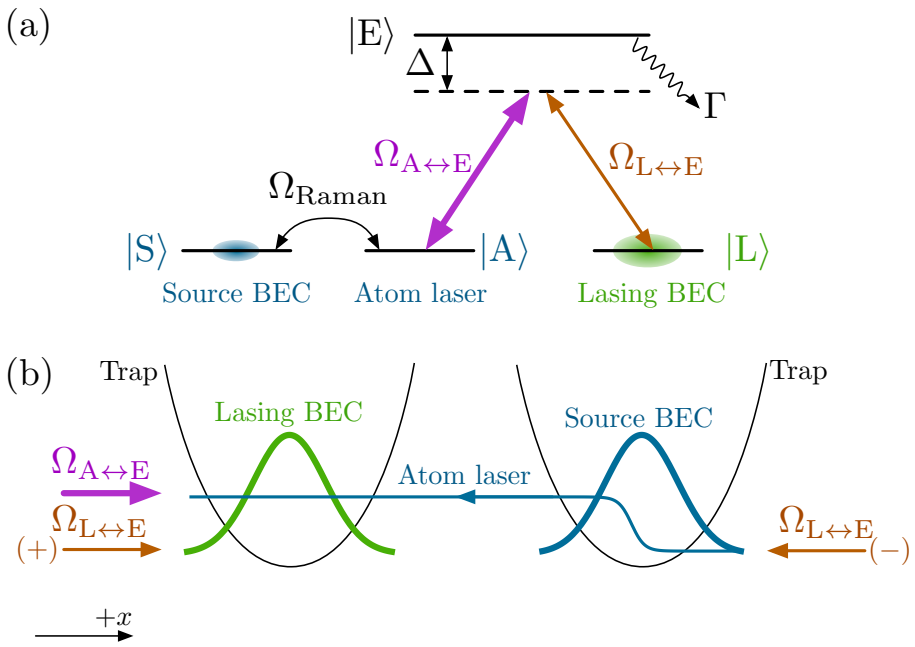

Figure 4.10: Schematic of the travelling beam model. The additional excited level that is a necessary part of the Raman outcoupling process has been suppressed to simplify the diagram. This scheme is governed by (4.67).

$\Omega_{1\leftrightarrow 3}$ is

$$|\Omega_{1\leftrightarrow 3}(+\infty)|^2 = |\Omega_{1\leftrightarrow 3}(-\infty)|^2 \left|1 + \frac{N_1}{N}(\alpha - 1)\right|^2. \tag{4.66}$$

For $N_1 \ll N$, $\Omega_{1\leftrightarrow 3}$ changes negligibly propagating through the system and is well approximated by a constant. Being constant, its propagation direction relative to that of $\Omega_{2\leftrightarrow 3}$ can have little effect on the system's dynamics. This is observed in simulations of (4.39).

4.5.3 Simple atom laser model

The previous model suggested that efficient population transfer with resonant light might be possible if the source and lasing modes partially overlap such that the first resonant atoms that the pumping photons encounter are in the lasing mode, and the last are in the source mode. One way this might occur which is relevant to the continuous pumping experiment is illustrated in Figure 4.10. In this model there are two trapped condensates, the source condensate $|\mathrm{S}\rangle$, and the lasing condensate $|\mathrm{L}\rangle$. Atoms are outcoupled from the source condensate via a Raman transition to form an atom laser $|\mathrm{A}\rangle$. The Raman process gives atoms a $2\hbar k$ momentum kick to the left as they are outcoupled from the source condensate.

The atom laser forms the source mode for the pumping process considered in the previous section (see Figure 4.7). In this pumping process, light on the $|A\rangle \leftrightarrow |\mathrm{E}\rangle$ transition is applied from the left with detuning Δ and an initial Rabi frequency of $\Omega_{\mathrm{A}\leftrightarrow\mathrm{E}}(-\infty)$. Light on the $|\mathrm{L}\rangle \leftrightarrow |\mathrm{E}\rangle$ transition is produced as atoms in the excited state $|\mathrm{E}\rangle$ are stimulated to emit into the lasing condensate $|\mathrm{L}\rangle$. Similarly to Section 4.5.2, we consider the cases in which the light on the $|\mathrm{L}\rangle \leftrightarrow |\mathrm{E}\rangle$ transition propagates from the right or the left. Physically, only the case in which $\Omega_{\mathrm{L}\leftrightarrow\mathrm{E}}$ propagates from the right can be momentum resonant as the $2\hbar k$ of momentum transferred in this process will cancel the momentum of the atoms in the atom laser. The process in which $\Omega_{\mathrm{L}\leftrightarrow\mathrm{E}}$ propagates from the left is interesting, however, as a model of the zero momentum-transfer pumping process described at the end of Section 4.3 in which atoms from the source condensate are outcoupled into the source mode and then immediately undergo the stimulated $|\mathrm{A}\rangle \rightarrow |\mathrm{E}\rangle \rightarrow |\mathrm{L}\rangle$ pumping process with no net momentum transfer. When considering this process in the present model, the equations of motion are slightly modified to make the otherwise unphysical process momentum-resonant.

The equations of motion for this system are similar to those for the previous model with the difference that the source mode (the atom laser) is coupled via a Raman transition to a second condensate,

$$\begin{aligned} i\hbar\frac{\partial}{\partial t}\Psi_{\mathrm{S}}(x) = &\left[-\frac{\hbar^2}{2M}\frac{d^2}{dx^2} + V_{\mathrm{S}}(x) + U_{1\mathrm{D}}\left(|\Psi_{\mathrm{S}}|^2 + |\Psi_{\mathrm{A}}|^2 + |\Psi_{\mathrm{L}}|^2\right)\right]\Psi_{\mathrm{S}} \\ &+\hbar\Omega_{\mathrm{Raman}}\Psi_{\mathrm{A}}, \end{aligned} \tag{4.67a}$$

$$\begin{aligned} i\hbar\frac{\partial}{\partial t}\Psi_{\mathrm{A}}(x) = &\left[-\frac{\hbar^2}{2M}\frac{d^2}{dx^2} + U_{1\mathrm{D}}\left(|\Psi_{\mathrm{S}}|^2 + |\Psi_{\mathrm{A}}|^2 + |\Psi_{\mathrm{L}}|^2\right)\right]\Psi_{\mathrm{A}} \\ &+\hbar\Omega^*_{\mathrm{Raman}}\Psi_{\mathrm{S}} - \hbar\frac{|\Omega_{\mathrm{A}\leftrightarrow\mathrm{E}}|^2\Psi_{\mathrm{A}} + \Omega^*_{\mathrm{A}\leftrightarrow\mathrm{E}}\Omega_{\mathrm{L}\leftrightarrow\mathrm{E}}\Psi_{\mathrm{L}}}{\Delta - \frac{i}{2}\Gamma}, \end{aligned} \tag{4.67b}$$

$$\begin{aligned} i\hbar\frac{\partial}{\partial t}\Psi_{\mathrm{L}}(x) = &\left[-\frac{\hbar^2}{2M}\frac{d^2}{dx^2} + V_{\mathrm{L}}(x) + U_{1\mathrm{D}}\left(|\Psi_{\mathrm{S}}|^2 + |\Psi_{\mathrm{A}}|^2 + |\Psi_{\mathrm{L}}|^2\right)\right]\Psi_{\mathrm{L}} \\ &-\hbar\frac{|\Omega_{\mathrm{L}\leftrightarrow\mathrm{E}}|^2\Psi_{\mathrm{L}} + \Omega^*_{\mathrm{L}\leftrightarrow\mathrm{E}}\Omega_{\mathrm{A}\leftrightarrow\mathrm{E}}\Psi_{\mathrm{A}}}{\Delta - \frac{i}{2}\Gamma}, \end{aligned} \tag{4.67c}$$

$$\frac{d}{dx}\Omega_{\mathrm{A}\leftrightarrow\mathrm{E}} = ik\Omega_{\mathrm{A}\leftrightarrow\mathrm{E}} + \frac{i}{8}\Gamma\frac{\sigma_0}{A_\perp}\frac{|\Psi_{\mathrm{A}}|^2\Omega_{\mathrm{A}\leftrightarrow\mathrm{E}} + \Psi^*_{\mathrm{A}}\Psi_{\mathrm{L}}\Omega_{\mathrm{L}\leftrightarrow\mathrm{E}}}{\Delta - \frac{i}{2}\Gamma}, \tag{4.67d}$$

$$\pm\frac{d}{dx}\Omega_{\mathrm{L}\leftrightarrow\mathrm{E}} = ik\Omega_{\mathrm{L}\leftrightarrow\mathrm{E}} + \frac{i}{8}\Gamma\frac{\sigma_0}{A_\perp}\frac{|\Psi_{\mathrm{L}}|^2\Omega_{\mathrm{L}\leftrightarrow\mathrm{E}} + \Psi^*_{\mathrm{L}}\Psi_{\mathrm{A}}\Omega_{\mathrm{A}\leftrightarrow\mathrm{E}}}{\Delta - \frac{i}{2}\Gamma}, \tag{4.67e}$$

where $\Omega_{\mathrm{Raman}}(x) = \Omega_{\mathrm{Raman}}(0)e^{-2ikx}$. In the absence of any clear limits in which these equations may be solved analytically, we investigate their behaviour numerically in the

limit of resonant and far detuned pumping light.

Zero detuning limit ($\Delta = 0$)

When an atom in the atom laser absorbs a photon from the $\Omega_{\mathrm{A}\leftrightarrow\mathrm{E}}$ mode and undergoes spontaneous emission, both the photon and the atom are removed from the system. If the fluxes of the two are balanced, then there will be a region of overlap between the two where they interact; outside this region there will either be no photons (in the $\Omega_{\mathrm{A}\leftrightarrow\mathrm{E}}$ mode) or no atom laser. If the fluxes are unbalanced even only slightly, this overlap region will begin to move. As the fluxes do not change in the absence of direct atom–light interactions, the overlap region will never reach equilibrium. If the photon flux exceeds the atom flux then the system will reach equilibrium when the atoms in the atom laser undergo spontaneous emission almost immediately after being outcoupled. If the atom flux exceeds the photon flux, the overlap region will move in the $-x$ direction at a constant velocity forever. This extreme sensitivity is an artefact of the reduction of the system to a single dimension, in higher dimensions it is the *flux densities* which must balance, not the *fluxes*. As the atom laser beam propagates, the beam will diffuse in the transverse dimensions reducing the atomic flux density along the line through the centres of the condensates. Variations in the total fluxes of either the atoms or photons will therefore simply alter the equilibrium position of the overlap region until the flux densities balance.

While this problem could be resolved by considering a two- or three-dimensional model instead of the one-dimensional model of (4.67), a simpler solution is to assume the instantaneous behaviour of the one-dimensional model as representative of equilibrium behaviour in a higher-dimensional model. In our modelling of this system, the pumping light ($\Omega_{\mathrm{A}\leftrightarrow\mathrm{E}}$) is turned on after some delay, and at an appropriate flux to approximately balance the atom laser flux.

For the pumping process to be efficient when operated with resonant pumping light, the photons must remain in the dark state of the system as much as possible. The length scale over which the system can adjust to changes in the dark state must be significantly shorter than the characteristic length scale over which the dark state changes. In the notation of this model, the dark state is

$$|D\rangle = \frac{1}{\sqrt{|\Psi_{\mathrm{A}}|^2 + |\Psi_{\mathrm{L}}|^2}} \left(\Psi_{\mathrm{L}}|\mathrm{A}\leftrightarrow\mathrm{E}\rangle - \Psi_{\mathrm{A}}|\mathrm{L}\leftrightarrow\mathrm{E}\rangle\right). \tag{4.68}$$

The length scale over which the system adjusts to changes in this dark state is

$$d = \frac{4A_\perp}{\sigma_0\left(|\Psi_\mathrm{A}|^2 + |\Psi_\mathrm{L}|^2\right)}. \tag{4.69}$$

If a large fraction of the atom laser is to be transferred to the lasing condensate, the density of the atom laser must reduce to zero within the lasing condensate. At this point, the dark state will have all of the photons in the $\Omega_{\mathrm{A}\leftrightarrow\mathrm{E}}$ mode. Outside of the lasing condensate, the atom laser density will be non-zero, but the density of the lasing condensate will be zero and the dark state will have all of the photons in the $\Omega_{\mathrm{L}\leftrightarrow\mathrm{E}}$ mode. The characteristic length scale for changes in the dark state can therefore be no larger than the Thomas-Fermi radius, which in this system is $r_\mathrm{TF} \approx 5\,\mu\mathrm{m}$. Numerical simulations of the system show that the actual length scale over which the dark state changes is closer to $1\,\mu\mathrm{m}$.

Ideally, a large fraction of the atom laser beam should be transferred to the lasing condensate. For this to occur, the dark state must be followed as much as possible. The dark state will be changing the fastest when the densities of the atom laser and the lasing condensate are approximately equal. The dark state following length scale at this position must therefore be much smaller than the length scale over which the dark state changes. For this requirement to be satisfied, the atom laser must be significantly greater than a minimum density,

$$d \ll r_\mathrm{TF}, \tag{4.70}$$

$$\frac{4A_\perp}{\sigma_0\left(|\Psi_\mathrm{A}|^2 + |\Psi_\mathrm{L}|^2\right)} \ll r_\mathrm{TF},$$

$$\frac{4A_\perp}{\sigma_0 2\,|\Psi_\mathrm{A}|^2} \ll r_\mathrm{TF},$$

$$|\Psi_\mathrm{A}|^2 \gg \frac{2A_\perp}{\sigma_0 r_\mathrm{TF}}. \tag{4.71}$$

Given that the atom laser has momentum $2\hbar k$, this density requirement can be rewritten as a requirement on the flux Φ_A of the atom laser,

$$\Phi_\mathrm{A} \gg \frac{4\hbar k A_\perp}{\sigma_0 M r_\mathrm{TF}} \approx 5\times10^6\,\mathrm{s}^{-1}, \tag{4.72}$$

where a numerical value for the minimum flux has been obtained using the experimentally-relevant values $\lambda = 780\,\mathrm{nm}$, $A_\perp = 3\times10^{-10}\,\mathrm{m}^2$, $r_\mathrm{TF} = 5\,\mu\mathrm{m}$. At this flux, a source condensate of $N_\mathrm{S} = 5\times10^5$ atoms would be depleted in 100 ms. For a high efficiency to

be achieved, the source condensate would need to be depleted in significantly less time than this. In the continuous pumping experiment, the source condensate of 6.7×10^5 atoms was outcoupled over 200 ms giving an average flux of $3.4 \times 10^6\,\mathrm{s}^{-1}$, lower than the above requirement. This only precludes efficient operation of the $2\hbar k$ momentum-transfer pumping process. For the $0\hbar k$ momentum-transfer pumping process, the requirement on the density of the atom laser still applies, however this cannot be simply translated into a requirement on the flux as the atom laser is approximately stationary when undergoing pumping into the lasing condensate.

Figure 4.11 illustrates these conclusions showing some results from the model (4.67) for high and low atom laser fluxes. In particular, the results for higher atom laser fluxes yield higher efficiencies (54% and 33% for (a) and (c) respectively) than for lower atom laser fluxes (3.5% and 2.7% for (b) and (d) respectively).

Far detuned limit ($\Delta \gg \Gamma$)

In the limit of large detuning, spontaneous emission should be reduced, however there is still the potential for losses as the atom laser propagates between the source and lasing condensates due to off-resonant interactions with the intense $\Omega_{\mathrm{A}\leftrightarrow\mathrm{E}}$ optical mode. These losses may be estimated fractionally as

$$r_{\mathrm{loss}} = 1 - \exp\left(-\frac{|\Omega_{\mathrm{A}\leftrightarrow\mathrm{E}}|^2}{\Delta^2}\Gamma t\right), \tag{4.73}$$

where t is the time the atom laser takes to propagate from the source to lasing condensates. Minimising this loss requires

$$\frac{|\Omega_{\mathrm{A}\leftrightarrow\mathrm{E}}|^2}{\Delta^2}\Gamma t \ll 1. \tag{4.74}$$

Although this is the dominant loss in the system, the remaining fraction of the atom laser may not be fully transferred into the lasing condensate. The transfer process itself must also be considered to determine the overall behaviour of the pumping mechanism in this limit.

For large detunings, spontaneous emission will be suppressed and the photon and atom laser fluxes need not be exactly balanced for a steady-state to be reached, as in the resonant case. To study the steady-state of the system in the limit that the source and lasing condensate numbers are not changing too quickly, the equations of motion (4.67) may be

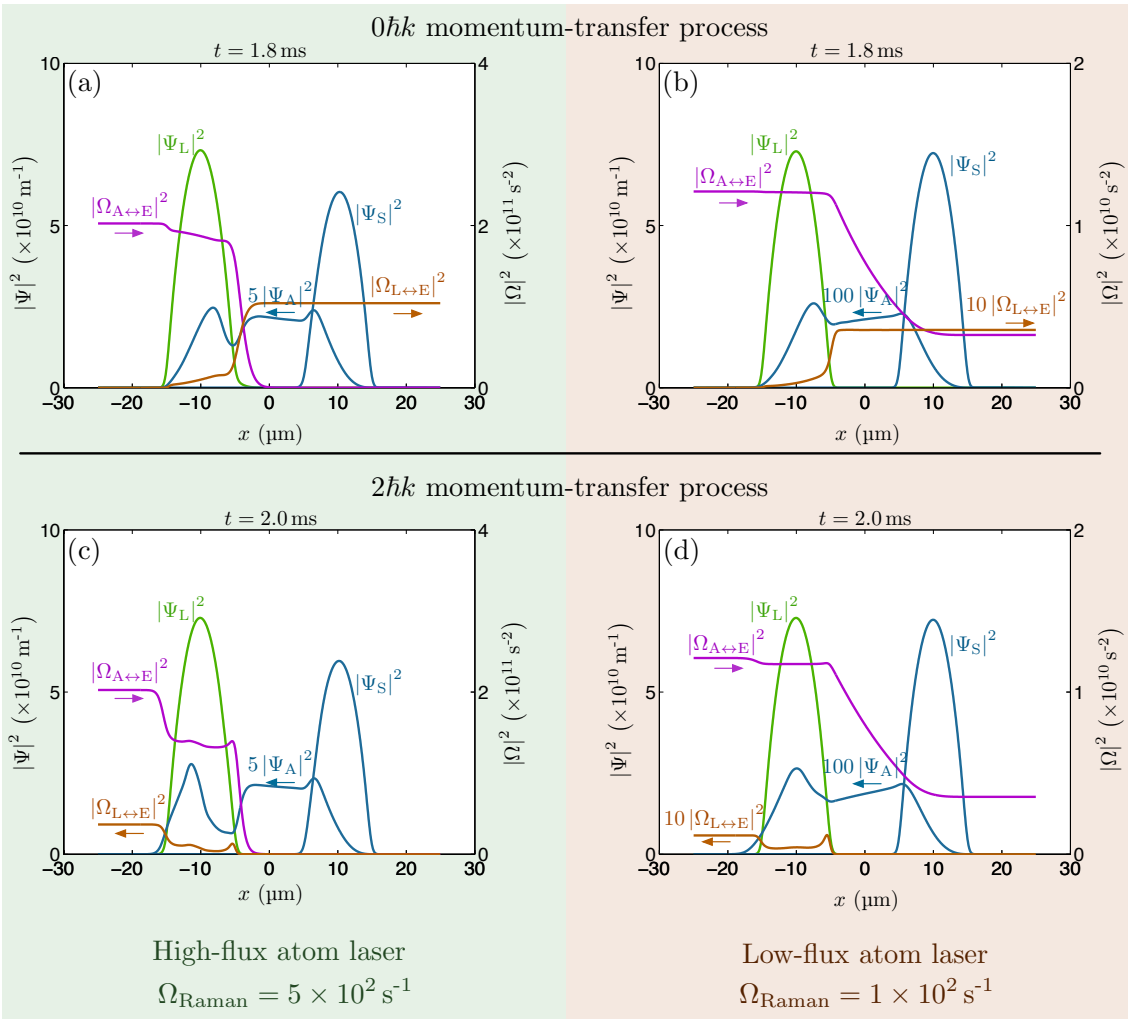

Figure 4.11: Simulation results of the simple atom laser model (4.67) driven resonantly. The top row depicts the $0\hbar k$ momentum-transfer process, which corresponds to the '+' sign of (4.67e). The bottom row depicts the $2\hbar k$ momentum-transfer process, corresponding to the '−' sign of (4.67e). The figures of the left column consider the limit of a high-flux atom laser ($\Omega_{\text{Raman}} = 5 \times 10^2\,\text{s}^{-1}$, $\Phi_{\text{A}} \approx 5 \times 10^7\,\text{s}^{-1}$, $\Omega_{\text{A}\leftrightarrow\text{E}}(-\infty) = 4.5 \times 10^5\,\text{s}^{-1}$) in which the transfer efficiency is expected to be greater (see main text). The figures of the right column are in the limit of a lower-flux atom laser ($\Omega_{\text{Raman}} = 1 \times 10^2\,\text{s}^{-1}$, $\Phi_{\text{A}} \approx 3 \times 10^6\,\text{s}^{-1}$, $\Omega_{\text{A}\leftrightarrow\text{E}}(-\infty) = 1.1 \times 10^5\,\text{s}^{-1}$) with a flux similar to that of the continuous pumping experiment. In all simulations the optical pumping laser $\Omega_{\text{A}\leftrightarrow\text{E}}$ is turned on when the atom laser is half-way inside the lasing condensate at $t = 1.6\,\text{ms}$ to approximate equilibrium conditions in a higher-dimensional model (see main text). The value of $\Omega_{\text{A}\leftrightarrow\text{E}}(-\infty)$ is chosen such that the photon flux balances the atom laser flux. Due to the limitations of the 1D nature of this model (see main text), the peak-efficiency of each simulation should be taken to be representative of possible steady-state efficiencies of higher-dimensional models. The peak-efficiencies of the four simulations are (a) 54%, (b) 3.5%, (c) 33%, (d) 2.7%. The different times for the snapshots are chosen to be close to the point of maximum efficiency to best illustrate the transfer process in each case. In all simulations the source and lasing condensates are trapped in $\omega = 2\pi \times 128\,\text{Hz}$ traps, separated by 20 μm and initially have $N_{\text{S}} = N_{\text{L}} = 5 \times 10^5$ atoms.

simplified by moving into appropriate rotating frames to remove simple phase rotation and neglecting spontaneous emission. In this limit, the source and lasing condensates can be assumed to be constant in time, and the Rabi frequency $\Omega_{\mathrm{A}\leftrightarrow\mathrm{E}}$ will be sufficiently large to be negligibly reduced after propagation through the system and may be assumed to be constant in space. Our interest is principally in the transfer process itself. This may be investigated by considering the simplified propagation equations for the atom laser Ψ_{A} and the $\Omega_{\mathrm{L}\leftrightarrow\mathrm{E}}$ optical mode as they traverse the lasing condensate in steady state,

$$\frac{\partial}{\partial x}\Psi_{\mathrm{A}} = -i\frac{M}{2\hbar k}\frac{\Omega^{*}_{\mathrm{A}\leftrightarrow\mathrm{E}}\Omega_{\mathrm{L}\leftrightarrow\mathrm{E}}}{\Delta}\Psi_{\mathrm{L}}, \tag{4.75a}$$

$$\frac{\partial}{\partial x}\Omega_{\mathrm{L}\leftrightarrow\mathrm{E}} = \pm\frac{i}{8}\frac{\Gamma}{\Delta}\frac{\sigma_0}{A_{\perp}}\Psi^{*}_{\mathrm{L}}\Psi_{\mathrm{A}}\Omega_{\mathrm{A}\leftrightarrow\mathrm{E}}, \tag{4.75b}$$

where the '$\pm$' sign in (4.75b) corresponds to propagation of $\Omega_{\mathrm{L}\leftrightarrow\mathrm{E}}$ in the $\pm x$ direction. These equations can be solved analytically as the phases of Ψ_{L} and $\Omega_{\mathrm{A}\leftrightarrow\mathrm{E}}$ may be absorbed into the remaining terms without changing the form of the equations.

The solution for the $0\hbar k$ momentum-transfer process [the '+' sign of (4.75b)] may be found by applying the boundary conditions

$$\Psi_{\mathrm{A}}(x=0) = \Psi_{\mathrm{A}}(0), \tag{4.76a}$$

$$\Omega_{\mathrm{L}\leftrightarrow\mathrm{E}}(-\infty) = 0, \tag{4.76b}$$

where $x = 0$ is chosen to be between the source and lasing condensates (see Figure 4.11). The steady-state solution for the atom laser (for $x < 0$) can be shown to be

$$\Psi_{\mathrm{A}}(x) = \Psi_{\mathrm{A}}(0)\frac{e^{w(x)-2w(-\infty)} + e^{-w(x)}}{1 + e^{-2w(x)}}, \tag{4.77}$$

where $w(x)$ is the dimensionless function

$$w(x) = \frac{1}{4}\frac{|\Omega_{\mathrm{A}\leftrightarrow\mathrm{E}}|}{\Delta}\sqrt{\frac{M\Gamma\sigma_0}{\hbar k A_{\perp}}}\int_{x}^{0}|\Psi_{\mathrm{L}}|\,dx. \tag{4.78}$$

For $w(x) \gg 1$, $|\Psi_{\mathrm{A}}(x)|^2 \ll |\Psi_{\mathrm{A}}(0)|^2$ and therefore the atom laser will be almost completely

transferred to the lasing condensate. The efficiency of the transfer process alone is

$$\eta = 1 - \frac{|\Psi_{\mathrm{A}}(-\infty)|^2}{|\Psi_{\mathrm{A}}(0)|^2} = 1 - \operatorname{sech}^2\left(\frac{1}{4}\frac{|\Omega_{\mathrm{A}\leftrightarrow\mathrm{E}}|}{\Delta}\sqrt{\frac{M\Gamma\sigma_0}{\hbar k A_\perp}}\int_{-\infty}^{0}|\Psi_{\mathrm{L}}|\,dx\right)$$
$$= 1 - \operatorname{sech}^2\left(\frac{1}{4}\frac{|\Omega_{\mathrm{A}\leftrightarrow\mathrm{E}}|}{\Delta}\sqrt{\frac{M\Gamma\sigma_0}{\hbar k A_\perp}}\int_{-\infty}^{+\infty}|\Psi_{\mathrm{L}}|\,dx\right), \tag{4.79}$$

where the integral has been extended to $+\infty$ as $\Psi_{\mathrm{L}}(x \geq 0) = 0$ (refer to Figure 4.11).

The behaviour of the $2\hbar k$ momentum-transfer process [the '$-$' sign of (4.75b)] contrasts strongly with that of the $0\hbar k$ momentum-transfer process just considered. For this process the boundary conditions are

$$\Psi_{\mathrm{A}}(x = 0) = \Psi_{\mathrm{A}}(0), \tag{4.80a}$$
$$\Omega_{\mathrm{L}\leftrightarrow\mathrm{E}}(+\infty) = \Omega_{\mathrm{L}\leftrightarrow\mathrm{E}}(0) = 0, \tag{4.80b}$$

and the solution for the atom laser (for $x < 0$) is

$$\Psi_{\mathrm{A}}(x) = \Psi_{\mathrm{A}}(0)\cos\left(\frac{1}{4}\frac{|\Omega_{\mathrm{A}\leftrightarrow\mathrm{E}}|}{\Delta}\sqrt{\frac{M\Gamma\sigma_0}{\hbar k A_\perp}}\int_{x}^{0}|\Psi_{\mathrm{L}}|\,dx\right), \tag{4.81}$$

In this process, the atoms in the atom laser oscillate between the lasing condensate and the atom laser. Fundamentally, this is because the $\Omega_{\mathrm{L}\leftrightarrow\mathrm{E}}$ photons and the atom laser propagate in the same direction. When an atom is transferred from the atom laser to the lasing condensate, a photon in the $\Omega_{\mathrm{L}\leftrightarrow\mathrm{E}}$ mode is created propagating in the same direction. The photon may later be absorbed by an atom in the lasing condensate transferring the atom back to the atom laser. In the $0\hbar k$ momentum-transfer process, the $\Omega_{\mathrm{L}\leftrightarrow\mathrm{E}}$ photons and the atom laser propagate in opposite directions. If by some point the atom laser were completely transferred to the lasing condensate, as the emitted photons propagate in the opposite direction (which are transparent to the atom laser), there will be no photons available past this point to transfer atoms from the lasing condensate to the atom laser. In steady-state, once an atom is transferred from the atom laser to the lasing condensate, the emitted photon propagating in the opposite direction will be unavailable to transfer an atom from the lasing mode back to the atom laser. The difference in the behaviour of the two processes is illustrated in Figure 4.12.

Through appropriate choice of detuning and $\Omega_{\mathrm{A}\leftrightarrow\mathrm{E}}$, the $2\hbar k$ momentum-transfer process can be operated with a high efficiency. This is however only strictly true for a 1D model.

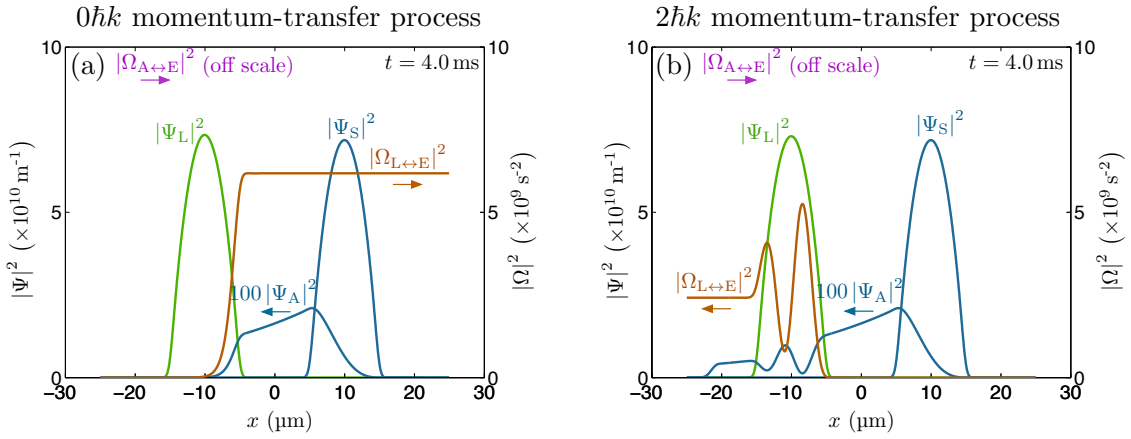

Figure 4.12: Simulation results of the simple atom laser model (4.67) driven by a $\Delta = 10^3\Gamma = 2\pi \times 5.9\,\text{GHz}$ detuned optical pumping laser. Figure (a) is of the $0\hbar k$ momentum-transfer process, which corresponds to the '+' sign of (4.67e). Figure (b) is of the $2\hbar k$ momentum-transfer process, corresponding to the '−' sign of (4.67e). The difference in behaviour of the two processes is quite marked: while in (a) the population transfer is complete, in (b) atoms Rabi flop between the atom laser and the lasing condensate. These oscillations are damped due to off-resonant spontaneous scattering by the atom laser. The steady-state efficiencies achieved for these two processes are (a) 48%, (b) 19%. There is an absorbing boundary layer (see Section 2.7.1) used in both simulations, and this is observed in the sharp decay of the atom laser at the left edge of (b). In all simulations the optical pumping laser $\Omega_{A\leftrightarrow E}$ is approximately constant as it propagates through the system with $\Omega_{A\leftrightarrow E}(-\infty) = 1.5 \times 10^8\,\text{s}^{-1}$. The atom laser is outcoupled from the source condensate with a Rabi frequency $\Omega_{\text{Raman}} = 1 \times 10^2\,\text{s}^{-1}$.

In higher dimensions, the transfer efficiency will reduce because the line integral $\int |\Psi_L|\,dx$ will vary across the condensate preventing maximum transfer efficiency from being achieved across the entire condensate. Efficient operation of the detuned $2\hbar k$ momentum-transfer process in a realistic system is therefore unlikely. The $0\hbar k$ momentum-transfer process will not suffer from this problem provided the line integral $\int |\Psi_L|\,dx$ is sufficiently large across most of the condensate; increases in the value of the line integral will only increase the transfer efficiency of the atom laser into the lasing condensate. Further investigation however is necessary for the $0\hbar k$ momentum-transfer process. While this process is promising because it displays Bose-enhancement by the lasing condensate and robustness to variation in the local condensate density, the $0\hbar k$ pumping process has been artificially made momentum-resonant. It would otherwise be impossible for an atom with momentum $2\hbar k$ to absorb and emit photons with the same momentum to decay into a stationary condensate. The model of the $0\hbar k$ momentum-transfer process considered in this section can be considered to approximate the situation in which atoms from the source condensate are outcoupled to form the atom laser before almost immediately undergoing a stimulated transition into the lasing condensate. This somewhat artificial model was used to permit

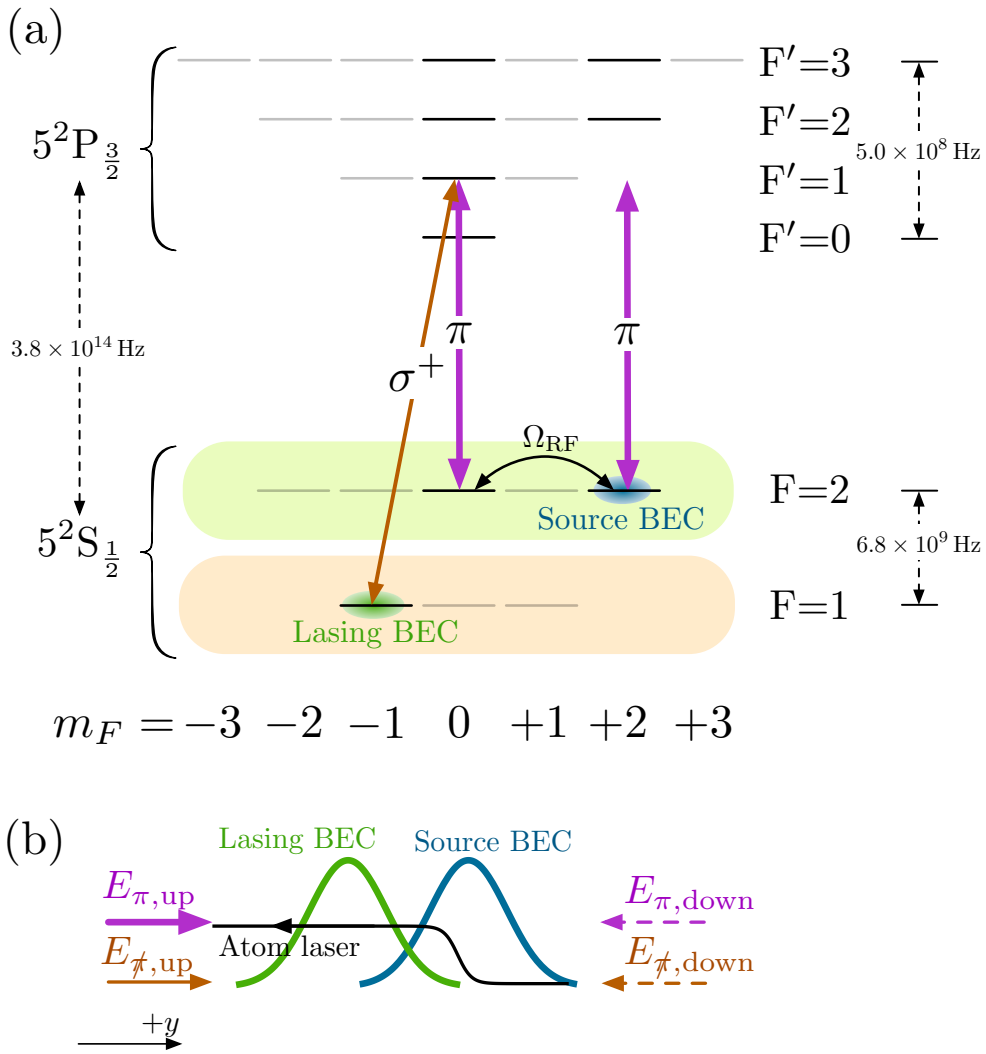

Figure 4.13: Level scheme and schematic of the 3-level pumping model. The level scheme (a) illustrates all of the levels in the physical system, however only the levels which have not been greyed out are included in this model. In the system schematic (b), gravity acts to the left accelerating the initially stationary atom laser from the source condensate towards the lasing condensate. See the main text for a definition of the $\not\pi$ electric field polarisation.

the $0\hbar k$ and $2\hbar k$ momentum-transfer processes to be compared on an equal footing where only one of the processes was resonant at a time. The $0\hbar k$ momentum-transfer process will be considered further in the next section in which a situation very similar to that of the continuous pumping experiment will be examined.

4.5.4 3-level atom laser model

The model of the previous section suggested that the most likely process occurring in the continuous pumping experiment was the $0\hbar k$ momentum-transfer process. In this section, this prediction will be investigated further by considering a system very similar

to that of the continuous pumping experiment. As it is well known that 5-level atom lasers lead to complicated dynamics [199] and our primary focus is on the pumping process itself, we consider a simplification in which the $F = 2$ manifold is effectively reduced to a 3-level system by directly coupling the untrapped $|F = 2, m_F = 0\rangle$ mode to the source condensate in the $|F = 2, m_F = 2\rangle$ state. In the weak-outcoupling limit considered here, the $|F = 2, m_F = -2\rangle$ state will be negligibly occupied, and it too may be neglected. A level diagram and schematic of the system under consideration is given in Figure 4.13.

In the present model, π-polarised pumping light resonant with the $|F = 2, m_F = 0\rangle \leftrightarrow |F' = 1, m_F = 0\rangle$ transition is applied from below. Pumping occurs when an atom in the $|F = 2, m_F = 0\rangle$ state absorbs a π-polarised photon and is stimulated by the lasing condensate to emit a 'σ^+-polarised' photon. Due to momentum conservation this 'σ^+-polarised' photon must propagate vertically upwards or downwards (corresponding to the $0\hbar k$ and $2\hbar k$ momentum-transfer processes, respectively), however pure $\sigma^\pm$-polarised light may only propagate along the direction of the bias field, which is in the horizontal plane in this experiment. This is because it is the direction of the bias field that defines the atomic polarisations. The polarisation vector for π-polarised light is $\check{\boldsymbol{u}}_\pi = \check{\boldsymbol{z}}$ where $\check{\boldsymbol{z}}$ is the unit vector in the direction of the bias field (also the weak trapping axis). Pure π-polarised light may therefore propagate vertically (i.e. in the $\pm\check{\boldsymbol{y}}$ direction). The polarisation vectors for $\sigma^\pm$-polarised light are $\check{\boldsymbol{u}}_{\sigma^\pm} = \frac{1}{\sqrt{2}}(\check{\boldsymbol{x}} \pm i\check{\boldsymbol{y}})$. As neither of these polarisation vectors are orthogonal to $\check{\boldsymbol{y}}$, they cannot propagate in this direction. The vertically-propagating polarisation coupled to the $|F = 1, m_F = -1\rangle \leftrightarrow |F' = 1, m_F = 0\rangle$ transition is the polarisation orthogonal to the π polarisation for this direction, i.e. the $\check{\boldsymbol{x}}$ polarisation. We label this polarisation $\not\pi$, with $\check{\boldsymbol{u}}_{\not\pi} = \check{\boldsymbol{x}}$. When an atom makes a transition from $|F' = 1, m_F = 0\rangle$ to $|F = 1, m_F = -1\rangle$ stimulated by the lasing condensate the emitted photon therefore is $\not\pi$-polarised, a superposition of the σ^+ and σ^- polarisations.

The equations of motion for this system are derived directly from the general multimode

model of (4.38). The evolution of the atomic fields is given by

$$i\hbar\frac{\partial}{\partial t}\Psi_{2,2} = \left[-\frac{\hbar^2}{2M}\frac{\partial^2}{\partial y^2} + 2V_{\text{trap}}(y) + Mgy + U_{1\text{D}}\left(|\Psi_{2,2}|^2 + |\Psi_{2,0}|^2 + |\Psi_{1,-1}|^2\right)\right]\Psi_{2,2} + \hbar\Omega_{\text{RF}}^*\Psi_{2,0} - i\hbar\, Q(2,2 \xrightarrow{\pi,\pi} 2,2)\,|E_\pi|^2\,\Psi_{2,2}, \tag{4.82a}$$

$$i\hbar\frac{\partial}{\partial t}\Psi_{2,0} = \left[-\frac{\hbar^2}{2M}\frac{\partial^2}{\partial y^2} + 2\hbar\Delta_{\text{RF}} + Mgy + U_{1\text{D}}\left(|\Psi_{2,2}|^2 + |\Psi_{2,0}|^2 + |\Psi_{1,-1}|^2\right)\right]\Psi_{2,0} + \hbar\Omega_{\text{RF}}\Psi_{2,2} - i\hbar\, Q(2,0 \xrightarrow{\pi,\pi} 2,0)\,|E_\pi|^2\,\Psi_{2,0} - i\hbar\, Q(2,0 \xrightarrow{\pi,\not\pi} 1,-1)E_\pi^* E_{\not\pi}\Psi_{1,-1}, \tag{4.82b}$$

$$i\hbar\frac{\partial}{\partial t}\Psi_{1,-1} = \left[-\frac{\hbar^2}{2M}\frac{\partial^2}{\partial y^2} + V_{\text{trap}}(y) + Mgy + U_{1\text{D}}\left(|\Psi_{2,2}|^2 + |\Psi_{2,0}|^2 + |\Psi_{1,-1}|^2\right)\right]\Psi_{1,-1} - i\hbar\, Q(1,-1 \xrightarrow{\not\pi,\not\pi} 1,-1)\left|E_{\not\pi}\right|^2\Psi_{1,-1} - i\hbar\, Q(1,-1 \xrightarrow{\not\pi,\pi} 2,0)E_{\not\pi}^* E_\pi\Psi_{2,0}, \tag{4.82c}$$

where $\Psi_{F,f}$ is the wavefunction for the atomic state $|F,f\rangle$, E_α is the electric field for polarisation α, $V_{\text{trap}}(y) = \frac{1}{2}M\omega_y^2 y^2$, Δ_{RF} is the detuning of the rf outcoupling, g is the acceleration due to gravity, and the two-photon coupling constants between atomic state $|F,f\rangle$ and $|G,g\rangle$ are

$$Q(F,f \xrightarrow{\alpha,\beta} G,g) = \sum_{F',f'}\frac{1}{\frac{1}{2}\Gamma + i\Delta_{F',f'}}\frac{(\boldsymbol{d}_{F,f;F',f'}\cdot\check{\boldsymbol{u}}_\alpha^*)}{\hbar}\frac{(\boldsymbol{d}_{G,g;F',f'}^*\cdot\check{\boldsymbol{u}}_\beta)}{\hbar}, \tag{4.83}$$

where the sum over $\{F',f'\}$ extends over all excited levels $|F',f'\rangle$ coupled to both $|F,f\rangle$ and $|G,g\rangle$, and $\Delta_{F',f'}$ is the detuning of the excited state $|F',f'\rangle$ relative to the optical modes.

To consider both the $0\hbar k$ and $2\hbar k$ momentum-transfer processes, we split the electric fields for each polarisation into both upward and downward propagating components,

$$E_\alpha(y) = E_{\alpha,\text{up}}(y) + E_{\alpha,\text{down}}(y). \tag{4.84}$$

These electric field components evolve as

$$\begin{aligned}\frac{\partial}{\partial y}E_{\pi,\mathrm{up}} &= ikE_{\pi,\mathrm{up}} - \frac{\hbar k}{2\varepsilon_0 A_\perp}Q(2,0 \xrightarrow{\pi,\not\pi} 1,-1)\Psi^*_{2,0}\Psi_{1,-1}E_{\not\pi} \\ &\quad -\frac{\hbar k}{2\varepsilon_0 A_\perp}\left[Q(2,2 \xrightarrow{\pi,\pi} 2,2)\left|\Psi_{2,2}\right|^2 + Q(2,0 \xrightarrow{\pi,\pi} 2,0)\left|\Psi_{2,0}\right|^2\right]E_{\pi,\mathrm{up}},\end{aligned} \tag{4.85a}$$

$$\begin{aligned}-\frac{\partial}{\partial y}E_{\pi,\mathrm{down}} &= ikE_{\pi,\mathrm{down}} - \frac{\hbar k}{2\varepsilon_0 A_\perp}Q(2,0 \xrightarrow{\pi,\not\pi} 1,-1)\Psi^*_{2,0}\Psi_{1,-1}E_{\not\pi} \\ &\quad -\frac{\hbar k}{2\varepsilon_0 A_\perp}\left[Q(2,2 \xrightarrow{\pi,\pi} 2,2)\left|\Psi_{2,2}\right|^2 + Q(2,0 \xrightarrow{\pi,\pi} 2,0)\left|\Psi_{2,0}\right|^2\right]E_{\pi,\mathrm{down}},\end{aligned} \tag{4.85b}$$

$$\begin{aligned}\frac{\partial}{\partial y}E_{\not\pi,\mathrm{up}} &= ikE_{\not\pi,\mathrm{up}} - \frac{\hbar k}{2\varepsilon_0 A_\perp}Q(2,0 \xrightarrow{\pi,\not\pi} 1,-1)\Psi^*_{1,-1}\Psi_{2,0}E_{\pi} \\ &\quad -\frac{\hbar k}{2\varepsilon_0 A_\perp}Q(1,-1 \xrightarrow{\not\pi,\not\pi} 1,-1)\left|\Psi_{1,-1}\right|^2 E_{\not\pi,\mathrm{up}},\end{aligned} \tag{4.85c}$$

$$\begin{aligned}-\frac{\partial}{\partial y}E_{\not\pi,\mathrm{down}} &= ikE_{\not\pi,\mathrm{down}} - \frac{\hbar k}{2\varepsilon_0 A_\perp}Q(2,0 \xrightarrow{\pi,\not\pi} 1,-1)\Psi^*_{1,-1}\Psi_{2,0}E_{\pi} \\ &\quad -\frac{\hbar k}{2\varepsilon_0 A_\perp}Q(1,-1 \xrightarrow{\not\pi,\not\pi} 1,-1)\left|\Psi_{1,-1}\right|^2 E_{\not\pi,\mathrm{down}}.\end{aligned} \tag{4.85d}$$

The dipole moments for the various transitions can be written as multiples of the reduced dipole matrix element for the D_2 transition by the Wigner-Eckart theorem [200, 201]

$$\boldsymbol{d}_{F,f;F',f'} = c_{F,f;F',f'}\, d_{\mathrm{reduced}}\check{\boldsymbol{u}}_\alpha, \tag{4.86}$$

where $\alpha \in \{\pi, \sigma^\pm\}$ is the polarisation corresponding to the $|F,f\rangle \leftrightarrow |F',f'\rangle$ transition, $d_{\mathrm{reduced}} = \left\langle J=\frac{1}{2}\middle\|er\middle\|J'=\frac{3}{2}\right\rangle = 3.6\times10^{-29}\,\mathrm{C.m}$ is the reduced dipole matrix element for the D_2 transition in ^{87}Rb, and $c_{F,f;F',f'}$ is a real constant given by [202]

$$c_{F,f;F',f'} = (-1)^{J+I+f}\sqrt{(2F+1)(2F'+1)(2J+1)}\begin{Bmatrix} J & J' & 1 \\ F' & F & I\end{Bmatrix}\begin{pmatrix} F' & 1 & F \\ f' & f-f' & -f\end{pmatrix}, \tag{4.87}$$

where the array in braces is a Wigner $6j$ symbol, and the array in parentheses is a Wigner $3j$ symbol. For the $5^2S_{\frac{1}{2}} \rightarrow 5^2P_{\frac{3}{2}}$ transition of ^{87}Rb, the remaining quantum numbers in (4.87) are $I=\frac{3}{2}$, $J=\frac{1}{2}$, and $J'=\frac{3}{2}$. Values for $c_{F,f;F',f'}$ may be found in standard tables

[202]. The two most important dipole moments are

$$\boldsymbol{d}_{1,-1;1',0'} = \sqrt{\frac{5}{24}} d_{\text{reduced}} \check{\boldsymbol{u}}_{\sigma^+}, \tag{4.88}$$

$$\boldsymbol{d}_{2,0;1',0'} = \sqrt{\frac{1}{30}} d_{\text{reduced}} \check{\boldsymbol{u}}_{\pi}. \tag{4.89}$$

The usual technique for reducing a 3D model to a 1D model cannot be applied to the present system without ambiguity. The usual method aims to derive an effective 1D interaction strength $U_{1\text{D}}$ from the 3D interaction strength $U_{3\text{D}}$ by dividing it by a representative transverse area $A_\perp$, i.e. $U_{1\text{D}} = U_{3\text{D}}/A_\perp$. This transverse area is typically chosen such that the chemical potentials of the two models are equal (and hence the corresponding Thomas-Fermi radii are equal). In the present model, there are two possible transverse areas to choose corresponding to each of the two condensates. Although the transverse areas depend on the condensate number, the primary difference is due to the different trapping frequencies: those for the $|2,2\rangle$ atoms are $\sqrt{2}$ times larger than those for the $|1,-1\rangle$ atoms. In resolving this problem, we would like to preserve the Thomas-Fermi radii of both condensates because, as discussed at the end of Section 4.3, the slight overlap of the two condensates may be crucially important for the operation of the pumping mechanism.

To make the dimension reduction, we choose the transverse area corresponding to the source condensate (the $|2,2\rangle$ state) $A_\perp = 2.8 \times 10^{-10}\,\text{m}^2$, as this should be representative for both the source condensate and the atom laser in the $|2,0\rangle$ state. To make the Thomas-Fermi radius of the lasing condensate (the $|1,-1\rangle$ state) match that of a 3D model, we decrease the number of atoms in this state. This reduces the effective number of atoms in the lasing condensate from $N_{\text{lasing}} = 5.0 \times 10^5$ to $N_{\text{lasing}}^{(\text{eff})} = 4.3 \times 10^5$. This reduction in the condensate number causes the density of the lasing condensate to be lower than it otherwise would be in the 1D model; in a 3D model the density would be lower because of the larger transverse area.

With the model itself explained, we may now use it to investigate the hypothesis that it is the $0\hbar k$ momentum-transfer process that occurs in the continuous pumping experiment. To this end, a parameter scan of the model was performed to find the maximum transfer efficiency as a function of outcoupling detuning for a fixed atom laser flux $\Phi = 1 \times 10^7\,\text{s}^{-1}$ for

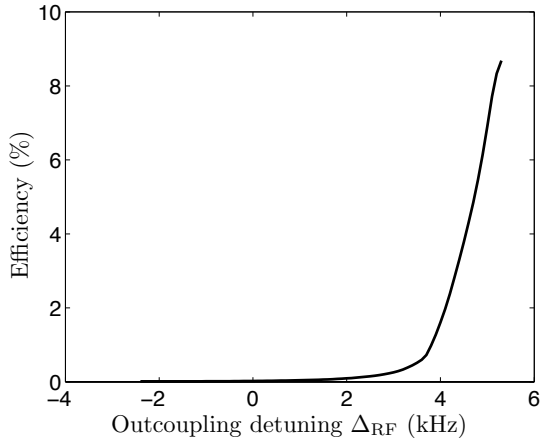

Figure 4.14: Optimum pumping efficiency over 3 ms as a function of outcoupling detuning Δ_{RF}. The optimisation was performed over the intensity of the applied pumping light [as determined by $E_{\pi,\mathrm{up}}(-\infty)$] at a constant flux of $\Phi = 1 \times 10^7\,\mathrm{s}^{-1}$. Zero outcoupling detuning ($\Delta_{\mathrm{RF}} = 0$) corresponds to the energy resonance of the outcoupling process being in the centre of the source condensate. As discussed in the main text, higher outcoupling detunings cannot be operated for longer times as the atom laser ceases to operate. There is therefore an optimum outcoupling detuning.

3 ms of outcoupling. For each outcoupling detuning Δ_{RF}, a parameter scan was performed as a function of the intensity of the applied optical pumping light [as determined by $E_{\pi,\mathrm{up}}(-\infty)$] to determine the optimum pumping efficiency. If the pumping light intensity is too low, the transfer process will proceed slowly, while if the pumping light is too intense, spontaneous losses from the atom laser and the source condensate will exceed the atom number transferred to the lasing condensate. The optimum pumping efficiency (ratio of the number of atoms transferred to the lasing condensate divided by the number of atoms lost from the source condensate) is plotted as a function of the outcoupling detuning in Figure 4.14.

The plot of pumping efficiency Figure 4.14 shows a clear increase in efficiency at large outcoupling detunings where the $0\hbar k$ momentum-transfer process is expected to occur. It is interesting to note that there isn't a local maximum near $\Delta_{\mathrm{RF}} = 0$ where the $2\hbar k$ momentum-transfer process would be expected to occur. Examining the dynamics of a simulation in this parameter regime [see Figure 4.15(a)] illuminates the reason. What is occurring is that as the atom laser falls, it first comes into momentum-resonance with the lasing condensate (via the $2\hbar k$ momentum-transfer process) towards the upper edge of the lasing condensate, however it goes out of momentum-resonance within the lower half of the lasing condensate as the atom laser continues to accelerate under gravity. As this occurs, the system attempts to follow the dark state by compensating for the reduction

in the density of the atom laser that is momentum-resonant with the lasing condensate by transferring atoms from the lasing condensate back to the atom laser. As this process requires photons in the $E_{\not\parallel,\mathrm{down}}$ mode to occur, the number of atoms transferred back to the atom laser is limited by the number of atoms transferred from the atom laser to the lasing condensate at the upper edge of the lasing condensate. As a result, there is a negligible net transfer of atoms to the lasing condensate. Counter-intuitively, according to this model the only way the $2\hbar k$ momentum-transfer process can operate is not by having the atom laser momentum-resonant at the *centre* of the lasing condensate where the condensate density is a maximum, but instead to have the atom laser momentum-resonant towards the lower edge of the lasing condensate. This way the lasing condensate density will reduce before the atom laser is no longer momentum-resonant with the lasing condensate. As the system follows the dark state it will attempt to compensate for the loss of density of the lasing condensate by transferring atoms from the atom laser into the lasing condensate. This therefore requires outcoupling from the lower part of the source condensate, the same parameter regime in which the $0\hbar k$ momentum-transfer process is expected to operate. However for the reasons discussed in Section 4.5.3, the $0\hbar k$ momentum-transfer process will be expected to dominate as it will suffer significantly less spontaneous loss.

Figure 4.15(b) illustrates a snapshot of a simulation of the system for $\Delta_{\mathrm{RF}} = 2\pi \times 5\,\mathrm{kHz}$, a parameter regime in which the $0\hbar k$ momentum-transfer process is expected to be significant. The operation of the $0\hbar k$ momentum-transfer process is signalled by the population of the $E_{\not\parallel,\mathrm{up}}$ mode after propagation through the system. Additionally, the occupation of the $E_{\not\parallel,\mathrm{down}}$ mode indicates that the $2\hbar k$ momentum-transfer process is also occurring, although to a lesser extent.

Over the simulated time of $t = 3\,\mathrm{ms}$, the pumping efficiency for the simulation illustrated in Figure 4.15(b) is 5.9%. While 3 ms of outcoupling and pumping cannot fully represent the behaviour of the system for the entire 100 ms to 200 ms over which the pumping occurred in the experiment, it does give a general indication of the behaviour of the system. For longer outcoupling times the atom laser will not operate for the entire period at the higher detunings pictured in Figure 4.14 as once the source condensate has reduced in size beyond the outcoupling position the atom laser will stop. Over longer outcoupling times, there will therefore be an optimum outcoupling position to maximise the transfer of atoms to the lasing condensate. While a parameter scan of the system over the full pumping time is computationally prohibitive, a numerical optimisation procedure can be

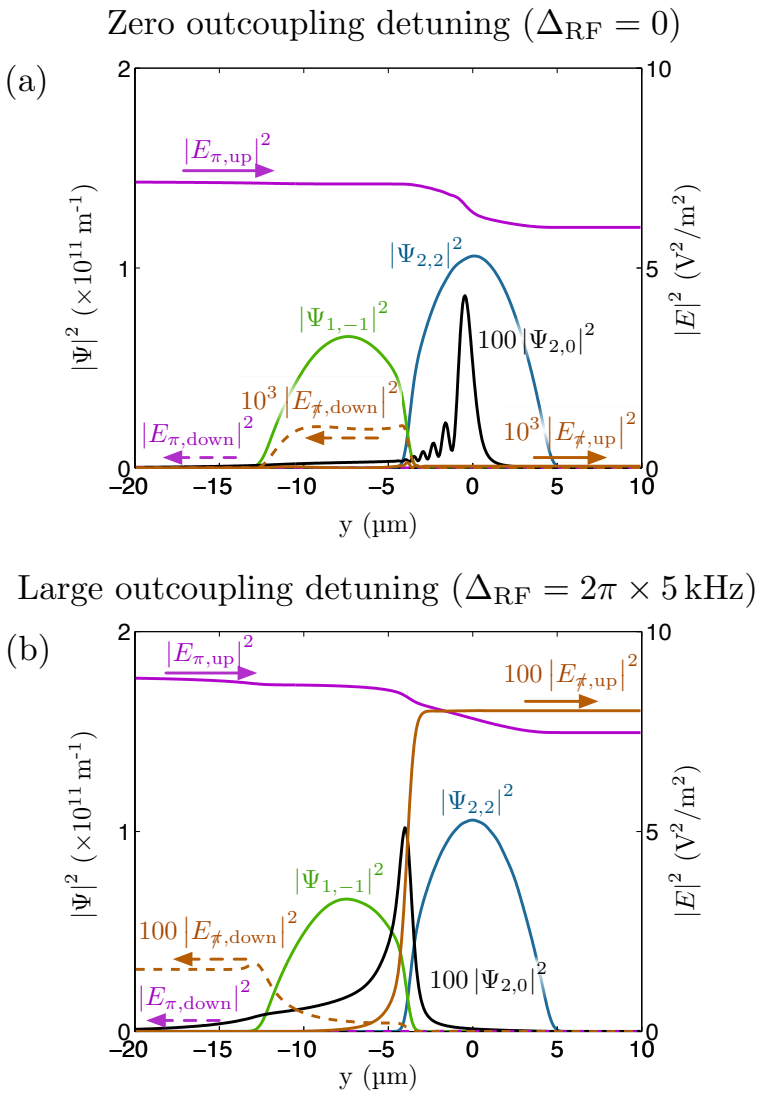

Figure 4.15: Simulation results of the 3-level model (4.82)–(4.85) driven resonantly. Figure (a) has resonant outcoupling $\Delta_{\mathrm{RF}} = 0$, with $E_{\pi,\mathrm{up}}(-\infty) = 2.7\,\mathrm{V/m}$, and $\Omega_{\mathrm{RF}} = 2\pi \times 42\,\mathrm{Hz}$. Figure (b) is in the limit of large outcoupling detuning, $\Delta_{\mathrm{RF}} = 2\pi \times 5\,\mathrm{kHz}$ with $E_{\pi,\mathrm{up}}(-\infty) = 3.0\,\mathrm{V/m}$, and $\Omega_{\mathrm{RF}} = 2\pi \times 110\,\mathrm{Hz}$. It is observed that the outcoupling position of the atom laser $\Psi_{2,0}$ is shifted significantly approximately 5 µm down into the region of overlap between the two condensates. All snapshots are taken at $t = 3\,\mathrm{ms}$.

used to determine the optimum efficiency achievable from the experiment over 150 ms. Over these longer timescales, it was observed that the $2\hbar k$ momentum-transfer process only contributed over the first 10 ms with the $0\hbar k$ momentum-transfer process operating over essentially the entire period. This is because the lower edge of the lasing condensate moved downwards as it increased in size while the position at which the atom laser was momentum-resonant via the $2\hbar k$ momentum-transfer process remained stationary. The highest achieved efficiency from the optimisation procedure was 6.7%, defined as the change in the number of atoms in the lasing condensate divided by the number of atoms initially in the source condensate. The parameters for this optimum pumping were $\Delta_{\mathrm{RF}} = 2\pi \times 4.6\,\mathrm{kHz}$, $E_{\pi,\mathrm{up}}(-\infty) = 4.8975\,\mathrm{V/m}$, and $\Omega_{\mathrm{RF}} = 2\pi \times 308.98\,\mathrm{Hz}$.

Comparison with experiment

The preceding modelling strongly indicates that the pumping process occurring in the continuous pumping experiment was the $0\hbar k$ momentum-transfer process. If true, this significantly impacts the potential applicability of the pumping mechanism of that experiment to a future continuously pumped atom laser.

It was intended that the continuous pumping experiment could be extended to the production of a continuously pumped atom laser by replacing the source condensate once it becomes depleted with an independently produced condensate which becomes the new source condensate. As the pumping mechanism is independent of the relative phase of the source and lasing condensates, this would enable the operation of a continuously pumped atom laser, the atomic analogue to the continuous optical laser. However if the lasing condensate must spatially overlap with the source condensate for the pumping mechanism to operate (as is the case for the $0\hbar k$ momentum-transfer process), the source condensate cannot be replaced without disturbing the lasing condensate. This unavoidable excitation would disrupt the narrow linewidth properties that are desired of a continuously pumped atom laser.

The conclusions drawn from the preceding model are however only valid to the extent that the model is representative of the system under study. There remain some details of the experiment that have not been fully considered.

The first is that the outcoupling process from the source condensate has been simplified to remove the $|F = 2, m_F = 1\rangle$ state [see Figure 4.13(a)]. In the continuous pumping experiment, the applied RF radiation coupled the entire $F = 2$ manifold, with each level coupled

to the next. While the anti-trapped levels $|F = 2, m_F = -1\rangle$ and $|F = 2, m_F = -2\rangle$ are unlikely to have played a significant role as the outcoupling was weak, the $|F = 2, m_F = 1\rangle$ level could potentially have an impact as it is via this level that atoms are outcoupled into the untrapped $|F = 2, m_F = 0\rangle$ state, the only state that can undergo stimulated transitions into the lasing condensate (via the $|F' = 1, m_F = 0\rangle$ state). The inclusion of the $|F = 2, m_F = 1\rangle$ level is unlikely to affect the conclusion that it is the $0\hbar k$ momentum-transfer process that is occurring in the experiment as the $|F = 2, m_F = 1\rangle$ level is resonant with the π-polarised pumping light (see Figure 4.5), leading to the same overall losses for the $2\hbar k$ momentum-transfer process independent of what proportion of their falling time the atoms spend in the $|F = 2, m_F = 1\rangle$ or $|F = 2, m_F = 0\rangle$ states. It is not feasible at present to further investigate this issue numerically as the system would need to be simulated in at least two dimensions when including the $|F = 2, m_F = 1\rangle$ state, for reasons discussed in Section 4.5.5.

The second detail of the experiment that is not fully understood is the difference between the optimum efficiency determined theoretically, 6.7%, and that observed in the experiment, $(35 \pm 10)\%$. It is unusual for theory to predict a lower efficiency than is observed experimentally. More frequently theory predicts a larger effect or efficiency than is observed experimentally (an exception being initial attempts at Doppler cooling) due to the experiment differing from the idealised scenario considered theoretically. It seems unlikely that the difference in this instance could be due to the absence of the $|F = 2, m_F = 1\rangle$ level as the spatial dynamics of the model should be simpler than those if the level were included, leading to a higher efficiency for the present model. Instead the difference in efficiency suggests that there are lower losses in the experiment due to an effect that has not been considered theoretically. The most likely approximation that could be the cause of the discrepancy is the assumption that if an atom undergoes spontaneous emission it will not interact further with the system and will therefore not undergo a stimulated transition into the lasing condensate. This discrepancy is investigated further in Section 4.5.6 in the context of a second pumping experiment that was performed in the pulsed regime to investigate the temporal dynamics of the pumping mechanism.

4.5.5 An aside on 5-level atom lasers

It is known that 5-level atom lasers (formed when outcoupling from a trapped $|F = 2, m_F = 2\rangle$ condensate) lead to complicated spatial dynamics [199], however while

their short-time dynamics can be reasonably approximated by a one-dimensional model that only includes spatial structure in the direction of gravity, complex spatial structures develop in transverse dimensions over longer time scales. The characteristic length scales of these structures in the tight trapping dimension perpendicular to gravity are significantly smaller than the condensate size in that dimension. As such spatial structures cannot be accurately represented by a one-dimensional model, the results of the model for longer times cannot be considered an accurate representation of the full system except to say that the dynamics are 'complicated'. Higher-dimensional models are necessary to resolve these structures.

An illustration of the significant higher-dimensional spatial structures is given in Figure 4.16. This figure presents the results of a two-dimensional model of the outcoupling of a 5-level atom laser in the weak outcoupling limit. The horizontal direction is the second tight trapping direction, the weak trapping dimension has been eliminated in this model using standard dimension-reduction techniques. For short times, before the trapped state $|F = 2, m_F = 1\rangle$ has undergone half an oscillation in its trap ($t < 3.8\,\text{ms}$ for a tight trapping frequency of $\omega_r = 2\pi \times 130\,\text{Hz}$), the system is reasonably uniform in the horizontal direction (see the top row of Figure 4.16), and would be well-approximated by a one-dimensional model. After the $|F = 2, m_F = 1\rangle$ state has undergone half an oscillation in its trap, a density spike forms at the classical turning point [see Figure 4.16(c)]. A similar density spike would appear in a one-dimensional model, however the two-dimensional density that this spike represents would be significantly lower than that observed in the two-dimensional model as the one-dimensional model assumes that the density is approximately constant over $\sim 6\,\mu\text{m}$ in the y direction, which is clearly false. It would be reasonable to presume that a two-dimensional model would lose accuracy once atoms in the $|F = 2, m_F = 1\rangle$ state have undergone half an oscillation in the weak trapping dimension leading to complex spatial structures in the weak trapping dimension. For a weak trapping frequency of $\omega_z = 2\pi \times 13\,\text{Hz}$, the $|F = 2, m_F = 1\rangle$ atoms will take $t = 38\,\text{ms}$ to undergo half an oscillation.

The difference between the spatial structures described by one- and two-dimensional models of 5-level atom laser outcoupling would have a significant affect on a pumping model. The density spike in the $|F = 2, m_F = 1\rangle$ state near the classical turning point would result in a significant reduction in the pumping light intensity and a corresponding loss of atoms from the $|F = 2, m_F = 1\rangle$ state negatively impacting achievable pumping

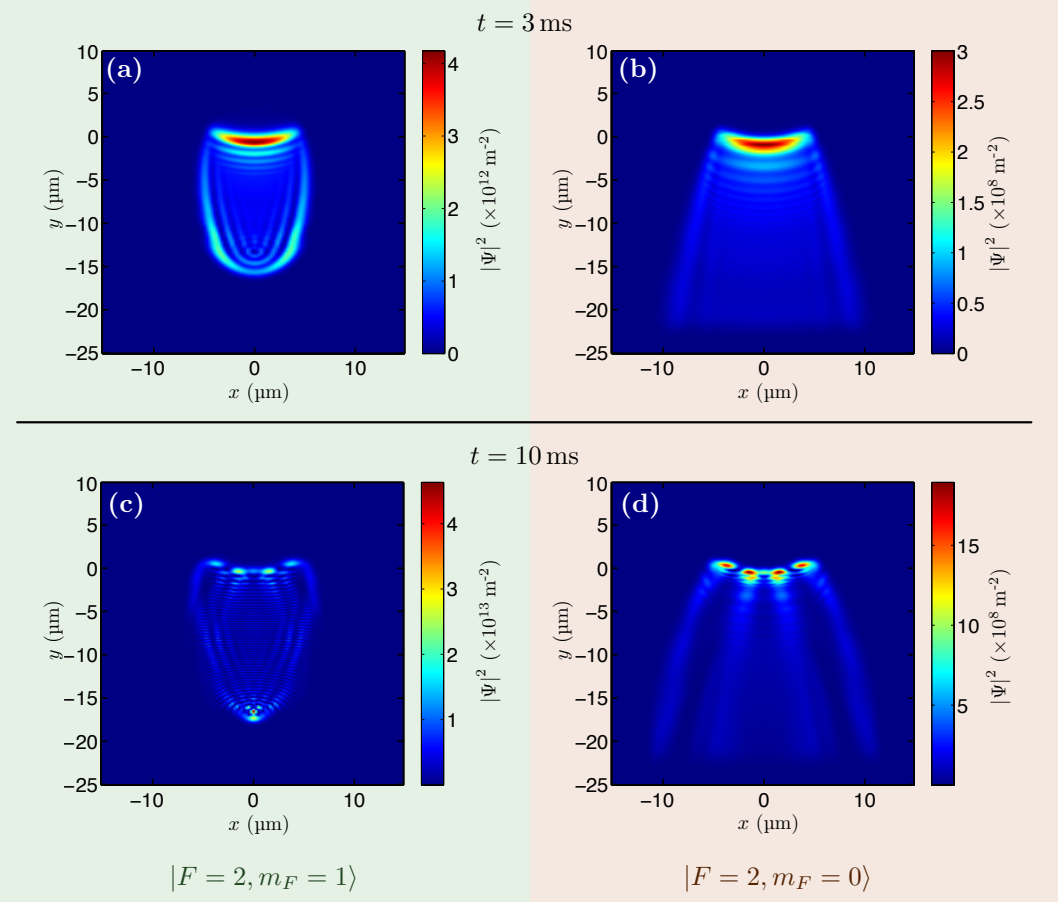

Figure 4.16: Simulation results of a 5-level atom laser in the weak outcoupling limit. The top row illustrates the early time behaviour at $t = 3\,\mathrm{ms}$, the bottom row illustrates the complex spatial structures formed at later times $t = 10\,\mathrm{ms}$. The left column is of the density of the trapped $|F = 2, m_F = 1\rangle$ state, and the right column is the density of the untrapped $|F = 2, m_F = 0\rangle$ state. Note the use of absorbing boundary layers (refer to Section 2.7.1) at the bottom of the images in the right column.

efficiencies. In a one-dimensional model, it will have been assumed that all of the incident pumping light over the characteristic length scale in that dimension of $x = 5.9\,\mu\text{m}$ will interact with the density spike, leading to higher losses than in a two-dimensional model in which the density spike will have its correct size in this dimension of $\sim 1\,\mu\text{m}$. It is for these reasons that a model of the continuous pumping experiment including all 5 levels of the $F = 2$ manifold must be solved in at least two dimensions given that the experiment operates on the timescale of many oscillation periods in the tight trapping dimensions. It may be necessary to solve the full three-dimensional system as the duration of the pumping experiment (100 ms–200 ms) is longer than a single oscillation period in the weak trapping dimension, 76 ms.

It would be computationally intensive, although achievable, to solve a two- or three-dimensional model of the continuous pumping experiment including the full $F = 2$ manifold over the pumping time of 100 ms–200 ms once or twice, it is not however feasible to consider performing a parameter scan similar to that in Section 4.5.4 in which hundreds or thousands of runs of the simulation would be necessary. Although such a system cannot yet be investigated numerically, the problems posed by the 5-level nature of the atom laser outcoupling is not fundamental to the pumping process itself. These are technical issues that relate to the transport of atoms to the lasing condensate, not fundamental issues affecting the pumping process.

4.5.6 The pulsed pumping experiment

To further investigate the pumping mechanism of the continuous pumping experiment described in Section 4.3, a second experiment was performed in the pulsed domain to enable the temporal dynamics of the pumping mechanism to be probed. A summary is provided here of the pulsed pumping experiment performed by *Daniel Döring*, *Nick Robins*, *Matthew Jeppesen*, and *Cristina Figl* at the Department of Quantum Science, ANU. Further details of the experimental setup and results are published in [176]. The theoretical results presented here are also published in [176].

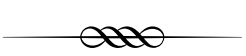

The experimental setup of the pulsed pumping experiment was very similar to that of the continuous pumping experiment. While in the continuous pumping experiment continuous outcoupling from the source condensate was used, in the pulsed pumping

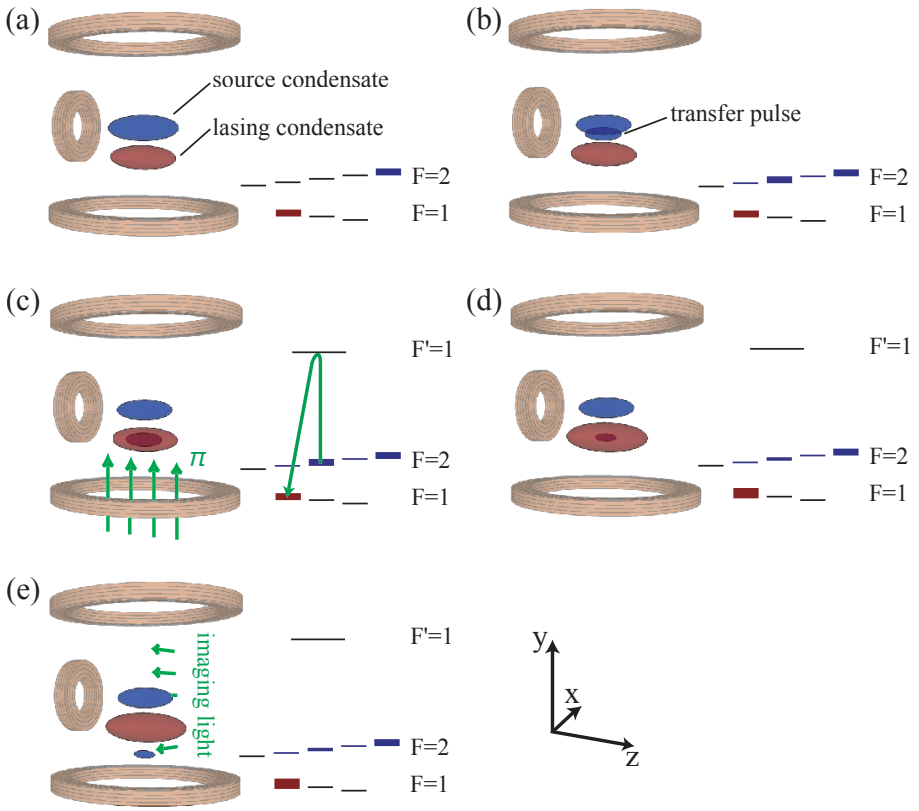

Figure 4.17: Sequential illustration of the pulsed pumping experiment. (a) The setup includes a source and a lasing condensate trapped in the same magnetic trap. (b) A pulse of atoms is outcoupled from the source cloud and is accelerated downward due to gravity. (c) As the atoms fall, a variable delay pulse of π-polarised light is applied. (e) The atoms in the transfer pulse continue to fall and are detected by absorption imaging.

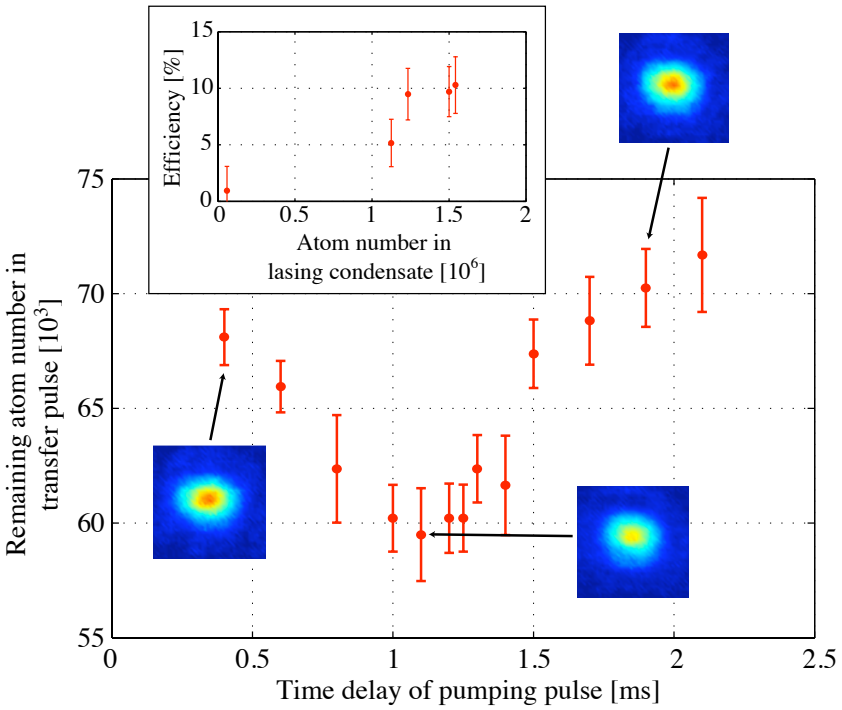

Figure 4.18: Remaining atom number in the transfer pulse as a function of the time delay of the pumping pulse. The absorption pictures show the remaining atoms in the transfer pulse after the pumping process. The inset depicts the efficiency of the pumping process as a function of the size of the lasing condensate.

experiment a short (40 µs) intense outcoupling pulse was applied. After outcoupling, the $|F = 2, m_F = 0\rangle$ pulse of atoms (the transfer pulse) then accelerated downward due to gravity and propagated through the $|F = 1, m_F = -1\rangle$ condensate. At a well-defined time during the travel of the transfer pulse, a pulse (150 µs) of π-polarised light was applied in the vertical direction opposite to the movement of the atoms as they fell under gravity.

The intensity of this pumping light was adjusted such that for the pulse length chosen, a loss of $\sim 20\%$ from the transfer pulse due to spontaneous emission was observed. Its intensity was approximately $30\,\mu\mathrm{W/cm^2}$. Thus there was a reasonable amount of interaction between the transfer pulse and the pumping light that could be significantly increased by Bose-stimulation in the presence of the lasing mode. The light was blue-detuned by two natural linewidths from the $F = 2 \rightarrow F' = 1$ transition. To investigate the pumping process the timing of the pumping light pulse applied to the system was varied. Figure 4.17 is a schematic of the pulsed pumping experiment.

Figure 4.18 displays the number of atoms left in the transfer pulse after the pumping when the time delay of the light pulse is varied. Changing the pulse delay clearly affects the atom number remaining in the transfer pulse. The data show a resonance centred at a

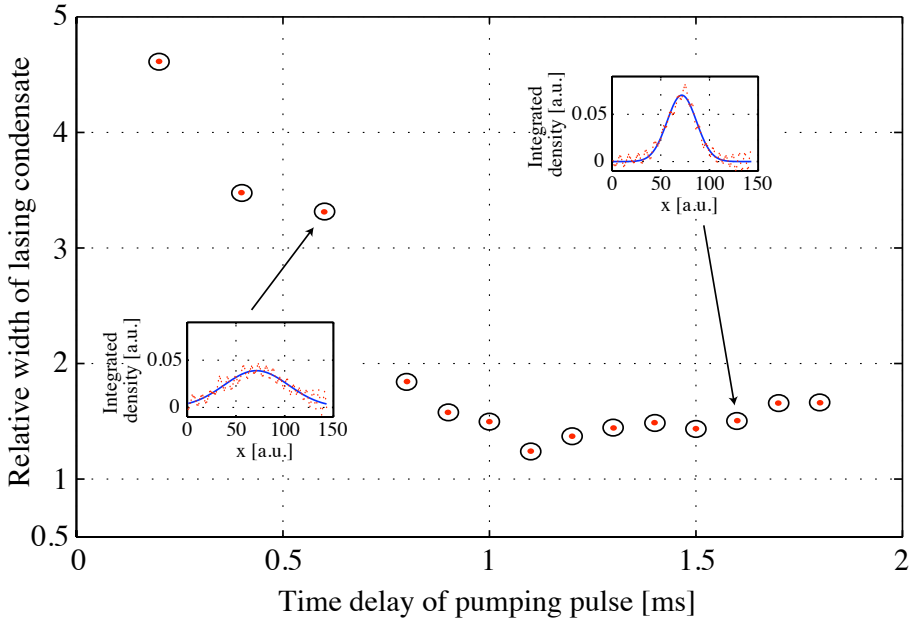

Figure 4.19: Width of the lasing condensate (normalised to the width with no pumping light applied) as a function of the time delay of the pumping pulse. The two insets show the integrated density profile of the (expanded) lasing condensate for two different time delays of the pumping pulse.

time 1.1 ms after the outcoupling pulse, suggesting an enhanced transfer of atoms into the lasing condensate. Figure 4.19 illustrates the heating of the $|F = 1, m_F = -1\rangle$ cloud as a function of the delay time, measured with a 100 µs long pumping light pulse. Again the curve reaches a minimum value with no significant heating at 1.1 ms. The heating does not increase for delay times above the centre of the resonance, which may be explained by the transfer pulse shielding the lasing condensate from the emitted resonant photons. The sets of data in Figures 4.18 and 4.19 indicate that the underlying process occurs predominantly at a pulse delay time of 1.1 ms, and the resonance data show that the $|F = 1, m_F = -1\rangle$ condensate mediates the process since without this condensate there is no additional loss from the pulse (see the inset of Figure 4.18).

The 1.1 ms resonance is consistent with the time a free-falling atom takes to travel the distance of 7.3 µm between the two condensate centres (1.2 ms). In this time, the atoms reach a velocity of 1.3 cm/s. This velocity is equal to that gained due to absorption and subsequent emission of a photon in the opposite direction, giving a $2\hbar k$ momentum kick. The 1.1 ms resonance therefore corresponds to the $2\hbar k$ momentum-transfer process. Operated in the pulsed regime, the $2\hbar k$ momentum-transfer process does not suffer from spontaneous loss from the transfer pulse (and subsequent heating of the lasing condensate) during transport as is the case in the continuous experiment. For shorter delay times for

which the $2\hbar k$ momentum-transfer process is not momentum-resonant, the spontaneously emitted photons from the transfer pulse are strongly scattered by the lasing condensate causing significant heating to that condensate. This behaviour is observed in Figure 4.19.

From the experimental data presented, three main conclusions can be drawn: (a) the $|F = 1, m_F = -1\rangle$ condensate significantly enhances transitions of atoms from the transfer pulse into the $|1, -1\rangle$ state. (b) These transitions primarily occur at a position in space that maximally overlaps with the lasing condensate. (c) This position allows the absorption of a pump beam photon and emission of a photon downward that exactly cancel the $2\hbar k$ momentum gained in falling to that position. The significantly lower heating of the lasing condensate near this resonance compared to shorter pump delays indicates that the photons emitted as a result of the pumping process do not significantly heat the lasing condensate despite propagating through it.

Theory

Due to the short duration of the pulsed pumping experiment ($t < 2\,\text{ms}$), the problems discussed in the previous section for applying a one-dimensional model to a 5-level atom laser do not apply. A natural extension of the model presented in Section 4.5.4 that was used for the continuous pumping experiment is used in this section for the pulsed experiment. We do not distract the reader by including the equations of motion explicitly; the relevant levels and atomic transitions included are illustrated in Figure 4.20.

The simulation results for the remaining atom number in the transfer pulse after the pumping process are given in Figure 4.21. The results are in approximate quantitative agreement with the experimental results in Figure 4.18. It is important to note that a reduction in the number of atoms in the transfer pulse does not necessarily correspond to an equivalent increase in the number of atoms in the lasing condensate; some atoms may instead have undergone spontaneous emission. This could not be probed directly in the experiment due to the difficulty in reliably measuring changes of $\sim 10^4$ atoms on a condensate of $\sim 10^6$ atoms. However, the notable absence of heating of the lasing condensate around 1.1 ms where the $2\hbar k$ momentum-transfer process is expected to occur suggests that relatively few of the atoms are likely to have undergone spontaneous emission. This is significant as simple estimates suggest that this should not be the case.

The heating of the lasing condensate in the two regimes (short delays and delays near the observed resonance at $t = 1.1\,\text{ms}$) can be compared by calculating the number

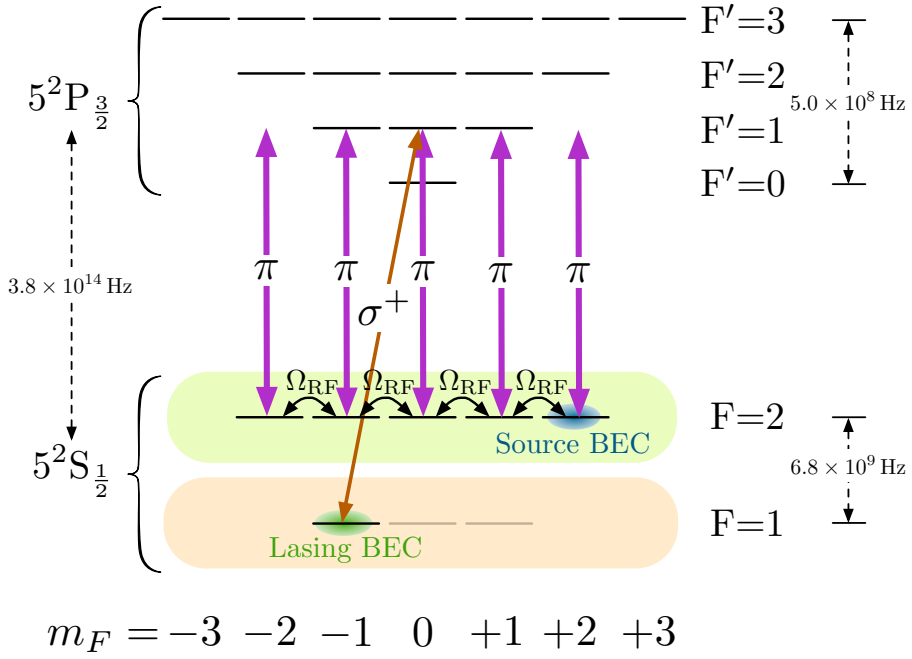

Figure 4.20: Level scheme for the pulsed pumping model. The only levels not included in the model of this system are the $|F = 1, m_F = 0\rangle$ and $|F = 1, m_F = 1\rangle$ levels, which are greyed out in the illustration. The contribution of all excited levels in the F' manifold have been included, however the levels themselves have been adiabatically eliminated.

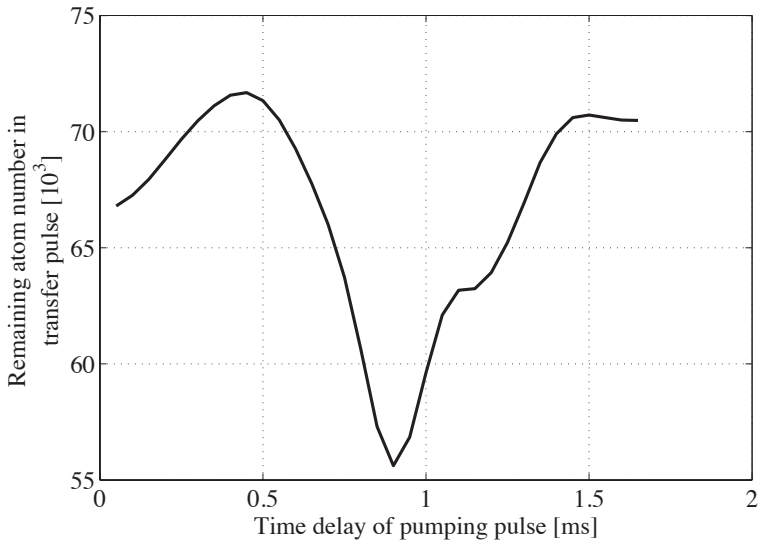

Figure 4.21: Theoretical results for the remaining atom number in the transfer pulse as a function of the time delay of the pumping pulse.

of photons that would be scattered by the lasing condensate. The number of photons scattered is determined by the number of photons incident on the lasing condensate and their transmission probability

$$N_{\text{scattered}} = N_{\text{incident}}(1 - p_{\text{transmission}}), \tag{4.90}$$

where the transmission probability is given by

$$p_{\text{transmission}} = \exp\left\{-\frac{\sigma_0}{A_\perp}\left[1 + \left(\frac{2\Delta}{\Gamma}\right)^2\right]^{-1} N_{\text{atoms}}\right\}, \tag{4.91}$$

where $\sigma_0 = 3\lambda^2/2\pi$ is the atomic scattering cross-section, and N_{atoms} is the number of atoms in the lasing condensate that the photons must propagate through.

For short delays, at most half of the photons scattered by the transfer pulse will be incident on the lasing condensate as half of the photons will propagate upwards, and some fraction of the photons propagating downwards will be incident on the lasing condensate. As there are initially 7.8×10^4 atoms in the transfer pulse, approximately 10^4 atoms are lost from the pulse after the pumping pulse is applied (see Figures 4.18 and 4.21). As the transfer pulse is not momentum-resonant with the lasing condensate for short delays, every atom lost from the transfer pulse will correspond to a photon scattered from the pumping pulse. At most, 5×10^3 of these photons are incident on the lasing condensate. However there are multiple states that an atom in the $|F' = 1, m_F = 0\rangle$ state can decay into. An atom in that state will decay into the $|F = 1, m_F = -1\rangle$ state 42% of the time and the emitted photon will be resonant with the lasing condensate. Approximately 2×10^3 resonant photons are then incident on the lasing condensate. The transmission probability through the entire condensate of 5×10^5 atoms is 0.07%, resulting in essentially all of the incident photons being scattered by the lasing condensate.

At the observed resonance of approximately 1.1 ms the transfer pulse will be in the middle of the lasing condensate. In this case, the transfer pulse is momentum-resonant with the lasing condensate and atoms in the $|F' = 1, m_F = 0\rangle$ state will be Bose-stimulated into decaying into the $|F = 1, m_F = -1\rangle$ lasing mode resulting in the emitted photon being resonant with the lasing condensate. Approximately 2×10^4 atoms are lost from the transfer pulse, which in the best case scenario are transferred to the lasing condensate generating 2×10^4 photons which are resonant with the lasing condensate. These photons must propagate through approximately half of the lasing condensate with a transmission

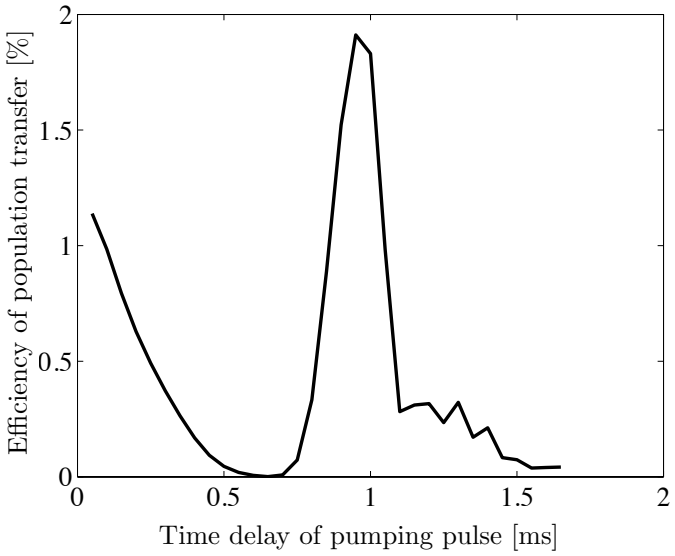

Figure 4.22: Theoretical results for the efficiency of the population transfer as a function of the time delay of the pumping pulse. Efficiency is defined as $\Delta N_{F=1,m_F=-1}/(-\Delta N_{F=2,m_F=0})$. The increase in efficiency for short delays corresponds to the $0\hbar k$ momentum-transfer process.

probability of 2.7%. Once again, almost all of the incident 2×10^4 photons will be scattered by the lasing condensate.

According to this simple calculation, more photons should be scattered by the lasing condensate when the transfer pulse is momentum-resonant with the lasing condensate than when it isn't, which would lead to correspondingly higher heating near the 1.1 ms resonance than for short delays. This is clearly in contradiction with the experiment (see Figure 4.19) which clearly shows *lower* heating near the 1.1 ms heating than for short delays. The prediction from the simple model is the same if instead it is assumed that the atoms lost from the transfer pulse initially undergo spontaneous emission instead of stimulated emission at the 1.1 ms resonance. The simulation results for the efficiency of the pumping process (Figure 4.22) are in good agreement with these simple calculations showing a maximum transfer efficiency of atoms lost from the transfer pulse of slightly less than 2%.

As the multimode simulations are in agreement with the simple calculations above, the reduction of heating cannot be explained by the existence of a dark state with the optical pumping light. This is expected as the emitted photons must propagate through a region of the lasing condensate that the transfer pulse has not reached (the part below the transfer pulse). In this region, the dark state of the system has all photons in the E_π mode. Neither can the reduction of heating be explained by collisional heating from the falling

atoms. Although each falling atom will at most have 1.4 times the chemical potential of the lasing condensate in kinetic energy, the atom number in the transfer pulse is only 20% of the number in the lasing condensate.

One possible explanation for the observed reduction in spontaneous heating is a quantum-mechanical destructive interference between two heating processes. This possibility has been shown theoretically to lead to a suppression of spontaneous heating in the boson-accumulation regime (BAR) [186, 195]. The pulsed pumping experiment is deep into the BAR, which requires that an excited atom is more likely to be stimulated to decay into the condensate mode than to emit a photon in a random direction. For the parameters of the pulsed pumping experiment, this branching ratio can be estimated as $\eta \approx 100$. The boson-accumulation regime is discussed further in the following section.

While there is good agreement between theory and experiment for the transfer of atoms *out* of the transfer pulse, the experiment yielded no direct information about the transfer of atoms *into* the condensate. For this question, we can only rely on the theory and the indirect evidence provided by the heating measurements. In this case, the theory suggests that there should be a significant number of photons scattered by the lasing condensate. This scattering should lead to observable heating of the lasing condensate. The fact that it doesn't suggests that one of the approximations made in the derivation of the theoretical model may not apply. This issue is discussed further in the following section.

4.6 The contribution of reabsorption

The agreement of theoretical results with the results of the continuous and pulsed pumping experiments is only partial. In both cases, the theoretically predicted efficiency has been *lower* than that measured or inferred experimentally. The differences between the theoretical and experimental results for the pulsed pumping experiment are suggestive that scattering of resonant photons is occurring at a lower rate than would otherwise be expected. Spontaneous emission is a well-understood phenomenon, good reason is needed before questioning its validity. The primary difference between the pumping experiments and the usual context in which spontaneous emission is examined is that the ground state of the decaying atoms is a highly-correlated Bose gas. In the derivation of the spontaneous emission term, it was assumed that if an atom decays into a mode that isn't the condensate

mode, neither the atom nor the photon will have any further interaction with the system. This approximation neglects the subsequent scattering of photons by these atoms, which may either result in further heating, or the scattered atom returning to the condensate mode. In the presence of a condensate, multiple scattering can be significant because, as shown in the previous section, the probability of a resonant photon propagating through a condensate without being absorbed is negligible in the absence of a dark state. Multiple scattering is not always a problem in the case of a $0\hbar k$ momentum-transfer process as the resonant photons are generated at the edge of the condensate and propagate *away* from the condensate; the absorption probability for these photons can be negligible. For the case of $2\hbar k$ momentum-transfer processes (such as that occurring in the pulsed pumping experiment), the problem of multiple scattering is significant and another theoretical framework must be used.

It was assumed in the derivation of the multimode pumping model in Section 4.5.1 that multiple scattering of photons would only lead to heating of the condensate. Neglecting this process would therefore make the model describe the best-case scenario for the pumping process and the pumping efficiencies determined from the model would be an upper-bound for that achievable experimentally. Cirac and Lewenstein have studied spontaneous emission in the presence of a condensate without neglecting multiple scattering [186] and have shown that spontaneous emission can be suppressed in the so-called 'boson-accumulation regime' (BAR) in which an excited atom is significantly more likely to be stimulated to decay into the condensate mode than to emit a photon in a random direction. This suppression results from the destructive interference of two processes that would otherwise result in the heating of the condensate. These two processes are illustrated in Figure 4.23(a) and (b). Figure 4.23(a) depicts the direct process in which an atom in the internal excited state $|e\rangle$ decays directly into the k^{th} single-particle mode of the atomic ground state; Figure 4.23(b) depicts the process in which an atom in the excited state decays into the k^{th} ground state mode with an atom in the condensate mode $|0\rangle$ absorbing the emitted photon before decaying back into the condensate mode. As these two processes have the same initial and final states, their amplitudes will interfere. In [186] it was shown that this interference is destructive. In the model derived in Section 4.5.1, only process (a) is included leading to a higher spontaneous loss (and heating rate) in the BAR than if reabsorption is included. In addition to the destructive interference between processes (a) and (b), reabsorption gives rise to the process illustrated in Figure 4.23(c) in which an excited atom decays into the

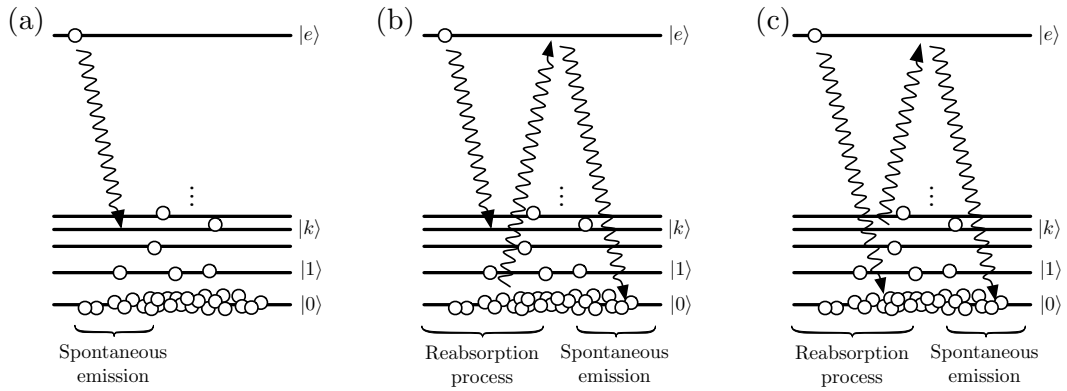

Figure 4.23: (a) Process in which the excited atom decays directly into the k^{th} mode of the atomic ground state. (b) Process in which the excited atom decays into the k^{th} level, the emitted photon is absorbed by an atom in the condensate mode and it subsequently decays back into the condensate mode. (c) Process in which the excited atom decays into the condensate mode, the emitted photon is absorbed by an atom in the k^{th} level and it decays into the condensate mode.

condensate mode and an atom in the k^{th} ground state mode absorbs the emitted photon before decaying into the condensate mode. In this process, two atoms are added to the condensate mode as a result of the decay of a single excited atom.

The work of Cirac and Lewenstein [186] (and the later work by Floegel *et al.* [195]) cannot be directly applied to either of the pumping experiments as several assumptions were made that do not hold. For example, it is assumed that the system is supplied with a source of atoms in the excited internal state while in the experiments the excited state is optically coupled to a source mode. As shown in Section 4.4, Bose-enhancement of the decay of the excited state can then lead to an overall reduction in the rate of the pumping process. Cirac and Lewenstein also make the simplifying assumption that there are only two relevant internal atomic states in the system, while in the experiment atoms in the excited $|F' = 1, m_F = 0\rangle$ state may decay to several levels, only one of which will yield a photon resonant with the lasing condensate. While the models of [186, 195] may not be directly applied to the experiments, they suggest that it is worthwhile pursuing more detailed models of the experiments that include the effect of reabsorption. Such models will include the counter-intuitive suppression of spontaneous emission due to the interference of the processes illustrated in Figure 4.23(a) and (b).

It is important to note that suppression of spontaneous emission predicted to occur in the BAR cannot be observed in experiments studying the spontaneous emission of condensates by illuminating them with resonant light. Due to the strong resonant absorption of condensates the incident photons cannot propagate into the centre of the condensate in

which the BAR will hold. The scattering will only occur within a small region near the condensate edge. By contrast, in the pumping experiments described in this chapter resonant photons are emitted near the centre of the lasing condensate (in the case of the $2\hbar k$ momentum-transfer process).

4.7 Conclusion

There are three parts to the optical pumping process underlying the pumping experiments discussed in this chapter:

(i) the delivery of atoms in an appropriate mode to the lasing condensate;

(ii) the transfer of those atoms into the lasing condensate; and

(iii) the propagation of the emitted photons within the lasing condensate.

This chapter has aimed to understand part (ii) of this process. Ideally we would also like to understand (iii) as it appears that there is some very interesting physics occurring there (at least for the $2\hbar k$ momentum-transfer process), however there is strong experimental evidence that physics beyond the mean-field are significant in this part of the process and more detailed theoretical modelling will be necessary to accurately describe this part of the process. By contrast process (i) is a detail determined by how one chooses to get the atoms to the lasing condensate with an appropriate mode. While it can be argued that this process is well understood in the context of the pulsed pumping experiment, significant approximations were used for the case of the continuous pumping experiment. While the details of the transfer of atoms into an appropriate source mode for the pumping mechanism are of course important, they are not of fundamental importance to the pumping mechanism.

One of the questions relevant to the continuous pumping experiment that we investigated theoretically was whether it was the $0\hbar k$ or $2\hbar k$ momentum-transfer process operating in the experiment. While theoretically we were unable to find a regime in which the $2\hbar k$ momentum-transfer process delivered efficient pumping, there is experimental evidence (see [176] for details) that the outcoupling position in the continuous pumping experiment was closer to the centre of the source condensate, not near the edge of the condensate as necessary for the operation of the $0\hbar k$ momentum-transfer process. As discussed in the previous section, it may be due to the neglect of the reabsorption process that the $2\hbar k$

momentum-transfer process was not found to operate efficiently. This does not discount the result that the $0\hbar k$ momentum-transfer process *can* operate. As the photons are emitted at the edge of the condensate and propagate away reabsorption does not significantly affect this process. It is somewhat surprising that there is a regime in which a resonant optical pumping process can be operated in which the resonant photons do not get the chance to interact significantly with the lasing condensate.

The question of whether it is the $0\hbar k$ or $2\hbar k$ momentum-transfer process operating in the continuous pumping experiment could also be resolved experimentally by detecting the photons emitted in the pumping process. This would be a difficult experiment as it would require separating the $\sim 2 \times 10^5$ $\not\pi$-polarised photons emitted over $\sim 100\,\text{ms}$ during the pumping process, from the $\sim 4 \times 10^6$ π-polarised pumping photons applied to the system over this time period.

The comparison of theoretical and experimental results suggests that physics beyond the mean field are significant in the $2\hbar k$ momentum-transfer process, which is certainly operating at least in the pulsed pumping experiment. Further investigation of the counter-intuitive possibility that reabsorption may decrease heating resulting from spontaneous emission is certainly warranted. The next step in this process would be to theoretically model and solve the full 3D atom–light system treating spontaneous emission and reabsorption fully. This will be a computationally intensive process and too prohibitive to apply to the continuous pumping experiment. However it could reasonably be applied to the pulsed pumping experiment where the optical degrees of freedom only need to be included during the short time for which the pumping light is applied. The fall of the atomic pulses under gravity may be treated separately using standard techniques.

The complication resulting from the reabsorption of resonant photons does not arise when the applied optical pumping light is significantly detuned. In this limit, it has been shown that in a simple atom laser model pumping efficiencies of about 50% are achievable. It is interesting to note that the relative propagation direction of the emitted light and atom laser can have a significant effect on the efficiency of the pumping process in the detuned limit. Although practical operation in this model was limited to the $0\hbar k$ momentum-transfer process, both processes may be feasible in a model closer to the continuous pumping experiment in which the effects of gravity are included. In such a model the atom laser will only be momentum-resonant with the lasing condensate for a short amount of time, reducing the possibility that multiple Rabi oscillations will limit the

efficiency (refer to Figure 4.12). This would be a straightforward extension of the present work.

Contrary to what has been expected previously [183, 185], this chapter has demonstrated that optical pumping of an atom laser is feasible without making the condensate so narrow as to make it essentially transparent in at least one dimension. The next step in the investigation of this pumping process must be the theoretical consideration of the potential positive contribution of reabsorption. When this is better understood, consideration can then be given to the integration of the pumping mechanism with a method for replacing the source condensates to produce a continuously pumped atom laser.

Chapter 5

Evaporation-induced pumping of an atom laser

The pumping process of an atom laser — just like that of an photon laser — is a necessarily irreversible process. This irreversibility enters through the coupling of the lasing mode to a much larger system (the reservoir). For the photon laser this is comprised of the (almost) empty modes of the optical field that the atoms decay into after emitting a photon into the lasing mode (see Section 1.1.4). In the case of the atom laser, there are two possible choices for the reservoir providing the irreversibility: empty modes of an optical field, or empty modes of an atomic field. The former case was considered in the previous chapter, the latter is the subject of this chapter.

The results and analysis presented in Section 5.4 of this chapter was my own work. The model presented in Section 5.3 is based on prior work [133, 134]. The derivation of the three-body loss term in Section C.3.3 and the code the results in this chapter are based on are the work of *Matthew Davis*.

5.1 Introduction

Continuous pumping of an atom laser is a key tool for producing superior atomic sources. Besides the obvious benefit of higher flux, it also promises improved modal stability [64, 203] and linewidth [48], much as it does for the photon laser.

There are two essential steps towards the continuous pumping of an atom laser. The first is a delivery system for filling an atomic reservoir with ultracold atoms. The second is a process that causes at least some of those atoms to make an irreversible, atom-stimulated

transition into the BEC.

Continuous delivery of ultracold atoms has been demonstrated in a number of experiments [112, 179–182, 204], and is an important component of thermal atomic interferometry experiments. The atom-stimulated transitions into the condensate can be made irreversible by coupling to a reservoir. In this chapter we consider the case in which the reservoir is comprised of empty modes of the atomic field accessible via evaporation.

Sequential reloading of a target BEC was achieved using optical tweezers [178], where a series of source condensates were added adiabatically by manipulating the trapping potentials, and excitations were subsequently removed by continuous evaporation. This milestone experiment maintained the condensate fraction, and therefore the flux of a potential atom laser. An atom laser produced from such an experiment would, however, not possess the desired narrow linewidth as the source condensates used were of a similar size to or larger than the condensate being replenished causing significant scattering into modes other than the target condensate. To produce an atom laser with a narrow linewidth it would be necessary for the atomic source to negligibly disrupt the target condensate. While this could be achieved by merging the target condensate with significantly smaller condensates more frequently, it is technically very challenging to develop high flux sources of Bose-condensed atoms compared to sources at higher temperature, which have a higher average flux. In this chapter it is shown that a similar experiment using an ultra-cold *thermal* source ought to be able to pump the target BEC and maintain a significant BEC population using a phase-preserving Bose-enhanced process.

5.2 Scheme

The proposed scheme for a pumped atom laser is illustrated in Figure 5.1 and is very similar to the processes used to evaporate a thermal cloud to condensation in a magnetic trap and produce a (quasi-continuous) atom laser. The additional element in this scheme is a process for replenishing the cloud of thermal atoms in the trap.

In this scheme the gain process for the condensate is the same Bose-enhanced scattering process between thermal atoms and the condensate that drives condensate growth when evaporating to produce BEC [133, 134, 205]. This process becomes irreversible when one of the scattered atoms has enough energy to cross the evaporation surface and be removed from the thermal cloud. The loss of atoms from the thermal cloud is balanced by a replenishment process that couples the thermal cloud to a source of atoms at finite

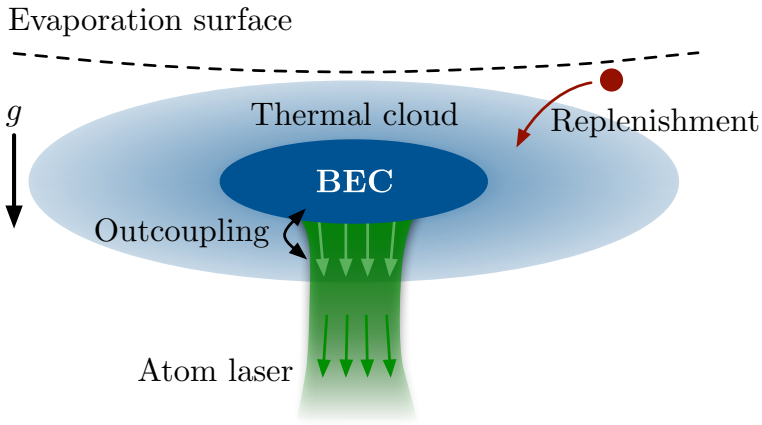

Figure 5.1: Schematic of the experimental setup.

temperature.

The atom laser beam itself is produced by outcoupling from the condensate. To minimise direct outcoupling from the thermal cloud, this outcoupling process should be a large momentum-transfer Raman process to limit the range of momenta of thermal particles that will be outcoupled. Outcoupling of thermal atoms can be reduced further by focussing the Raman lasers to only intersect in the immediate vicinity of the condensate.

A dynamic equilibrium will be reached when the rate of atom loss from the condensate due to outcoupling balances the rate of atoms gained due to scattering with the thermal cloud. If the evaporative surface is tuned so that atoms of energy ε_{cut} and higher are rapidly and continually removed from the trap, then all collisions that give atoms energy greater than ε_{cut} will become irreversible. As ε_{cut} is lowered, a larger fraction of the scattering processes that leave atoms in the condensate mode will become irreversible. This suggests that there must be some value of ε_{cut} for which the condensate experiences net gain. What is not clear is whether the net gain can proceed efficiently, i.e. on a timescale much shorter than other losses from the condensate. Lowering ε_{cut} also reduces the total number of thermal atoms present. In the limit that ε_{cut} reaches the condensate energy, there will be no background gas at all, and the condensate cannot experience net gain. We therefore expect that for a given set of parameters, there will be an optimal value for ε_{cut} that maximises the net gain, which may or may not be positive. In order to examine this issue, quantum kinetic theory (QKT) [133, 135–140] has been employed, which has been effective in describing the growth of condensates [133].

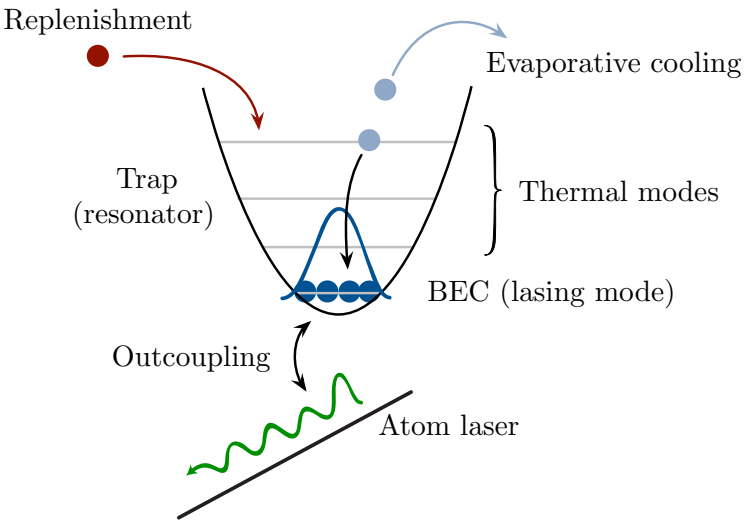

Figure 5.2: Schematic of the theoretical model.

5.3 Model

The theoretical model described in this section is an extension of the kinetic model of Bijlsma *et al.* [134], which was successfully used to study condensate growth in an experiment in which a cloud of thermal atoms just above condensation temperature were shock-cooled below transition [78]. After shock-cooling, the atoms were left to equilibrate, with condensate formation being driven by the same collisional processes that would drive condensate growth in the proposed pumped atom laser experiment described in the previous section. To fully describe this proposed experiment, the kinetic model of Bijlsma *et al.* must be modified to include the effects of the replenishment and outcoupling processes illustrated in Figure 5.1.

Another important process that must be included in the model is three-body recombination, which is the dominant loss process in typical BEC experiments [206, 207]. Without the inclusion of this process, for given replenishment and outcoupling rates, the largest condensate would be formed in the absence of evaporation as outcoupling from the condensate would be the only loss process in the system. In fact, this condensate number would be independent of the temperature of the replenishment source, depending only on the flux of atoms delivered to the system and the outcoupling rate from the condensate. This unphysical result is because in the absence of a density-dependent loss process, simply increasing the density is a feasible method of approaching degeneracy. It would be possible to reach condensation with room-temperature atoms in a harmonic trap simply by confining enough atoms! To avoid such unphysical results, the effect of three-body loss as the

dominant density-dependent loss process must be included in the model.

The starting point of the kinetic model presented here is to treat separately the thermal and condensed components of the system in Figure 5.1.

The condensed component is assumed to be a quantum fluid obeying a Gross-Pitaevskii-type equation, however we make a further approximation and assume that the condensate is sufficiently occupied that it has a Thomas-Fermi profile. The condensate dynamics are then fully described by the number of condensed atoms $N_0(t)$.

The thermal cloud is assumed to be well described within the Hartree-Fock approximation [20, Chapter 8] as comprised of particle-like excitations moving in the effective potential of the harmonic trap plus condensate mean field. To reduce the dimensionality of the full phase-space distribution function for the thermal cloud $f(\boldsymbol{r}, \boldsymbol{p}, t)$, it is assumed that the system is ergodic, i.e. that all points in the phase space having the same energy are equally probable. Under this approximation, the thermal cloud is then described by its energy distribution function $g(\varepsilon, t)$ and the density of states $\rho(\varepsilon, t)$. The assumption of ergodicity has been shown in the past to give good agreement with experiment when asymmetric spatial or momentum dynamics are not significant [133, 134]. Note that the time-dependence of the density of states $\rho(\varepsilon, t)$ comes from the contribution of the condensate mean field to the effective potential experienced by the thermal atoms.

As the model presented here is very similar to that presented in [134] with some additional terms, a derivation of the common terms is omitted. As a summary, the derivation proceeds by taking a semiclassical Boltzmann equation for the phase-space distribution function of the thermal cloud $f(\boldsymbol{r}, \boldsymbol{p}, t)$ including collisional terms and using the ergodic approximation to obtain an equation of motion for the energy distribution function $g(\varepsilon, t)$. This equation is self-consistently matched with a Gross-Pitaevskii equation for the condensate before making the Thomas-Fermi approximation to obtain an equation of motion for the number of condensed atoms $N_0(t)$. An example application of this method to derive the appropriate terms for three-body loss is given in Section C.3.3. Further, a detailed discussion of this theory is given in the review article [130].

Separating the contributions of the different processes involved, the equations of motion

for the model for a collision-driven pumped atom laser considered here are

$$\frac{dN_0}{dt} = \left.\frac{dN_0}{dt}\right|_{\text{thermal–condensate}} + \left.\frac{dN_0}{dt}\right|_{\text{3-body loss}} + \left.\frac{dN_0}{dt}\right|_{\text{outcoupling}}, \qquad \frac{\partial(\rho g)}{\partial t} = \left.\frac{\partial(\rho g)}{\partial t}\right|_{\text{thermal–thermal}} + \left.\frac{\partial(\rho g)}{\partial t}\right|_{\text{thermal–condensate}} + \left.\frac{\partial(\rho g)}{\partial t}\right|_{\text{3-body loss}} + \left.\frac{\partial(\rho g)}{\partial t}\right|_{\text{replenishment}} + \left.\frac{\partial(\rho g)}{\partial t}\right|_{\text{redistribution}}, \tag{5.1}$$

where the subscripts 'thermal–thermal' and 'thermal–condensate' denote Bose-enhanced collisional processes between atoms in the corresponding states [Figure 5.3(a) and (b), respectively], the subscript '3-body loss' indicates the contribution due to three-body recombination [Figure 5.3(f)], the subscript 'replenishment' indicates the contribution due to the replenishment of the thermal cloud [Figure 5.3(d)], the subscript 'outcoupling' indicates the contribution due to outcoupling from the condensate to form the atom laser [Figure 5.3(e)], and the subscript 'redistribution' indicates the contribution due to the redistribution of population in energy space due to the changes of the energies of the occupied levels as the mean-field of the condensate changes [Figure 5.3(c)]. It is assumed that atoms with energy greater than the evaporative energy cut-off ε_{cut} are removed from the system sufficiently quickly that $g(\varepsilon > \varepsilon_{\text{cut}}) = 0$.

The forms of the 'thermal–thermal', 'thermal–condensate' and 'redistribution' terms in (5.1) are given in Section C.3.2 and derivations are given in [134].

The outcoupling process from the condensate is modelled as a simple linear loss process with corresponding rate constant γ,

$$\left.\frac{dN_0}{dt}\right|_{\text{outcoupling}} = -\gamma N_0. \tag{5.2}$$

In modelling the outcoupling in this way, any outcoupling from thermal modes has been neglected. As discussed in Section 5.2, this is a reasonable approximation if focused Raman lasers are used for the outcoupling which only intersect in the immediate vicinity of the condensate.

The thermal cloud is modelled as being continuously replenished from a source that provides a constant flux Φ of atoms at a temperature T. To avoid tying the model to any

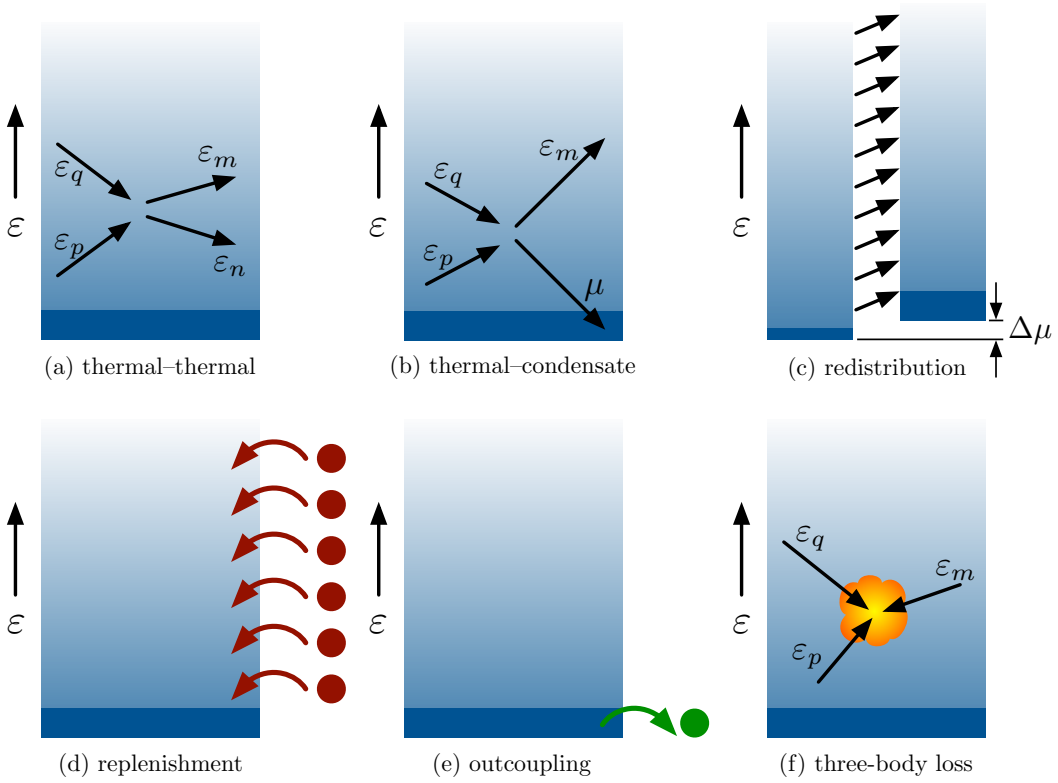

Figure 5.3: Schematic of processes involved in the evolution of the kinetic model described by (5.1). The upper shaded rectangle in each subfigure represents the energy distribution function $g(\varepsilon, t)$ of the thermal cloud, and the bottom dark blue rectangle represents the condensate with occupancy $N_0(t)$ and energy $\varepsilon = \mu(t)$. Figures (a) and (b) represent collisional processes involving two thermal atoms and one thermal and one condensate atom respectively. Figure (c) represents the change in the energy distribution function $g(\varepsilon, t)$ if the condensate occupation (and hence chemical potential) changes, changing the energies of every energy level. Figure (d) represents the replenishment of the thermal cloud from an atomic reservoir, Figure (e) represents outcoupling from the condensate mode to produce the atom laser, and Figure (f) represents the loss of atoms due to three-body recombination.

particular replenishment mechanism, we assume a best-case scenario in which each energy level ε in the source is coupled directly to the level in the thermal cloud with the same energy above the condensate chemical potential $\mu(t)$, i.e. the lowest energy level of the source ($\varepsilon = 0$) is coupled directly to the lowest energy level in the trap ($\varepsilon = \mu(t)$). This simple model gives the form of the contribution due to replenishment as

$$\left.\frac{\partial\big(\rho(\varepsilon,t)g(\varepsilon,t)\big)}{\partial t}\right|_{\text{replenishment}} = \Gamma\rho_0(\varepsilon-\mu(t))g_T(\varepsilon-\mu(t)), \tag{5.3}$$

where $\rho_0(\varepsilon)$ is the density of states in the absence of a condensate, $g_T(\varepsilon)$ is the Bose-Einstein distribution at temperature T, and Γ is a rate constant such that

$$\Gamma\int_0^\infty \rho_0(\varepsilon)g_T(\varepsilon)\,d\varepsilon = \Phi, \tag{5.4}$$

where Φ is the flux of atoms from the source *before* evaporation. The derivation of the contributions to (5.1) due to three body loss were performed by *Matthew Davis*, and are given in Section C.3.3.

We summarise here the approximations made in obtaining the kinetic model (5.1):

(i) The energy scale of the thermal cloud is large enough that all excitations are particle-like and not collective excitations such as phonons. Phonon-like excitations are only important for particle energies $\varepsilon \lesssim 2\mu(t)$ [20, §8.3.1]. Hence, we require that the energy scale for the thermal cloud ε_{cut} be much larger than $\mu(t)$.

(ii) The phase-space distribution of the thermal cloud is ergodic and hence is purely a function of energy. This assumption is true at equilibrium, however it needs some justification when used in non-equilibrium scenarios. In this case, asymmetric behaviour of the condensate is not expected in either position or momentum space

(iii) The condensate density is sufficiently large that it is well-described by a Thomas-Fermi profile. This approximation is justified as it is only the large-condensate limit that is of interest as a large condensate will be necessary for the production of a high-flux atom laser in this scheme. In making this approximation, the effects of both the normal and anomalous densities of the thermal cloud on the condensate have also been neglected.

(iv) Evaporation occurs on a time-scale faster than collisions. This is the usual requirement during evaporation to condensation, and so should be satisfied in the proposed experiment.

The computer code used to solve the kinetic model (5.1) was written by *Matthew Davis*. This code is a modified version of that used in [133], which has shown good agreement with an independently created code by Bijlsma *et al.* [134]. The results and analysis presented in the remainder of this chapter are my own work.

5.4 Simulation results

For a given trap geometry, the model is fully defined by the flux of replenishment atoms Φ, the temperature T of those atoms, the energy of the evaporative cut $\varepsilon_{\rm cut}$, and the outcoupling rate from the condensate γ. In this section the results of the kinetic model for some 'typical' parameter values are presented, and the dependence of the model on each of the parameters is examined.

Our numerical simulations are based on a trap and conditions similar to that of [208], who precooled a cloud of ^{87}Rb atoms to an initial temperature slightly greater than the critical temperature before performing evaporative cooling to study condensate growth. The trap in the experiment was axially-symmetric with radial and axial trapping frequencies of $\omega_r = 2\pi \times 110\,\text{Hz}$ and $\omega_z = 2\pi \times 14\,\text{Hz}$ respectively.

To numerically solve the kinetic model, (5.1) is discretised along the energy dimension and the resulting coupled differential equations are solved with an adaptive fourth-fifth Runge-Kutta [209] method. Our results are mainly concerned with the steady-state of the kinetic model, which we define as being reached when the condensate number has changed by less than either 0.1% or 1 atom in 100 ms. The initial state for the simulation is chosen to be a truncated Bose-Einstein distribution containing (before truncation) $N_{\rm initial} = 4.2 \times 10^6$ atoms at the same temperature as the replenishment reservoir. This state is chosen as a representation of the steady-state of the system prior to evaporation. In the trap considered, the critical temperature for 4.2×10^6 atoms is $T_c = 400\,\text{nK}$.

5.4.1 Typical dynamics and parameter studies

As a depiction of the 'typical' time-dependence of the results obtained from the kinetic theory model (5.1), we consider the case of pumping the system continuously with a source

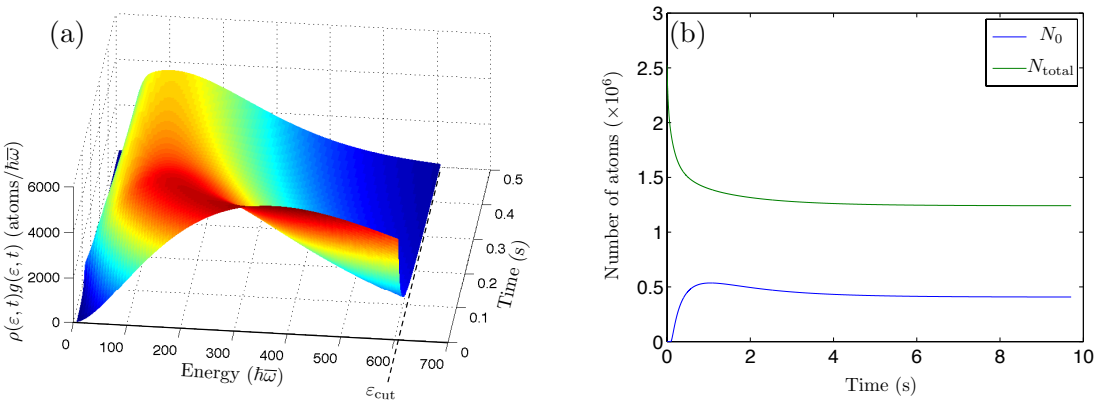

Figure 5.4: Results of the kinetic model for $\Phi = 8.4 \times 10^5$ atoms/s, $T = 540\,\text{nK}$, $\varepsilon_{\rm cut} = 3k_BT \approx 610\hbar\overline{\omega}$, and $\gamma = 0.3\,\text{s}^{-1}$. Figure (a) highlights the dynamics of the occupation of the thermal energy levels for $t < 0.5\,\text{s}$, while (b) illustrates the equilibration of the total and condensed atom numbers over $\sim 10\,\text{s}$. The energy distribution at $t = 0$ is a truncated Bose-Einstein distribution containing (before truncation) $N = 4.2 \times 10^6$ atoms at $T = 540\,\text{nK}$.

such that the initial number $N = 4.2 \times 10^6$ is transferred to the system once every 5 seconds giving a flux of $\Phi = 8.4 \times 10^5$ atoms/s. The temperature of the replenishment source is chosen to be $T = 540\,\text{nK}$, 60% above the condensation temperature of the system before evaporation. For the remaining model parameters, we choose the evaporative cut-off to be $\varepsilon_{\rm cut} = 3k_BT$, and the outcoupling rate from the condensate to be $\gamma = 0.3\,\text{s}^{-1}$.

Figure 5.4 illustrates the results of the simulation of this system. Figure 5.4(a) shows the energy distribution of the thermal cloud cooling from the initial truncated Bose-Einstein distribution to a distribution with a lower average energy per particle. Figure 5.4(b) demonstrates that despite pumping the system with an atomic reservoir above critical temperature that it is possible to reach a steady-state in which the condensate is macroscopically occupied. In this example, the steady-state condensate fraction is 33%.

The details of the equilibration of the system are not the subject of investigation here, instead our interest is in the equilibrium itself, and in determining the feasibility of creating a pumped atom laser driven by a non-condensed atomic source. As a first step towards this investigation we consider the dependence of the equilibrium condensate number on the parameters of the system: Φ, T, $\varepsilon_{\rm cut}$, and γ. The results of such a parameter study are presented in Figure 5.5 in which the dependence on these parameters of the steady-state of the results of Figure 5.4 is investigated.

The majority of the parameter dependences depicted in Figure 5.5 are trivial; increasing the relevant parameter causes a monotonic change in the equilibrium condensate number. Increasing the flux of atoms to the system increases the equilibrium condensate number

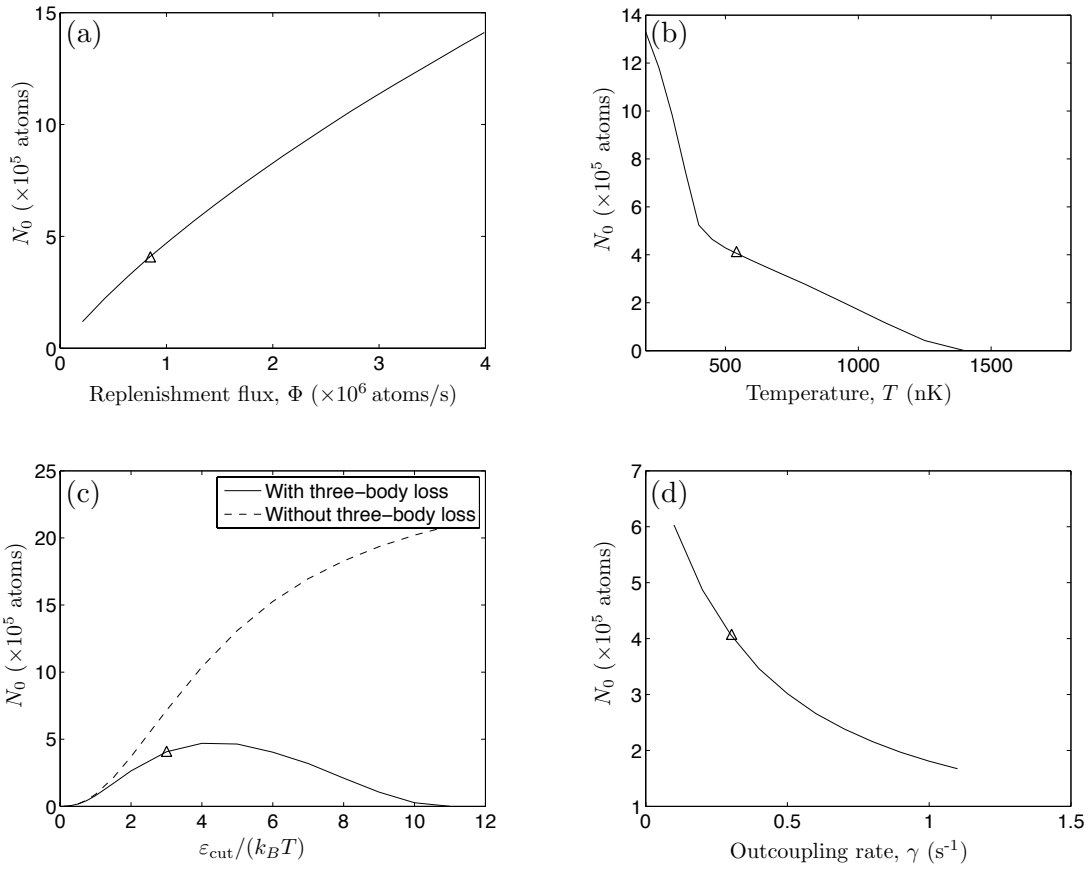

Figure 5.5: The dependence of the equilibrium condensate number N_0 on the parameters of the quantum kinetic model (5.1). The equilibrium condensate number has a monotonic dependence on the replenishment flux (a), the temperature of the replenishment source (b) and the outcoupling rate (d). For a given choice of the remaining parameters of the model there is an optimum $\varepsilon_{\rm cut}$ (c) for which the equilibrium condensate number is a maximum. For each parameter being varied, the remaining parameters are chosen to be the same as for the results depicted in Figure 5.4. The triangle in each plot marks the point that corresponds to the precise conditions of Figure 5.4.

[Figure 5.5(a)], while increasing the temperature of the replenishment source or increasing the outcoupling rate reduces the equilibrium condensate number [Figure 5.5(b) and Figure 5.5(d) respectively]. The sharp kink in Figure 5.5(b) occurs exactly at $T = T_c$ and is due to condensation of the source cloud. The only non-trivial behaviour is displayed by Figure 5.5(c) in which the dependence on the evaporative cut-off $\varepsilon_{\rm cut}$ is illustrated. For large evaporative cut-offs, few atoms will be lost due to evaporation and the system will reach equilibrium when the flux of atoms into the system is balanced by three-body losses and outcoupling from the condensate. As $\varepsilon_{\rm cut}$ is reduced, more atoms are lost due to evaporation and the mean energy per particle reduces, causing the condensate size to increase. As $\varepsilon_{\rm cut}$ continues to reduce, an increasing fraction of the replenishment atoms have an energy greater than $\varepsilon_{\rm cut}$, causing a lower effective atomic flux to be delivered to the system. This reduces the potential size of any condensate formed. These two competing effects are the origin of the existence of an optimum equilibrium condensate number as a function of $\varepsilon_{\rm cut}$ in Figure 5.5(c).

As discussed earlier, in the absence of three-body loss, the equilibrium condensate number would continue to increase as $\varepsilon_{\rm cut}$ is increased, which would lead to the unphysical conclusion that evaporating *reduces* the equilibrium condensate number. This is demonstrated by the dashed line in Figure 5.5(c) which asymptotes towards $N_0 = \Phi/\gamma = 2.8 \times 10^6$ atoms in the limit $\varepsilon_{\rm cut} \to \infty$. As observed in the remaining panels of Figure 5.5 (in which the effects of three-body loss have been included) three-body loss does not give rise to optimum values for the corresponding parameters of the model as it is only changes to $\varepsilon_{\rm cut}$ that affect the evaporative and three-body losses in contrary fashions. An increase in the replenishment flux will increase both evaporative and three-body losses. Similarly, changes to the temperature of the replenishment source or the outcoupling rate either increase both or decrease both of the evaporative and three-body losses.

At this point the fairly obvious recommendation could be made that to have the largest equilibrium condensate number one should use a replenishment source with the highest possible flux and the lowest possible temperature. It is an experimental reality, however, that these parameters are not orthogonal; while a 300 K oven might produce a significantly larger flux than a 50 mK 2D-MOT, it is simply not realistic to create a 50 mK atomic source with the same flux as the 300 K oven. It is this trade-off between the temperature and flux in the context of experimentally-realisable sources that is the subject of the remainder of the chapter.

5.4.2 Behaviour in the high-temperature limit

In the previous section, the dependence of the equilibrium condensate number on the model parameters was investigated. The physical question that we desire to address with this model is what are the requirements on the replenishment source to produce a pumped atom laser?

Although it would be possible to create a pumped atom laser by combining condensates in a manner similar to the experiment by Chikkatur *et al.* [178], such an atom laser would have significantly reduced phase-stability unless the replenishment process were essentially continuous. However, to replenish a condensate by collisional interactions with a continuous source of condensed atoms, the replenishment source would itself need to have many of the desired properties of a pumped atom laser! Instead, it is necessary to be able to use a source *above* condensation temperature for replenishment.

We consider now the experimentally-relevant limit of replenishing the thermal cloud using a high-flux source of thermal atoms. For such sources two simplifications are possible. First, for temperatures greater than T_c the Bose-Einstein energy distribution of the source $g_T(\varepsilon)$ is well approximated by the Boltzmann distribution $g_T(\varepsilon) \approx \zeta e^{-\beta\varepsilon}$ for some constant ζ, and $\beta = (k_B T)^{-1}$. Secondly, for high temperature sources the optimum evaporation cut-off $\varepsilon_{\rm cut}$ will be much smaller than the characteristic energy of the source $k_B T$, and hence $\varepsilon_{\rm cut} \ll k_B T$. From these simplifications it can be seen that the energy distribution below the evaporation cut-off is well described by the single parameter ζ as $g_T(\varepsilon \leq \varepsilon_{\rm cut}) \approx \zeta$.

At this point, no overall simplification has occurred as we have simply rewritten the temperature dependence of the replenishment source in terms of the parameter ζ. However, as the energy distribution of the replenishment source only affects the kinetic model through (5.3), its influence on the system dynamics is only through the combined quantity $\kappa = \Gamma\zeta$. An expression for κ directly in terms of relevant experimental quantities can be obtained

using the definition (5.4),

$$\begin{aligned}\Phi &= \Gamma \int_0^\infty \rho_0(\varepsilon) g_T(\varepsilon)\, d\varepsilon \\ &= \Gamma \int_0^\infty \frac{\varepsilon^2}{2(\hbar\overline{\omega})^3} \zeta e^{-\beta\varepsilon}\, d\varepsilon \\ &= \Gamma\zeta \frac{1}{2(\hbar\overline{\omega})^3} \int_0^\infty \varepsilon^2 e^{-\beta\varepsilon}\, d\varepsilon \\ &= \left(\frac{k_B T}{\hbar\overline{\omega}}\right)^3 \Gamma\zeta \qquad (5.5)\end{aligned}$$

$$\kappa \equiv \Gamma\zeta = \Phi \left(\frac{\hbar\overline{\omega}}{k_B T}\right)^3 \qquad (5.6)$$

where $\overline{\omega} = (\omega_x \omega_y \omega_z)^{\frac{1}{3}}$ is the geometric mean of the trapping frequencies, and $\rho_0(\varepsilon) = \dfrac{\varepsilon^2}{2(\hbar\overline{\omega})^3}$ is the density of states in a harmonic trap in the absence of a condensate [20].

We term κ the *phase-space flux* of the source as it is directly related to the rate at which the phase-space density of the thermal source is delivered. For a trap of N thermal atoms at temperature T, the peak phase-space density ϖ is [20, Chapter 2]

$$\varpi = N \left(\frac{\hbar\overline{\omega}}{k_B T}\right)^3. \qquad (5.7)$$

If these N atoms are delivered over a time τ providing a flux $\Phi = N/\tau$ the peak phase-space flux is

$$\frac{\varpi}{\tau} = \frac{N}{\tau} \left(\frac{\hbar\overline{\omega}}{k_B T}\right)^3 = \Phi \left(\frac{\hbar\overline{\omega}}{k_B T}\right)^3 \equiv \kappa. \qquad (5.8)$$

The phase-space flux κ is a figure-of-merit for the thermal source. It quantifies the qualitative behaviour already known: for the same atomic flux Φ, a source with a lower temperature will result in a larger condensate [Figure 5.5(b)]; and for the same temperature, a source with a higher atomic flux will also result in a larger condensate [Figure 5.5(a)]. The phase-space flux also describes exactly how a trade-off between the flux and temperature of the replenishment source will affect the equilibrium condensate number. If two sources with different fluxes and temperatures have the same value of phase-space flux, then the equilibrium condensate number produced by the two sources will be the same (assuming the high-temperature limit applies to both sources). Our interest is in determining what values of κ are necessary to produce a pumped atom laser, and whether such values are achievable.

For the limit of high-temperature atomic sources, we have reduced the four variables $(\Phi, T, \varepsilon_{\rm cut}, \gamma)$ required to define the model (5.1) down to three $(\kappa, \varepsilon_{\rm cut}, \gamma)$. Of these three, our main interest is in the dependence of the system on the properties of the atomic source through κ. In contrast, the dependence of the equilibrium condensate number on the outcoupling rate γ is simple [see Figure 5.5(d)] and the results would not be expected to change qualitatively with γ. It is therefore appropriate to choose a representative value for the outcoupling rate (here $\gamma = 0.3\,\mathrm{s}^{-1}$) and focus on the remaining two quantities.

As discussed in the previous section, there is an optimal choice for the evaporative cut-off $\varepsilon_{\rm cut}$. Our interest here is in the best-case scenario: for a given thermal source, what is the largest condensate we can produce? To examine this question and to verify that κ does fully describe the properties of the thermal source in the appropriate limit we have performed a parameter scan of the model (5.1) for a range of fluxes $1.3 \times 10^5\,\mathrm{s}^{-1} < \Phi < 5 \times 10^{10}\,\mathrm{s}^{-1}$ and temperatures $2 \times 10^{-7}\,\mathrm{K} < T < 6 \times 10^{-4}\,\mathrm{K}$ of the atomic source, for each combination determining the optimum evaporative cut $\varepsilon_{\rm cut}$ to give the largest steady-state condensate number. The results of this parameter scan are displayed in Figure 5.6.

The results illustrated in Figure 5.6 are separated into three groups based on the ratio $\varepsilon_{\rm cut}/(k_B T)$. The first group marked by black circles have $\varepsilon_{\rm cut}/(k_B T) < 0.1$, and are the results for which the high-temperature limit can be considered to be a good approximation (satisfying the requirement $\varepsilon_{\rm cut} \ll k_B T$) and κ completely determines the properties of the replenishment source. For this group of results, any equilibrium property of the system should appear to be a single (not necessarily straight) line when plotted as a function of κ. The results in Figure 5.6 demonstrate that these results can be viewed as a single function of κ. The second group marked by red triangles have $0.1 \leq \varepsilon_{\rm cut}/(k_B T) < 0.5$, and can be considered to be the results for which the high-temperature limit is almost a good approximation. These results are reasonably close to the results of the first group, however there is a greater deviation for a given value of κ indicating that the results can be almost seen as purely a function of κ. All remaining results fall into the third group for which $\varepsilon_{\rm cut}/(k_B T) \geq 0.5$. It can be seen that these points correspond to a broad range of equilibria for a given value of κ indicating that the replenishment source cannot be described by κ alone.

The first two panels of Figure 5.6 both display the equilibrium condensate number as a function of the phase-space flux κ. Figure 5.6(a) uses a log-log scale to highlight the behaviour for small and large values of κ, while Figure 5.6(b) uses a linear-linear scale to

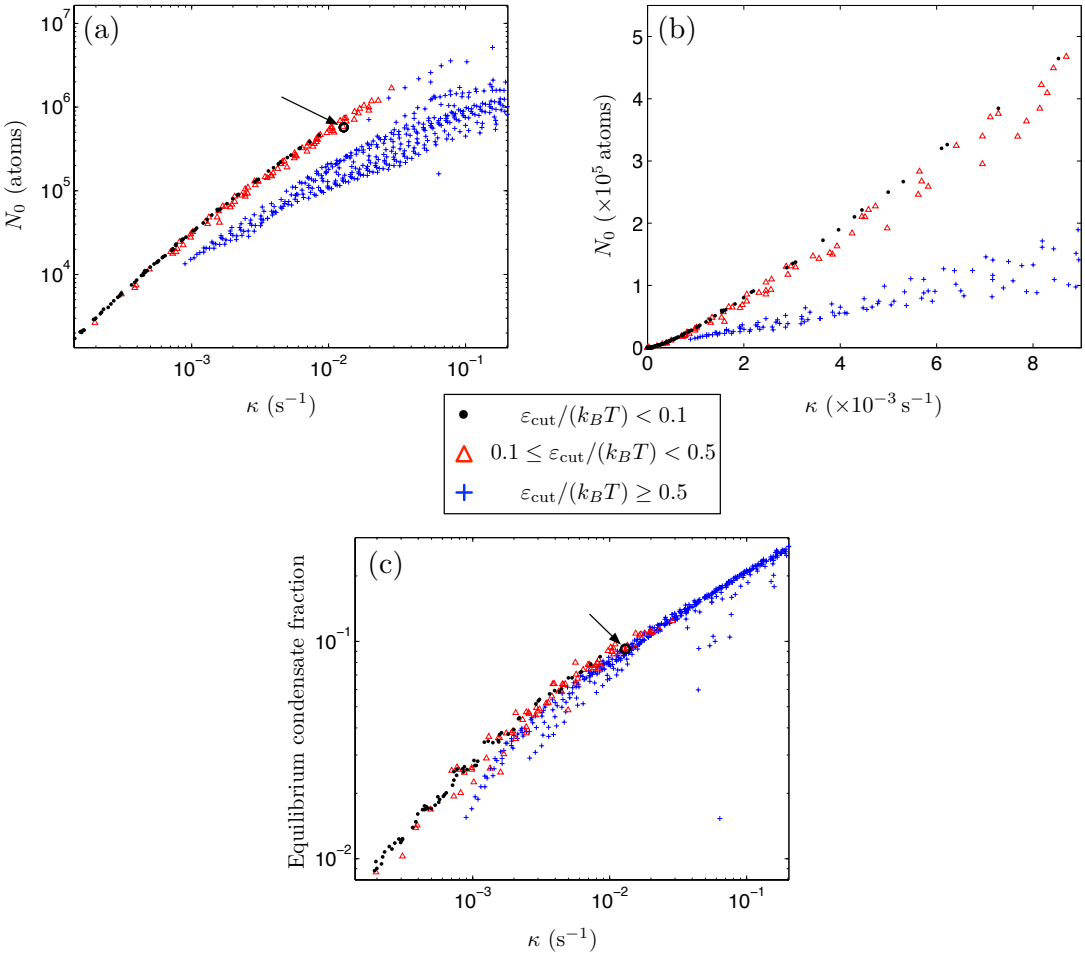

Figure 5.6: Plot of equilibrium condensate properties as a function of the phase-space flux for the replenishment source κ. Figures (a) and (b) plot the equilibrium condensate number on different scales. Figure (c) plots the equilibrium condensate fraction N_0/N. The results of the parameter scan are broken up into three groups (the black circles, red triangles and blue crosses) based on the extent to which the high-temperature limit discussed in this section applies to the results. The circled point with the arrow pointing to it corresponds to a simulation of the parameters for the last source in Table 5.1, which has $\kappa = 1.1 \times 10^{-2}\,\mathrm{s}^{-1}$ (see main text).

Atomic source	Atomic flux Φ	Temperature T	Phase-space flux κ	
BECs in dipole traps	$10^5\,\mathrm{s}^{-1}$ $(55\,\mathrm{mHz})^{ab}$	$< 1\,\mu\mathrm{K}$	$> 1.9 \times 10^{-3}\,\mathrm{s}^{-1}$	[178]
$2\mathrm{D}^+$-MOT	$9 \times 10^9\,\mathrm{s}^{-1}$	$38\,\mathrm{mK}^{cd}$	$3 \times 10^{-12}\,\mathrm{s}^{-1}$	[210]
$2\mathrm{D}^+$-MOT	$2 \times 10^{10}\,\mathrm{s}^{-1}$	$42\,\mathrm{mK}^{cd}$	$5 \times 10^{-12}\,\mathrm{s}^{-1}$	[211]
MM-MOT	$10^9\,\mathrm{s}^{-1}$	$61\,\mu\mathrm{K}^{c}$	$8 \times 10^{-5}\,\mathrm{s}^{-1}$	[212]
LVIS	$5 \times 10^9\,\mathrm{s}^{-1}$	$25\,\mathrm{mK}^{cd}$	$6 \times 10^{-12}\,\mathrm{s}^{-1}$	[213]
Zeeman slower	$3.2 \times 10^{12}\,\mathrm{s}^{-1}$	$32\,\mathrm{mK}^{cd}$	$2 \times 10^{-9}\,\mathrm{s}^{-1}$	[214]
Magnetic guide loaded from 3D-MOT	$7 \times 10^9\,\mathrm{s}^{-1}$	$400\,\mu\mathrm{K}^{c}$	$2 \times 10^{-6}\,\mathrm{s}^{-1}$	[180]
3D-MOT loaded from Zeeman slower	$2 \times 10^{10}\,\mathrm{s}^{-1}$ $(0.5\,\mathrm{Hz})^{a}$	$500\,\mu\mathrm{K}$	$3 \times 10^{-6}\,\mathrm{s}^{-1}$	[112]
3D-MOT loaded from $2\mathrm{D}^+$-MOT	$3 \times 10^8\,\mathrm{s}^{-1}$ $(3\,\mathrm{Hz})^{a}$	$8\,\mu\mathrm{K}$	$1.1 \times 10^{-2}\,\mathrm{s}^{-1}$	[204]

[a] This source is pulsed, and the flux is the mean flux over one cycle with the repetition rate listed in parentheses.

[b] This repetition rate it too low for this source to be useful (see main text). It is listed for purposes of comparison only.

[c] In keeping with the best-case scenario investigation being performed, this temperature assumes that the mean velocity of the atoms can be reduced to zero without affecting the distribution. This could be achieved, for example, by firing the source vertically below the main pumped atom laser experiment and taking the atoms from the mean turning point.

[d] The dominant contribution to this temperature is the spread in the longitudinal velocities of the atoms.

Table 5.1: Relevant properties of selected experimental cold atomic sources. The phase-space flux κ is evaluated from the atomic flux and temperature values listed using (5.6).

demonstrate that the black circles lying on a single line in (a) is not simply an artefact of plotting the results using a logarithmic scale. Finally, Figure 5.6(c) displays the equilibrium condensate fraction as a function of κ.

Figure 5.6(a) and (b) demonstrate that it would be possible to produce atom lasers with respectable condensate numbers $N_0 \gtrsim 10^5$ (corresponding to atom laser fluxes of $\gtrsim 3 \times 10^4\,\mathrm{atoms/s}$ for the outcoupling rate $\gamma = 0.3\,\mathrm{s}^{-1}$ chosen) by using replenishment sources that have a phase-space flux $\kappa \gtrsim 10^{-3}\,\mathrm{s}^{-1}$. To determine if this is experimentally feasible, the properties of a range of experimental atomic sources are detailed in Table 5.1 and the corresponding values of the phase-space flux κ calculated.

The first source listed in Table 5.1 is the experiment by Chikkatur *et al.* [178] that merged independently produced BECs in optical dipole traps that was discussed earlier. This experiment is certainly not in the high-temperature limit, but it has been included for comparison purposes. Of the remaining sources listed in Table 5.1, most are many orders of magnitude away from being useful potential sources for a pumped atom laser (cf. Figure 5.6). The fluxes obtainable from these sources are insufficient to compensate for

their higher temperatures. An increase of three-orders of magnitude in flux is necessary to compensate for an increase of a single order of magnitude in temperature [see (5.6)]. Only the last atomic source satisfies the requirement $\kappa \gtrsim 10^{-3}\,\mathrm{s}^{-3}$. This experiment by Müller *et al.* [204] is one of the sources in a dual atom interferometer designed for the precision measurement of accelerations and rotations [215]. A direct simulation has been performed for the parameters of this source, and the results are marked by a circle with an arrow pointing to it in Figure 5.6.

The equilibrium condensate number for the source of Müller *et al.* [204] is $N_0 = 5 \times 10^5$ atoms, which would be a sufficiently large condensate to serve as a stable phase-reference for a produced atom laser were it a pure BEC. However the equilibrium condensate fraction for this source is only 10% [see Figure 5.6(c)]. With 90% of the atoms in the thermal cloud, one cannot help but suspect that the significant thermal fluctuations would rule out the use of any atom laser produced by this source for interferometric use, which was our original motivation. However, previous theoretical work investigating the transfer of statistics from a trapped (quasi-)condensate to an atom laser found that using high-momentum kick Raman outcoupling such as that proposed in the scheme presented here can filter some of these fluctuations causing the atom laser to have a larger coherence length than the condensate from which it was produced [216].

It is not possible to investigate the transfer of statistics from the trapped component to the atom laser within the present model due to the simplifying assumption that it is only the condensate mode that is outcoupled to form the atom laser. A more detailed three-dimensional model taking into account the full spatial dependence of the Raman outcoupling process would be necessary to fully determine the feasibility of using an atomic source such as that described by Müller *et al.* [204] in the production of a truly continuous pumped atom laser.

5.5 Conclusion

The purpose of this chapter has been to investigate the feasibility of producing a continuously pumped atom laser driven by collisions with a cloud of thermal atoms. The method has been to investigate the best-case scenario in which the replenishment process introduces no heating to the trapped thermal component beyond that due to bringing the replenishing atoms into contact with the thermal cloud. With these caveats in mind, it is a promising result that using an existing experimental source [204] it appears possible to produce

steady-state condensates with large atom number ($\sim 5 \times 10^5$ atoms) using the scheme presented in Section 5.2. Should the atomic flux of this source be increased by an order of magnitude, the condensate number produced by this scheme could be pushed to 5×10^6 atoms.

As the scheme considered in this chapter uses the same evaporation technique (and in the same geometry) that is used to produce BEC, the question was never whether it would work, but what the flux and coherence length of the produced atom laser would be. The largest flux is achieved by the largest condensate in this scheme (for constant outcoupling rate), and for the parameters used in Section 5.4.2, the flux obtained is $1.5 \times 10^5\,\mathrm{s}^{-1}$. Referring to Table 5.1, it is clear that this flux can also be achieved by producing independent condensates, and therefore provides no advantage over such a source for atom interferometry. It is also not clear how the statistics of the thermal atoms will affect the coherence length of the produced atom laser. The model used in this chapter cannot answer this question. To investigate this further it will be necessary to include the full multimode behaviour of the Raman outcoupler and the fluctuations of the thermal cloud. This can be achieved through using a more general kinetic theory such as the 'ZNG theory' [130, 142] or the Stochastic Projected Gross-Pitaevskii equation (SPGPE) [141].

The results of this chapter suggest that the evaporatively-driven pumped atom laser scheme proposed is not a promising candidate for use in atom interferometers. This does not, however, rule out other geometries for evaporatively-driven pumping schemes such as that proposed by Mandonnet *et al.* [217] in which a thermal atomic beam is evaporatively cooled *transversely*. Initial experimental work investigating this scheme [180, 212, 218–221] has suggested that the transverse thermalisation time may be too long for evaporation to proceed efficiently, however there is ongoing research in this direction.

Chapter 6

Conclusion

Atom lasers show extraordinary promise. Using atoms instead of photons for interferometric measurements potentially increases the sensitivity by up to 10 orders of magnitude. Although much of this gain is offset due to the much lower fluxes of available atomic sources, current atom interferometers are competitive or world-leading in the precision measurement of accelerations and rotations. Coherent atomic sources (i.e. atom lasers) have fluxes even lower than the available thermal atomic sources that are used in current atom interferometers. Coherent sources do, however, have two potentially significant advantages over thermal sources for atom interferometry.

The first is their narrower linewidth, and therefore velocity spread. This enables more efficient operation of large momentum-transfer processes (which are highly velocity selective). Large momentum-transfer processes are important for increasing the interaction time of the atoms, and therefore the phase shift to be measured. Also, for larger interaction times the expansion of the atomic source increases signal loss [222], an effect which is reduced by the use of a condensed source.

The second advantage of coherent sources is their potential for producing squeezed and entangled atomic sources. In the context of quantum optics, squeezing has been used to reduce the shot noise limit (the standard quantum limit $\propto 1/\sqrt{N}$ where N is the number of particles observed) in precision measurement by about a factor of 10 [223, 224]. This is equivalent to an increase in the flux of the source of a factor of 100. Entanglement has the possibility of even more dramatic improvements, however it relies on the creation of very fragile entangled sources. The best that has been achieved in the context of quantum optics are entangled sources containing less than 10 photons [225]. In the context of atom optics, squeezed atomic sources offer the possibility of increasing measurement sensitivity,

while entangled sources are of greater interest for fundamental tests of quantum mechanics.

Atom lasers, as a technology, are still in their infancy. The first pulsed atom lasers were demonstrated in 1997, and since then researchers have extracted them from condensates quasi-continuously, guided them, split them, and probed condensates with them. They are an atomic analogue of the photon laser, except in one respect: they are not truly continuous. When the condensate runs out of atoms, the atom laser stops. Present-day atom lasers are more analogous to a leaky cavity than a laser in this respect.

Creating a truly continuous coherent source for atoms is tricker than for photons. Perhaps the largest challenge is that atom number is conserved. It is not simply possible by adding more energy to the system to create additional atoms (at least not without adding a *lot* of energy) like it is for photons. A source of atoms is necessary to produce a truly continuous atom laser, and a mechanism is needed to replenish the condensate using this source, and the replenishment process must operate without significantly disturbing the coherence properties of the condensate. It is this replenishment or pumping process that we have investigated theoretically in this thesis.

There are two choices for the reservoir providing the irreversibility for a pumping process for an atom laser: the empty modes of an optical field, or the empty modes of an atomic field. A pumping process of each form has been considered in each of Chapters 4 and 5.

In Chapter 4, a pumping mechanism in which the system is driven optically was considered. In this process, the emission of photons makes the pumping process irreversible. This process has the advantage that atoms are not necessarily lost in the evaporation process, potentially making the pumping process highly efficient. In an experimental realisation of this scheme using a condensate as the source, a 35% efficiency for this transfer process was observed. The flux of this particular realisation, however, would be limited by the rate at which the source condensates can be produced. The interesting property of this system, however, is that following a detailed comparison of the theoretical and experimental results, there is some intriguing evidence that the harmful reabsorption processes in the experiment may be suppressed due to a quantum-mechanical interference effect. A better theoretical understanding of this process could enable the source condensate to be replaced with a thermal source. If possible, this would greatly increase the potential flux of the produced atom laser, creating a competitive coherent atomic source for atom interferometry.

A second, evaporatively-driven pumping process was considered in Chapter 5. The

removal of atoms from the system due to evaporation makes this process irreversible. This pumping process is supplied by a thermal source, and could therefore have a higher flux than any pumping process supplied by condensates. However, the actual flux of the produced coherent source is necessarily lower as the evaporation process removes atoms from the system as part of the pumping mechanism. One of the aims of Chapter 5 was to determine just how much lower the flux of the condensed source would be. It was found that the largest flux achievable from an available thermal atomic source was $\sim 10^5\,\mathrm{s}^{-1}$ operating at an efficiency of just 0.05%. As this was a 'best-case scenario'-type calculation, the fact that a similar, if not larger flux can be achieved by producing independent condensates essentially rules out this type of pumped atom laser as a viable alternative to thermal sources for atom interferometry. There is also some experimental evidence that the proposed geometry is not appropriate for the operation of a pumped atom laser [177]. This does not rule out other geometries for evaporatively-driven pumping mechanisms such as that proposed by Mandonnet *et al.* [217] in which a guided thermal atomic beam is evaporatively cooled *transversely* as it propagates. By decreasing the evaporation cut-off as the beam propagates, it may be cooled to degeneracy forming a continuous beam of coherent atoms. This proposal has been investigated experimentally [180, 212, 218–221], in which it was found that transverse thermalisation occurred too slowly for evaporation to proceed efficiently. There has been a recent reinvigoration of experimental effort in this direction [226–228].

While neither of the proposed pumped atom lasers in their present forms would be competitive with thermal sources for atom interferometry, pumping could improve other atom laser experiments. In particular, experiments in which squeezing or entanglement of atomic beams is being produced and measured. In these experiments, the atomic beam will be condensed as it would be more difficult to detect squeezing or entanglement with a thermal source. For these experiments, a pumped atom laser could potentially offer a narrower linewidth, increased flux, and continuous operation, all of which would increase the sensitivity of measurements of atomic squeezing and entanglement.

Chapter 3 discussed one such process that leads to the formation of entangled atomic beams. In the experiment discussed in that chapter, multimode effects limit the potential for this entanglement to be observed directly. It is likely that only number-difference squeezing and correlations in atom detection events could be observed in this experiment. A different experiment was proposed in which these multimode effects do not occur,

potentially enabling the entanglement of the produced atomic beams to be measured. This chapter has also demonstrated the excellent agreement that is achievable between theory and experiment for BEC systems. This is possible due to extraordinary degree of control over external noise sources that is possible in experiments, and the effectiveness of the theoretical techniques available for modelling them.

This thesis documents the work of a theorist working, for the most part, in close collaboration with experimentalists. This is particularly evident in Chapter 3 and Chapter 4, but it is also true for other work not documented here. I have attempted to resolve the minor mysteries that sometimes arise in experimental physics by working closely with the experimentalists as the discovery is made, causes confusion, and for the most part, is resolved.

Appendix A

Elementary excitations of temporally periodic Hamiltonians

A.1 Evolution of the excitations

The theory of elementary excitations in unstable Bose-Einstein Condensates has been considered before [152]. In this section, restrictions on the Floquet exponents for the system under consideration in Section 3.4 are obtained, from which the equations of motion for the instabilities may be solved. This is achieved by applying the methods discussed in [152] and consideration of the symmetries of the system Hamiltonian. This Hamiltonian can be obtained by making a perturbative expansion of the Hamiltonian (3.16) about the time-dependent (but periodic) mean-field.

Consider a general quadratic, spatially-homogeneous Hamiltonian $\hat{H}(t)$ of period T in terms of the operators $\hat{\phi}_i(\boldsymbol{x},t)$ which obey the usual equal-time bosonic commutation relations. As the Hamiltonian $\hat{H}(t)$ is homogenous by assumption, the operator equations of motion will take their simplest form in a Fourier basis. In this basis the equations of motion for the operators $\hat{\phi}_i(\boldsymbol{k},t)$ can be written in matrix form[1],

$$i\hbar\frac{\partial}{\partial t}\hat{\boldsymbol{\Upsilon}}(\boldsymbol{k},t) = \mathcal{H}(\boldsymbol{k},t)\hat{\boldsymbol{\Upsilon}}(\boldsymbol{k},t), \tag{A.1a}$$

$$\hat{\boldsymbol{\Upsilon}}(\boldsymbol{k},t) = \begin{pmatrix}\hat{\phi}_1(\boldsymbol{k},t) & \hat{\phi}_1^\dagger(-\boldsymbol{k},t) & \hat{\phi}_2(\boldsymbol{k},t) & \hat{\phi}_2^\dagger(-\boldsymbol{k},t) & \dots\end{pmatrix}^{\mathrm{T}}, \tag{A.1b}$$

[1]Due to conservation of momentum, the Hamiltonian $\hat{H}(t)$ can only contain terms of the form $\hat{\phi}_i^\dagger(\boldsymbol{k},t)\hat{\phi}_j(\boldsymbol{k},t)$, $\hat{\phi}_i^\dagger(\boldsymbol{k},t)\hat{\phi}_j^\dagger(-\boldsymbol{k},t)$ and $\hat{\phi}_i(\boldsymbol{k},t)\hat{\phi}_j(-\boldsymbol{k},t)$. Consequently the terms $\hat{\phi}_j(-\boldsymbol{k},t)$ and $\hat{\phi}_j^\dagger(\boldsymbol{k},t)$ cannot occur on the RHS of (A.1a).

where the matrix $\mathcal{H}(\boldsymbol{k}, t)$ obeys

$$\mathcal{H}(\boldsymbol{k}, t+T) = \mathcal{H}(\boldsymbol{k}, t), \tag{A.2}$$

$$\mathcal{H}(\boldsymbol{k}, t) = \mathcal{H}(-\boldsymbol{k}, t), \tag{A.3}$$

where the last equality holds because $\hat{H}(t)$ is isotropic.

If the Hamiltonian $\hat{H}(t)$ were not time-dependent, $\mathcal{H}(\boldsymbol{k}, t)$ could be diagonalised to find the (potentially complex) eigenvalues $\Omega_j(\boldsymbol{k})$ and corresponding operators $\hat{Q}_j(\boldsymbol{k}, t)$ which would evolve as

$$i\hbar \frac{\partial}{\partial t} \hat{Q}_j(\boldsymbol{k}, t) = \hbar \Omega_j(\boldsymbol{k}) \hat{Q}_j(\boldsymbol{k}, t), \tag{A.4}$$

where the $\hat{Q}_j(\boldsymbol{k}, t)$ need not obey boson commutation relations. The real parts of the eigenvalues of $\mathcal{H}(\boldsymbol{k}, t)$ would give the excitation spectrum of the Hamiltonian $\hat{H}(t)$ with non-zero imaginary components giving the growth rates of the corresponding unstable mode.

In the case of a periodic matrix $\mathcal{H}(\boldsymbol{k}, t)$, it is instead the monodromy matrix $\mathcal{M}(\boldsymbol{k})$ (see Section 3.4.4) that we wish to diagonalise. The monodromy matrix $\mathcal{M}(\boldsymbol{k})$ satisfies

$$\hat{\boldsymbol{\Upsilon}}(\boldsymbol{k}, nT) = \mathcal{M}(\boldsymbol{k})^n \hat{\boldsymbol{\Upsilon}}(\boldsymbol{k}, 0), \tag{A.5}$$

where n is a positive integer. In place of (A.4), we seek the operators $\hat{Q}_j(\boldsymbol{k}, t)$ that obey

$$\hat{Q}_j(\boldsymbol{k}, T) = \lambda_j(\boldsymbol{k}) \hat{Q}_j(\boldsymbol{k}, 0), \tag{A.6}$$

where the $\hat{Q}_j(\boldsymbol{k}, t)$ are defined by

$$\hat{Q}_j(\boldsymbol{k}, t) = \boldsymbol{c}_j^\dagger(\boldsymbol{k}) \hat{\boldsymbol{\Upsilon}}(\boldsymbol{k}, t), \tag{A.7}$$

for some vectors $\boldsymbol{c}_j(\boldsymbol{k})$, where $\boldsymbol{c}_j^\dagger(\boldsymbol{k})$ denotes its conjugate transpose.

Using definitions (A.5)–(A.7), it follows that the $\lambda_j(\boldsymbol{k})$ and $\boldsymbol{c}_j^\dagger(\boldsymbol{k})$ are respectively the

eigenvalues and left eigenvectors of $\mathcal{M}(\boldsymbol{k})$,

$$\hat{Q}_j(\boldsymbol{k},T) = \boldsymbol{c}_j^\dagger(\boldsymbol{k})\hat{\boldsymbol{\Upsilon}}(\boldsymbol{k},T) = \boldsymbol{c}_j^\dagger(\boldsymbol{k})\mathcal{M}(\boldsymbol{k})\hat{\boldsymbol{\Upsilon}}(\boldsymbol{k},0), \tag{A.8}$$

$$\hat{Q}_j(\boldsymbol{k},T) = \lambda_j(\boldsymbol{k})\hat{Q}_j(\boldsymbol{k},0) = \lambda_j(\boldsymbol{k})\boldsymbol{c}_j^\dagger\hat{\boldsymbol{\Upsilon}}(\boldsymbol{k},0), \tag{A.9}$$

$$\implies \boldsymbol{c}_j^\dagger(\boldsymbol{k})\mathcal{M}(\boldsymbol{k})\hat{\boldsymbol{\Upsilon}}(\boldsymbol{k},0) = \lambda_j(\boldsymbol{k})\boldsymbol{c}_j^\dagger\hat{\boldsymbol{\Upsilon}}(\boldsymbol{k},0), \tag{A.10}$$

$$\implies \boldsymbol{c}_j^\dagger(\boldsymbol{k})\mathcal{M}(\boldsymbol{k}) = \lambda_j(\boldsymbol{k})\boldsymbol{c}_j^\dagger(\boldsymbol{k}), \tag{A.11}$$

where (A.11) follows from (A.10) as the components of $\hat{\boldsymbol{\Upsilon}}(\boldsymbol{k},0)$ are linearly independent operators.

The operators $\hat{Q}_j(\boldsymbol{k},t)$ are not necessarily bosonic annihilation or creation operators. To determine the conditions under which they are, we consider their Hermitian conjugates $\hat{Q}_j^\dagger(\boldsymbol{k},t)$. As every operator in $\hat{\boldsymbol{\Upsilon}}(-\boldsymbol{k},t)$ is the Hermitian conjugate of an operator in $\hat{\boldsymbol{\Upsilon}}(\boldsymbol{k},t)$, the $\hat{Q}_j^\dagger(\boldsymbol{k},t)$ can be written as

$$\hat{Q}_j^\dagger(\boldsymbol{k},t) = \boldsymbol{d}_j^\dagger(\boldsymbol{k})\hat{\boldsymbol{\Upsilon}}(-\boldsymbol{k},t), \tag{A.12}$$

for some vectors $\boldsymbol{d}_j(\boldsymbol{k})$. It follows from (A.6) that the $\hat{Q}_j^\dagger(\boldsymbol{k},t)$ will obey

$$\hat{Q}_j^\dagger(\boldsymbol{k},T) = \lambda_j^*(\boldsymbol{k})\hat{Q}_j^\dagger(\boldsymbol{k},0). \tag{A.13}$$

The commutators of the $\hat{Q}_j^{(\dagger)}(\boldsymbol{k},t)$ will be constant as the $\hat{Q}_j^{(\dagger)}(\boldsymbol{k},t)$ are constant linear combinations of the $\hat{\phi}^{(\dagger)}(\pm\boldsymbol{k},t)$, the commutators of which are themselves constant. Using this requirement gives

$$\begin{aligned}\left[\hat{Q}_i(\boldsymbol{k},T),\, \hat{Q}_j^\dagger(\boldsymbol{k},T)\right] &= \left[\lambda_i(\boldsymbol{k})\hat{Q}_i(\boldsymbol{k},0),\, \lambda_j^*(\boldsymbol{k})\hat{Q}_j^\dagger(\boldsymbol{k},0)\right] \\ &= \lambda_i(\boldsymbol{k})\lambda_j^*(\boldsymbol{k})\left[\hat{Q}_i(\boldsymbol{k},0),\, \hat{Q}_j^\dagger(\boldsymbol{k},0)\right].\end{aligned} \tag{A.14}$$

For (A.14) to be true either $\lambda_i(\boldsymbol{k})\lambda_j^*(\boldsymbol{k}) = 1$ or the two operators commute. Specifically, for $\hat{Q}_i(\boldsymbol{k},t)$ to be an annihilation or creation operator it is required that $\lambda_i^*(\boldsymbol{k})^{-1} = \lambda_i(\boldsymbol{k})$. In terms of the Floquet exponents (see Section 3.4.4) $\xi_i(\boldsymbol{k}) = \dfrac{i}{T}\ln\lambda_i(\boldsymbol{k})$, this requirement becomes $\xi_i(\boldsymbol{k}) = \omega_i(\boldsymbol{k})$. Hence it is only for purely real Floquet exponents that the eigenvalues of $\mathcal{M}(\boldsymbol{k})$ correspond to bosonic annihilation or creation operators. Note that in the degenerate case in which $\mathcal{H}(\boldsymbol{k},t)$ is time-independent, the Floquet exponents $\xi(\boldsymbol{k})$ are equal to the eigenvalues $\Omega(\boldsymbol{k})$ of $\mathcal{H}(\boldsymbol{k},t)$. Hence the real components of the Floquet

exponents are related to the excitation spectrum and non-zero imaginary components are related to the existence of instabilities.

Generally, the Floquet exponents ξ_i may have a non-zero imaginary component. In this case, the $\hat{Q}_i(\boldsymbol{k},t)$ will not be bosonic annihilation or creation operators, although such operators can be constructed from linear combinations of the $\hat{Q}_i(\pm\boldsymbol{k},t)$. Before constructing such operators, we first consider the restrictions on the possible eigenvalues of $\mathcal{M}(\boldsymbol{k})$.

First, it is noted that if $\lambda_i(\boldsymbol{k})$ is an eigenvalue of $\mathcal{M}(\boldsymbol{k})$, then from (A.12) and (A.13), $\lambda_i^*(\boldsymbol{k})$ must be an eigenvalue of $\mathcal{M}(-\boldsymbol{k})$. However, from the reflection symmetry of $\mathcal{H}(\boldsymbol{k})$ defined by (A.3) we have that $\mathcal{M}(-\boldsymbol{k}) = \mathcal{M}(\boldsymbol{k})$ and hence $\lambda_i^*(\boldsymbol{k})$ must also be an eigenvalue of $\mathcal{M}(\boldsymbol{k})$.

Secondly, not all of the operators $\hat{Q}_i^{(\dagger)}(\boldsymbol{k},t)$ can commute. As the $\hat{Q}_i^{(\dagger)}(\boldsymbol{k},t)$ form a complete basis over the same space as the $\hat{\phi}_i^{(\dagger)}(\boldsymbol{k},t)$ which themselves do not all commute, for every operator $\hat{Q}_i(\boldsymbol{k},t)$ there must be at least one other operator with which it does not commute. From (A.14) then follows the requirement that if $\lambda_i(\boldsymbol{k})$ is an eigenvalue, $\lambda_i^*(\boldsymbol{k})^{-1}$ must also be an eigenvalue.

Combining these two requirements gives a consistency condition for the eigenvalues of $\mathcal{M}(\boldsymbol{k})$: if λ is an eigenvalue, λ^*, λ^{-1}, and λ^{*-1} must all be eigenvalues. These conditions can be met using 1, 2 or 4 distinct eigenvalues of $\mathcal{M}(\boldsymbol{k})$.

For the degenerate case in which all of λ, λ^*, λ^{-1}, and λ^{*-1} are equal, the eigenvalue $\lambda = \pm 1$. The corresponding Floquet exponent is $\xi = 0$ or $\xi = \pi\nu_0$ where $\nu_0 = T^{-1}$. This is not an interesting case and does not occur in Figure 3.5.

There are two ways that two distinct eigenvalues can be used to satisfy the consistency condition for the eigenvalues. The first possibility is that $\lambda = \lambda^{*-1}$ (with λ^* being the second eigenvalue). In this case, the Floquet exponents are $\xi = \pm\omega$. In this case, the operators corresponding to the eigenvalues are bosonic annihilation or creation operators as shown above. The second possibility is that $\lambda = \lambda^*$ (with λ^{-1} being the second eigenvalue). In this case the Floquet exponents are $\xi = \pm i\gamma$ or $\xi = \pi\nu_0 \pm i\gamma$. This situation is seen in Figure 3.5 around $k \approx 1.5 \times 10^6\,\mathrm{m}^{-1}$ and $k \approx 2.25 \times 10^6\,\mathrm{m}^{-1}$.

The final possibility is that four distinct eigenvalues are used to satisfy the consistency condition. In this case the four eigenvalues λ, λ^*, λ^{-1}, and λ^{*-1} are different and the corresponding Floquet exponents are $\xi = \omega \pm i\gamma$ and $\xi' = -\omega \pm i\gamma$. It is this situation that occurs in Figure 3.5 around $k \approx 0.75 \times 10^6\,\mathrm{m}^{-1}$.

In summary, the Floquet exponents with nonzero real parts come in pairs $\xi(\boldsymbol{k}) = \omega(\boldsymbol{k}) \pm i\gamma(\boldsymbol{k})$. From the operators corresponding to these pairs of exponents, bosonic annihilation and creation operators can be constructed.

Consider the eigenvalues $\lambda = e^{r+i\phi}$ and $\lambda' = e^{-r+i\phi}$, and the corresponding operators $\hat{Q}(\boldsymbol{k},t)$ and $\hat{Q}'(\boldsymbol{k},t)$. From these operators we define the following two operators which will respectively be shown to be bosonic annihilation and creation operators,

$$\hat{\Lambda}_1(\boldsymbol{k},t) = \frac{1}{\sqrt{2}}\left(\hat{Q}(\boldsymbol{k},t) + \hat{Q}'(\boldsymbol{k},t)\right), \tag{A.15}$$

$$\hat{\Lambda}_2(\boldsymbol{k},t) = \frac{1}{\sqrt{2}}\left(\hat{Q}(\boldsymbol{k},t) - \hat{Q}'(\boldsymbol{k},t)\right). \tag{A.16}$$

As $\lambda\lambda'^* = 1$, $\hat{Q}(\boldsymbol{k},t)$ and $\hat{Q}'^{\dagger}(\boldsymbol{k},t)$ will not commute. By appropriate rescaling of the operators, we can define their commutator to be

$$\left[\hat{Q}(\boldsymbol{k},t),\, \hat{Q}'^{\dagger}(\boldsymbol{k},t)\right] = 1. \tag{A.17}$$

This choice defines the value of the other nonzero commutator,

$$\left[\hat{Q}'(\boldsymbol{k},t),\, \hat{Q}^{\dagger}(\boldsymbol{k},t)\right] = 1. \tag{A.18}$$

From these two commutators it can then be shown that $\hat{\Lambda}_1(\boldsymbol{k},t)$ obeys the commutation relations appropriate for an annihilation operator, while $\hat{\Lambda}_2(\boldsymbol{k},t)$ obeys the commutation relations for a creation operator. For example,

$$\left[\hat{\Lambda}_1(\boldsymbol{k},t),\, \hat{\Lambda}_1^{\dagger}(\boldsymbol{k},t)\right] = \frac{1}{2}\left[\hat{Q}(\boldsymbol{k},t) + \hat{Q}'(\boldsymbol{k},t),\, \hat{Q}^{\dagger}(\boldsymbol{k},t) + \hat{Q}'^{\dagger}(\boldsymbol{k},t)\right] = 1. \tag{A.19}$$

Defining $\hat{\Lambda}_1'(-\boldsymbol{k},t) = \hat{\Lambda}_2^{\dagger}(\boldsymbol{k},t)$, the evolution of the operators $\hat{\Lambda}_1(\boldsymbol{k},t)$ and $\hat{\Lambda}_1'(\boldsymbol{k},t)$ can now be determined. $\hat{\Lambda}_1(\boldsymbol{k},t)$ evolves as

$$\hat{\Lambda}_1(\boldsymbol{k},nT) = \frac{1}{\sqrt{2}}\left(\hat{Q}(\boldsymbol{k},nT) + \hat{Q}'(\boldsymbol{k},nT)\right) \tag{A.20}$$

$$= \frac{1}{\sqrt{2}}\left(e^{nr+in\phi}\hat{Q}(\boldsymbol{k},0) + e^{-nr+in\phi}\hat{Q}'(\boldsymbol{k},0)\right) \tag{A.21}$$

$$\begin{aligned} = e^{in\phi}\Bigg[&\frac{1}{2}\left(e^{nr} - e^{-nr}\right)\frac{1}{\sqrt{2}}\left(\hat{Q}(\boldsymbol{k},0) - \hat{Q}'(\boldsymbol{k},0)\right) \\ &+\frac{1}{2}\left(e^{nr} + e^{-nr}\right)\frac{1}{\sqrt{2}}\left(\hat{Q}(\boldsymbol{k},0) + \hat{Q}'(\boldsymbol{k},0)\right)\Bigg] \end{aligned} \tag{A.22}$$

$$= e^{in\omega T}\left(\sinh(n\gamma T)\hat{\Lambda}_1'^{\dagger}(-\boldsymbol{k},0) + \cosh(n\gamma T)\hat{\Lambda}_1(\boldsymbol{k},0)\right), \tag{A.23}$$

where n is a positive integer. Similarly, $\hat{\Lambda}_1'(\boldsymbol{k},t)$ can be shown to evolve as

$$\hat{\Lambda}_1'(\boldsymbol{k},nT) = e^{-in\omega T}\left(\sinh(n\gamma T)\hat{\Lambda}_1^\dagger(-\boldsymbol{k},0) + \cosh(n\gamma T)\hat{\Lambda}_1'(\boldsymbol{k},0)\right). \tag{A.24}$$

The evolution represented by (A.23) and (A.24) is the same as that for the non-degenerate parametric down-conversion [148] which generates EPR entanglement (see next section) between the $\hat{\Lambda}_1(\boldsymbol{k},t)$ and $\hat{\Lambda}_1'(-\boldsymbol{k},t)$ modes.

Finally, if the $\hat{Q}(\boldsymbol{k},t)$ and $\hat{Q}'(\boldsymbol{k},t)$ operators correspond to only two distinct eigenvalues (i.e. $\lambda = \lambda^*$), then by the uniqueness of the eigenvectors $\hat{\Lambda}_1'(\boldsymbol{k},t) = \hat{\Lambda}_1(\boldsymbol{k},t)$. For this case $e^{in\omega T} = \pm 1$, making (A.23) and (A.24) consistent.

A.2 EPR entanglement of unstable excitations

EPR entanglement exists between two states when, for two conjugate observables of state 2, a measurement of one can be inferred with a high degree of certainty from a measurement on state 1. This 'high degree of certainty' must be such that the differences between the inferred and measured quantities are smaller than the Heisenberg uncertainty limit for the conjugate observables. In the case of the quadrature operators

$$\hat{X}_j^\theta = \hat{a}_j e^{i\theta} + \hat{a}_j^\dagger e^{-i\theta} \quad (j = 1,\, 2), \tag{A.25}$$

where $\hat{a}_j$ are bosonic annihilation operators, the Heisenberg uncertainty limit for the conjugate observables $\hat{X}_2^\phi$, $\hat{X}_2^{\phi+\frac{\pi}{2}}$ is

$$V\big(\hat{X}_2^\phi\big)V\big(\hat{X}_2^{\phi+\frac{\pi}{2}}\big) \geq 1, \tag{A.26}$$

where $V(\hat{X})$ denotes the variance of the observable $\hat{X}$. The condition for EPR entanglement between states 1 and 2 is therefore

$$V\big(\hat{X}_2^\phi\big|\hat{X}_1^\theta\big)V\big(\hat{X}_2^{\phi+\frac{\pi}{2}}\big|\hat{X}_1^{\theta'}\big) < 1, \tag{A.27}$$

where $\hat{X}_1^\theta$ and $\hat{X}_1^{\theta'}$ are arbitrary quadrature observables on state 1, and $V(\hat{X}|\hat{Y})$ denotes the conditional variance of $\hat{X}$ given a measurement of the observable $\hat{Y}$. For perfect EPR entanglement, the outcome of a measurement of $\hat{X}_2^\phi$ can be predicted with certainty from a measurement of $\hat{X}_1^\theta$ (for some θ); in this case $V\big(\hat{X}_2^\phi\big|\hat{X}_1^\theta\big) \to 0$. For more detail about

EPR entanglement see, for example, [148].

The highest correlation between $\hat{X}_1^\theta$ and $\hat{X}_2^\phi$ will exist when the conditional expectation $\mathbb{E}\big[\hat{X}_2^\phi \big| \hat{X}_1^\theta\big] = \pm \hat{X}_1^\theta$. For simplicity, we choose the '+' sign. In this case the conditional variances above become

$$V(\theta,\phi) \equiv V\big(\hat{X}_2^\phi \big| \hat{X}_1^\theta\big) = \big\langle \big(\hat{X}_2^\phi - \hat{X}_1^\theta\big)^2 \big\rangle. \tag{A.28}$$

For the case of the unstable modes described by (A.23)–(A.24), these variances are minimised by the choice $\theta = -\phi$. At time $t = nT > 0$, the EPR-criterion (A.27) for the modes $\hat{\Lambda}_1(\boldsymbol{k},t)$ and $\hat{\Lambda}_1'(-\boldsymbol{k},t)$ is

$$V\big(\hat{X}_2^{-\theta} \big| \hat{X}_1^\theta\big) V\big(\hat{X}_2^{-\theta+\frac{\pi}{2}} \big| \hat{X}_1^{\theta-\frac{\pi}{2}}\big) = K^2 e^{-4\gamma t}, \tag{A.29}$$

where K is a constant of order $O\left(1 + |\alpha|^2 + |\alpha'|^2\right)$, with $\big\langle \hat{\Lambda}_1(\boldsymbol{k}, t=0)\big\rangle = \alpha$ and $\big\langle \hat{\Lambda}_1'(-\boldsymbol{k}, t=0)\big\rangle = \alpha'$. Note that $K = 1$ if the $\hat{\Lambda}_1^{(\prime)}$ are initially in vacuum states. For sufficiently large times (A.29) is less than 1 indicating that the modes $\hat{\Lambda}_1^{(\prime)}$ are EPR-entangled. This is true both for the case where the $\hat{\Lambda}_1^{(\prime)}$ are spontaneously-seeded (as in Figure 3.9), and for the more general case in which the $\hat{\Lambda}_1^{(\prime)}$ are seeded by different coherent states.

Appendix B

Penning ionisation in metastable condensates

In this appendix a derivation of the master equation, Gross-Pitaevskii and Truncated Wigner terms for Penning ionisation (refer to Section 2.5.1) are given. In the following derivation, the ionisation of the total angular momentum $S = 2$ quasimolecule states are neglected as the corresponding rate constant is 5 orders of magnitude smaller than that for the $S = 0$ quasimolecule state at BEC temperatures [118].

B.1 Penning ionisation master equation

Penning ionisation is a highly exothermic process. The combined internal energy of the two atoms exceeds the ionisation energy of He by 15 eV. Hence the products of the Penning ionisation reaction will exit the He^* sample rapidly. Penning ionisation is therefore well approximated by considering the ionising $S = 0$ quasimolecule state to be coupled to a vacuum reservoir. As it is only the behaviour of the condensate in which we are interested and the coupling between the condensate and the reservoir will be weak and irreversible, the reservoir's evolution may be traced over to yield the usual kind of loss term for the master equation (see for example [113, Chapter 8]),

$$\left.\frac{d\hat{\rho}}{dt}\right|_{\mathrm{PI}} = \gamma_{\mathrm{PI}} \int d\boldsymbol{x}\, \mathcal{D}\left[\hat{\Xi}_{S=0,m_S=0}\right] \hat{\rho}, \tag{B.1}$$

where $\mathcal{D}[\hat{c}]\hat{\rho} = \hat{c}\hat{\rho}\hat{c}^\dagger - \frac{1}{2}(\hat{c}^\dagger\hat{c}\hat{\rho} + \hat{\rho}\hat{c}^\dagger\hat{c})$ is the usual decoherence superoperator, and γ_{PI} is a positive rate constant. The $\hat{\Xi}_{S=0,m_S=0}$ quasimolecule state can be expressed in terms of

the atomic fields $\hat{\Psi}_j$ in the $F = 1$ total angular momentum manifold as

$$\hat{\Xi}_{S=0,m_S=0} = \frac{1}{\sqrt{3}}\left(2\hat{\Psi}_1\hat{\Psi}_{-1} - \hat{\Psi}_0\hat{\Psi}_0\right), \tag{B.2}$$

which follows from the appropriate Clebsch-Gordan coefficients [90].

The unknown coefficient $\gamma_{\rm PI}$ can be determined by calculating the dynamics given by the master equation (B.1) for an unpolarised thermal cloud, and comparing it to the result given in [120],

$$\frac{dN_{\rm ions}}{dt} = K_{^4{\rm He}}^{(\rm unpol)} \int d\boldsymbol{x}\, n(\boldsymbol{x})^2, \tag{B.3}$$

where $n(\boldsymbol{x})$ is the total density, $dN_{\rm ions}/dt$ is the rate of ion production and $K_{^4{\rm He}}^{(\rm unpol)} = 7.7 \times 10^{-17}\,{\rm m^3 s^{-1}}$ at BEC temperatures [120].

For each ion that is produced, two atoms will be lost from the sample [refer to (2.39)]. We therefore consider the equation of motion for the rate of loss of atoms from a thermal sample governed by master equation (B.1),

$$\begin{aligned}\frac{d\langle\hat{N}\rangle}{dt} = &-\gamma_{\rm PI}\frac{2}{3}\int d\boldsymbol{x}\,\left(4\langle\hat{\Psi}_{-1}^\dagger\hat{\Psi}_1^\dagger\hat{\Psi}_1\hat{\Psi}_{-1}\rangle + \langle\hat{\Psi}_0^\dagger\hat{\Psi}_0^\dagger\hat{\Psi}_0\hat{\Psi}_0\rangle\right)\\ &+\gamma_{\rm PI}\frac{4}{3}\int d\boldsymbol{x}\,\left(\langle\hat{\Psi}_1^\dagger\hat{\Psi}_{-1}^\dagger\hat{\Psi}_0\hat{\Psi}_0\rangle + \langle\hat{\Psi}_0^\dagger\hat{\Psi}_0^\dagger\hat{\Psi}_1\hat{\Psi}_{-1}\rangle\right).\end{aligned} \tag{B.4}$$

For a thermal state, the last pair of terms in (B.4) are each zero, and $\langle\hat{a}^\dagger\hat{a}^\dagger\hat{a}\hat{a}\rangle = 2\langle\hat{a}^\dagger\hat{a}\rangle^2$. The equation of motion for the total number of atoms can then be written in terms of the number densities in each state $n_j(\boldsymbol{x}) = \langle\hat{\Psi}_j^\dagger\hat{\Psi}_j\rangle$,

$$\left.\frac{d\langle\hat{N}\rangle}{dt}\right|_{\rm thermal} = -\gamma_{\rm PI}\frac{4}{3}\int d\boldsymbol{x}\,\left(2n_1(\boldsymbol{x})n_{-1}(\boldsymbol{x}) + n_0^2(\boldsymbol{x})\right). \tag{B.5}$$

In an unpolarised sample, the three internal states are equally occupied, and as two atoms are lost for each ion that is produced the ion production rate is

$$\frac{dN_{\rm ion}}{dt} = -\frac{1}{2}\left.\frac{d\langle\hat{N}\rangle}{dt}\right|_{\rm thermal} = \frac{2}{9}\gamma_{\rm PI}\int d\boldsymbol{x}\, n^2(\boldsymbol{x}), \tag{B.6}$$

where $n(\boldsymbol{x}) = \frac{1}{3}n_j(\boldsymbol{x})$ is the total number density. Comparing (B.3) and (B.6) gives the

rate constant $\gamma_{\rm PI} = \frac{9}{2}K_{^4\rm He}^{(\rm unpol)}$ and the corresponding term in the master equation to be

$$\left.\frac{d\hat{\rho}}{dt}\right|_{\rm PI} = \frac{9}{2}K_{^4\rm He}^{(\rm unpol)}\int d\boldsymbol{x}\,\mathcal{D}\left[\hat{\Xi}_{S=0,m_S=0}\right]\hat{\rho}. \tag{B.7}$$

B.2 Gross-Pitaevskii Penning ionisation terms

The Gross-Pitaevskii terms corresponding to the master equation (B.7) can be obtained by considering the equations of motion for the expectation values of the atomic fields $\hat{\Psi}_j$ and assuming that the system is in a coherent state, $\hat{\rho} = |\Psi_1(\boldsymbol{x}), \Psi_0(\boldsymbol{x}), \Psi_{-1}(\boldsymbol{x})\rangle\langle\Psi_1(\boldsymbol{x}), \Psi_0(\boldsymbol{x}), \Psi_{-1}(\boldsymbol{x})|$.

Using the master equation (B.7), the equations of motion for the expectation values of the atomic fields are

$$\left.\frac{\partial}{\partial t}\langle\hat{\Psi}_j\rangle\right|_{\rm PI} = {\rm Tr}\left\{\hat{\Psi}_j\left.\frac{d\hat{\rho}}{dt}\right|_{\rm PI}\right\} = \frac{9}{2}K_{^4\rm He}^{(\rm unpol)}\,{\rm Tr}\left\{\hat{\Psi}_j\int d\boldsymbol{x}'\mathcal{D}\left[\hat{\Xi}_{S=0,m_S=0}(\boldsymbol{x}')\right]\hat{\rho}\right\}, \tag{B.8}$$

$$\left.\frac{\partial}{\partial t}\langle\hat{\Psi}_1\rangle\right|_{\rm PI} = -\frac{3}{2}K_{^4\rm He}^{(\rm unpol)}\left(2\langle\hat{\Psi}^\dagger_{-1}\hat{\Psi}_{-1}\hat{\Psi}_1\rangle - \langle\hat{\Psi}^\dagger_{-1}\hat{\Psi}_0\hat{\Psi}_0\rangle\right), \tag{B.9a}$$

$$\left.\frac{\partial}{\partial t}\langle\hat{\Psi}_0\rangle\right|_{\rm PI} = -\frac{3}{2}K_{^4\rm He}^{(\rm unpol)}\left(\langle\hat{\Psi}^\dagger_0\hat{\Psi}_0\hat{\Psi}_0\rangle - 2\langle\hat{\Psi}^\dagger_0\hat{\Psi}_1\hat{\Psi}_{-1}\rangle\right), \tag{B.9b}$$

$$\left.\frac{\partial}{\partial t}\langle\hat{\Psi}_{-1}\rangle\right|_{\rm PI} = -\frac{3}{2}K_{^4\rm He}^{(\rm unpol)}\left(2\langle\hat{\Psi}^\dagger_1\hat{\Psi}_1\hat{\Psi}_{-1}\rangle - \langle\hat{\Psi}^\dagger_1\hat{\Psi}_0\hat{\Psi}_0\rangle\right). \tag{B.9c}$$

The Penning ionisation terms in (3.46) are obtained applying the assumption that the system is in a coherent state. This gives the replacements $\langle\hat{\Psi}_j\rangle \to \Psi_j$ and $\langle\hat{\Psi}^\dagger_j\hat{\Psi}_k\hat{\Psi}_l\rangle \to \Psi^*_j\Psi_k\Psi_l$.

B.3 Truncated Wigner Penning ionisation terms

The Truncated Wigner terms corresponding to the master equation (B.7) are very similar to the GP equation terms with an additional term to correct for the loss of 'virtual' particles (see Section 2.6.1) due to Penning ionisation. Applying the operator correspondences for the Wigner distribution described in Section 2.6.1 to (B.7) and truncating third order

derivatives yields the functional Fokker-Planck equation

$$\begin{aligned}\frac{\partial}{\partial t}W(\{\Psi_i,\Psi_i^*\}) = \int d\boldsymbol{x}\Bigg\{ &-\frac{3}{2}K_{^4\mathrm{He}}^{(\mathrm{unpol})}\Bigg[\frac{\delta}{\delta\Psi_1}\left(-2\left|\Psi_{-1}\right|^2\Psi_1+\Psi_{-1}^*\Psi_0\Psi_0+\delta(0)\Psi_1\right)\\ &+\frac{\delta}{\delta\Psi_0}\left(2\Psi_0^*\Psi_1\Psi_{-1}-\left|\Psi_0\right|^2\Psi_0+\delta(0)\Psi_0\right)\\ &+\frac{\delta}{\delta\Psi_{-1}}\left(-2\left|\Psi_1\right|^2\Psi_{-1}+\Psi_1^*\Psi_0\Psi_0+\delta(0)\Psi_{-1}\right)+\mathrm{h.c.}\Bigg]\\ &+3K_{^4\mathrm{He}}^{(\mathrm{unpol})}\Bigg[\frac{\delta}{\delta\Psi_1}\frac{\delta}{\delta\Psi_1^*}\left(\left|\Psi_{-1}\right|^2-\frac{1}{2}\delta(0)\right)+\frac{\delta}{\delta\Psi_0}\frac{\delta}{\delta\Psi_0^*}\left(\left|\Psi_0\right|^2-\frac{1}{2}\delta(0)\right)\\ &+\frac{\delta}{\delta\Psi_{-1}}\frac{\delta}{\delta\Psi_{-1}^*}\left(\left|\Psi_1\right|^2-\frac{1}{2}\delta(0)\right)\Bigg]\\ &+3K_{^4\mathrm{He}}^{(\mathrm{unpol})}\Bigg[\frac{\delta}{\delta\Psi_1}\frac{\delta}{\delta\Psi_{-1}^*}\Psi_{-1}^*\Psi_1-\frac{\delta}{\delta\Psi_1}\frac{\delta}{\delta\Psi_0^*}\Psi_{-1}^*\Psi_0\\ &-\frac{\delta}{\delta\Psi_0}\frac{\delta}{\delta\Psi_{-1}^*}\Psi_0^*\Psi_1+\mathrm{h.c.}\Bigg]\Bigg\}W(\{\Psi_i,\Psi_i^*\}),\end{aligned} \tag{B.10}$$

where $\delta(0)$ is the three-dimensional Dirac delta function evaluated at the origin. While the $\delta(0)$ terms are pathological, they will later be approximated on a computational grid by ΔV^{-1} where ΔV is the local volume element[1]. This equation of motion is in the form of a (functional) Fokker-Planck equation, and using the methods of Section 2.6.1 we may transform this equation into stochastic (partial) differential equations.

As the master equation (B.7) is local in the position basis, the $\boldsymbol{D}$ and $\boldsymbol{B}$ matrices can be constructed independently at each spatial position. Discretising (B.10) onto a computational grid (this implies the replacement $\delta(0)\to\Delta V^{-1}$ where ΔV is the local

[1] An alternative treatment of the Truncated Wigner method can be used [125, 126] in which it is assumed from the beginning a restricted basis is being used. In this alternative treatment, the Dirac delta function $\delta(\boldsymbol{x})$ is replaced by a truncated version $\delta_{\mathcal{P}}(\boldsymbol{x})$ which is contained within the restricted basis. This is a formalisation of the discretisation process later used in which $\delta(0)$ is replaced by ΔV^{-1}. The two methods are essentially equivalent.

volume element), the $\boldsymbol{D}$ matrix at position $\boldsymbol{x}$ is

$$\boldsymbol{D}(\{\Psi_i\,,\Psi_i^*\}\,,t) = 3K_{^4\mathrm{He}}^{(\mathrm{unpol})} \begin{pmatrix} |\Psi_{-1}|^2 & -\Psi_{-1}^*\Psi_0 & \Psi_{-1}^*\Psi_1 & 0 & 0 & 0 \\ -\Psi_0^*\Psi_{-1} & |\Psi_0|^2 & -\Psi_0^*\Psi_1 & 0 & 0 & 0 \\ \Psi_1^*\Psi_{-1} & -\Psi_1^*\Psi_0 & |\Psi_1|^2 & 0 & 0 & 0 \\ 0 & 0 & 0 & |\Psi_{-1}|^2 & -\Psi_0^*\Psi_{-1} & \Psi_1^*\Psi_{-1} \\ 0 & 0 & 0 & -\Psi_{-1}^*\Psi_0 & |\Psi_0|^2 & -\Psi_1^*\Psi_0 \\ 0 & 0 & 0 & \Psi_{-1}^*\Psi_1 & -\Psi_0^*\Psi_1 & |\Psi_1|^2 \end{pmatrix} - \frac{3K_{^4\mathrm{He}}^{(\mathrm{unpol})}}{2\Delta V}\mathbb{I}, \tag{B.11}$$

where $\mathbb{I}$ is the identity matrix, and the rows of the matrix $\boldsymbol{D}$ are constructed from the derivatives in the order: Ψ_1, Ψ_0, Ψ_{-1}, Ψ_1^*, Ψ_0^*, Ψ_{-1}^*, and the columns from the derivatives in the order: Ψ_1^*, Ψ_0^*, Ψ_{-1}^*, Ψ_1, Ψ_0, Ψ_{-1} [see (2.46)].

The matrix $\boldsymbol{D}$ in (B.11) contains negative eigenvalues due to the ΔV^{-1} term that corrects for the 'virtual' particles added to the initial state of the Wigner function (refer to Section 2.6.1). At positions where the field is highly occupied this will be a small correction and can safely be neglected compared to the local density. Inevitably there will be some positions within the computational domain at which the field will be negligibly occupied and the ΔV^{-1} term cannot be neglected. At such positions however the Penning ionisation process itself will be negligible[2]. Although in this case the approximation is unjustified for a system undergoing only Penning ionisation, it is justified in the system under consideration in Chapter 3 in which other processes occur on significantly shorter timescales.

Neglecting the ΔV^{-1} term, the eigenvalues of $\boldsymbol{D}$ are positive or zero, and the matrix $\boldsymbol{D}$ can be written in the form $\boldsymbol{B}\boldsymbol{B}^\dagger$ where

$$\boldsymbol{B}(\{\Psi_i\,,\Psi_i^*\}\,,t) = \sqrt{\frac{3K_{^4\mathrm{He}}^{(\mathrm{unpol})}}{2}} \begin{pmatrix} \Psi_{-1}^* & i\Psi_{-1}^* \\ -\Psi_0^* & -i\Psi_0^* \\ \Psi_1^* & i\Psi_1^* \\ \Psi_{-1} & -i\Psi_{-1} \\ -\Psi_0 & i\Psi_0 \\ \Psi_1 & -i\Psi_1 \end{pmatrix}. \tag{B.12}$$

[2]For the simulation grids used in Chapter 3, the relevant timescale is $\sim 1\,\mathrm{s}$ which is much longer than the simulated time of $\sim 10\,\mathrm{ms}$.

The lower three rows of (B.12) are necessarily the conjugate of the upper three rows as they correspond to the evolution of the conjugates of the atomic fields [see (2.47)].

It now remains to evaluate the middle term in (2.47), the Stratonovich correction. Using (B.12) this term is

$$-\frac{1}{2}\sum_{j,k} B_{k,j}\frac{\delta}{\delta\Psi_k}B_{i,j} = -\frac{3}{2}\frac{1}{\Delta V}K^{(\mathrm{unpol})}_{^4\mathrm{He}}\Psi_i. \tag{B.13}$$

This term exactly cancels the ΔV^{-1} terms ($\delta(0)$ before discretisation onto a computational grid) in the first three lines of (B.10). The Truncated Wigner SDEs in Stratonovich form for the Penning ionisation terms are then

$$d\Psi_j|_{\mathrm{TW}} = \left.\frac{\partial\Psi_j}{\partial t}\right|_{\mathrm{GP}} dt + \sqrt{\frac{3K^{(\mathrm{unpol})}_{^4\mathrm{He}}}{2}}\begin{pmatrix}\Psi^*_{-1}\\ -\Psi^*_0\\ \Psi_1\end{pmatrix}_j (dW + idW'), \tag{B.14}$$

where dW and dW' are real independent Gaussian noises. Defining $dW_p = \frac{1}{\sqrt{2}}(dW + idW')$ to be a complex Gaussian noise which satisfies

$$\overline{dW_p(t)dW_p(t')} = 0, \tag{B.15}$$

$$\overline{dW_p(t)dW^*_p(t')} = \delta(t-t'), \tag{B.16}$$

gives the Penning ionisation terms in (3.47).

It is unsurprising that the Gross-Pitaevskii terms for Penning ionisation appear in (B.14) as the Gross-Pitaevskii equation and the Truncated Wigner method can be considered to be the zeroth and first order terms in an expansion of the system dynamics in terms of its response to quantum fluctuations [127].

Appendix C

Derivations and calculations

C.1 Proof of the periodicity of the nonlinear optical Bloch equations

In this section, we prove the periodicity of the solutions to the nonlinear optical Bloch equations considered in Section 3.4.1. We restate the nonlinear optical Bloch equations (3.19) here for convenience,

$$\frac{d}{dt}\rho_{10} = -i\frac{g}{2}(1-w)\rho_{10} + i\Omega w, \tag{C.1a}$$

$$\frac{d}{dt}w = -4\Omega \,\mathrm{Im}\{\rho_{10}\}, \tag{C.1b}$$

where ρ_{10} is the off-diagonal element of the density matrix, and $w = \rho_{11} - \rho_{00}$.

These equations describe motion on the surface of a sphere, known as the Bloch sphere (see Figure 3.3), with each point on the sphere corresponding to a different physical state. A generalisation of the Poincaré-Bendixson theorem that applies to compact, connected, two-dimensional orientable manifolds [160] (such as the surface of the sphere) states that every trajectory either approaches one or more fixed points, or approaches a periodic orbit. The possibility of a space-filling trajectory is precluded as the surface of a sphere is not homeomorphic to a torus (see [160]). Periodic trajectories and fixed points trivially approach themselves.

We next aim to show that there are no limit cycles in this system, i.e. there exist no trajectories that approach periodic orbits which are not themselves periodic.

We first write the equations of motion for the system in the usual spherical polar

coordinates as

$$\frac{d\theta}{dt} = 2\Omega \sin\phi, \tag{C.2a}$$

$$\frac{d\phi}{dt} = 2\Omega \cos\phi \cot\theta - \frac{1}{2}g(1 - \cos\theta). \tag{C.2b}$$

We note that these equations are of the form

$$\dot{\boldsymbol{r}} = \frac{2}{\hbar}\check{\boldsymbol{r}} \times \nabla E, \tag{C.3}$$

where E is the energy per particle previously defined in (3.20), and an inverted hat is used to denote unit vectors.

As the evolution has the form (C.3), a given point moves in the direction perpendicular to the gradient of E at a rate proportional to the magnitude of that gradient, and hence the energy E is conserved along any given trajectory.

Assuming a limit cycle exists, there will exist a trajectory approaching the limit cycle which is not the limit cycle. For each point in the limit cycle $\boldsymbol{x}$, there exists an infinite sequence of points $\boldsymbol{s}_i$ that approach $\boldsymbol{x}$ which are the intersection of a curve which intersects no trajectory tangentially (a *transversal*, see [160]) and the trajectory approaching the limit cycle. As the energy E is continuous, we have $\lim_{i\to\infty} E(\boldsymbol{s}_i) = E(\boldsymbol{x})$, and therefore the energy of the approaching trajectory must be the same as the energy of the limit cycle, i.e. $E(\boldsymbol{s}_i) = E(\boldsymbol{x})$. The derivative of E in the direction of the transversal is then zero as $\lim_{i\to\infty} \dfrac{E(\boldsymbol{s}_i) - E(\boldsymbol{x})}{|\boldsymbol{s}_i - \boldsymbol{x}|} = 0$. It is already known that the derivative of the energy is zero parallel to the limit cycle as energy is conserved along any trajectory. As the direction of the transversal and the limit cycle at $\boldsymbol{x}$ are linearly independent (a transversal intersects no trajectory tangentially) and the manifold is two-dimensional, the gradient of E at $\boldsymbol{x}$ must necessarily be zero. From (C.3), this implies that $\boldsymbol{x}$ is a fixed point, which is a contradiction with $\boldsymbol{x}$ being part of a limit cycle. Our original assumption that a limit cycle exists is therefore false.

It now remains to be shown that no trajectories approach fixed points (with the exception of the fixed points themselves). With the possibility of limit cycles excluded, by the generalised Poincaré-Bendixson theorem this will show that all remaining trajectories are periodic.

To analyse the stability of the fixed points, it is first necessary to determine their location. It immediately follows from (C.2a) that fixed points will satisfy $\sin\phi = 0$, i.e.

fixed points are restricted to the great circle in the x–z plane. To parameterise this circle by a single coordinate, we alter the usual ranges of the spherical polar coordinates such that $\phi \in \left[-\frac{\pi}{2}, \frac{\pi}{2}\right)$ and $\theta \in [-\pi, \pi)$. With this definition, $\cos\phi = 1$ over the entire circle, instead of $\cos\phi = \pm 1$ over opposite halves.

Using the tan-half substitution $s = \tan\frac{1}{2}\theta$, it can be shown from (C.2b) that all fixed points satisfy

$$gs^3 = \Omega(1 - s^4). \tag{C.4}$$

The stability of (C.2) about the fixed points may be investigated to demonstrate that there are no trajectories that approach the fixed points (with the exception of the fixed points themselves). Linearising (C.2) about the fixed points yields

$$\frac{d}{dt}\delta\theta = 2\Omega\delta\phi, \tag{C.5}$$

$$\frac{d}{dt}\delta\phi = -\frac{\Omega}{2s^2}(s^4 + 3)\delta\theta, \tag{C.6}$$

where $\delta\theta$ and $\delta\phi$ are the deviations from the fixed point and the identity (C.4) has been used to simplify the result. The eigenvalues of this linear system of differential equations are

$$\lambda = \pm\sqrt{-\frac{\Omega^2}{s^2}(s^4 + 3)}, \tag{C.7}$$

which are pure imaginary as both Ω and s are real. This implies that there exist no trajectories near any fixed points of the system that asymptotically approach the fixed point. It may then be concluded that with the exception of the fixed points themselves, all trajectories of the system (C.1) are periodic, and Floquet's theorem may be applied in Section 3.4.5.

C.2 Example calculation of the momentum density flux

As a demonstration of the efficacy of the method described in Section 3.5.2 for determining the rate of loss of momentum density from a region of space, we consider a wave of wavenumber k_0 incident from the left on an imperfect absorbing boundary layer in a 1D computational domain (see Figure C.1), and compare $\Phi(k, t)$ [refer to (3.45)] to the result expected in the case of a perfect absorbing boundary layer of $\dfrac{\hbar k_0}{M}\delta(k - k_0)$. In this

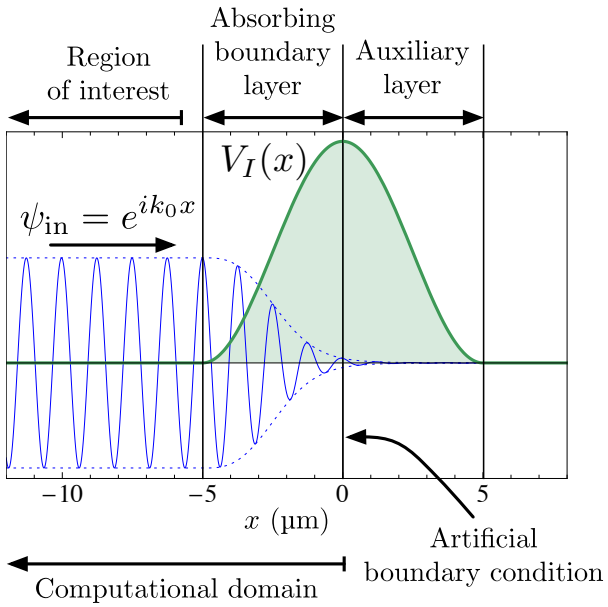

Figure C.1: An incident wave of wavenumber k_0 incident on an absorbing boundary layer. The region of interest is the part of the computational domain in which the absorbing potential $V_I(x)$ is zero. An auxiliary layer is added outside of the absorbing boundary layer as a model for a number of artificial boundary conditions (see main text).

example s-wave scattering will be neglected. As the computational domain in this example is effectively infinite, the wavefunction used in the evaluation of (3.45) will be restricted to be nonzero only in the absorbing boundary layer to demonstrate the finite momentum resolution obtainable from this method due to the (except in this example) finite extent of the computational domain.

As a model for a number of different artificial boundary conditions we consider there to be *no* artificial boundary condition at the edge of the computational domain, and instead it to be surrounded by an 'auxiliary layer' in which there is a negative imaginary potential the reflection of that in the absorbing boundary layer. The negative imaginary potential is then symmetric about the edge of the computational domain. In the case of periodic boundary conditions, the auxiliary layer will correspond to the absorbing boundary layer on the other side of the computational domain in which it is assumed that the reflected negative imaginary potential is used. In the case of Dirichlet or Neumann boundary conditions in which respectively the wavefunction or its derivative is set to zero on the boundary, the auxiliary layer corresponds to the absorbing boundary layer reflected. In either of these latter two cases, the wavefunction for the actual artificial boundary conditions will be a linear combination of the wavefunction *without* the artificial boundary conditions in the absorbing boundary layer and in the auxiliary layer. Specifically, in the case of

Dirichlet boundary conditions in which the wavefunction is set to zero on the boundary, the wavefunction in the presence of the artificial boundary condition $\psi_{\text{abc}}(\boldsymbol{x})$ will be given by $\psi_{\text{abc}}(\boldsymbol{x}) = \psi(\boldsymbol{x}) - \psi(-\boldsymbol{x})$ where $\psi(\boldsymbol{x})$ is the wavefunction in the absence of the artificial boundary condition, and $x = 0$ corresponds to the edge of the computational domain.

To calculate $\Phi(k, t)$ from (3.45) it is necessary to know the solution $\psi(x)$ to the time-independent Schrödinger equation subject to the boundary conditions that there is an incident wave from the left with wavenumber k_0 and no incident wave from the right. Given two linearly independent solutions to the Schrödinger equation in the doubled absorbing boundary layer (the absorbing boundary layer / auxiliary layer region), $\psi(x)$ can be found by applying these boundary conditions. It now remains to obtain two linearly independent solutions to the time-independent Schrödinger equation within the doubled absorbing boundary layer.

Solutions to the time-independent Schrödinger equation within the doubled absorbing boundary layer can be obtained with relative ease in one dimension as it is simply an ordinary differential equation,

$$-\frac{\hbar^2}{2M}\frac{d^2\psi}{dx^2} + V(x)\psi(x) = E(k_0)\psi(x) = \frac{\hbar^2 k_0^2}{2M}\psi(x), \tag{C.8}$$

which is equivalent to

$$\frac{d^2\psi}{dx^2} = \frac{2M}{\hbar^2}V(x)\psi(x) - k_0^2\psi(x). \tag{C.9}$$

Two linearly independent (but not necessarily orthogonal) solutions $\phi_1(x)$, $\phi_2(x)$ to (C.9) can be found by simply choosing two linearly independent initial conditions and numerically propagating the solutions through the potential $V(x) = -iV_I(x)$. The solution $\psi(x) = c_1\phi_1(x) + c_2\phi_2(x)$ can then be found by requiring continuity of the wavefunction and its derivative at the left and right edges of the doubled absorbing boundary layer,

$$e^{ikx} + \alpha_R e^{-ikx}\Big|_{\text{left}} = c_1\phi_1(x) + c_2\phi_2(x)\Big|_{\text{left}}, \tag{C.10a}$$

$$\frac{d}{dx}\big(e^{ikx} + re^{-ikx}\big)\Big|_{\text{left}} = \frac{d}{dx}\big(c_1\phi_1(x) + c_2\phi_2(x)\big)\Big|_{\text{left}}, \tag{C.10b}$$

$$\alpha_T e^{ikx}\Big|_{\text{right}} = c_1\phi_1(x) + c_2\phi_2(x)\Big|_{\text{right}}, \tag{C.10c}$$

$$\frac{d}{dx}\big(\alpha_T e^{ikx}\big)\Big|_{\text{right}} = \frac{d}{dx}\big(c_1\phi_1(x) + c_2\phi_2(x)\big)\Big|_{\text{right}}, \tag{C.10d}$$

where α_R and α_T are the reflected and transmitted amplitudes respectively.

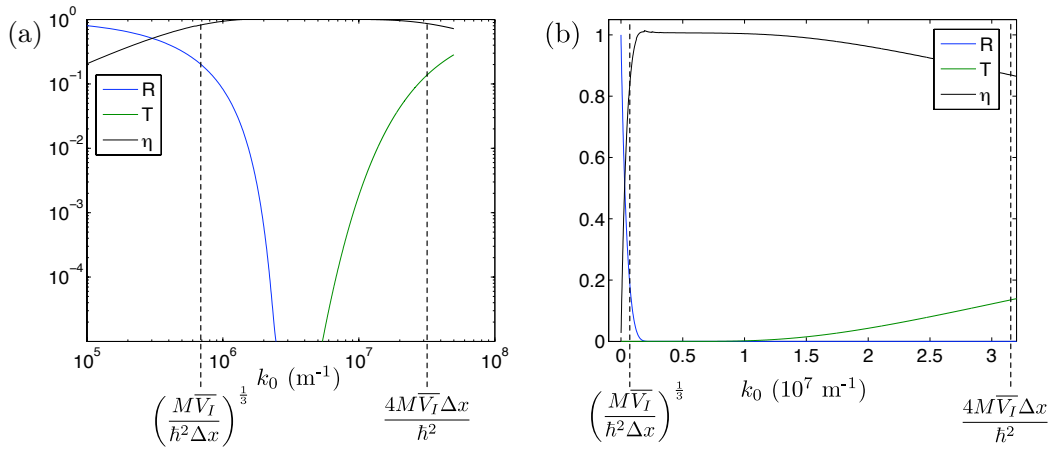

Figure C.2: The reflection R and transmission T coefficients from a typical absorbing boundary layer as a function of wavenumber. The potential used was $V_I(x) = \hbar\omega\cos^2\left(\frac{\pi x}{2\Delta x}\right)$ where $\omega = 5\times10^4$ rad.s^{-1} and $\Delta x = 5\,\mu$m is the size of the absorbing boundary layer. Also marked on this figure are the approximate lower and upper bounds of the effectiveness of the absorbing boundary layer as given by (2.64). Figures (a) and (b) plot the same data on logarithmic and linear scales respectively.

As a by-product of solving (C.10) for $\psi(x)$, the reflection and transmission fractions $R = |\alpha_R|^2$ and $T = |\alpha_T|^2$ respectively can be obtained, giving a quantitative description of the effectiveness of a given absorbing boundary layer. For reflecting artificial boundary conditions, the reflection coefficient is $R' = |\alpha_R \mp \alpha_T|^2$ respectively for Dirichlet and Neumann boundary conditions, and as α_R and α_T cannot both be significant simultaneously for any absorbing boundary layer that is effective over some range of wavenumbers, the approximation $R' \approx \max(R, T)$ can be used. Hence R and T are useful measures of the effectiveness of an absorbing boundary layer independent of the artificial boundary conditions used.

In Figure C.2 the reflected and transmitted fractions R and T are plotted as a function of the incident wavenumber and a comparison is made to the approximate range of validity of the absorbing boundary as given by (2.64).

With $\psi(x)$ determined, the steady state momentum density flux $\Phi_{k_0}(k)$ can be obtained for a given incident wavenumber k_0. This distribution is plotted in Figure C.3 for the same absorbing boundary used in Figure C.3. As any real absorbing boundary layer will have finite extent, the resolution of $\Phi_{k_0}(k)$ will be limited by $\Delta k = \pi/\Delta x$, where Δx is the width of the absorbing boundary layer. This finite resolution will prevent $\Phi_{k_0}(k)$ reproducing the exact result in the limit of a perfect absorbing boundary layer of $\frac{\hbar k_0}{M}\delta(k - k_0)$. As a measure of the accuracy of $\Phi_{k_0}(k)$, its integral over a range of a few Δk should be compared

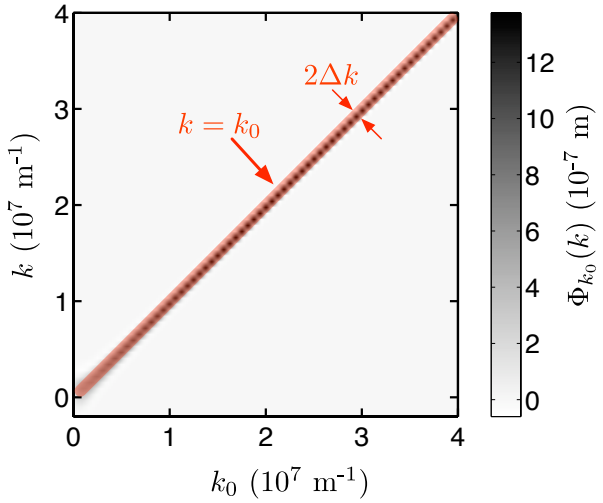

Figure C.3: The momentum flux density $\Phi_{k_0}(k)$ leaving the region of interest in Figure C.1 as a function of the incident wavenumber k_0. As expected, $\Phi_{k_0}(k)$ is sharply peaked around $k = k_0$. The resolution of $\Phi_{k_0}(k)$, Δk is indicated by the width of the $k = k_0$ line.

to the exact answer. To this aim we define

$$\eta(k_0) = \left(\frac{\hbar k_0}{M}\right)^{-1} \int_{k_0-5\Delta k}^{k_0+5\Delta k} dk\, \Phi_{k_0}(k), \tag{C.11}$$

where $\eta(k_0)$ is plotted in Figure C.2. As expected, $\eta \approx 1$ over the same range of incident wavenumbers for which the absorbing boundary layer is effective.

C.3 Solving the Quantum Kinetic Theory model of Chapter 5

One of the difficulties involved in solving the kinetic model of Chapter 5 is that the energy range that the problem is defined over changes in time. The maximum energy is simply the energy of the evaporative cut-off $\varepsilon_{\rm cut}$, while the minimum energy is the chemical potential of the condensate $\mu(t)$. A discretisation of the energy dimension over the range $[0, \varepsilon_{\rm cut}]$ will suffer from problems accurately representing the lower-end of the distribution which has a larger occupation. An alternative is write the problem in terms of a shifted energy coordinate $\overline{\varepsilon} \equiv \varepsilon - \mu(t)$ so that the minimum energy of the system is now fixed. Of course the same problem now exists at the upper end of the energy range where the maximum energy $\overline{\varepsilon}_{\rm max} = \varepsilon_{\rm cut} - \mu(t)$ is now time-dependent. However, at equilibrium there will be significantly fewer thermal atoms at the evaporation cut-off than there will be near the condensate [this is illustrated in Figure 5.4(a)]. This choice will then result in smaller numerical errors than the alternative.

Written in terms of the shifted energy variable $\overline{\varepsilon}$, the contribution due to the replenishment is

$$\left.\frac{\partial\big(\overline{\rho}(\overline{\varepsilon},t)\overline{g}(\overline{\varepsilon},t)\big)}{\partial t}\right|_{\text{replenishment}} = \Gamma\overline{\rho}_0(\overline{\varepsilon})\overline{g}_T(\overline{\varepsilon}), \tag{C.12}$$

where a bar over a function is used to indicate that it is defined in terms of the shifted energy coordinate. The original form of this term is given by (5.3).

C.3.1 Density of states

Although the evolution equations for the kinetic model (5.1) are written in terms of the product of the density of states $\rho(\varepsilon,t)$ and the energy distribution function $g(\varepsilon,t)$, it will be necessary to separately determine the energy distribution function to evaluate the collisional contributions given in the following section. To extract the energy distribution function it is necessary to have an explicit expression for the density of states for the thermal cloud. This density of states is not simply the same as that for a harmonic trap as the thermal modes will experience a mean-field repulsion due to the condensate mode. The effective potential experienced by the thermal atoms is

$$V_{\text{eff}}(\boldsymbol{r},t) = V_{\text{trap}}(\boldsymbol{r}) + 2gn_c(\boldsymbol{r},t), \tag{C.13}$$

where $V_{\text{trap}}(\boldsymbol{r})$ is the potential due to the magnetic trap, $g = 4\pi\hbar^2 a/m$, a is the s-wave scattering length and $n_c(\boldsymbol{r},t)$ is the condensate density, which was assumed to follow a Thomas-Fermi distribution in Chapter 5. Note that the '2' in the above expression is the full Hartree-Fock mean field experienced by the thermal atoms (refer to the discussion at the end of Section 3.3, or [20, Chapter 8] for further details) which is twice the mean-field repulsion experienced by condensate atoms. This is essentially due to the thermal atoms being distinguishable from the condensate atoms, while the condensate atoms are indistinguishable from one another.

The density of states in the presence of the effective potential (C.13) is given by

$$\rho(\varepsilon,t) = \int \frac{d\boldsymbol{r}\,d\boldsymbol{p}}{(2\pi\hbar)^3}\,\delta\left(\varepsilon - V_{\text{eff}}(\boldsymbol{r},t) - \boldsymbol{p}^2/2m\right). \tag{C.14}$$

The integrals are performed in [134] giving the following result in terms of the shifted

energy coordinate (Eqs. (49) and (50) in [134])

$$\overline{\rho}(\overline{\varepsilon},t) = \frac{2}{\pi\hbar\overline{\omega}}\left[I_-(\overline{\varepsilon}) + I_+(\overline{\varepsilon})\right], \tag{C.15}$$

where the functions $I_\pm(\overline{\varepsilon})$ are

$$I_-(\overline{\varepsilon}) = \frac{u_-^3 x}{4} - \frac{a_- u_- x}{8} - \frac{a_-^2}{8}\ln(x+u_-)\Big|_{x=\sqrt{\max\{0,-a_-\}}}^{x=\sqrt{2\mu/\hbar\overline{\omega}}}, \tag{C.16}$$

$$I_+(\overline{\varepsilon}) = -\frac{u_+^3 x}{4} + \frac{a_+ u_+ x}{8} + \frac{a_+^2}{8}\arcsin\left(\frac{x}{\sqrt{a_+}}\right)\Big|_{x=\sqrt{2\mu/\hbar\overline{\omega}}}^{x=\sqrt{a_+}}, \tag{C.17}$$

with $a_\pm = 2(\overline{\varepsilon}\pm\mu)/\hbar\overline{\omega}$, and $u_\pm = \sqrt{a_\pm \mp x^2}$. Note that there is a minor typo in Bijlsma *et al.* [134], the lower limit of $I_-(\overline{\varepsilon})$ is given as $x = \sqrt{\max\{0, a_-\}}$, while it should read $x = \sqrt{\max\{0,-a_-\}}$ as in (C.16).

C.3.2 Collision and energy-redistribution in Quantum Kinetic Theory

The forms of the collision and energy-redistribution terms of the kinetic model described in Chapter 5 were omitted there for sake of clarity as their derivation was not part of the work presented there. A full derivation of these terms is given in [130, 134].

The contribution due to thermal–thermal collisions is given in Eq. (26) of [134] and has the form

$$\begin{aligned}\left.\frac{\partial\big(\overline{\rho}(\overline{\varepsilon}_1,t)\overline{g}(\overline{\varepsilon}_1,t)\big)}{\partial t}\right|_{\text{thermal–thermal}} &= \frac{m^3 g^2}{2\pi^3\hbar^7}\int d\overline{\varepsilon}_2\int d\overline{\varepsilon}_3\int d\overline{\varepsilon}_4\,\overline{\rho}(\overline{\varepsilon}_{\min},t)\\ &\quad\times\delta(\overline{\varepsilon}_1+\overline{\varepsilon}_2-\overline{\varepsilon}_3-\overline{\varepsilon}_4)\\ &\quad\times[(1+\overline{g}_1)(1+\overline{g}_2)\overline{g}_3\overline{g}_4 - \overline{g}_1\overline{g}_2(1+\overline{g}_3)(1+\overline{g}_4)],\end{aligned} \tag{C.18}$$

where $\overline{\varepsilon}_{\min}$ is the minimum of the $\overline{\varepsilon}_i$, and $\overline{g}_i = \overline{g}(\overline{\varepsilon}_i,t)$.

The contribution due to thermal–condensate collisions is given by Eq. (53) and Eq. (58)–

(60) of [134] and has the form

$$\left.\frac{\partial\big(\overline{\rho}(\overline{\varepsilon}_1,t)\overline{g}(\overline{\varepsilon}_1,t)\big)}{\partial t}\right|_{\text{thermal–condensate}} = \frac{m^3g^2}{2\pi^3\hbar^7}\int d\overline{\varepsilon}_2\int d\overline{\varepsilon}_3\int d\overline{\varepsilon}_4\,\delta(\overline{\varepsilon}_2-\overline{\varepsilon}_3-\overline{\varepsilon}_4) \times\left[\delta(\overline{\varepsilon}_1-\overline{\varepsilon}_2)-\delta(\overline{\varepsilon}_1-\overline{\varepsilon}_3)-\delta(\overline{\varepsilon}_1-\overline{\varepsilon}_4)\right] \times\left[(1+\overline{g}_2)\overline{g}_3\overline{g}_4-\overline{g}_2(1+\overline{g}_3)(1+\overline{g}_4)\right] \times\int_{\overline{U}_{\text{eff}}(\boldsymbol{r},t)\le\overline{U}_-} d\boldsymbol{r}\,n_c(\boldsymbol{r},t), \tag{C.19}$$

where $\overline{U}_- = \frac{2}{3}\left[(\overline{\varepsilon}_3+\overline{\varepsilon}_4)-\sqrt{\overline{\varepsilon}_3^2-\overline{\varepsilon}_3\overline{\varepsilon}_4+\overline{\varepsilon}_4^2}\right]$, and $\overline{U}_{\text{eff}}(\boldsymbol{r},t) = U_{\text{eff}}(\boldsymbol{r},t)-\mu(t)$. The corresponding contribution to the evolution of the condensate number is simply

$$\left.\frac{dN_0}{dt}\right|_{\text{thermal–condensate}} = -\int d\overline{\varepsilon}\;\left.\frac{\partial\big(\overline{\rho}(\overline{\varepsilon},t)\overline{g}(\overline{\varepsilon},t)\big)}{\partial t}\right|_{\text{thermal–condensate}}. \tag{C.20}$$

Finally, the contribution due to energy redistribution is (Eqs. (32) and (52) in [134])

$$\left.\frac{\partial\big(\overline{\rho}(\overline{\varepsilon}_1,t)\overline{g}(\overline{\varepsilon}_1,t)\big)}{\partial t}\right|_{\text{redistribution}} = -\frac{\partial\big(\overline{\rho}_{\text{w}}\overline{g}\big)}{\partial\overline{\varepsilon}}, \tag{C.21}$$

where $\overline{\rho}_{\text{w}}$ is the weighted density of states

$$\overline{\rho}_{\text{w}}(\overline{\varepsilon}) = \frac{2}{\pi\hbar\overline{\omega}}\left[I_-(\overline{\varepsilon})-I_+(\overline{\varepsilon})\right]\frac{d\mu}{dt}, \tag{C.22}$$

where the functions $I_\pm(\overline{\varepsilon})$ are given in (C.16) and (C.17).

C.3.3 Three-body loss in Quantum Kinetic Theory

The dominant density-dependent loss process in Bose-Einstein condensates is three-body loss [206, 207]. In Chapter 5 it was argued that three-body loss was an important process in the operation of the pumped atom laser scheme proposed there. The following derivation of the three-body loss contribution to the kinetic model (5.1) was performed by *Matthew Davis* and is presented for completeness.

Three-body loss (or three-body recombination) is the process in which three atoms collide forming a bound dimer with the third necessary to ensure both energy and momentum conservation. The binding energy is sufficient to give the products of a three-body recombination process sufficient kinetic energy to rapidly escape the trap. Three-body loss

is then well-described by the master equation term

$$\left.\frac{d\hat{\rho}}{dt}\right|_{\text{3-body loss}} = \frac{1}{3}L_3 \int d\boldsymbol{x}\, \mathcal{D}\left[\hat{\Psi}^3(\boldsymbol{x})\right]\hat{\rho}, \tag{C.23}$$

where $\mathcal{D}[\hat{c}]\hat{\rho} = \hat{c}\hat{\rho}\hat{c}^\dagger - \frac{1}{2}(\hat{c}^\dagger\hat{c}\hat{\rho} + \hat{\rho}\hat{c}^\dagger\hat{c})$ is the usual decoherence superoperator, and $L_3 = 5.8 \times 10^{-30}\,\text{cm}^6\text{s}^{-1}$ [206] is the three-body recombination loss rate constant. This equation, first derived by [229] has the familiar form of a decoherence superoperator with the state undergoing loss as the argument (cf. Section B.1).

The loss rate of atoms from the system due to three-body loss is readily obtained from (C.23) as

$$\left.\frac{dN}{dt}\right|_{\text{3-body loss}} = \text{Tr}\left\{\int d\boldsymbol{r}\, \hat{\Psi}^\dagger(\boldsymbol{r})\hat{\Psi}(\boldsymbol{r})\left.\frac{d\hat{\rho}}{dt}\right|_{\text{3-body loss}}\right\} = -L_3\int d\boldsymbol{r}\left\langle\hat{\Psi}^\dagger(\boldsymbol{r})^3\hat{\Psi}(\boldsymbol{r})^3\right\rangle. \tag{C.24}$$

To separate the contributions to (C.24) due to the thermal and condensed components, we use an approach similar to that of the Bogoliubov theory discussed in Section 3.3. We write the annihilation operator $\hat{\Psi}$ in terms of its mean value $\Psi \equiv \langle\hat{\Psi}\rangle$ and the fluctuation operator $\delta\hat{\Psi} \equiv \hat{\Psi} - \Psi$ and substitute this into (C.24). In contrast to Section 3.3 in which the zero-temperature limit was considered, the fluctuation operator defined here represents thermal fluctuations, which cannot be considered to be small. Higher powers of $\delta\hat{\Psi}$ can therefore not be neglected. However, thermal fluctuations have no well-defined phase relationship to one another or to the condensate. Expectation values containing an unequal number of creation and annihilation fluctuation operators such as $\langle\delta\hat{\Psi}\delta\hat{\Psi}\rangle$ can therefore be assumed to be zero [cf. (3.7) in which the $\delta\hat{\Psi}^\dagger\delta\hat{\Psi}^\dagger$ and $\delta\hat{\Psi}\delta\hat{\Psi}$ terms were retained as there is a well-defined phase relationship between the quasiparticles and the condensate].

Performing the substitution described, (C.24) becomes

$$\begin{aligned}\left.\frac{dN}{dt}\right|_{\text{3-body loss}} = -L_3\int d\boldsymbol{r}\,\Big\{&[n_c(\boldsymbol{r})]^3 + 9[n_c(\boldsymbol{r})]^2\langle\delta\hat{\Psi}^\dagger(\boldsymbol{r})\delta\hat{\Psi}(\boldsymbol{r})\rangle \\ &+9n_c(\boldsymbol{r})\langle\delta\hat{\Psi}^\dagger(\boldsymbol{r})^2\delta\hat{\Psi}(\boldsymbol{r})^2\rangle + \langle\delta\hat{\Psi}^\dagger(\boldsymbol{r})^3\delta\hat{\Psi}(\boldsymbol{r})^3\rangle\Big\},\end{aligned} \tag{C.25}$$

where $n_c(\boldsymbol{r}) = |\Psi(\boldsymbol{r})|^2$ is the condensate density.

The non-condensate density is given by $n_T(\boldsymbol{r}) = \langle\delta\hat{\Psi}^\dagger(\boldsymbol{r})\delta\hat{\Psi}(\boldsymbol{r})\rangle$. As thermal states are Gaussian, the higher-order expectation values in the previous expression may be simplified

by the application of Wick's theorem [131] giving

$$\left\langle \delta\hat{\Psi}^\dagger(\boldsymbol{r})^2 \delta\hat{\Psi}(\boldsymbol{r})^2 \right\rangle = 2[n_T(\boldsymbol{r})]^2, \tag{C.26}$$

$$\left\langle \delta\hat{\Psi}^\dagger(\boldsymbol{r})^3 \delta\hat{\Psi}(\boldsymbol{r})^3 \right\rangle = 6[n_T(\boldsymbol{r})]^3. \tag{C.27}$$

Substituting these expressions back into (C.25) yields

$$\left.\frac{dN}{dt}\right|_{\text{3-body loss}} = -L_3 \int d\boldsymbol{r}\, [n_c(\boldsymbol{r})]^3 + 9[n_c(\boldsymbol{r})]^2 n_T(\boldsymbol{r}) + 18 n_c(\boldsymbol{r})[n_T(\boldsymbol{r})]^2 + 6[n_T(\boldsymbol{r})]^3. \tag{C.28}$$

The evaluation of this loss rate requires the evaluation of the condensate and thermal densities. The condensate density $n_c(\boldsymbol{r})$ is fully determined by the condensate occupation $N_0(t)$ within the Thomas-Fermi approximation that has already been made elsewhere in the derivation of the kinetic model. The first term of (C.28) only involves the condensate density and may be evaluated analytically

$$\frac{dN_0}{dt} = -L_3 \frac{15^{4/5}}{168\pi^2} \left(\frac{m\overline{\omega}}{\hbar\sqrt{a}}\right)^{12/5} N_0^{9/5}. \tag{C.29}$$

The remaining terms of (C.28) require an expression for the thermal density $n_T(\boldsymbol{r})$, which can be obtained from the energy distribution function $g(\varepsilon)$ and the density of states $\rho(\varepsilon)$.

The total number of thermal atoms N_T can be written as

$$N_T = \int d\varepsilon\, \rho(\varepsilon) g(\varepsilon), \tag{C.30}$$

where the density of states is defined by (C.14). Substituting this into (C.30) and rearranging the order of integrals gives

$$N_T = \int d\boldsymbol{r} \int d\varepsilon\, \rho(\varepsilon, \boldsymbol{r}) g(\varepsilon), \tag{C.31}$$

where we have defined

$$\rho(\varepsilon, \boldsymbol{r}) = \int d\boldsymbol{p}\, \delta\left(\varepsilon - V_{\text{eff}}(\boldsymbol{r}, t) - \boldsymbol{p}^2/2m\right) = \frac{m^{3/2}}{\sqrt{2}\pi^2\hbar^3} \sqrt{\varepsilon - V_{\text{eff}}(\boldsymbol{r})}. \tag{C.32}$$

The thermal density can be identified from (C.31)

$$n_T(\boldsymbol{r}) = \int d\varepsilon\, \rho(\varepsilon, \boldsymbol{r}) g(\varepsilon). \tag{C.33}$$

The remaining terms of (C.28) can now be expressed in terms of the energy distribution function $g(\varepsilon)$ and the density of states $\rho(\varepsilon)$ by substituting (C.33) for one of the factors of $n_T(\boldsymbol{r})$ in each term

$$-L_3 \int d\boldsymbol{r}\, 9[n_c(\boldsymbol{r})]^2 n_T(\boldsymbol{r}) = -L_3 \int d\varepsilon\, g(\varepsilon) \int d\boldsymbol{r}\, 9\rho(\varepsilon, \boldsymbol{r})[n_c(\boldsymbol{r})]^2, \tag{C.34}$$

$$-L_3 \int d\boldsymbol{r}\, 18 n_c(\boldsymbol{r})[n_T(\boldsymbol{r})]^2 = -L_3 \int d\varepsilon\, g(\varepsilon) \int d\boldsymbol{r}\, 18\rho(\varepsilon, \boldsymbol{r}) n_c(\boldsymbol{r}) n_T(\boldsymbol{r}), \tag{C.35}$$

$$-L_3 \int d\boldsymbol{r}\, 6[n_T(\boldsymbol{r})]^3 = -L_3 \int d\varepsilon\, g(\varepsilon) \int d\boldsymbol{r}\, 6\rho(\varepsilon, \boldsymbol{r})[n_T(\boldsymbol{r})]^2. \tag{C.36}$$

From these expressions the rate of loss of atoms of energy ε from the distribution can be identified

$$\left.\frac{\partial\big(\rho(\varepsilon)g(\varepsilon)\big)}{\partial t}\right|_{\text{3-body loss}} = -L_3 \int d\boldsymbol{r}\, \rho(\varepsilon, \boldsymbol{r}) g(\varepsilon) \left\{3[n_c(\boldsymbol{r})]^2 + 12 n_c(\boldsymbol{r}) n_T(\boldsymbol{r}) + 6[n_T(\boldsymbol{r})]^2\right\}, \tag{C.37}$$

where the contributions due to the terms involving only one or two thermal atoms have been multiplied by 1/3 and 2/3 respectively to share appropriately the total loss. The corresponding term for the condensate number evolution is

$$\begin{aligned}\left.\frac{dN_0}{dt}\right|_{\text{3-body loss}} = &-L_3 \frac{15^{4/5}}{168\pi^2} \left(\frac{m\overline{\omega}}{\hbar\sqrt{a}}\right)^{12/5} N_0^{9/5} \\ &-L_3 \int d\varepsilon \int d\boldsymbol{r}\, \rho(\varepsilon, \boldsymbol{r}) g(\varepsilon) \left\{6[n_c(\boldsymbol{r})]^2 + 6 n_c(\boldsymbol{r}) n_T(\boldsymbol{r})\right\},\end{aligned} \tag{C.38}$$

where the contributions due to the terms involving only one or two condensate atoms have been multiplied by 1/3 and 2/3 respectively.

Appendix D

Calculational tools

A significant part of any theoretical physics work is spent in the technical task of using computational tools. It is unsurprising therefore that just as experimental PhD candidates will spend a significant portion of their time building and designing the apparatus for their experiments, so too will a theorist spend time developing the codes that they need in the pursuit of their work. In this appendix I describe the tool that I have developed in the course of my PhD to simplify the process of developing these codes.

A wide variety of simulations have been necessary in pursuit of the goals of this thesis. These have included simulations for the calculation of condensate ground states, the propagation of both Gross-Pitaevskii and Truncated Wigner atom laser models of different atomic species in systems of different dimensionality, the evolution of matrices describing quasiparticles, the evolution of a variety of optical pumping models, and the evolution of an evaporation-driven pumped atom laser. With the exception of the last of these simulations, which was written by *Matthew Davis*, all of these simulations have been written by myself. The work necessary to hand-write all of these codes from scratch would have been prohibitive. Each would have needed independent testing, and the associated time fixing errors. Instead, codes for almost all of the simulations in this thesis were produced by the computational package `XMDS` [143], or its successor, `xpdeint`. Each of these tools take a high-level description of a problem (an input script) and produce a fast low-level simulation (written in `C++`) that solves the problem. By testing these packages extensively, the common aspects of simulations can be generated reliably.

A large number of problems solved within the fields of quantum and atom optics are very similar on a mathematical level as they fall into the class of systems of initial-value (stochastic) partial differential equations. Due to the similarity of problems of this form, it is feasible to create packages such as `XMDS` and `xpdeint` which focus purely on solving this type of problem. These problems can also be solved with more general purpose tools like `MATLAB` and `Mathematica`, and these tools are ideal when the problem is sufficiently small that it may be solved with their built-in integrators. However, when the problem becomes sufficiently large that the overheads of these tools become significant, traditionally a hand-coded solution has been necessary. `XMDS` and `xpdeint` provide an alternative to writing such codes by hand. Both of these tools are free and open source, and available to anyone[1].

`XMDS` and `xpdeint` particularly excel at providing a smooth transition from a low-dimensional simulation to a higher-dimensional one, from a deterministic simulation to a stochastic one, or from a single-processor simulation to a distributed simulation running in parallel across multiple computers (or on a supercomputer). In hand-written codes, unless they were initially written with such a potential future extension in mind, each such change would require significant effort in rewriting the code. In `XMDS` and `xpdeint`, such changes require only minimal change to the input script. This encourages users to create test simulations of a simpler system (e.g. reduced dimensionality), which makes the code run faster, allowing problems in the input script to be found and fixed more quickly. Later, the simulation can be scaled up to the full problem. Fundamentally, the ease with which codes can be generated encourages *experimentation* with different types of simulations, as the time taken to create the code is no longer the rate-limiting factor.

`XMDS` was originally created in 2001 by Collecutt and Drummond [143], and has been improved over the intervening years by a large number of contributors (including myself) adding a variety of integrators, interaction picture algorithms [101], cross-propagation algorithms, and the ability to solve deterministic problems in parallel. Over this period of time, `XMDS` has been employed for wide range of problems, including quantum optical information storage in two-level atoms [230], the influence of mobility on biodiversity [231],

[1] See `www.xmds.org` for further information. Note that this website has not yet been updated (at the time of printing) to mention `xpdeint`. Further information about `xpdeint` may be obtained from `github.com/grahamdennis/xpdeint`.

polarisation squeezing in optical fibres [232], and quantum superchemistry in molecular Bose-Einstein condensates [233].

Since the development of XMDS, there have been other problems to which it has been desired to apply XMDS, but as it was not designed with such systems in mind, either less-than-satisfactory solutions were used, or a separate code was written by hand. A good example of such problems were simulations involving cylindrical or spherical symmetry. As XMDS calculates spatial derivatives using Fourier transforms, the solution is necessarily assumed to be periodic over the computational domain. This is a complication when it is desired to use cylindrical or spherical symmetry as the solution near the origin is not necessarily similar in value to the solution at the outer edge of the computational domain (and would thus be in conflict with the assumed periodicity). This problem has been resolved by including an unphysical negative range to the radius (for example, this technique was used in [146, 234]). This solution is unsatisfying as it increases by at least a factor of 2 the computational resources required to the solve the problem, reduces the order of convergence of the solution (when considered as a function of the number of spatial grid points used), and care must be taken in the choice of the grid to exclude the origin as a point. This step is necessary as the Laplacian operator in cylindrical and spherical coordinates contains terms involving inverse powers of the radius. Were the origin included as a point in the computational grid, it would be necessary to divide by zero.

The actual motivation for the creation of a successor to XMDS was the need for an algorithm to solve the optical pumping model (4.38), specifically an algorithm which could solve partial differential equations in time coupled with auxiliary equations which propagate in space in *opposite* directions. A specific example of such a system is the $2\hbar k$ momentum transfer 'simple atom laser model' of Section 4.5.3. XMDS implements an algorithm that can solve such auxiliary equations when they propagate in a single direction. This 'cross-propagation' algorithm needed to be extended to implement the Alternating-Direction Implicit algorithm [209], which can handle the more general case. While this algorithm could have been implemented in XMDS, it would have required significant effort. For although XMDS was a powerful tool, its internal workings had become somewhat of a tangled mess. XMDS worked more as a result of the sheer effort of those who modified it than because it was designed in such a way as to make any extensions require an appropriate amount of effort. Nevertheless, the effort necessitated in adding features to XMDS, without a doubt, saved more effort overall for XMDS's users.

I felt that by designing and implementing a successor to XMDS, I could not only address my specific problem and the other limitations discussed above, but could make it easier to extend in the future. This was no minor task as XMDS contained approximately 38,000 lines of code. While none of XMDS's code could be directly copied, the parts implementing the various integrators could be translated fairly simply, and some of the ideas in XMDS could be directly implemented in xpdeint, making the rewrite a slightly less daunting task. The current version of xpdeint (at the time of printing) contains approximately 22,000 lines of code, and implements almost all of the features of XMDS, while also improving upon it in several key areas. The features of xpdeint are the subject of the remainder of this appendix.

D.1 xpdeint

As discussed in the previous section, the class of problem that can be solved with xpdeint (and XMDS) is that of systems of initial-value (stochastic) partial differential equations. To solve such problems numerically, they must be restricted to a finite domain with boundary conditions imposed at the edges. xpdeint discretises this problem by applying the pseudo-spectral method [167]: the solution is decomposed as a weighted sum of a finite set of basis functions,

$$f(x) = \sum_{n=1}^{N} c_n g_n(x), \tag{D.1}$$

where $f(x)$ is the spatial representation of the solution, $g_n(x)$ are the basis functions, and $\{c_n\}$ are constants which form an equivalent representation of the solution (the *spectral* representation [167]). The choice of basis functions is significant as it determines the boundary conditions at the edge of the computational domain, and some sets of basis functions are more appropriate for some problems than others.

The most common problem that xpdeint is applied to is the solution of Schrödinger-like equations. For such problems, the potential and s-wave scattering terms are local in the spatial representation, and are therefore accurately calculated with any set of basis functions. The kinetic energy term, being proportional to the Laplacian operator, does not share this property as knowledge of the solution in the region near a point is necessary to evaluate it. By choosing the basis functions to be the eigenfunctions of the Laplacian operator, the kinetic energy may be evaluated more accurately in the spectral representation. For

example,

$$\frac{-\hbar^2\nabla^2}{2M}f(x) = \frac{-\hbar^2}{2M}\sum_{n=1}^{N}\lambda_n c_n g_n(x), \tag{D.2}$$

where λ_n is the eigenvalue for the Laplacian eigenfunction $g_n(x)$, i.e. $\nabla^2 g_n(x) = \lambda_n g_n(x)$. `xpdeint` implements a range of different types of basis functions for use in problems exhibiting different types of symmetries: the Fourier basis for translation-invariant problems, the sine and cosine bases for problems with reflection symmetry, the Bessel and spherical-Bessel bases for problems with cylindrical and spherical symmetry, and the Hermite-Gauss basis where the basis functions are the harmonic oscillator eigenstates. This last basis is useful in (stochastic) projected-GP models in which it permits an implementation of a self-consistent energy cut-off [141]. Of these different types of bases, only the first, the Fourier basis, was available in `XMDS`. The advantage of the Fourier basis is that it permits the use of the Fast Fourier Transform (FFT), a 'fast' algorithm ($O(N \log N)$ operations for an N-point 1D Fourier transform) for transforming between the spatial and spectral representations. Similar algorithms may also be used for the sine and cosine bases, but all of the other bases require the use of a matrix multiplication to transform between the spatial and spectral representations. In contrast, matrix multiplication requires $O(N^2)$ operations for an N-point 1D transform. In practice, this cost can be reduced by a factor of two when every basis function has a definite parity (i.e. even or odd with respect to the origin, an example is the Hermite-Gauss basis), and such an algorithm is implemented in `xpdeint`. Although the matrix multiplication transform is slower than the FFT, for sufficiently small numbers of grid points ($\lesssim 100$), the cost is not significantly larger, and may be outweighed by the better convergence afforded by using a more appropriate set of basis functions. This feature was used in Section 3.5, in which the Bessel basis was used in the solution of Gross-Pitaevskii and Truncated Wigner models of outcoupling from a cylindrically-symmetric He* condensate.

The details of pseudo-spectral methods and their implementation via Gaussian quadrature are beyond the scope of this appendix. This topic is discussed in significant depth elsewhere [167].

A second significant new feature included in `xpdeint` is the capability to solve systems of coupled partial differential equations of different dimensionalities (previously, all solution quantities needed to have the same dimensionality). This is important for Hartree-Fock-

Bogoliubov problems (see Section 2.6.2), where the system is described by the mean-field $\Psi(\boldsymbol{x})$, and the correlation functions $G_N(\boldsymbol{x}, \boldsymbol{x}')$ and $G_A(\boldsymbol{x}, \boldsymbol{x}')$. This is also useful in the Gaussian phase-space method [235, 236] (a generalisation of the phase-space methods that are described in Section 2.6.1), which can be applied to fermions as well as bosons. This feature was used in Section 3.4 to solve for the dynamics of a matrix-valued function of wavenumber coupled to a zero-dimensional mean-field.

A third significant new feature included in `xpdeint` is the capability to evaluate convolutions and other composite operations. Convolutions are of particular use in the evaluation of non-local atomic interaction terms in which the inter-particle potential only depends on the relative separation of the two particles. Such interaction terms may be efficiently evaluated with Fourier transforms by an application of the convolution theorem [168]. An important example of such an interaction is the dipole–dipole interaction [237]. Independently, this feature of `xpdeint` has been applied to study the resonant Einstein de-Haas effect [238] in metastable Helium [239], an effect driven by the dipole–dipole interaction. In this thesis, this feature has been applied (although not in the form of calculating a convolution) in Section 3.5 in the calculation of the momentum-density flux leaving the computational domain (refer to Section 3.5.2).

The motivating reason for developing `xpdeint`, the need for an implementation of the Alternating-Direction Implicit algorithm [209], has been extensively used in Chapter 4.

A list of other features of `xpdeint` (all of which are shared with `XMDS`) is given below.

- A variety of interchangeable integration algorithms including the classical fourth-order Runge-Kutta algorithm, a ninth-order Runge-Kutta algorithm, adaptive Runge-Kutta algorithms, and the midpoint method (a second-order semi-implicit algorithm).

- The interaction-picture algorithm [101]. This algorithm is an application of the interaction-picture method in quantum mechanics to calculate exactly the contribution of one of the linear terms of the partial differential equation (typically the derivative component).

- A semi-implicit algorithm for the solution of stochastic (partial) differential equations [240, 241] with stochastic strong order 1 and deterministic order 2.

- The capability to solve deterministic problems of two or greater dimensions in parallel across multiple computers. Different realisations of stochastic simulations may also be solved in parallel.

- Quantification of discretisation error in time. With this option, `XMDS` and `xpdeint` solve the problem twice, once with the parameters specified, and once more with a smaller time-step (or in the case of adaptive algorithms, with a smaller tolerance). Both the finer solution, and the difference between the solutions are then output. While not a comprehensive guarantee of numerical convergence, this feature somewhat simplifies the process of validating numerical simulations.

Outside of my own work, `xpdeint` has been used in the stochastic simulation of conditional master equations [242], the simulation of measurement feedback control of a Bose-Einstein condensate [243], and the simulation of a number-phase Wigner representation [129]. `xpdeint` is in use for a variety of other problems, the results of which have not yet been published.

D.1.1 Tools and packages used by `xpdeint`

`xpdeint` takes advantage of several tools and packages created by others, the most important of which are listed here.

- `xpdeint` is written in Python [244] and much of the `C++` code is generated using Cheetah templates [245].
- The implementation of the Fast Fourier Transform is provided by `FFTW3` [246]. This package also provides the functionality necessary to distribute deterministic simulations across multiple computers.
- The Message Passing Interface (MPI) [247] is used for communications between computers participating in a distributed computation.
- Tools for reading and writing the primary input and output format, `HDF5`, are provided by the `HDF5` package [248].

Bibliography

[1] G. F. Missiroli, G. Pozzi, and U. Valdre, J. Phys. E **14**, 649 (1981).

[2] H. Rauch, W. Treimer, and U. Bonse, Phys. Lett. A **47**, 369 (1974).

[3] D. W. Keith, C. R. Ekstrom, Q. A. Turchette, and D. E. Pritchard, Phys. Rev. Lett. **66**, 2693 (1991).

[4] O. Carnal and J. Mlynek, Phys. Rev. Lett. **66**, 2689 (1991).

[5] F. Riehle, T. Kisters, A. Witte, J. Helmcke, and C. J. Bordé, Phys. Rev. Lett. **67**, 177 (1991).

[6] M. Kasevich and S. Chu, Phys. Rev. Lett. **67**, 181 (1991).

[7] J. M. McGuirk, G. T. Foster, J. B. Fixler, M. J. Snadden, and M. A. Kasevich, Phys. Rev. A **65**, 033608 (2002).

[8] T. L. Gustavson, A. Landragin, and M. A. Kasevich, Classical and Quantum Gravity **17**, 2385 (2000).

[9] K. Schreiber, J. Wells, and G. Stedman, Gen. Relativ. Gravit. **40**, 935 (2008).

[10] M. V. Moody and H. J. Paik, Phys. Rev. Lett. **70**, 1195 (1993).

[11] F. J. van Kann, M. J. Buckingham, C. Edwards, and R. Matthews, Physica B: Condensed Matter **194-196**, 61 (1994).

[12] H. Müller, S.-w. Chiow, S. Herrmann, S. Chu, and K.-Y. Chung, Phys. Rev. Lett. **100**, 031101 (2008).

[13] M. H. Anderson, J. R. Ensher, M. R. Matthews, C. E. Wieman, and E. A. Cornell, Science **269**, 198 (1995).

[14] C. C. Bradley, C. A. Sackett, J. J. Tollett, and R. G. Hulet, Phys. Rev. Lett. **75**, 1687 (1995).

[15] K. B. Davis, M. O. Mewes, M. R. Andrews, N. J. van Druten, D. S. Durfee, D. M. Kurn, and W. Ketterle, Phys. Rev. Lett. **75**, 3969 (1995).

[16] W. Ketterle, D. Durfee, and D. M. Stamper-Kurn, in *Bose-Einstein Condensation in Atomic Gases*, edited by M. Inguscio, S. Stringari, and C. E. Wieman, Proc. Int. School of Physics Enrico Fermi (IOS Press, Amsterdam, 1999), pp. 67–176, `arXiv:cond-mat/9904034`.

[17] H. M. Wiseman, Phys. Rev. A **56**, 2068 (1997).

[18] J. P. Gordon, H. J. Zeiger, and C. H. Townes, Phys. Rev. **99**, 1264 (1955).

[19] E. E. Müller, Physica A: Statistical Mechanics and its Applications **139**, 165 (1986).

[20] C. J. Pethick and H. Smith, *Bose-Einstein Condensation in Dilute Gases* (Cambridge University Press, 2002).

[21] M. Lewenstein, A. Sanpera, V. Ahufinger, B. Damski, A. Sen, and U. Sen, Advances in Physics **56**, 243 (2007).

[22] I. Buluta and F. Nori, Science **326**, 108 (2009).

[23] M. P. A. Fisher, P. B. Weichman, G. Grinstein, and D. S. Fisher, Phys. Rev. B **40**, 546 (1989).

[24] M. Greiner, O. Mandel, T. Esslinger, T. W. Hänsch, and I. Bloch, Nature **415**, 39 (2002).

[25] S. Levy, E. Lahoud, I. Shomroni, and J. Steinhauer, Nature **449**, 579 (2007).

[26] M. Girardeau, J. Math. Phys. **1**, 516 (1960).

[27] E. H. Lieb and W. Liniger, Phys. Rev. **130**, 1605 (1963).

[28] B. Paredes, A. Widera, V. Murg, O. Mandel, S. Folling, I. Cirac, G. V. Shlyapnikov, T. W. Hansch, and I. Bloch, Nature **429**, 277 (2004).

[29] J. R. Abo-Shaeer, C. Raman, J. M. Vogels, and W. Ketterle, Science **292**, 476 (2001).

[30] N. S. Ginsberg, S. R. Garner, and L. V. Hau, Nature **445**, 623 (2007).

[31] T. Jeltes, J. M. McNamara, W. Hogervorst, W. Vassen, V. Krachmalnicoff, M. Schellekens, A. Perrin, H. Chang, D. Boiron, A. Aspect, *et al.*, Nature **445**, 402 (2007).

[32] L. Deng, E. W. Hagley, J. Wen, M. Trippenbach, Y. Band, P. S. Julienne, J. E. Simsarian, K. Helmerson, S. L. Rolston, and W. D. Phillips, Nature **398**, 218 (1999).

[33] M. Olshanii, Phys. Rev. Lett. **81**, 938 (1998).

[34] T. Kinoshita, T. Wenger, and D. S. Weiss, Science **305**, 1125 (2004).

[35] S. Inouye, M. R. Andrews, J. Stenger, H.-J. Miesner, D. M. Stamper-Kurn, and W. Ketterle, Nature **392**, 151 (1998).

[36] B. Damski, J. Zakrzewski, L. Santos, P. Zoller, and M. Lewenstein, Phys. Rev. Lett. **91**, 080403 (2003).

[37] J. E. Lye, L. Fallani, M. Modugno, D. S. Wiersma, C. Fort, and M. Inguscio, Phys. Rev. Lett. **95**, 070401 (2005).

[38] D. Clément, A. F. Varón, M. Hugbart, J. A. Retter, P. Bouyer, L. Sanchez-Palencia, D. M. Gangardt, G. V. Shlyapnikov, and A. Aspect, Phys. Rev. Lett. **95**, 170409 (2005).

[39] C. Fort, L. Fallani, V. Guarrera, J. E. Lye, M. Modugno, D. S. Wiersma, and M. Inguscio, Phys. Rev. Lett. **95**, 170410 (2005).

[40] T. Schulte, S. Drenkelforth, J. Kruse, W. Ertmer, J. Arlt, K. Sacha, J. Zakrzewski, and M. Lewenstein, Phys. Rev. Lett. **95**, 170411 (2005).

[41] J. Stenger, S. Inouye, A. P. Chikkatur, D. M. Stamper-Kurn, D. E. Pritchard, and W. Ketterle, Phys. Rev. Lett. **82**, 4569 (1999).

[42] A. Robert, O. Sirjean, A. Browaeys, J. Poupard, S. Nowak, D. Boiron, C. I. Westbrook, and A. Aspect, Science **292**, 461 (2001).

[43] M.-O. Mewes, M. R. Andrews, D. M. Kurn, D. S. Durfee, C. G. Townsend, and W. Ketterle, Phys. Rev. Lett. **78**, 582 (1997).

[44] I. Bloch, T. W. Hänsch, and T. Esslinger, Phys. Rev. Lett. **82**, 3008 (1999).

[45] G. M. Moy, J. J. Hope, and C. M. Savage, Phys. Rev. A **55**, 3631 (1997).

[46] E. W. Hagley, L. Deng, M. Kozuma, J. Wen, K. Helmerson, S. L. Rolston, and W. D. Phillips, Science **283**, 1706 (1999).

[47] N. P. Robins, C. Figl, S. A. Haine, A. K. Morrison, M. Jeppesen, J. J. Hope, and J. D. Close, Phys. Rev. Lett. **96**, 140403 (2006).

[48] M. Johnsson, S. Haine, J. Hope, N. Robins, C. Figl, M. Jeppesen, J. Dugué, and J. Close, Phys. Rev. A **75**, 043618 (2007).

[49] M. T. Johnsson and J. J. Hope, Phys. Rev. A **75**, 043619 (2007).

[50] J. P. Dowling, Phys. Rev. A **57**, 4736 (1998).

[51] J. Jeffers, P. Horak, S. M. Barnett, and P. M. Radmore, Phys. Rev. A **62**, 043602 (2000).

[52] N. P. Robins, C. M. Savage, J. J. Hope, J. E. Lye, C. S. Fletcher, S. A. Haine, and J. D. Close, Phys. Rev. A **69**, 051602(R) (2004).

[53] T. Busch, M. Köhl, T. Esslinger, and K. Mølmer, Phys. Rev. A **65**, 043615 (2002).

[54] M. Köhl, T. Busch, K. Molmer, T. W. Hänsch, and T. Esslinger, Phys. Rev. A **72**, 063618 (2005).

[55] J.-F. Riou, W. Guerin, Y. L. Coq, M. Fauquembergue, V. Josse, P. Bouyer, and A. Aspect, Phys. Rev. Lett. **96**, 070404 (2006).

[56] M. Jeppesen, J. Dugué, G. R. Dennis, M. T. Johnsson, C. Figl, N. P. Robins, and J. D. Close, Phys. Rev. A **77**, 063618 (2008).

[57] A. Öttl, S. Ritter, M. Köhl, and T. Esslinger, Phys. Rev. Lett. **95**, 090404 (2005).

[58] W. Guerin, J.-F. Riou, J. P. Gaebler, V. Josse, P. Bouyer, and A. Aspect, Phys. Rev. Lett. **97**, 200402 (2006).

[59] D. Döring, N. P. Robins, C. Figl, and J. D. Close, Opt. Express **16**, 13893 (2008).

[60] M. T. Johnsson and S. A. Haine, Phys. Rev. Lett. **99**, 010401 (2007).

[61] S. A. Haine and J. J. Hope, Phys. Rev. A **72**, 033601 (2005).

[62] S. A. Haine, M. K. Olsen, and J. J. Hope, Phys. Rev. Lett. **96**, 133601 (2006).

[63] B. E. A. Saleh and M. C. Teich, *Fundamentals of Photonics* (Wiley, 1991).

[64] S. A. Haine, J. J. Hope, N. P. Robins, and C. M. Savage, Phys. Rev. Lett. **88**, 170403 (2002).

[65] B. Kneer, T. Wong, K. Vogel, W. P. Schleich, and D. F. Walls, Phys. Rev. A **58**, 4841 (1998).

[66] N. Robins, C. Savage, and E. A. Ostrovskaya, Phys. Rev. A **64**, 043605 (2001).

[67] A. E. Siegman, *Lasers* (University Science Books, 1986).

[68] S. Inouye, T. Pfau, S. Gupta, A. P. Chikkatur, A. Gorlitz, D. E. Pritchard, and W. Ketterle, Nature **402**, 641 (1999).

[69] M. Kozuma, Y. Suzuki, Y. Torii, T. Sugiura, T. Kuga, E. W. Hagley, and L. Deng, Science **286**, 2309 (1999).

[70] O. Zobay and G. M. Nikolopoulos, Phys. Rev. A **73**, 013620 (2006).

[71] S. Inouye, A. P. Chikkatur, D. M. Stamper-Kurn, J. Stenger, D. E. Pritchard, and W. Ketterle, Science **285**, 571 (1999).

[72] D. Schneble, G. K. Campbell, E. W. Streed, M. Boyd, D. E. Pritchard, and W. Ketterle, Phys. Rev. A **69**, 041601 (2004).

[73] Y. Yoshikawa, T. Sugiura, Y. Torii, and T. Kuga, Phys. Rev. A **69**, 041603 (2004).

[74] H. F. Hess, Phys. Rev. B **34**, 3476 (1986).

[75] W. Ketterle and N. J. van Druten, in *Advances in Atomic, Molecular, and Optical Physics*, edited by B. Bederson and H. Walther (Academic Press, San Diego, 1996), vol. 37, pp. 181–236.

[76] O. J. Luiten, M. W. Reynolds, and J. T. M. Walraven, Phys. Rev. A **53**, 381 (1996).

[77] C. W. Gardiner, P. Zoller, R. J. Ballagh, and M. J. Davis, Phys. Rev. Lett. **79**, 1793 (1997).

[78] H.-J. Miesner, D. M. Stamper-Kurn, M. R. Andrews, D. S. Durfee, S. Inouye, and W. Ketterle, Science **279**, 1005 (1998).

[79] J. M. Vogels, K. Xu, and W. Ketterle, Phys. Rev. Lett. **89**, 020401 (2002).

[80] A. Perrin, H. Chang, V. Krachmalnicoff, M. Schellekens, D. Boiron, A. Aspect, and C. I. Westbrook, Phys. Rev. Lett. **99**, 150405 (2007).

[81] R. G. Dall, L. J. Byron, A. G. Truscott, G. R. Dennis, M. T. Johnsson, M. Jeppesen, and J. J. Hope, Opt. Express **15**, 17673 (2007).

[82] M. Fierz and W. Pauli, Proceedings of the Royal Society of London. Series A, Mathematical and Physical Sciences **173**, 211 (1939).

[83] A. Einstein, Sitzber. Kgl. Preuss. Akad. Wiss **261**, 1924 (1924).

[84] A. Einstein, Sitzungsber. Kgl. Preuss. Akad. Wiss **261**, 3 (1925).

[85] S. Bose, Zeitschrift für Physik **26**, 178 (1924).

[86] A. J. Leggett, Rev. Mod. Phys. **73**, 307 (2001).

[87] R. Shankar, *Principles of Quantum Mechanics* (Plenum Press, New York, 1994).

[88] L. Bergmann and C. Schaefer, *Constituents of Matter* (Walter de Gruyter, 1997).

[89] H. J. Metcalf and P. van der Straten, *Laser Cooling and Trapping* (Springer-Verlag, New York, 1999).

[90] T.-L. Ho, Phys. Rev. Lett. **81**, 742 (1998).

[91] E. G. M. van Kempen, S. J. J. M. F. Kokkelmans, D. J. Heinzen, and B. J. Verhaar, Phys. Rev. Lett. **88**, 093201 (2002).

[92] E. Noether, Gott. Nachr pp. 235–257 (1918).

[93] M. Greiner, O. Mandel, T. W. Hänsch, and I. Bloch, Nature **419**, 51 (2002).

[94] A. J. Leggett and F. Sols, Found. Phys. **21**, 353 (1991).

[95] K. Mølmer, Phys. Rev. A **55**, 3195 (1997).

[96] P. A. Ruprecht, M. Edwards, K. Burnett, and C. W. Clark, Phys. Rev. A **54**, 4178 (1996).

[97] M. Edwards, P. A. Ruprecht, K. Burnett, R. J. Dodd, and C. W. Clark, Phys. Rev. Lett. **77**, 1671 (1996).

[98] F. Dalfovo and S. Stringari, Phys. Rev. A **53**, 2477 (1996).

[99] M. Edwards, R. J. Dodd, C. W. Clark, P. A. Ruprecht, and K. Burnett, Phys. Rev. A **53**, R1950 (1996).

[100] B. M. Caradoc-Davies, R. J. Ballagh, and K. Burnett, Phys. Rev. Lett. **83**, 895 (1999).

[101] B. M. Caradoc-Davies, Phd thesis, University of Otago (2000).

[102] F. Dalfovo, C. Minniti, S. Stringari, and L. Pitaevskii, Phys. Lett. A **227**, 259 (1997).

[103] S. Burger, K. Bongs, S. Dettmer, W. Ertmer, K. Sengstock, A. Sanpera, G. V. Shlyapnikov, and M. Lewenstein, Phys. Rev. Lett. **83**, 5198 (1999).

[104] M. A. Kasevich, Science **298**, 1363 (2002).

[105] R. G. Dall and A. G. Truscott, Optics Communications **270**, 255 (2007).

[106] J.-F. Riou, Ph.D. thesis, Université Paris Sud (2006).

[107] N. P. Robins, A. K. Morrison, J. J. Hope, and J. D. Close, Phys. Rev. A **72**, 031606(R) (2005).

[108] J. Ruostekoski, T. Gasenzer, and D. A. W. Hutchinson, Phys. Rev. A **68**, 011604 (2003).

[109] A. Couvert, M. Jeppesen, T. Kawalec, G. Reinaudi, R. Mathevet, and D. Guéry-Odelin, Europhys. Lett. **83**, 50001 (2008).

[110] R. G. Dall, S. S. Hodgman, M. T. Johnsson, K. G. H. Baldwin, and A. G. Truscott, Phys. Rev. A **81**, 011602 (2010).

[111] Y. Le Coq, J. A. Retter, S. Richard, A. Aspect, and P. Bouyer, Applied Physics B: Lasers and Optics **84**, 627 (2006).

[112] E. W. Streed, A. P. Chikkatur, T. L. Gustavson, M. Boyd, Y. Torii, D. Schneble, G. K. Campbell, D. E. Pritchard, and W. Ketterle, Rev. Sci. Instrum. **77**, 023106 (2006).

[113] M. O. Scully and M. S. Zubairy, *Quantum Optics* (Cambridge University Press, Cambridge, 1997).

[114] I. R. Senitzky, Phys. Rev. **119**, 670 (1960).

[115] I. R. Senitzky, Phys. Rev. **124**, 642 (1961).

[116] C. W. Gardiner and P. Zoller, *Quantum Noise*, Springer Series in Synergetics (Springer, 2004), 3rd ed.

[117] F. Bardou, O. Emile, J.-M. Courty, C. I. Westbrook, and A. Aspect, Europhys. Lett. **20**, 681 (1992).

[118] G. V. Shlyapnikov, J. T. M. Walraven, U. M. Rahmanov, and M. W. Reynolds, Phys. Rev. Lett. **73**, 3247 (1994).

[119] V. Venturi and I. B. Whittingham, Phys. Rev. A **61**, 060703 (2000).

[120] R. J. W. Stas, J. M. McNamara, W. Hogervorst, and W. Vassen, Phys. Rev. A **73**, 032713 (2006).

[121] C. W. Gardiner, *Handbook of Stochastic Methods*, Springer Series in Synergetics (Springer, Berlin, 2004), 3rd ed.

[122] A. Gilchrist, C. W. Gardiner, and P. D. Drummond, Phys. Rev. A **55**, 3014 (1997).

[123] A. Sinatra, C. Lobo, and Y. Castin, J. Phys. B **35**, 3599 (2002).

[124] A. Norrie, PhD Thesis, University of Otago (2005).

[125] A. A. Norrie, R. J. Ballagh, and C. W. Gardiner, Phys. Rev. A **73**, 043617 (2006).

[126] A. A. Norrie, R. J. Ballagh, C. W. Gardiner, and A. S. Bradley, Phys. Rev. A **73**, 043618 (2006).

[127] A. Polkovnikov, Phys. Rev. A **68**, 053604 (2003).

[128] R. Scott, C. Gardiner, and D. Hutchinson, Laser Phys. **17**, 527 (2007).

[129] M. R. Hush, A. R. R. Carvalho, and J. J. Hope, Phys. Rev. A **81**, 033852 (2010).

[130] N. P. Proukakis and B. Jackson, J. Phys. B **41**, 203002 (2008).

[131] G. C. Wick, Phys. Rev. **80**, 268 (1950).

[132] J.-P. Blaizot and G. Ripka, *Quantum Theory of finite systems* (MIT Press, 1986).

[133] M. J. Davis, C. W. Gardiner, and R. J. Ballagh, Phys. Rev. A **62**, 063608 (2000).

[134] M. J. Bijlsma, E. Zaremba, and H. T. C. Stoof, Phys. Rev. A **62**, 063609 (2000).

[135] C. W. Gardiner and P. Zoller, Phys. Rev. A **55**, 2902 (1997).

[136] D. Jaksch, C. W. Gardiner, and P. Zoller, Phys. Rev. A **56**, 575 (1997).

[137] C. W. Gardiner and P. Zoller, Phys. Rev. A **58**, 536 (1998).

[138] D. Jaksch, C. W. Gardiner, K. M. Gheri, and P. Zoller, Phys. Rev. A **58**, 1450 (1998).

[139] C. W. Gardiner and P. Zoller, Phys. Rev. A **61**, 033601 (2000).

[140] M. D. Lee and C. W. Gardiner, Phys. Rev. A **62**, 033606 (2000).

[141] P. B. Blakie, A. S. Bradley, M. J. Davis, R. J. Ballagh, and C. W. Gardiner, Advances in Physics **57**, 363 (2008).

[142] E. Zaremba, T. Nikuni, and A. Griffin, J. Low Temp. Phys. **116**, 277 (1999).

[143] G. Collecutt and P. D. Drummond, Computer Physics Communications **142**, 219 (2001), see also `www.xmds.org`.

[144] R. Kosloff and D. Kosloff, J. Comput. Phys. **63**, 363 (1986).

[145] D. Neuhasuer and M. Baer, J. Chem. Phys. **90**, 4351 (1989).

[146] R. G. Dall, L. J. Byron, A. G. Truscott, G. R. Dennis, M. T. Johnsson, and J. J. Hope, Phys. Rev. A **79**, 011601(R) (2009).

[147] M. D. Reid and P. D. Drummond, Phys. Rev. Lett. **60**, 2731 (1988).

[148] D. F. Walls and G. J. Milburn, *Quantum Optics* (Springer-Verlag, Berlin, 1994).

[149] M. Fattori, C. D'Errico, G. Roati, M. Zaccanti, M. Jona-Lasinio, M. Modugno, M. Inguscio, and G. Modugno, Phys. Rev. Lett. **100**, 080405 (2008).

[150] M. Gustavsson, E. Haller, M. J. Mark, J. G. Danzl, G. Rojas-Kopeinig, and H.-C. Nägerl, Phys. Rev. Lett. **100**, 080404 (2008).

[151] R. Ozeri, N. Katz, J. Steinhauer, and N. Davidson, Rev. Mod. Phys. **77**, 187 (2005).

[152] U. Leonhardt, T. Kiss, and P. Öhberg, Phys. Rev. A **67**, 033602 (2003).

[153] N. N. Bogoliubov, J. Phys. (Moscow) **11**, 23 (1947).

[154] D. M. Stamper-Kurn, A. P. Chikkatur, A. Görlitz, S. Inouye, S. Gupta, D. E. Pritchard, and W. Ketterle, Phys. Rev. Lett. **83**, 2876 (1999).

[155] F. Zambelli, L. Pitaevskii, D. M. Stamper-Kurn, and S. Stringari, Phys. Rev. A **61**, 063608 (2000).

[156] P. J. Leo, V. Venturi, I. B. Whittingham, and J. F. Babb, Phys. Rev. A **64**, 042710 (2001).

[157] A. Widera, F. Gerbier, S. Fölling, T. Gericke, O. Mandel, and I. Bloch, New J. Phys. **8**, 152 (2006).

[158] A. L. Fetter and J. D. Walecka, *Quantum Theory of Many-Particle Systems* (McGraw-Hill, New York, 1971).

[159] A. H. Nayfeh and B. Balachandran, *Applied Nonlinear Dynamics*, Wiley Series in Nonlinear Science (Wiley, 1995).

[160] A. J. Schwartz, Amer. J. Math. **85**, 453 (1963).

[161] J. H. Shirley, Phys. Rev. **138**, B979 (1965).

[162] P. Hanggi, Phys. Rep. **304**, 229 (1998).

[163] J. C. Garrison, Am. J. Phys. **67**, 196 (1999).

[164] F. Moulton, *Differential Equations* (MacMillan Company, New York, 1958).

[165] A. Einstein, B. Podolsky, and N. Rosen, Phys. Rev. **47**, 777 (1935).

[166] A. Aspect, J. Dalibard, and G. Roger, Phys. Rev. Lett. **49**, 1804 (1982).

[167] J. P. Boyd, *Chebyshev and Fourier Spectral Methods* (Dover, 2000), 2nd ed.

[168] G. B. Arfken and H. J. Weber, *Mathematical Methods for Physicists* (Harcourt, San Diego, 2005), 6th ed.

[169] S. Ronen, D. C. E. Bortolotti, and J. L. Bohn, Phys. Rev. A **74**, 013623 (2006).

[170] P. E. Kloeden and E. Platen, *Numerical Solution of Stochastic Differential Equations* (Springer, 1992).

[171] K. Burrage, P. Burrage, and J. Belward, BIT Numerical Mathematics **37**, 771 (1997).

[172] A. Rößler, BIT Numerical Mathematics **47**, 657 (2007).

[173] A. Rößler, SIAM Journal on Numerical Analysis **47**, 1713 (2009).

[174] A. Javan, W. R. Bennett, and D. R. Herriott, Phys. Rev. Lett. **6**, 106 (1961).

[175] T. H. Maiman, Nature **187**, 493 (1960).

[176] D. Döring, G. R. Dennis, N. P. Robins, M. Jeppesen, C. Figl, J. J. Hope, and J. D. Close, Phys. Rev. A **79**, 063630 (2009).

[177] N. P. Robins, C. Figl, M. Jeppesen, G. R. Dennis, and J. D. Close, Nat. Phys. **4**, 731 (2008).

[178] A. P. Chikkatur, Y. Shin, A. E. Leanhardt, D. Kielpinski, E. Tsikata, T. L. Gustavson, D. E. Pritchard, and W. Ketterle, Science **296**, 2193 (2002).

[179] S. Schmid, G. Thalhammer, K. Winkler, F. Lang, and J. H. Denschlag, New J. Phys. **8**, 159 (2006).

[180] T. Lahaye, J. M. Vogels, K. J. Günter, Z. Wang, J. Dalibard, and D. Guéry-Odelin, Phys. Rev. Lett. **93**, 093003 (2004).

[181] M. Greiner, I. Bloch, T. W. Hänsch, and T. Esslinger, Phys. Rev. A **63**, 031401 (2001).

[182] A. Greiner, J. Sebastian, P. Rehme, A. Aghajani-Talesh, A. Griesmaier, and T. Pfau, J. Phys. B **40**, F77 (2007).

[183] M. Olshanii, Y. Castin, and J. Dalibard, in *Proceedings of the 12th International Conference on Laser Spectroscopy*, edited by M. Inguscio, M. Allegrini, and A. Lasso (World Scientific, Singapore, 1996).

[184] U. Janicke and M. Wilkens, Europhys. Lett. **35**, 561 (1996).

[185] R. J. C. Spreeuw, T. Pfau, U. Janicke, and M. Wilkens, Europhys. Lett. **32**, 469 (1995).

[186] J. I. Cirac and M. Lewenstein, Phys. Rev. A **53**, 2466 (1996).

[187] J. I. Cirac, M. Lewenstein, and P. Zoller, Europhys. Lett. **35**, 647 (1996).

[188] L. Santos, Z. Idziaszek, J. I. Cirac, and M. Lewenstein, J. Phys. B **33**, 4131 (2000).

[189] Y. Castin, J. I. Cirac, and M. Lewenstein, Phys. Rev. Lett. **80**, 5305 (1998).

[190] J. I. Cirac, M. Lewenstein, and P. Zoller, Phys. Rev. A **50**, 3409 (1994).

[191] M. Vengalattore, W. Rooijakkers, R. Conroy, and M. Prentiss, Phys. Rev. A **67**, 063412 (2003).

[192] L. Santos, F. Floegel, T. Pfau, and M. Lewenstein, Phys. Rev. A **63**, 063408 (2001).

[193] S. Wolf, S. J. Oliver, and D. S. Weiss, Phys. Rev. Lett. **85**, 4249 (2000).

[194] L. Santos and M. Lewenstein, Phys. Rev. A **60**, 3851 (1999).

[195] F. Floegel, L. Santos, and M. Lewenstein, Europhys. Lett. **54**, 279 (2001).

[196] C. J. Myatt, E. A. Burt, R. W. Ghrist, E. A. Cornell, and C. E. Wieman, Phys. Rev. Lett. **78**, 586 (1997).

[197] O. Zobay and G. M. Nikolopoulos, Phys. Rev. A **72**, 041604 (2005).

[198] J. R. Kuklinski, U. Gaubatz, F. T. Hioe, and K. Bergmann, Phys. Rev. A **40**, 6741 (1989).

[199] J. Dugué, N. P. Robins, C. Figl, M. Jeppesen, P. Summers, M. T. Johnsson, J. J. Hope, and J. D. Close, Phys. Rev. A **75**, 053602 (2007).

[200] C. Eckart, Rev. Mod. Phys. **2**, 305 (1930).

[201] D. M. Brink and G. R. Satchler, *Angular Momentum* (Oxford, 1962).

[202] D. A. Steck, *Rubidium 87 D Line Data* (2009), revision 2.1.2, URL `http://steck.us/alkalidata`.

[203] S. A. Haine and J. J. Hope, Phys. Rev. A **68**, 023607 (2003).

[204] T. Müller, T. Wendrich, M. Gilowski, C. Jentsch, E. M. Rasel, and W. Ertmer, Phys. Rev. A **76**, 063611 (2007).

[205] C. W. Gardiner, Phys. Rev. A **56**, 1414 (1997).

[206] E. A. Burt, R. W. Ghrist, C. J. Myatt, M. J. Holland, E. A. Cornell, and C. E. Wieman, Phys. Rev. Lett. **79**, 337 (1997).

[207] J. Söding, D. Guéry-Odelin, P. Desbiolles, F. Chevy, H. Inamori, and J. Dalibard, Applied Physics B: Lasers and Optics **69**, 257 (1999).

[208] M. Köhl, M. J. Davis, C. W. Gardiner, T. W. Hänsch, and T. Esslinger, Phys. Rev. Lett. **88**, 080402 (2002).

[209] W. H. Press, S. A. Teukolsky, W. T. Vetterling, and B. P. Flannery, *Numerical Recipes* (Cambridge University Press, 2007), 3rd ed.

[210] K. Dieckmann, R. J. C. Spreeuw, M. Weidemüller, and J. T. M. Walraven, Phys. Rev. A **58**, 3891 (1998).

[211] S. Chaudhuri, S. Roy, and C. S. Unnikrishnan, Phys. Rev. A **74**, 023406 (2006).

[212] P. Cren, C. F. Roos, A. Aclan, J. Dalibard, and D. Guéry-Odelin, Eur. Phys. J. D **20**, 107 (2002).

[213] Z. T. Lu, K. L. Corwin, M. J. Renn, M. H. Anderson, E. A. Cornell, and C. E. Wieman, Phys. Rev. Lett. **77**, 3331 (1996).

[214] C. Slowe, L. Vernac, and L. V. Hau, Rev. Sci. Instrum. **76**, 103101 (2005).

[215] T. Müller, M. Gilowski, M. Zaiser, P. Berg, C. Schubert, T. Wendrich, W. Ertmer, and E. M. Rasel, Eur. Phys. J. D **53**, 273 (2009).

[216] N. P. Proukakis, Laser Phys. **13**, 527 (2003).

[217] E. Mandonnet, A. Minguzzi, R. Dum, I. Carusotto, Y. Castin, and J. Dalibard, Eur. Phys. J. D **10**, 9 (2000).

[218] C. F. Roos, P. Cren, D. Guéry-Odelin, and J. Dalibard, Europhys. Lett. **61**, 187 (2003).

[219] C. F. Roos, P. Cren, T. Lahaye, J. Dalibard, and D. Guéry-Odelin, Laser Phys. **13**, 605 (2003).

[220] J. Vogels, T. Lahaye, C. Roos, J. Dalibard, and D. Guéry-Odelin, J. Phys. IV France **116**, 259 (2004).

[221] T. Lahaye, Z. Wang, G. Reinaudi, S. P. Rath, J. Dalibard, and D. Guery-Odelin, Phys. Rev. A **72**, 033411 (2005).

[222] S. Dimopoulos, P. W. Graham, J. M. Hogan, and M. A. Kasevich, Phys. Rev. Lett. **98**, 111102 (2007).

[223] H. Vahlbruch, M. Mehmet, S. Chelkowski, B. Hage, A. Franzen, N. Lastzka, S. Goßler, K. Danzmann, and R. Schnabel, Phys. Rev. Lett. **100**, 033602 (2008).

[224] M. Mehmet, H. Vahlbruch, N. Lastzka, K. Danzmann, and R. Schnabel, Phys. Rev. A **81**, 013814 (2010).

[225] D. Leibfried, M. D. Barrett, T. Schaetz, J. Britton, J. Chiaverini, W. M. Itano, J. D. Jost, C. Langer, and D. J. Wineland, Science **304**, 1476 (2004).

[226] C. Hempel, R. Mhaskar, M. Traxler, V. Vaidya, S. Olson, and G. Raithel, in *DAMOP* (2008), URL `http://meetings.aps.org/link/BAPS.2008.DAMOP.R1.91`.

[227] M. Traxler, C. Hempel, V. Vaidya, and G. Raithel, in *DAMOP* (2009), URL `http://adsabs.harvard.edu/abs/2009APS..DMP.E1091T`.

[228] M. Traxler, E. Power, and G. Raithel, in *DAMOP* (2010), URL `http://meetings.aps.org/Meeting/DAMOP10/Event/126082`.

[229] M. W. Jack, Phys. Rev. Lett. **89**, 140402 (2002).

[230] G. Hétet, J. J. Longdell, A. L. Alexander, P. K. Lam, and M. J. Sellars, Phys. Rev. Lett. **100**, 023601 (2008).

[231] T. Reichenbach, M. Mobilia, and E. Frey, Nature **448**, 1046 (2007).

[232] J. F. Corney, P. D. Drummond, J. Heersink, V. Josse, G. Leuchs, and U. L. Andersen, Phys. Rev. Lett. **97**, 023606 (2006).

[233] J. J. Hope and M. K. Olsen, Phys. Rev. Lett. **86**, 3220 (2001).

[234] S. Wüster, J. J. Hope, and C. M. Savage, Phys. Rev. A **71**, 033604 (2005).

[235] P. Drummond, P. Deuar, and J. Corney, Optics and Spectroscopy **103**, 7 (2007).

[236] P. D. Drummond, P. Deuar, T. G. Vaughan, and J. F. Corney, J. Mod. Opt. **54**, 2499 (2007).

[237] K. Góral and L. Santos, Phys. Rev. A **66**, 023613 (2002).

[238] K. Gawryluk, M. Brewczyk, K. Bongs, and M. Gajda, Phys. Rev. Lett. **99**, 130401 (2007).

[239] R. Stevenson, Honours thesis, The Australian National University (2008).

[240] P. D. Drummond and I. K. Mortimer, J. Comput. Phys. **93**, 144 (1991).

[241] M. J. Werner and P. D. Drummond, J. Comput. Phys. **132**, 312 (1997).

[242] M. R. Hush, A. R. R. Carvalho, and J. J. Hope, Phys. Rev. A **80**, 013606 (2009).

[243] S. S. Szigeti, M. R. Hush, A. R. R. Carvalho, and J. J. Hope, Phys. Rev. A **80**, 013614 (2009).

[244] G. van Rossum, *Python programming language*, URL `www.python.org`.

[245] T. Rudd, *Cheetah — The Python-Powered Template Engine*, URL `www.cheetahtemplate.org`.

[246] M. Frigo and S. G. Johnson, Proceedings of the IEEE **93**, 216 (2005), special issue on "Program Generation, Optimization, and Platform Adaptation".

[247] MPI Forum, *Message Passing Interface*, URL `www.mpi-forum.org`.

[248] HDF Group, *HDF5*, URL `www.hdfgroup.org/HDF5`.